Remote sensing investigations of immature faulting and distributed coseismic deformation

by

Élyse Gaudreau
B.Sc., University of Ottawa, 2016
M.Sc., University of Ottawa, 2018

A Dissertation Submitted in Partial Fulfillment of the
Requirements for the Degree of

DOCTOR OF PHILOSOPHY

in the School of Earth and Ocean Sciences


University of Victoria

I acknowledge and respect the lək$^{w}$əŋən peoples on whose traditional territory the university stands and the Songhees, Esquimalt and W̱SANEC peoples whose historical relationships with the land continue to this day.

Remote sensing investigations of immature faulting and distributed coseismic deformation

by

Élyse Gaudreau
B.Sc., University of Ottawa, 2016
M.Sc., University of Ottawa, 2018

Supervisory Committee

---

Dr. Edwin Nissen, Supervisor
(School of Earth and Ocean Sciences)

---

Dr. Lucinda Leonard, Departmental Member
(School of Earth and Ocean Sciences)

---

Dr. Andrew Schaeffer, Departmental Member
(School of Earth and Ocean Sciences)

---

Dr. Randy Scharien, Outside Member
(Department of Geography)

## ABSTRACT

Anticipating future earthquake behavior requires active faults to be accurately mapped as well as a wealth of knowledge on their physical properties and tectonic histories, but many incipient faults are unknown until after a damaging earthquake strikes. Earthquakes on so-called immature faults are also associated with near-surface slip that is distributed over zones hundreds to thousands of meters wide, rather than focused along a narrow fault with a clear surface expression as are their mature counterparts. This results in an underestimation of seismic hazard, as field surveys cannot capture the full coseismic displacement field, and typical fault slip inversions are unable to model this distributed deformation.

In this dissertation, a suite of cutting edge geodetic remote sensing techniques — Interferometric Synthetic Aperture Radar (InSAR), photogrammetry and correlation of historical optical imagery — are exploited to investigate what controls the localization of surface slip and the consequences of common modeling assumptions such as approximating a fault as a series of infinitely thin planes in an elastic halfspace. In doing so, I also shed light on the active tectonics of three study regions — northern Alaska, southern California and the Tibetan plateau — with important implications for seismic hazard assessments.

The 1971 $M_w$ 6.6 San Fernando, California, 2018 $M_w$ 6.4 and $M_w$ 6.0 Kaktovik, Alaska, and 2021 $M_w$ 7.4 Maduo, China earthquakes are three examples of major earthquakes to have ruptured immature faults that were previously unknown or considered inactive, demonstrating that incipient faults pose a significant seismic hazard. The coseismic displacement field of the 1971 San Fernando, California earthquake, extracted from historical aerial imagery, reveals in unprecedented detail the complexity of the surface deformation. There is a discrepancy between seismic data and surface (geologic and geodetic) displacement data that may be explained by the strong dynamic stresses inferred from nearby accelerometer recordings. For the 2018 Kaktovik, Alaska earthquakes, a combined analysis of InSAR and seismological data reveals that deformation in this region is accommodated by a complex network of unmapped faults that may be influenced by inherited Cordilleran structures. A survey of well-studied earthquakes from across the Tibetan plateau suggests that inherited structures may have also played a significant role in the 2021 Maduo earthquake, possibly enabling its unusually long rupture and therefore large magnitude.

Surface displacements mapped with optical imagery and InSAR show that surface slip during the 1971 San Fernando, California earthquake and multiple recent earthquakes in the Tibetan plateau was distributed over zones hundreds of meters wide. I show that this may partly explain why InSAR-derived coseismic slip models systematically underestimate

near-surface slip, with the degree of bias partly dependent on fault complexity and thus likely influenced by fault maturity. I also demonstrate that independently inverted geodetic slip models are unreliable in the shallowest 1 km of the crust, suggesting that the proportion of this shallow slip deficit that can be attributed to distributed, inelastic surface deformation cannot be meaningfully estimated.

# Contents

# List of Tables

# List of Figures

# ACKNOWLEDGEMENTS

First and foremost, I would like to thank my supervisor, Edwin Nissen for his guidance, knowledge, thoroughness and encouragement, for enabling my foray into the wonderful world of remote sensing and active tectonics, for always seeing the best in all of his students, and having a leadership style that lays the foundation of a great research group dynamic.

I would also like to thank the graduate students I overlapped with, particularly those in Ed's group, for the stimulating discussions and just being great.

This body of work would not have been possible without my collaborators, who provided data, code, enlightening discussions and advice: Eric Bergman, Harley Benz, Fengzhou Tan, Ezgi Karasozen, Gareth Funning and Jinrui Liu. James Hollingsworth deserves a separate sentence: I am really grateful to James for hosting my research visit in Grenoble and transferring so much knowledge, it was so valuable. I also need to include David Oglesby in this list, who was nice enough to host me at University of California, Riverside to teach me a thing or two about dynamic rupture modeling.

I am grateful to my supervisory committee for their helpful guidance throughout this process: Lucinda Leonard, Andrew Schaeffer and Randy Scharien.

I also need to thank the Natural Sciences and Engineering Research Council of Canada, the Southern California Earthquake Center, the Montalbano Scholars Fellowship, and the University of Victoria for funding my work.

Finally, and in keeping with being a notoriously private person, I would like to sincerely thank my close support group for their absolutely invaluable support and encouragement. You know who you are.

# Chapter 1

# Introduction

Fault zones evolve over successive earthquake cycles, growing in length and width, accumulating damage, and connecting with nearby segments, to eventually form a smoother, through-going fault that efficiently localizes deformation over a narrow zone (Dolan and Haravitch, 2014; Hatem et al., 2017; Shipton and Cowie, 2003; Wesnousky, 1988). The evolving physical properties of a fault may significantly influence earthquake behavior, which has important implications for seismic hazard (Ben-Zion and Sammis, 2003; Bruhat et al., 2016; Manighetti et al., 2007; Perrin et al., 2016; Radiguet et al., 2009). However, the process of fault evolution and how fault properties affect earthquake behavior are poorly understood since each individual fault has a distinct, complex combination of physical characteristics, tectonic history, and regional crustal stress field. Many incipient faults are also inconspicuous as they have not developed a clear topographic expression. Therefore, clues of past earthquake behavior are difficult to find in the geomorphology and these faults are often not widely known about until after a significant earthquake occurs. Moreover, models of earthquake behavior and crustal deformation that inform our understanding of seismic hazard of a given area — such as the elastic rebound model of crustal deformation, the approximation of a fault as an infinitely thin plane, and the characteristic earthquake model — have limitations that change depending on the stage of evolution of a fault, and these differences are not well-known. In this dissertation, earthquakes on faults of various maturities from a variety of tectonic settings — northern Alaska, southern California, and the Tibetan Plateau — are imaged using a mix of geodetic techniques, some of them well established (InSAR, photogrammetry) and others novel (correlation of historical optical imagery). I analyze coseismic displacement fields, geodetic slip models, field observations and fault maturity proxies to better understand the shortcomings of the routine approximation that a fault is a planar feature embedded in an elastic medium. In some instances, I gain a better

understanding of poorly characterized active tectonic settings obscured by the immaturity of their faults. Summarized below are some fundamentals of the data, techniques and modeling that feature heavily in this dissertation, followed by a summary of the structure of the dissertation, explaining how each of the three studies helps fill identified knowledge gaps.

## 1.1 SAR

Synthetic Aperture Radar (SAR) satellites are powerful Earth observation systems that are widely used to detect surface change at a millimetre scale. SAR satellites are a form of active remote sensing, equipped with an antenna that emits a radar pulse of a certain wavelength towards the Earth, then detects the backscattered energy. The amplitude and phase of the returning signal are affected by the geometry, roughness and dielectric properties of the target. The location of the target is deduced from the two-way distance between the satellite and the ground, and the Doppler shift, which indicates whether the satellite is moving towards or away from the target. The sensors emit radar pulses at an angle from the vertical, imaging a region usually to the right of the satellite path (Figure 1.1). If the sensor was oriented vertically (nadir), the return time and Doppler shift would lead to an ambiguity of the target location, at two symmetric equidistant points on the ground, to the left and right of the satellite track. This ambiguity disappears when the sensor is positioned at an angle from the vertical, imaging only the area to one side of the satellite (Figure 1.1).

The spatial resolution of SAR data in the direction of the satellite path (the along-track or azimuth direction) is lower than the resolution in the direction perpendicular to it (the range direction). In the along-track direction, the spatial resolution ($r_a$) depends on the length of the antenna, the slant range (the distance to the ground in the line-of-sight (LOS) direction) and the signal wavelength:

$$r_a = \frac{\lambda R}{2L}, \tag{1.1}$$

where $\lambda$ is the wavelength, $R$ is the slant range distance to the target, and $L$ is the antenna length (see diagram in Figure 1.1).

In order to achieve a reasonable spatial resolution (of tens of meters) in the azimuth direction, successive radar pulses are processed to simulate the effect of a large antenna, giving the term 'synthetic' aperture radar (otherwise the antenna would need to be much larger than what a satellite can carry). This is based on the concept that an array of antennas emitting radar pulses in phase will create a wider beam than can be created with a

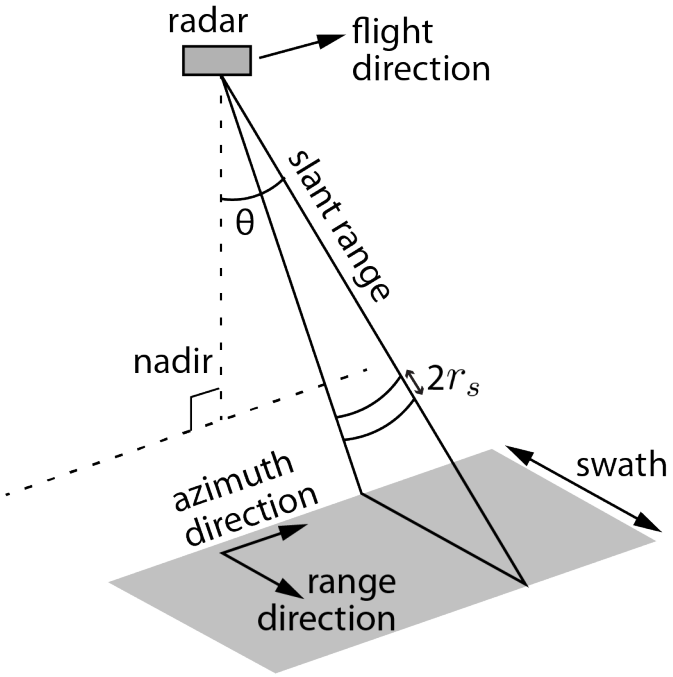


Figure 1.1: SAR satellite geometry (modified from the Canada Centre for Remote Sensing). $\theta$ is the line-of-sight (LOS) incidence angle and $2r_s$ is the pulse length.

single antenna. Since the spatial resolution is inversely proportional to the antenna length (equation 1.1), the data from the array can be combined to obtain a finer spatial resolution than would normally be obtained using a single antenna. SAR satellites that have a single antenna form this 'array' using successive radar pulses emitted at different times and locations along a section of the orbital path.

The range direction resolution ($r_s$) depends on the signal's pulse duration:

$$r_s = \frac{cr_p}{2}, \tag{1.2}$$

where $c$ is the speed of light (the speed at which the radar pulse travels) and $r_p$ is the duration of the pulse. The slant-range resolution can be projected on the ground, to obtain the ground resolution:

$$r_g = \frac{cr_p}{2\sin\theta}, \tag{1.3}$$

where $\theta$ is the LOS incidence angle.

### 1.1.1 InSAR

Some SAR satellites collect data over a given area at regular intervals with the same viewing geometry. Interferometric SAR (InSAR) is a technique that exploits the phase information of repeat data acquisitions to map horizontal and vertical changes in ground deformation. For example, coseismic surface deformation can be precisely mapped over hundreds of kilometers given a pre-earthquake and a post-earthquake image.

The spatial distribution of the phase in an individual SAR image is random. This reflects that the phase of a return from an individual pixel is not only a function of the distance between the sensor and the ground (the range phase), but also incorporates an additional random component from the coherent sum of a varying number and arrangement of scatterers within the pixel area. Tracking ground deformation requires isolating the range phase. The random component will be constant if the scatterers do not change between data acquisitions, allowing the range phase to be isolated using interferometry, wherein the random component is cancelled out by processing two or more SAR images. The result is called an interferogram, a map of the difference in phase at corresponding points in a pair of images. Interferograms reveal a fringe pattern of bands or concentric shapes that cycle through 0 – $2\pi$. If two images are taken simultaneously from different positions in space, the resulting interferogram will represent the topography of the imaged area. Alternatively, repeat-track

interferometry calculates the phase difference from SAR images acquired at different times from a similar location. In this case, the phase difference captures the topography as well as any shifts in the ground towards or away from the sensor that occurred between data acquisitions, so long as the acquisition geometry is the same and the distance between the sensor positions at the time of sensing (known as the baseline) is small (Figure 1.2; Gabriel et al., 1989; Goldstein et al., 1993; Massonnet et al., 1993).

For repeat-pass interferometry, the phase difference is generally given by

$$\phi = \frac{4\pi\rho}{\lambda}\delta\rho, \tag{1.4}$$

where $\rho$ is the slant-range of the first image, $\delta\rho$ is the slant-range difference between the two images and $\lambda$ is the wavelength.

If the ground stayed motionless between the two data acquisitions, equation 1.4 can be written in terms of the LOS unit vector of the first acquisition $\hat{l}_1$ and the baseline $\vec{B}$ (the vector connecting the satellite locations of the first and second acquisitions), since $\delta\rho$ can be approximated as the projection of $\vec{B}$ onto $\hat{l}_1$, (Figure 1.2 Rosen et al., 2000)):

$$\phi = -\frac{4\pi\rho}{\lambda}\langle\hat{l}_1, \vec{B}\rangle. \tag{1.5}$$

If surface displacements are contributing towards the phase difference, then

$$\phi = \frac{4\pi\rho}{\lambda}(-\langle\hat{l}_1, \vec{B}\rangle + \langle\hat{l}_1, \vec{D}\rangle), \tag{1.6}$$

where the displacement term is $\vec{D}$. Using a pre-existing topography model, $\langle\hat{l}_1, \vec{B}\rangle$ can be eliminated, isolating the contribution of the surface displacements (Figure 1.2; Massonnet et al., 1993). This is known as differential interferometry (Rosen et al., 2000).

Interferograms are usually unwrapped (converted to a continuous displacement field) by integrating the phase gradient between adjacent pixels. This makes them easier to interpret. The range change obtained through interferometry is in the oblique line-of-sight (LOS) direction, and any surface change that is detected will thus have a horizontal and vertical component. Since InSAR satellites follow roughly polar orbits and look towards the right, they will image any given area from two different view points: 1) as they travel along the north to south leg of the orbit (the descending track), where the horizontal component of the LOS vector points WNW, then 2) from south to north (the ascending track) where the horizontal component of the LOS vector points ENE. Interferograms created from the two perspectives can be combined to reduce ambiguities between vertical and horizontal

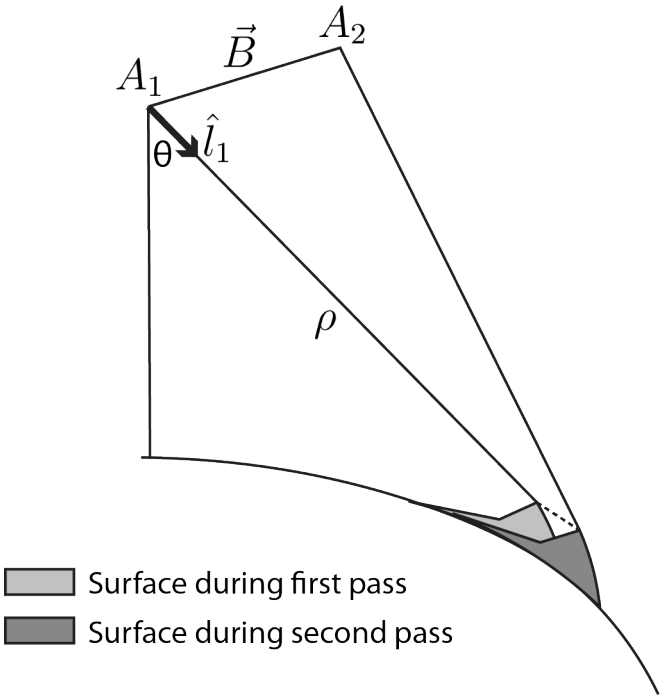


Figure 1.2: Geometry of repeat-pass SAR interferometry with a component of displacement represented by the dashed line. Modified from Rosen et al. (2000).

displacements caused by the slanted LOS vector.

InSAR was first applied to active tectonics when Massonnet et al. (1993) imaged coseismic deformation of the 1992 $M_W$ 7.2 Landers earthquake in eastern California. Since then, sensor technology and data analysis techniques have rapidly progressed: there are currently dozens of SAR satellites operated by government agencies and private companies that are constantly monitoring the Earth's surface, and numerous proprietary and open source InSAR processing software have been developed. These data are routinely used for applications such as natural hazard mitigation and subsidence monitoring. Much progress has been made in time series processing, allowing for detailed mapping of interseismic deformation and strain accumulation over areas spanning thousands of kilometers (e.g., Grandin et al., 2016; Weiss et al., 2020).

### 1.1.2 Advantages and Disadvantages

SAR satellites have many advantages. As previously mentioned, InSAR data enable the precise monitoring of horizontal and vertical changes on the Earth's surface. Furthermore, SAR satellites are highly productive as they can acquire data at any time of day (emitting the signal that they detect rather than relying on natural illumination), can image the Earth's surface even in the presence of cloud cover, and may revisit the same area several times per month.

Unfortunately, many InSAR data sets decorrelate in snow-covered or densely vegetated areas, and areas of steep mountainous topography. This is particularly an issue for C-band satellites such as the European Space Agency's Sentinel-1 satellites that emit a $\sim$5.547 cm-wavelength signal. The ALOS-2 satellites (Japan Aerospace Exploration Agency) emit a 22.9 cm-wavelength signal (L-band) which can penetrate forest canopy, offering a much better signal in densely vegetated areas. Decorrelation has reduced in recent years due to shortened revisit periods. Coseismic interferograms also tend to decorrelate near surface ruptures, principally because of the steep displacement gradients that accompany major surface faulting (decorrelation will occur if the change in phase over the area of one pixel is $> 2\pi$, e.g., Massonnet et al., 1993), and secondarily because of changes to pixel back scattering characteristics induced by strong ground shaking (e.g., building damage, landsliding, liquefaction). I return to this point later on in the Introduction chapter. Also, "coseismic" interferograms usually include postseismic deformation because SAR satellite revisit periods are multiple days to weeks.

Furthermore, InSAR is much more sensitive to east-west and vertical than north-south

deformation due to the orientation of the polar orbits and the slanted viewing geometry (Funning et al., 2005). However, recent advances in data processing enable the robust estimation of north-south deformation in narrow but regularly-spaced zones within an InSAR image (burst overlap interferometry; Grandin et al., 2016). This is particularly useful when imaging long-wavelength signals.

Finally, the number of earthquakes and interseismic processes that can be studied with InSAR are very limited, since the data record only spans a few decades.

## 1.2 Optical imagery

Optical sensors are 'passive' meaning that they measure solar radiation that has been reflected on the Earth's surface. The sensors measure the total amplitude for at least one band of the electromagnetic spectrum. Geodesists started using photographs for topographic surveying as early as 1849, only a few years after film photography was first developed (Wolf and Dewitt, 2000). Subsequently, the early 20th century saw the invention of the airplane, which proliferated in use following World War I and World War II. As a result, aerial photography technologies rapidly evolved as reconnaissance and topographic surveys became a priority for government agencies and private companies in Western countries. Vast improvements in sensor technology and processing techniques have since expanded the use of optical data to encompass military surveillance, urban planning, agriculture, climate change, and geophysics, among others.

Most contemporary optical satellites, such as Landsat, SPOT (Système Pour l'Observation de la Terre), IRS (Indian Remote Sensing), and WorldView, are equipped with multispectral sensors and higher-resolution panchromatic sensors. Multispectral sensors partition the optical data into several narrow spectral bands which often span $<0.1\,\mu\mathrm{m}$, creating multilayered images. Panchromatic sensors are sensitive to a wider band, spanning several of the multispectral bands on the electromagnetic spectrum. Since panchromatic images are created using the energy from a wider band, the measured intensity and signal to noise ratio are higher than in a multispectral image, allowing the sensor to detect smaller intensity variations given a certain radiometric resolution, at the expense of spectral information. Since panchromatic sensors only detect a single band, a panchromatic image can have many times the amount of pixels yet take up a similar amount of data volume as a lower-resolution multispectral image because of its many layers. Given data volume limitations, panchromatic images therefore usually have a much higher spatial resolution than their multispectral counterparts.

### 1.2.1 Pixel tracking

Pixel tracking, or optical image correlation, is a quantitative method of mapping Earth surface horizontal displacements by finding matching groups of pixels in images taken at different times and measuring how much they've shifted laterally. SAR amplitude images can be correlated in a similar way in a pair of methods known as SAR range and azimuth offsets, though I will focus on the optical case. This requires the images first to be accurately orthorectified (have image distortions removed) and co-registered (the images must accurately superimpose), the accuracy of which determines the detection threshold of ground displacements.

#### Orthorectification

Orthorectifying each image involves firstly projecting each pixel from the camera's focal plane to a ground projection with reference to a datum, using constraints from the sensor's acquisition geometry and a digital elevation model (DEM), and secondly resampling the data according to the new projection. Reprojecting all images to a common reference system before calculating displacements removes any baseline constraints such that images acquired from different viewing geometries and even different sensors may be used to track changes (in marked contrast with InSAR which requires exactly the same sensor specification). Modern, digital sensors record precise metadata on the camera parameters with every data acquisition. However, most historical photographs do not have detailed metadata describing the camera lens or the camera location at the time of data acquisition, making the orthorectification process lengthy and tedious, especially for larger datasets comprising tens or hundreds of photographs. This process is explained in more detail in chapter 3.

Projecting a photograph to an accurate map geometry requires correcting for distortions caused by camera lenses and by topography, as well as orienting the photograph in space. Lens properties affecting the camera distortions are called the 'intrinsic' camera parameters, and include the focal length, optical center and radial distortion. The focal length is the distance between the center of the lens and the plane of infinite focus, which changes depending on the lens shape, and controls the camera's field of view and most of the photographic distortions (Figure 1.3).

The optical center is theoretically the center point of the photograph, but is usually shifted because of imperfections stemming from the manufacturing of the lens and camera. Radial distortions are symmetric distortions radiating outwards from the optical center. The 'extrinsic' camera parameters describe the orientation of the camera in space using two

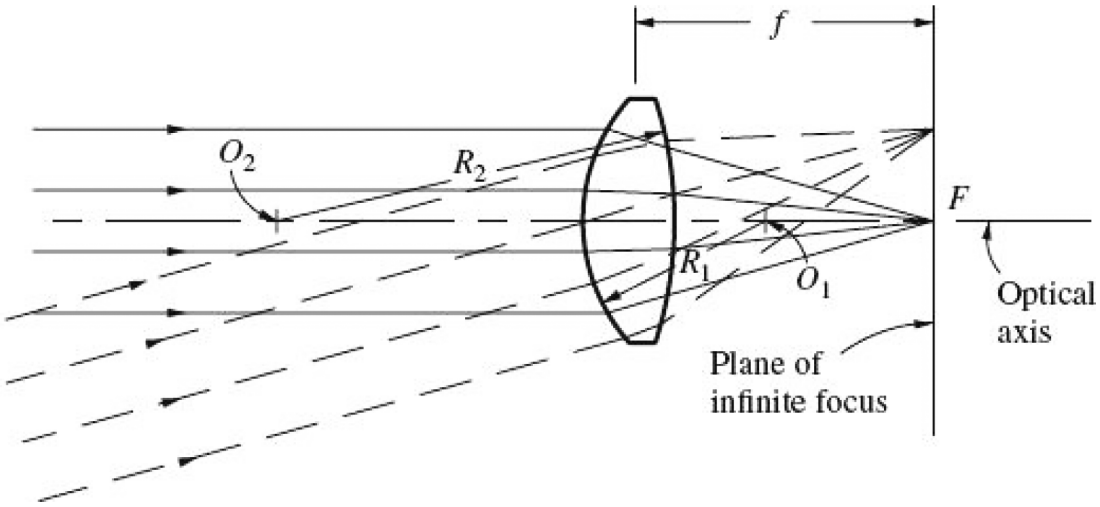


Figure 1.3: Lens geometry. Optical axis (connecting centers of curvature $O_1$ and $O_2$), focal length $f$, and plane of infinite focus. $R_1$ and $R_2$ are the lens surface radii and $F$ is the focal point. Modified from Wolf and Dewitt (2000).

parameters: (i) the geocentric coordinates of the camera center when the image was taken, and (ii) the rotation matrix that gives the absolute orientation of the camera in the geocentric coordinate system. Topographic distortions increase outwards of the optical center for nadir-oriented film cameras, since the increasingly oblique viewing angle towards the edges of the film creates perspective distortions. These distortions are corrected for using a reference DEM.

**Phase correlation**

There are a number of signal processing techniques that can be used to detect lateral displacements of objects by searching for similar groups of pixels between two orthorectified images taken at different times. For example, a phase correlation is performed on some of the data in this dissertation with a multi-scale sliding window using the COSI-Corr software (Ayoub et al., 2009; Ayoub et al., 2017; Leprince et al., 2007). A window of varying size is used to capture longer and shorter wavelength displacements: the correlation will be calculated using the largest size specified, and if successful, progressively smaller window sizes will be used until decorrelation occurs. The displacement calculated using the smallest window size before decorrelation is chosen. Phase correlation uses the Fourier shift theorem to measure displacements between two datasets: if image subsets $i_1$ and $i_2$ are identical except for a shift in the $x$ and $y$ directions $(\Delta x, \Delta y)$ such that

$$i_2(x, y) = i_1(x - \Delta x, y - \Delta y), \tag{1.7}$$

then the Fourier transform of $i_2$ becomes

$$I_2(\omega_x, \omega_y) = I_1(\omega_x, \omega_y) e^{-j(\omega_x \Delta x + \omega_y \Delta y)} \tag{1.8}$$

where $\omega_x$,$\omega_y$ are the frequency variables of the $x$ and $y$ components. By taking the normalized cross-spectrum of the two images

$$C_{i_1 i_2}(\omega_x, \omega_y) = \frac{I_1(\omega_x, \omega_y) I_2^*(\omega_x, \omega_y)}{I_1(\omega_x, \omega_y) I_2^*(\omega_x, \omega_y)} = e^{-j(\omega_x \Delta x + \omega_y \Delta y)} \tag{1.9}$$

then computing its inverse Fourier transform

$$F^{-1}\{e^{-j(\omega_x \Delta x + \omega_y \Delta y)}\} = \delta(x + \Delta x, y + \Delta y), \tag{1.10}$$

the shift between $i_1$ and $i_2$ is then isolated, at the location where the similarity value (normalized cross-spectrum) is highest.

### 1.2.2 Photogrammetry

Photogrammetry is widely used in the geosciences to create DEMs or 3-D models of hand specimens, outcrops or paleoseismic trenches. While optical image correlation described above only measures horizontal ground displacements, multiple DEMs of the same location acquired at different times can be used to extract information on vertical ground deformation. Stereo images are required to build photogrammetric DEMs, where adjacent photographs from the same survey typically overlap by at least 60% such that ground objects are imaged at least twice and from different angles. Hundreds to thousands of corresponding points between overlapping images are matched using some measure of correlation. The key to extracting topographic information from stereo photographs lies in the parallax: the apparent shift of an object within a reference frame when observed from a different angle. For aerial surveys, the shifts (or disparities) in the location of objects with respect to the camera frame between successive overlapping photographs depends on the focal length ($f$), baseline distance of the camera location between successive data acquisitions ($B$), and the distance to the ground ($H - h_A$) (Figure 1.4). Disparity maps are produced based on the match points of overlapping photographs, before the topography is estimated. The relationship between the focal length, baseline, parallax of a point ($x_a - x'_a$), and topography ($h_A$) is:

$$h_A = H - \frac{Bf}{x_a - x'_a} \tag{1.11}$$

### 1.2.3 Advantages and Disadvantages

For the purposes of this dissertation, the main advantage of mapping surface deformation using optical (or SAR amplitude) imagery over InSAR is that with pixel tracking and DEM differencing, high coseismic displacement gradients near a fault can be resolved. Furthermore, the optical image data record goes back several decades farther than the InSAR record, with the potential to capture many more, and earlier, earthquakes.

However, the optical data record is limited in other ways. Since photographic sensors are passive, they only acquire useful data in daylight. Clouds are an obstacle, making optical sensing particularly challenging in areas with persistent or seasonal cloud cover.

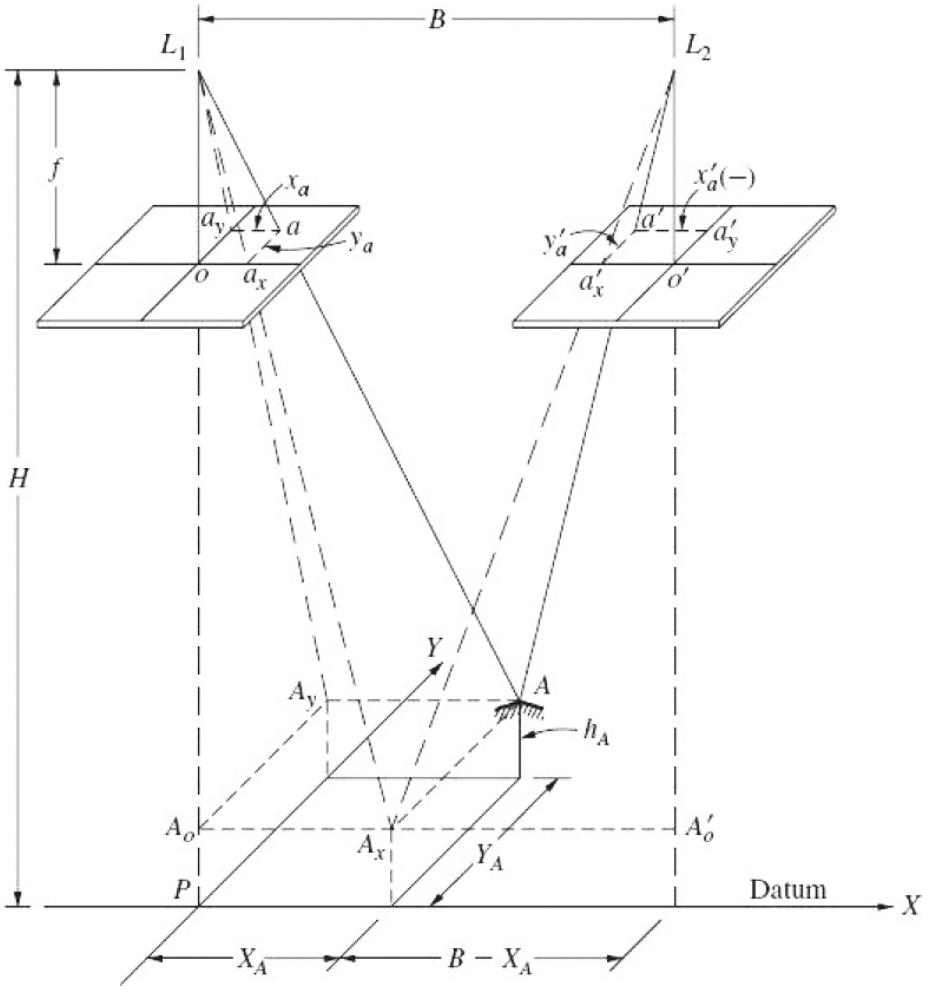


Figure 1.4: Viewing geometry of overlapping photographs. From Wolf and Dewitt (2000).

Similar to InSAR, pixel tracking of optical and SAR amplitude data can decorrelate due to changes related to vegetation, snow, landslides, agriculture, or land use changes.

Another disadvantage of pixel tracking is that the noise level and change detection threshold are higher than InSAR, limiting the earthquakes that can realistically be imaged using this technique to shallow events with large magnitudes (typically $\sim$M$_W$ $>$6.5, crustal earthquakes, though it depends somewhat on the image resolution). Pixel tracking is also limited to mapping lateral displacements. In the relatively rare cases that multiple stereo data sets are available, vertical deformation can also be measured through DEM differencing.

## 1.3 Geodetic slip models

Coseismic deformation mapped by InSAR is routinely used to invert for earthquake fault geometries and slip distributions. Earthquake faulting is typically modeled as dislocations in a homogeneous elastic halfspace (Funning, 2005; Okada, 1985; Wright et al., 1999), after the elastic rebound model of crustal deformation (Reid, 1910). Many of these models are based on the analytical solutions by Okada (1985) that calculate surface displacements due to uniform slip on one or many rectangular dislocations in various fault-like configurations (e.g., vertical and dipping faults, and strike-slip, dip-slip, oblique slip motion). Inversions are usually constrained by multiple InSAR images, preferably with at least one from an ascending track and at least one from a descending track, to better capture the horizontal and vertical components of the displacement field. Monte Carlo restarts can be used to find a best-fit solution: hundreds of inversions are run and the calculated surface displacement vectors are projected to the LOS geometry (e.g., Wright et al., 1999). The final solution is one that minimizes the misfit between observed and modeled LOS displacements. For particularly complex earthquakes, the model fault geometry is sometimes prescribed ahead of time — based on discontinuities or steep deformation gradients in the InSAR or pixel tracking coseismic displacement field, or on geologic mapping, the topographic expression of faulting, or relocated hypocenters — and the geographic centerpoints, lengths, and strikes of the model fault segments are fixed in the inversion. For simpler earthquakes, the best-fit fault geometry can usually be inverted for, requiring only the imposition of realistic boundaries for each of the free parameters. These inversions usually assume uniform slip on each model fault, but once a satisfactory fault geometry has been established, the slip distribution can then be estimated by subdividing the model fault into a grid of rectangular dislocations. When inverting for the slip distribution, a smoothing constraint is usually

applied such that the inversion is stable and physically realistic (i.e., there is a relationship between slip at one location and the slip around it; e.g., Jónsson et al., 2002). A more detailed description of a common inversion procedure is described in Chapter 2.

Checkerboard tests have repeatedly shown that earthquake slip models based on the inversion of InSAR data are more sensitive to near-surface slip, while those based on far-field Global Navigation Satellite Systems (GNSS) displacements or seismic waveform data are more sensitive to deeper slip (Elliott et al., 2013; Li et al., 2020a; Wright et al., 2003). InSAR, GNSS and seismic data can also be jointly inverted, potentially providing good resolution of slip throughout the seismogenic zone. For surface-rupturing earthquakes, the model fit is typically poor near the fault surface trace, since a planar dislocation in a homogeneous elastic medium is inconsistent with our current understanding of fault zone architecture and deformation. Not only does the model fault geometry have to be simplified, but fault zones typically have a few main slip surfaces within a high-strain fault core, surrounded by a damage zone of fractured rock (Ben-Zion and Sammis, 2003; Dolan and Haravitch, 2014; Mitchell and Faulkner, 2009). The damage zone widens dramatically near the surface, sometimes reaching hundreds of meters to kilometers in width, and inelastic coseismic deformation can be distributed across this area which standard geodetic slip models cannot resolve (e.g., Li et al., 2022a). The poor fit near the fault is often compounded by a lack of InSAR data near the fault, the consequence of decorrelation due to the steep displacement gradients as explained in section 1.1.2. The lack of near-fault InSAR data can be addressed by jointly inverting InSAR with displacement fields estimated from pixel offset tracking of SAR amplitude or optical data. Another limitation of InSAR slip models is that because post-earthquake data acquisitions usually occur days after an earthquake, most coseismic interferograms contain the bulk of the postseismic deformation too, potentially including aseismic afterslip. The postseismic component is usually assumed to be negligible, and most InSAR slip models are presented as being coseismic even when the observations span a substantial postseismic interval.

## 1.4 Dissertation structure

The body of this dissertation comprises three chapters in the format of scientific journal publications, as chapters 2 and 3 have already been peer-reviewed and published and chapter 4 is a manuscript ready for submission. These are self-contained studies that contribute towards our understanding of the knowledge gaps introduced in brief at the start of this chapter, therefore are each structured as having their own abstract, introduction and litera-

ture review, conclusions and supporting information. Chapter 5 discusses the overarching findings of the dissertation and directions of future research. Below I summarize the three studies that form the bulk of the dissertation.

Chapter 2 focuses on the 2018 $M_W$ 6.4 and 6.0 Kaktovik earthquakes and their aftershock sequence in northeastern Alaska. These were the strongest earthquakes in this area's recorded history, and were unexpected. As a consequence, relatively little is known about the active tectonics of northeastern Alaska, yet oil and gas companies have been wanting to drill in this area for decades. I use InSAR, coseismic slip modeling, back projection seismology and relocated aftershocks to show that deformation in this region is accommodated by a complex network of unmapped active faults, the location of which may be influenced by inherited crustal fabric.

In chapter 3, historical stereo aerial imagery is used to produce a 3-D coseismic deformation field of the 1971 $M_W$ 6.6 San Fernando, California earthquake. This is one of the most infamous earthquake case studies due to the intense damage this event caused to a densely populated area in southern California, an area highly influential to the history of seismology. I use the 3-D displacement field to better understand what controls the delocalization of slip at the surface in an oblique earthquake on a dipping fault. Most previous studies of off-fault deformation focus on vertical strike-slip earthquakes, but thrust earthquakes have distinct rupture characteristics that are important to explore. This study uncovers a more complex surface rupture than was previously mapped, with a zone of distributed deformation that is conspicuously wider than the minimum fault distances at which buildings can be constructed according to California state building codes. Extracting displacement fields from historical imagery is uncommon and pushes the boundaries of the Earth observation data record, as more commonly used satellite data sets only span the last $\sim$30 years.

Chapter 4 aims to investigate whether fault maturity controls the degree to which coseismic surface offsets distributed across the fault zone diverge from surface slip modeled using InSAR due to common but technically incorrect modeling assumptions. Rather than focus on a single earthquake of interest, as in the previous chapters, I instead undertake a survey of ten, well-recorded and previously modelled earthquakes from across the Tibetan Plateau, a region which exhibits a particularly wide range of fault structural maturities. Most previous studies that consider the robustness of InSAR slip distributions at shallow depths compare inversions of a single earthquake in which just one or two data or modelling choices are varied. This study advances this body of knowledge by demonstrating with a compilation of independent models the significant influence of other, often over-

looked factors on earthquake slip distributions, and mapping where these models are less robust along strike and at depth.

# Chapter 2

# The August 2018 Kaktovik earthquakes: Active tectonics in northeastern Alaska revealed with InSAR and seismology

## 2.1 Article Information

This chapter was published in the American Geophysical Union's Geophysical Research Letters. I undertook the InSAR fault modeling and back projection seismology, created the figures, interpreted all results, wrote and edited the text. Dr. Edwin Nissen supervised this work, provided manuscript edits and funding. Dr. Eric Bergman and Dr. Ezgi Karasözen performed the hypocenter relocations, and provided minor manuscript edits. Dr. Harley Benz provided the regional moment tensors and minor manuscript edits. Fengzhou Tan contributed guidance for performing the back projections.

### 2.1.1 Citation

Gaudreau, É., Nissen, E. K., Bergman, E. A., Benz, H. M., Tan, F., and Karasözen, E. (2019). The August 2018 Kaktovik Earthquakes: Active Tectonics in Northeastern Alaska Revealed With InSAR and Seismology. Geophysical Research Letters, 46(24):14,412–14,420.

### 2.1.2 Author Names and Affiliations

É. Gaudreau[1], E. K. Nissen[1], E. A. Bergman[2], H. M. Benz[3], F. Tan[1], and E. Karasözen [4]

[1]University of Victoria, Victoria, Canada
[2]Global Seismological Services, Golden, Colorado, USA
[3]U.S. Geological Survey, Golden, Colorado, USA
[4]Alaska Earthquake Center, University of Alaska Fairbanks, Fairbanks, Alaska, USA

## 2.2 Abstract

The largest earthquakes recorded in northern Alaska ($M_W$ 6.4 and $M_W$ 6.0) occurred $\sim$6 hours apart on August 12, 2018, in the northeastern Brooks Range. The earthquakes were captured by Sentinel-1 InSAR satellites and Earthscope Transportable Array seismic data, giving insight into the little-known active tectonic processes of Arctic Alaska, obscured until recently by sparse data availability. In this study, InSAR modelling, teleseismic back projections, calibrated hypocentral relocations and regional moment tensor solutions resolve two previously unknown, SSW-dipping right-lateral fault segments. These are the first active faults identified as conjugate to the NE-trending sinistral Canning displacement zone directly to the west, which is therefore a more complex zone of diffuse faulting than previously thought. The northeastern Brooks Range has been characterized as an area of low to moderate seismic hazard, but these earthquakes illustrate the potential for larger, possibly destructive events in a region earmarked for rapid resource development.

## 2.3 Plain Language Summary

The largest earthquakes recorded in northern Alaska (magnitude 6.4 and magnitude 6.0) occurred $\sim$6 hours apart on August 12, 2018. Few active faults are mapped in this region despite widespread seismicity, and the current tectonic setting remains unclear due to limited available data and the remote location. We use satellite radar images and seismic data to resolve two previously unknown fault segments, along which the magnitude 6.4 earthquake ruptured unilaterally eastwards. This fault geometry demonstrates that the Canning displacement zone, the main tectonic feature in the area, is a more complex zone of diffuse faulting than previously thought. These results are also important for reassessing seismic hazard by illustrating the potential for damaging earthquakes on seemingly aseismic faults.

## 2.4 Introduction

The $M_W$ 6.4 earthquake that occurred on August 12th, 2018, ~80 km SW of Kaktovik, Alaska, is the largest ever recorded in the Brooks Range or its foreland basin to the north (Figure 2.1). The second largest earthquake in this region, a $M_W$ 6.0 aftershock, occurred ~6 hours later, ~35 km to the east (Figure 2.1b). More than 6000 aftershocks recorded within one year of the mainshock form a WNW–ESE-striking trend at the northern margin of the eastern Brooks Range, beneath the Sadlerochit Mountains (Ruppert and West, 2020). The only known faults in this area are mapped as pre-Quaternary and do not align with the 2018 seismicity (Koehler, 2013).

Despite widespread seismicity in Arctic Alaska, few active faults are mapped, and currently published GPS velocities are sparse (e.g., Snay et al., 2016). The current tectonic setting is equivocal (e.g., Finzel et al., 2015; Fuis et al., 2008; Haeussler, 2008; Koehler, 2013; Leonard et al., 2008; Mazzotti et al., 2008), but a relatively recent increase in seismic and geodetic data available from this area, with the deployment of the USArray in Alaska since 2014 and launch of the Sentinel-1 satellite pair in 2014 and 2016, permit a more detailed characterization of active tectonics in the Brooks Range.

We use Sentinel-1 InSAR data and elastic dislocation modelling to characterize the fault geometry and slip distribution of the 2018 Kaktovik sequence, which are the most northerly earthquakes ever imaged in this way. We use seismic back-projections, calibrated hypocentral relocations and regional moment tensors to map the mainshock rupture and aftershock activity over time and space. These new constraints are used to reassess regional tectonics and provide new information for seismic hazard assessments in an area of keen interest to the petroleum industry for oil drilling.

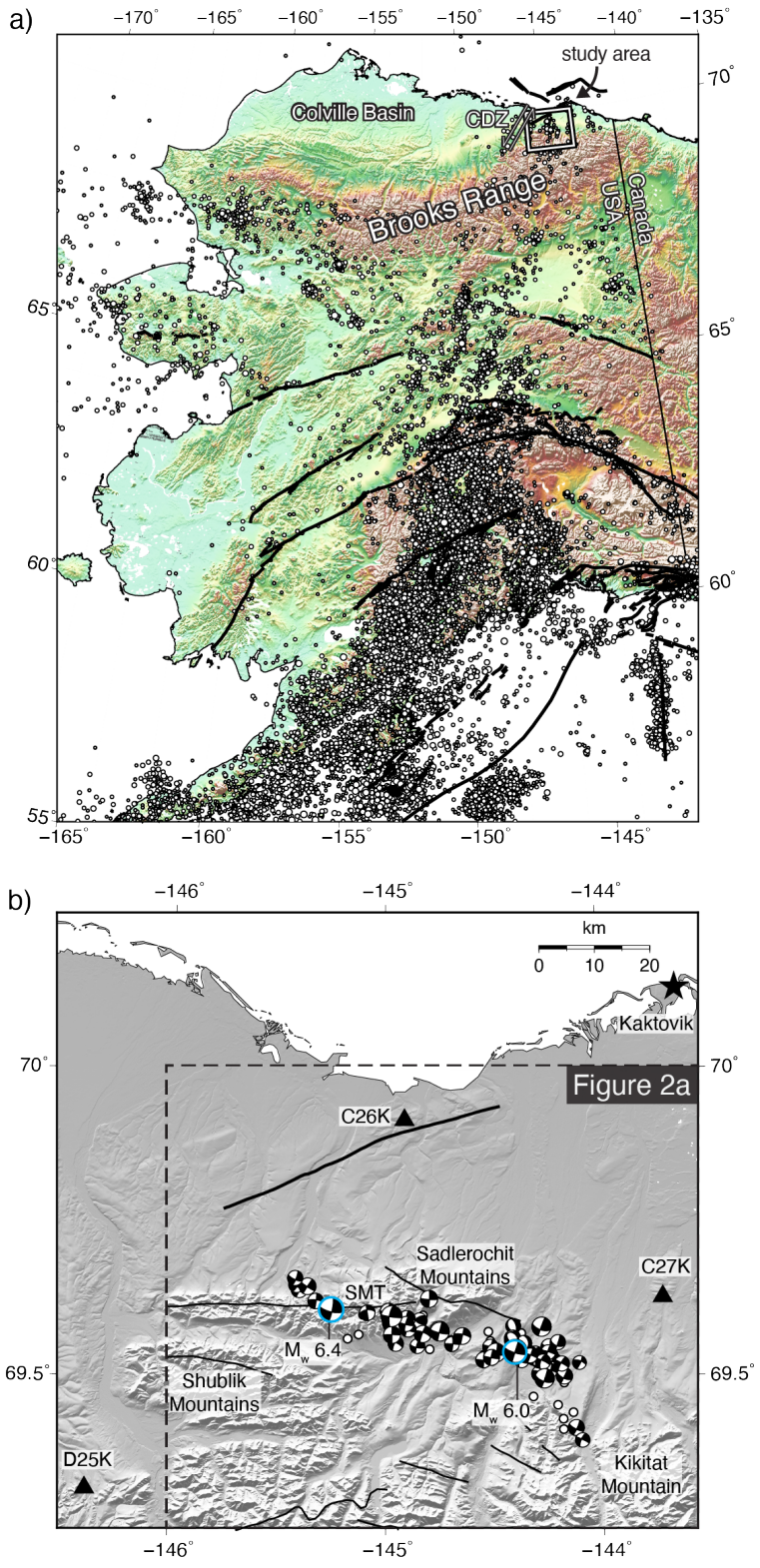


Figure 2.1: (a) Digital elevation model (DEM) of Alaska (USGS 30 ARC-second Global Elevation Data, GTOPO30; `https://doi.org/10.5066/F7DF6PQS`) with location of epicenters prior to the 2018 Kaktovik sequence in USGS Comcat Catalog (white circles; `https://earthquake.usgs.gov/earthquakes/search/`) and Quaternary faults are bold black lines (Koehler, 2013). Study area is located in the white rectangle. CDZ: Canning displacement zone. (b) Shaded-relief DEM (Porter et al., 2018) with regional moment tensor solutions for the 2018 Kaktovik mainshock and $M_W$ 3.5+ aftershocks from the following 5 months plotted at the relocated epicenter locations. White circles represent additional relocated epicenters. Pre-Quaternary faults are thin black lines (Koehler, 2013). SMT: south-dipping Sadlerochit Mountains thrust. Location of closest seismic stations used for calibrated relocations are indicated by black triangles.

## 2.5 Geologic and Tectonic Setting

The Brooks Range (Figure 2.1a) is underlain by a thick crustal root where the Moho is mapped to depths of ∼50 km (compared to ∼30– 35 km in central Alaska) and the lithosphere is up to ∼200 km thick (Fuis et al., 1997; Jiang et al., 2018; Miller et al., 2018; O'Driscoll and Miller, 2015; Ward and Lin, 2018). Gravitational potential energy from crustal thickness contrasts, or northward motion of the Yakutat indentor, are thought to be driving current tectonic activity (Finzel et al., 2015; Mazzotti and Hyndman, 2002; Mazzotti et al., 2008). According to moment tensor solutions, the northeastern Brooks Range is currently dominated by a transtensional tectonic regime, in contrast to transpression south of the Brooks Range, where the lithosphere is weaker and deforming at a faster rate (Jiang et al., 2018; Leonard et al., 2008; O'Driscoll and Miller, 2015). The main mapped tectonic feature in the northeastern Brooks Range is the Canning displacement zone (CDZ), a NE-SW left-lateral diffuse deformation zone first identified by Grantz et al. (1983) located between the northeastern Brooks Range and the North Slope Deep Magnetic High (Figure 2.1a), a domain of mechanically strong crust to the west (e.g., Saltus et al., 1999).

The Brooks Range is composed of multiple arc and continental margin terranes which accreted onto the North American margin at the onset of the Brookian orogeny in the latest Jurassic-Cretaceous (Moore, 1992; Moore et al., 1997). The first phase of the Brookian orogeny resulted in thin-skinned deformation in the Brooks Range south of the study area (Moore and Box, 2016) and was followed by middle-Late Cretaceous extension at the southern margin of the Brooks Range (e.g., Amato and Miller, 2004; Hannula et al., 1995). A Paleogene episode of thick-skinned deformation formed large-scale duplex structures in the northeastern Brooks Range and is coeval with accretionary deformation in the forearc in southern Alaska and right-lateral strike-slip faulting in the interior (e.g., Fuis et al., 2008; Wallace, 1992). This synchronicity suggests that these structures may be linked by a detachment (Moore and Box, 2016).

The 2018 Kaktovik earthquakes occurred beneath the Sadlerochit Mountains, at the northern margin of the northeastern Brooks Range (Figure 2.1). The geology of these mountains is dominated by Neoproterozoic dolomite overlain by Cambrian to Ordovician limestone (Molenaar et al., 1987, and references therein). Most of the mapped tectonic features in this area formed during the later reactivation of the Brookian orogeny in the Paleogene, expressed on the surface as north-vergent listric thrusts and east-west-trending folds in the Sadlerochit Mountains and adjacent Kikitat and Shublik Mountains (Figure 2.1b; Moore et al., 1997; O'Sullivan et al., 1993; Wallace and Hanks, 1990).

## 2.6 InSAR Analysis

### 2.6.1 InSAR Data

The European Space Agency's Sentinel-1 satellites captured the coseismic surface deformation of the 2018 Kaktovik earthquakes. Two 12-day descending track interferograms and one 42-day ascending track interferogram (the shortest repeat time available on ascending orbits) were used in this study, obtained from the automated SARVIEWS program (Figure 2.2a; Meyer et al., 2016). Since available interferogram pairs capture the coseismic deformation from both the $M_W$ 6.4 and $M_W$ 6.0 events, in this section we discuss the cumulative coseismic deformation without specifying the causative earthquake.

The radar line-of-sight (LOS) coseismic deformation appears as three lobes in the ascending and descending track interferograms, with one northern lobe and two southern ones (Figure 2.2a). In all interferograms, peak displacements are greatest in the southern lobes, which are LOS range increase in descending interferograms and range decrease in the ascending interferogram. The northern lobes exhibit the opposite sense of motion, broadly consistent with right-lateral faulting along an ∼E–W trend.

### 2.6.2 InSAR Modeling

To characterize the causative faulting, the LOS displacements were downsampled using a quadtree algorithm (Jónsson et al., 2002) and the reduced data were inverted for slip on rectangular dislocations embedded within a uniform elastic half-space with Lamé parameters $\mu = \lambda = 3.2 \times 10^{10}$ Pa (Okada, 1985; Wright et al., 1999). The single ascending dataset was given equal weighting to the two descending datasets in the inversion. We used Powell's algorithm (Press et al., 1992) to solve for the best-fit fault strike, dip, rake, slip, surface projection center point, length, and top and bottom depths, avoiding local minima by repeating the inversion 500 times with starting parameters sampled randomly from the ranges given in Table 2.1 in Supplementary section 2.11 (Wright et al., 1999).

Our preferred slip model was determined using the two-step methodology outlined by Elliott et al. (2012). In the first step, fault geometry was established using a small number of rectangular, uniform slip model faults. A single rectangular fault cannot reproduce the three-lobed fringe pattern (Table 2.2, Figure 2.4 in Supplementary section 2.11), however two faults provide a good visual fit (root mean square residual displacements of $1.20 \times 10^{-2}\,\mathrm{m}$). Both *en echelon* segments strike ESE, involve right-lateral slip and dip towards the SSW, explaining the greater deformation observed in the southern lobes of the

interferograms (Figure 2.5, Table 2.3 in Supplementary section 2.11). The $\sim$15 km-long western segment is steeper (82°) than the $\sim$12 km-long eastern segment (64°). Uncertainties in these uniform slip parameters were estimated using Monte Carlo inversions of 100 datasets perturbed with realistic noise (Table 2.4 in Supplementary section 2.11; Elliott et al., 2012). Strike, rake, length, and center point easting and northing are well constrained for both faults, with relative standard deviations $<9\%$ (Figures 2.6-2.7 in Supplementary section 2.11). Dip is less well constrained for the eastern fault, but a shallower angle than that of the western fault is resolved. The results also show that the rupture did not reach the surface; thus slip, fault width, minimum depth, maximum depth, and seismic moment are less well constrained (relative standard deviations $>20\%$) due to strong trade-offs between these parameters. We also explored the possibility of a listric fault—as the Sadlerochit Mountains thrust is believed to be (O'Sullivan and Wallace, 2002)—-which would extend the rupture area farther south. Listric slip models were created using a steeper slip plane near the surface and a deeper segment with a shallower dip; the results were very similar for each model that was created, one such model is described in Tables 2.5 – 2.6 in Supplementary section 2.11. In all cases, slip predominantly occurs on the steeper fault segments near the surface; thus, the slip does not extend farther south in the listric models. Therefore, slip on two steep fault segments remains our preferred model.

In the second step, we solved for the distribution of slip and rake across the two fault planes (Funning et al., 2005). The western and eastern fault lengths were increased to 30 and 20 km, respectively; their bottom depths increased to 10 and 15 km, and were subdivided into 1 km $\times$ 1 km patches. We solved for the rake and slip magnitude of each patch using a Laplacian smoothing operator to ensure realistic slip gradients (Figure 2.2). Allowing for distributed slip and rake reduced the root mean square residual displacements to $1.066 \times 10^{-2}\,\mathrm{m}$, though notable residuals remain between the two faults and at the eastern termination of the eastern fault (Figure 2.2a). Rake is consistently right-lateral on both faults. Slip is concentrated between depths of 2.7 and 11.0 km on the eastern fault, peaking at 1.8 m at 6 km depth. Slip is concentrated between 1.5 and 9.5 km of slip on the western fault, peaking at 1.3 m at 4 km depth.

The InSAR moments for the western and eastern faults are $2.798 \times 10^{18}\,\mathrm{N\,m}$ and $3.259 \times 10^{18}\,\mathrm{N\,m}$, respectively, and the combined moment magnitude from slip on both faults is 6.5. For comparison, the U.S. Geological Survey (USGS) W-phase moment magnitude for this event is estimated at 6.4.

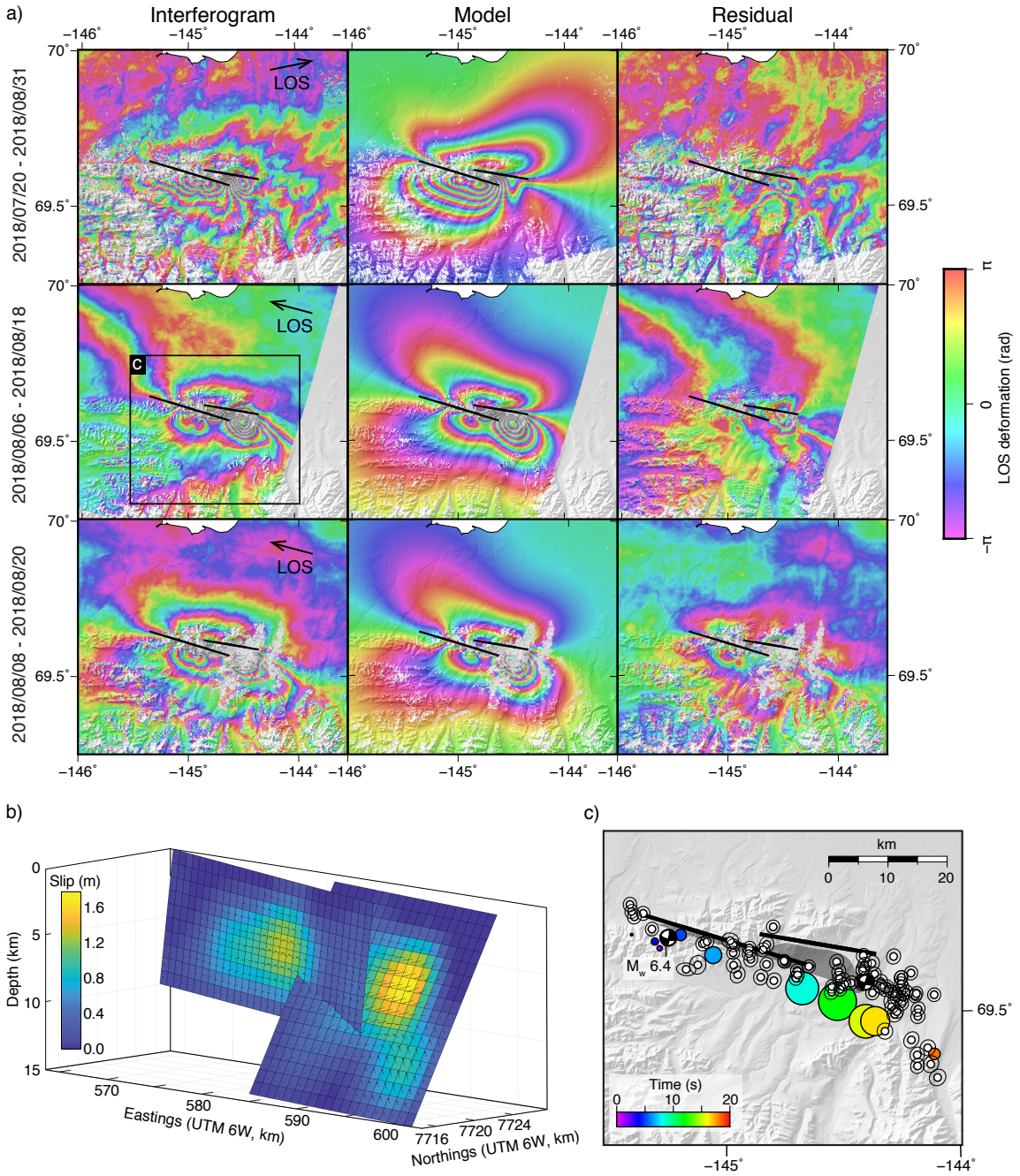


Figure 2.2: (a) Sentinel-1 interferograms, models based on distributed slip with variable rake on two fault planes, and residuals superimposed onto topography from ArcticDEM (Porter et al., 2018). Surface projections of the modelled, buried fault segments are in black. (b) Slip distribution on the fault planes with variable rake. Each fault segment measures 1 km $\times$ 1 km. (c) The model slip area is shaded, with the mainshock and aftershocks superimposed (white circles with 95% confidence ellipses). Colored circles represent back-projected 0.2–2 Hz energy for the $M_W$ 6.4 mainshock, colored by time since rupture initiation and scaled by relative energy. The average rupture velocity is 2.6 km/s.

## 2.7 Seismological Constraints

### 2.7.1 Calibrated Earthquake Relocations

We reevaluated hypocenter locations of the Kaktovik mainshock and 109 of the best-recorded aftershocks using the *mloc* calibrated earthquake relocation technique (Bergman and Solomon, 1990; Walker et al., 2011). This minimizes location bias by assuming that ray paths of events clustered in space and recorded at common stations sample roughly the same portion of Earth, such that travel time differences more likely reflect the relative epicenter locations within the cluster rather than the 3-D velocity structure. The *mloc* method splits the relocation into two independent steps, each utilizing a specific, tailored set of arrival time data (Jordan and Sverdrup, 1981). Firstly, relative locations of each hypocenter within the cluster are estimated from differences in arrival times picked at common stations at all distances. Secondly, the absolute location of the hypocentroid—the geometric mean of the cluster—is calculated based on the observed travel times at local distances, since nearby stations will have accumulated less travel time error. This step is a direct calibration—an indirect calibration (i.e. using an independent dataset to constrain the absolute location of the hypocentroid) may be used in the event that a cluster of events cannot be reliably calibrated using travel times. The azimuthal coverage is not ideal in this case since only one regional station (C26K) is located north of the cluster.

Using a direct calibration, the relocated mainshock hypocenter lies $\sim$7 km south of the western model fault plane, as do most aftershocks. Three hypotheses for this discrepancy were explored: (1) a timing error at the only station north of the cluster (C26K), exerting a strong influence on the latitude of the relocated cluster; (2) lateral heterogeneities in crustal seismic velocity, notably those north of the cluster in the Colville basin (Moore et al., 1994; Fuis et al., 1997); and (3) the fault that ruptured was listric, thus the true slip patch could extend farther south than that shown in Figure 2.2c. As described in section 2.6.2, listric fault models were tested; however, the slip in these models is concentrated on the steep parts of the fault, which would not extend the slip patch farther south. On the other hand, the InSAR data are mostly sensitive to shallow slip, thus it is possible that some unresolvable component of slip occurred on deeper parts of the faults that have a shallower dip. As for the possibility of a timing error, clock quality at station C26K was assessed using the IRIS timeseries Web Service (`https://service.iris.edu/irisws/timeseries/docs/`). From these data, we conclude that time errors are not large enough to affect the location of the calibrated cluster. Moreover, an unreasonably large timing error of 1.2 s at

station C26K is required to shift the cluster northward to correct the discrepancy with the InSAR model; thus, a heterogeneous crust is a more likely explanation.

An indirect calibration was performed using the InSAR model faults due to the likelihood of strong lateral heterogeneities in the crust biasing the epicenters ∼7 km to the south (stations C26K and C27K are located on foreland sedimentary rocks where crustal velocities are much lower than in the Brooks Range to the south, e.g., Fuis et al., 1997). The mainshock and $M_W$ 6.0 aftershock were used as calibration events (Figure 2.2c; Table 2.11 in Supplementary section 2.11). The origin times for calibration were set so that the arrival times at the local station in the Brooks Range, D25K, agreed with a typical crustal model. The $M_W$6.4 mainshock nucleated close to the western end of the western model fault, implying that it ruptured unilaterally eastwards. The $M_W$6.0 aftershock hypocenter is near the eastern end of the eastern model fault, among a concentration of smaller events.

There was also an increase in seismic activity southwest of the study area starting in late July 2018 and peaking in October 2018 (Ruppert and West, 2020). These events will be referred to as the Niviak cluster, after the nearby Niviak Pass. Some of these events cluster in multiple NW-SE trends similar to the Kaktovik cluster, while others form more diffuse groups. We investigate whether both clusters are related to the larger-scale left-lateral motion of the CDZ by relocating the 155 best-recorded earthquakes in this area using a direct calibration (Figure 2.8 in Supplementary section 2.11). Some of these events cluster in a NW-SE trend while others form more diffuse groups.

### 2.7.2 Regional Moment Tensors

Regional moment tensor solutions (RMTs) were calculated for the mainshock and 87 best-recorded aftershocks. The RMTs were computed using the same Green's functions, fit function and filtering strategy found in Herrmann et al. (2011). Unlike the grid search approach of Herrmann et al. (2011), we used a linear inversion to solve for the moment tensor components and assumed a pure double-couple source. For events $M_W$ 4.0 or smaller, waveform filtering is typically done in the passband 16–50 s, while for larger events waveform filtering is typically done in the passband 20–50 s. For all events, we used the central US velocity model of Herrmann et al. (2011), an observational distance range 0–500 km, and three-component waveforms that included body waves and surface waves. RMT solutions were computed in the depth range 2–24 km in increments of 1 km. The RMT solution for each event is the one with the best fit as a function of depth. All RMT solutions were computed using the single event locations found in the USGS earthquake catalog

(https://earthquake.usgs.gov/earthquakes/map/). Given the good azimuthal distribution of stations surrounding the source region and longer period signals used in the inversion, we expect little differences in computed mechanisms whether using the single or multiple locations in this study.

The large majority of regional moment tensors are consistent with E-W right-lateral strike-slip motion. The southward dips (mostly $>60°$) of the E-W nodal planes are in agreement with the dips of the modelled fault segments (Figure 2.1b, Figure 2.9 and Table 2.11 in Supplementary section 2.11). Centroid depths range from 0–22.7 km, with most $<10$ km. The mainshock has a centroid depth of 2.2 km.

### 2.7.3 Teleseismic Back Projection

We applied a phase-weighted relative back-projection method (Tan et al., 2019) to track the rupture energy in time and space. This provides a measure of relative energy release, rather than true moment release, since the amplitudes are normalized and the phases are used as a weighting factor. The phase-weighted stacking emphasizes both large amplitudes and the coherency of the signal, reducing biases introduced by incoherent signals with large amplitudes.

We performed back-projections for both the $M_W$ 6.4 mainshock and $M_W$ 6.0 aftershock using teleseismic stations from the contiguous United States, and the teleseismic travel times are estimated using the IASP91 reference model (Kennett and Engdahl, 1991). The 10 s window that was used gave rise to artefacts in the form of multiple energy radiators at the same latitude and longitude, but with slightly different source times. Of the energy radiators at the same coordinates, the result with the median source time was chosen and the rest discarded. Other array configurations were considered; however, they had less suitable distance and azimuth ranges (Tan et al., 2019). Relocated epicenters from Section 2.7.1 were used to constrain the location of each rupture. For the mainshock, the back-projection indicates linear rupture propagation from WNW to ESE at an average velocity of 2.6 km/s (Figure 2.2c, Figure 2.10a, Table 2.9 in Supplementary section 2.11). Coherent back-projected energy encompasses the full length of the InSAR model faults, with peak energy release occurring after $\sim$10 s on the eastern fault. Though close to the limit of what a back-projection can resolve, the $M_W$ 6.0 aftershock also seems to have propagated from WNW to ESE and thus likely occurred on the same eastern fault segment rather than on a conjugate fault (Figure 2.10b, Table 2.9 in Supplementary section 2.11).

## 2.8 Discussion

### 2.8.1 Faulting in the 2018 Kaktovik Sequence

The InSAR modelling suggests rupture of two *en echelon*, ESE-striking right-lateral faults within the Sadlerochit Mountains (Figure 2.2a). This is supported by distributions of back-projected energy and aftershocks, which are both oriented WNW-ESE, and their RMT solutions (Figures 2.1b, 2.2c). The lack of decorrelation between the northern and southern lobes in the 2018/08/06-2018/08/18 interferogram (Figure 2.2a) suggests that neither segment ruptured to the surface, in agreement with our InSAR slip model. The mainshock centroid depth of 2.2 km is much shallower than both the relocated focal depth of 11 km and most of the slip in the InSAR model (Figure 2.2b). The hypocenter depth is located near the bottom of the rupture, as is often the case (e.g., Karasözen et al., 2016). We interpret that this discrepancy reflects uncertainties of $\sim$5 km in RMT centroid depths (Herman et al., 2014).

Back-projection results indicate that the $M_W$ 6.4 mainshock ruptured both faults, with greater relative energy release on the eastern segment, consistent with the high slip patch in the InSAR slip model (Figure 2.2). Relative energy mapped at 18 s is located $\sim$15 km SE of the modelled rupture area (Figure 2.2c) and this most likely constitutes a 'swimming artefact' since this is approximately the same azimuth as the seismic stations used in the contiguous United States (e.g., Koper et al., 2012), though we cannot rule out an off-fault, near-instantaneous aftershock (e.g., Fan and Shearer, 2016). The $M_W$ 6.0 aftershock probably enlarged the eastern slip patch or ruptured a shallower part of the fault (Figure 2.10 in Supplementary section 2.11). Smaller aftershocks concentrate in this same area, with a number located farther east and south, a spatial bias in the direction of mainshock rupture propagation that may indicate a component of dynamic triggering (e.g., Gomberg et al., 2003).

The western fault cuts obliquely across the Paleogene Sadlerochit Mountains thrust, mapped as a S-dipping listric thrust in this area (Figure 2.1b; O'Sullivan and Wallace, 2002). However, the eastern fault (strike 98°) is parallel to the eastern segment of the Sadlerochit Mountains thrust, thus it is possible that the steep, shallower part of this listric fault was reactivated. The 2018 Kaktovik earthquakes may have ruptured a combination of unknown and known faults. The steep, southward nodal plane dip angles in nearly all of the Kaktovik focal mechanisms also hint that the structural fabric of the Sadlerochit Mountains may have influenced the geometry of the strike-slip rupture plane.

### 2.8.2 Regional Tectonics

The Kaktovik earthquakes exposed the first known active faults in the northeastern Brooks Range that are conjugate to the NE-SW left-lateral CDZ directly to the west (Figures 2.1a, 2.2). Previous moment tensor solutions have been interpreted as representing NNE-SSW left-lateral faulting based on the known slip sense of the CDZ. However, diffuse zones of shearing are often associated with conjugate strike-slip faults (e.g., Cunningham, 2005; Ghods et al., 2015; Soumaya et al., 2018) and the faults in the Sadlerochit Mountains are optimally oriented with respect to the local maximum horizontal principal stress for right-lateral slip (Hanks et al., 2000).

To explore whether faulting of this orientation may be widespread within the eastern Brooks Range, we performed an additional relocation of the Niviak cluster (Figure 2.3). The results highlight several discrete concentrations of events along similar NW-SE trends, that presumably represent similar faults conjugate to the CDZ. These right-lateral faults must rotate counterclockwise around vertical axes in order to accommodate overall left-lateral motion along the main CDZ trend (Figure 2.3; e.g., Kim et al., 2004).

The northeastern Brooks Range exhibits low seismic deformation rates and is underlain by a thick Moho ($\sim$50 km depth), and thick and strong lithosphere ($\sim$200 km; Fuis et al., 2008; Jiang et al., 2018; Leonard et al., 2008; O'Driscoll and Miller, 2015). We interpret that faults involved in the Kaktovik sequence and the CDZ compose a diffuse zone of active faulting that accommodates slow strain between two mechanically strong lithospheric domains: the NE Brooks Range to the east, and the North Slope Deep Magnetic High to the west (e.g., Jiang et al., 2018; O'Driscoll and Miller, 2015; Saltus et al., 1999). This has parallels with other diffuse deformation zones such as in northwestern Iran (e.g., Ghods et al., 2015), the Mongolian Altai (e.g., Cunningham, 2005), and the Alboran-Rif domain in northwestern Africa (e.g., Soumaya et al., 2018), many of which exhibit low levels of instrumental seismicity, and low strain rates, but are capable of hosting large earthquakes. The Kaktovik earthquakes thus highlight the importance of reassessing the seismic hazard of areas of low internal deformation.

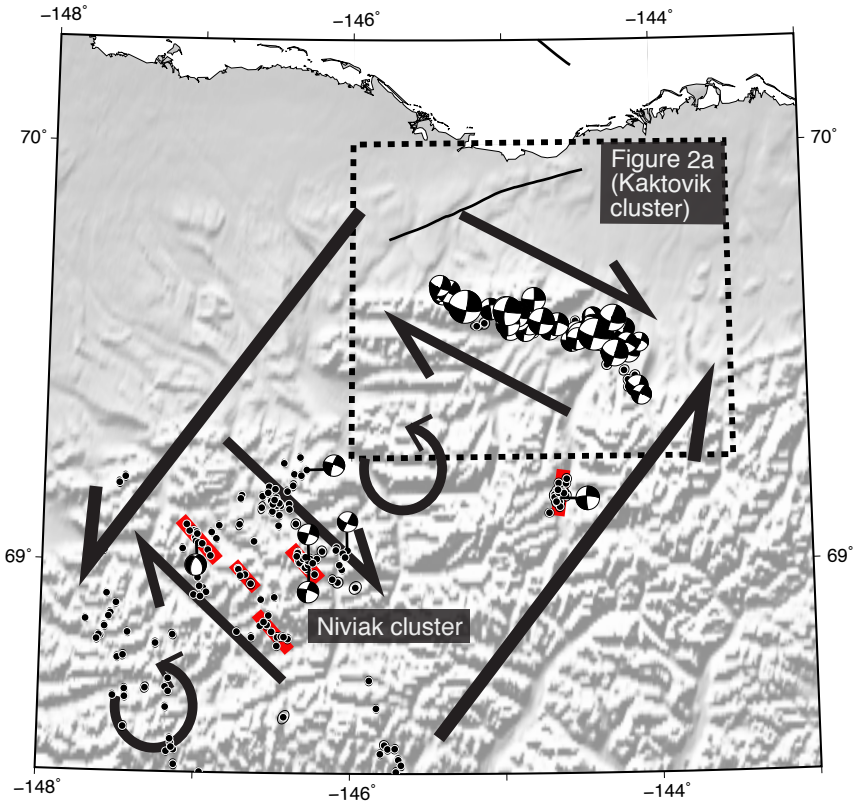


Figure 2.3: Relocated epicenters for the Kaktovik mainshock and best-recorded aftershocks from the following 12 months. The Niviak cluster includes the seismic events southwest of the Kaktovik sequence. Some of these events potentially highlight similar conjugate structures to the CDZ (highlighted in red). The arrows demonstrate a simplified version of the block rotation model for northeastern Alaska where the primary faults are NE-SW-oriented left-lateral, and the secondary faults are NW-SE-oriented right-lateral.

## 2.9 Conclusion

The August 12 2018 $M_W$ 6.4 and $M_W$ 6.0 Kaktovik earthquakes occurred on previously unknown active right-lateral faults that are conjugate to the CDZ, striking ESE. The $M_W$ 6.4 mainshock nucleated on the western fault and propagated unilaterally eastwards onto the eastern fault, where most of the slip and energy release occurred. The $M_W$ 6.0 aftershock likely further extended the slip area of the mainshock. A direct calibration results in hypocenters systematically biased to the south by $>$7 km, possibly due to the 1-D velocity model and less-than-ideal azimuthal coverage used in the relocations. Using an indirect calibration, relocated mainshock and aftershock hypocenters lie on the rupture area of the InSAR-derived model faults. These earthquakes are the largest magnitude events recorded in northern Alaska and the first determined as conjugate to the CDZ. Other areas with po-

tential NW-SE right-lateral faulting have been identified from relocated earthquake trends south of the study area. Together, these right-lateral faults may accommodate the overall left-lateral motion of the CDZ by rotating about vertical axes. The relatively low seismicity and deformation rates in the northeastern Brooks Range reflect its thickened crust and lithosphere, but the Kaktovik earthquakes nevertheless highlight the potential for damaging earthquakes on seemingly aseismic faults.

## 2.10 Acknowledgments

É. G. was supported through a Graduate Scholarship from the University of Victoria and an Alexander Graham Bell Canada Graduate Scholarship from the Natural Sciences and Engineering Research Council of Canada (NSERC). E. N. was supported through NSERC Discovery Grant 2017 04029, a Canada Research Chair, and grants from the Canada Foundation for Innovation and B. C. SAR interferograms were made using European Space Agency Copernicus Sentinel data [2018] and the University of Alaska Fairbanks SARVIEWS web portal (Meyer et al. 2017; `http://sarviews-hazards.alaska.edu/Earthquakes/`), which is funded by the National Aeronautics and Space Administration (NASA). Seismic back-projection data were obtained from Incorporated Research Institutions for Seismology (`https://ds.iris.edu/wilber3/find\_event`) and data used in the relocations and regional moment tensors were gathered from the U.S. Geological Survey (USGS) National Earthquake Information Center (NEIC; `https://earthquake.usgs.gov/earthquakes/map/`). Computer programs used in the paper are available from the references cited in the text. We also thank two anonymous reviewers and Morgan Moschetti (USGS) for helpful comments.

## 2.11 Supporting Information for "The August 2018 Kaktovik earthquakes: active tectonics in northeastern Alaska revealed with InSAR and seismology"

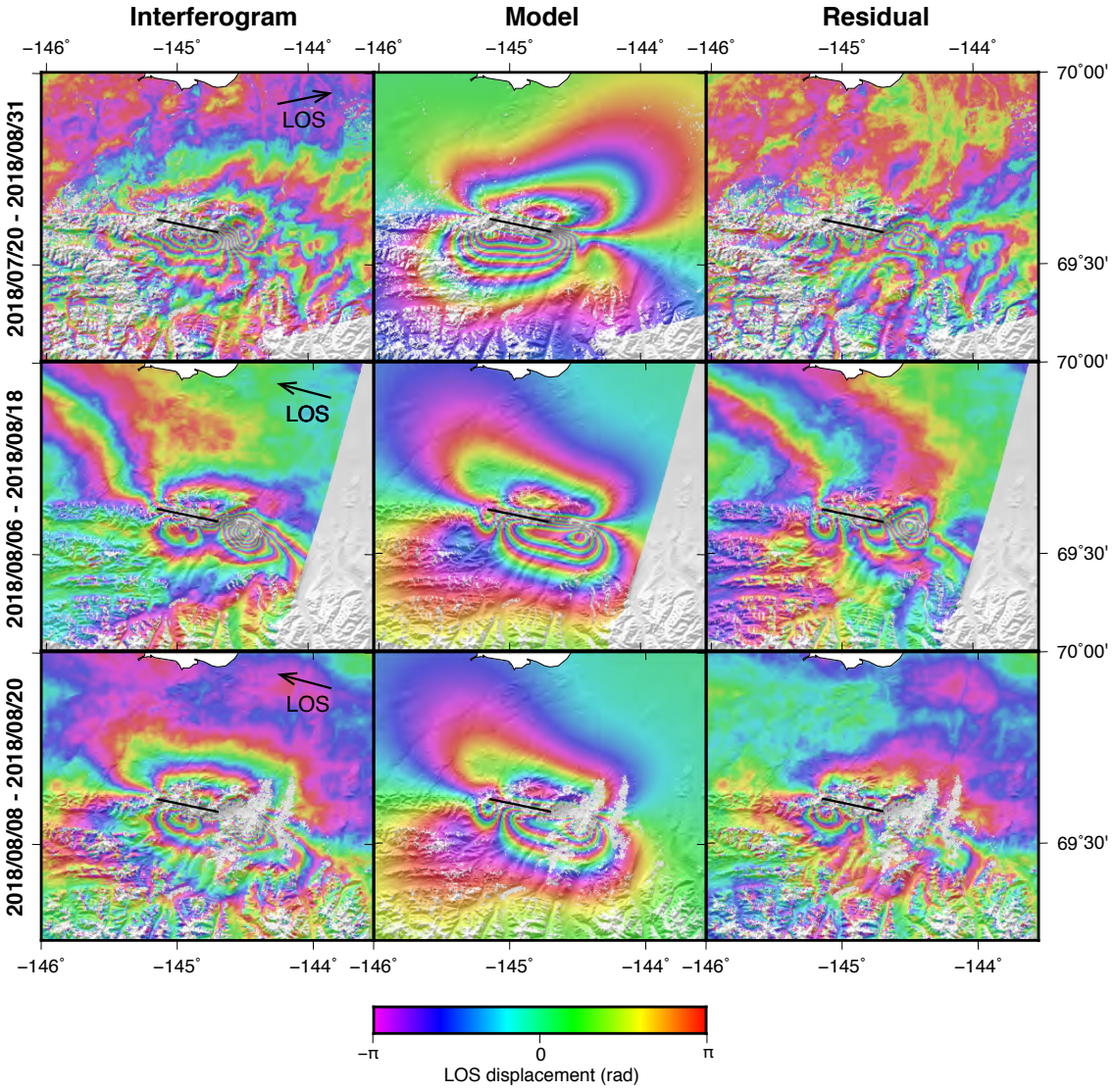


Figure 2.4: Sentinel-1 interferograms, models based on uniform slip on a single fault plane, and residuals superimposed onto topography from ArcticDEM (Porter et al., 2018). The black line is the projected surface break of the modelled fault plane.

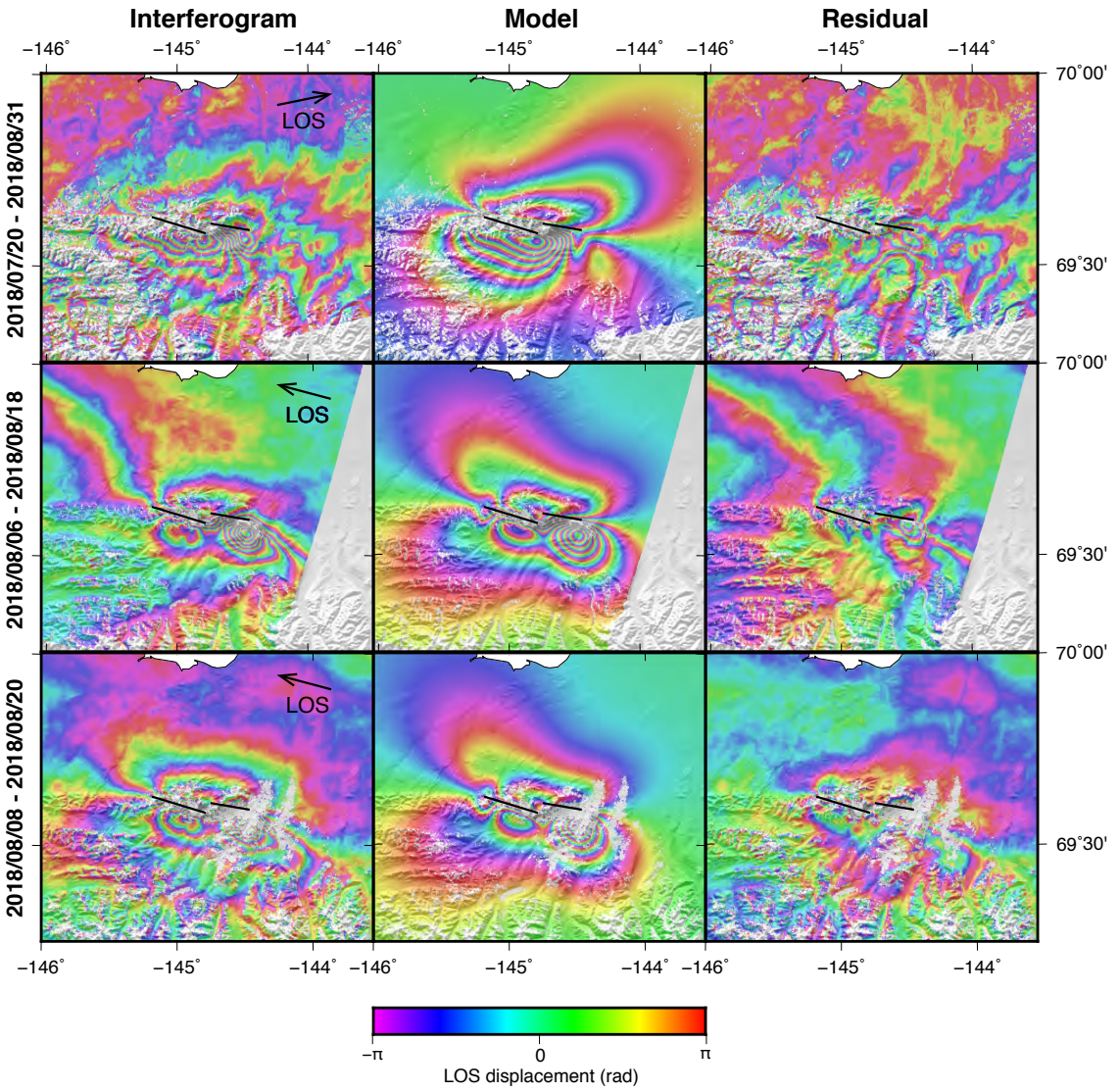


Figure 2.5: Sentinel-1 interferograms, models based on uniform slip on two fault planes, and residuals superimposed onto topography from ArcticDEM (Porter et al., 2018). The projected surface break of the modelled western and eastern fault segments are the black lines.

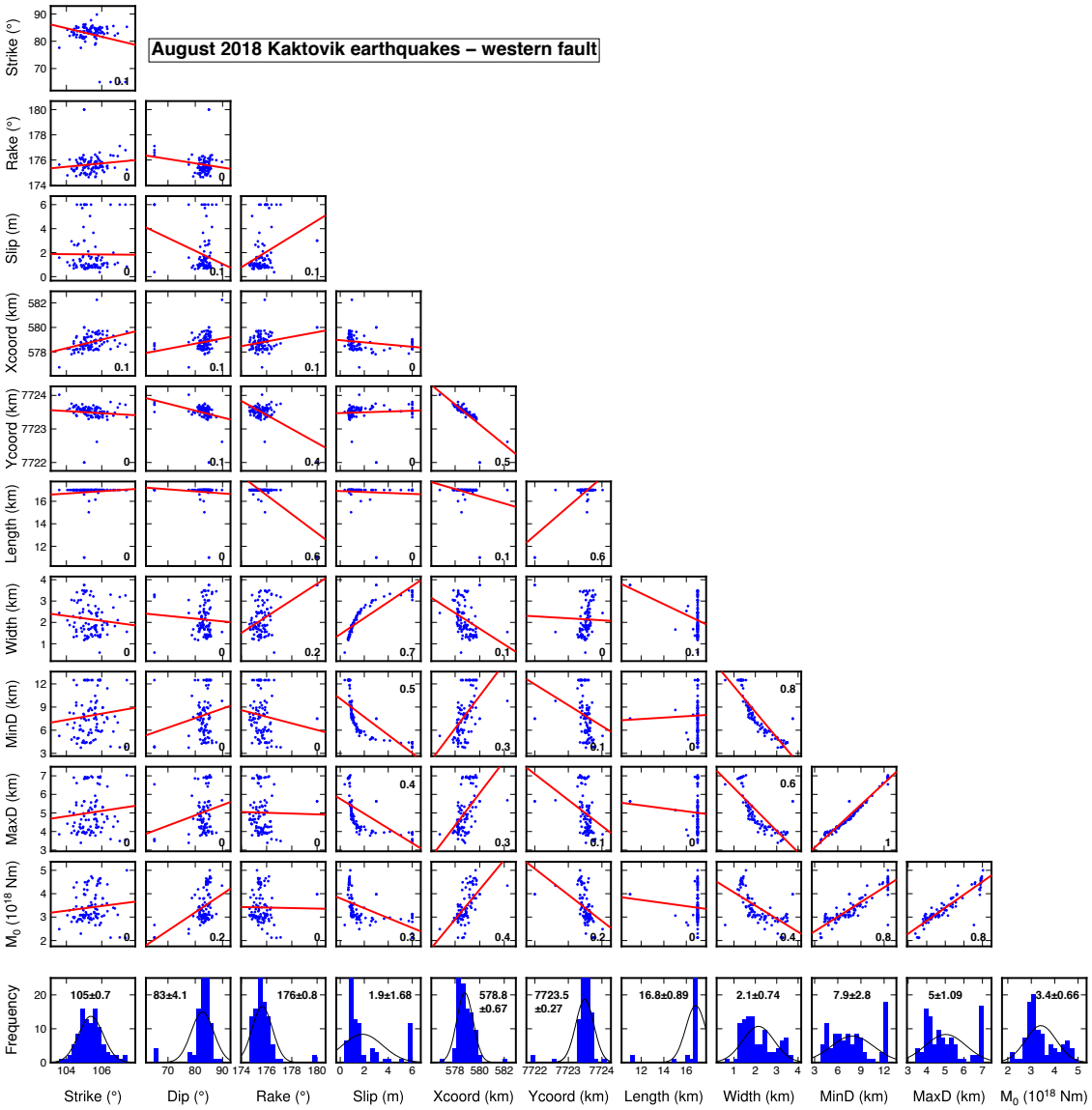


Figure 2.6: Model parameter tradeoffs (first 10 lines) from a Monte Carlo analysis of a uniform slip model for the western fault of the 2018 Kaktovik earthquake. The inversion was performed 100 times, and each model included both the western and eastern faults, with spatially correlated noise based on far-field noise added to each iteration. The linear regression is shown by the red line, and the number in each box is the correlation coefficient. The distribution for each parameter is illustrated by the histograms, where the red curve is the normal distribution, and the mean is written in each box. See Figure 2.7 for the model parameter tradeoffs for the eastern fault.

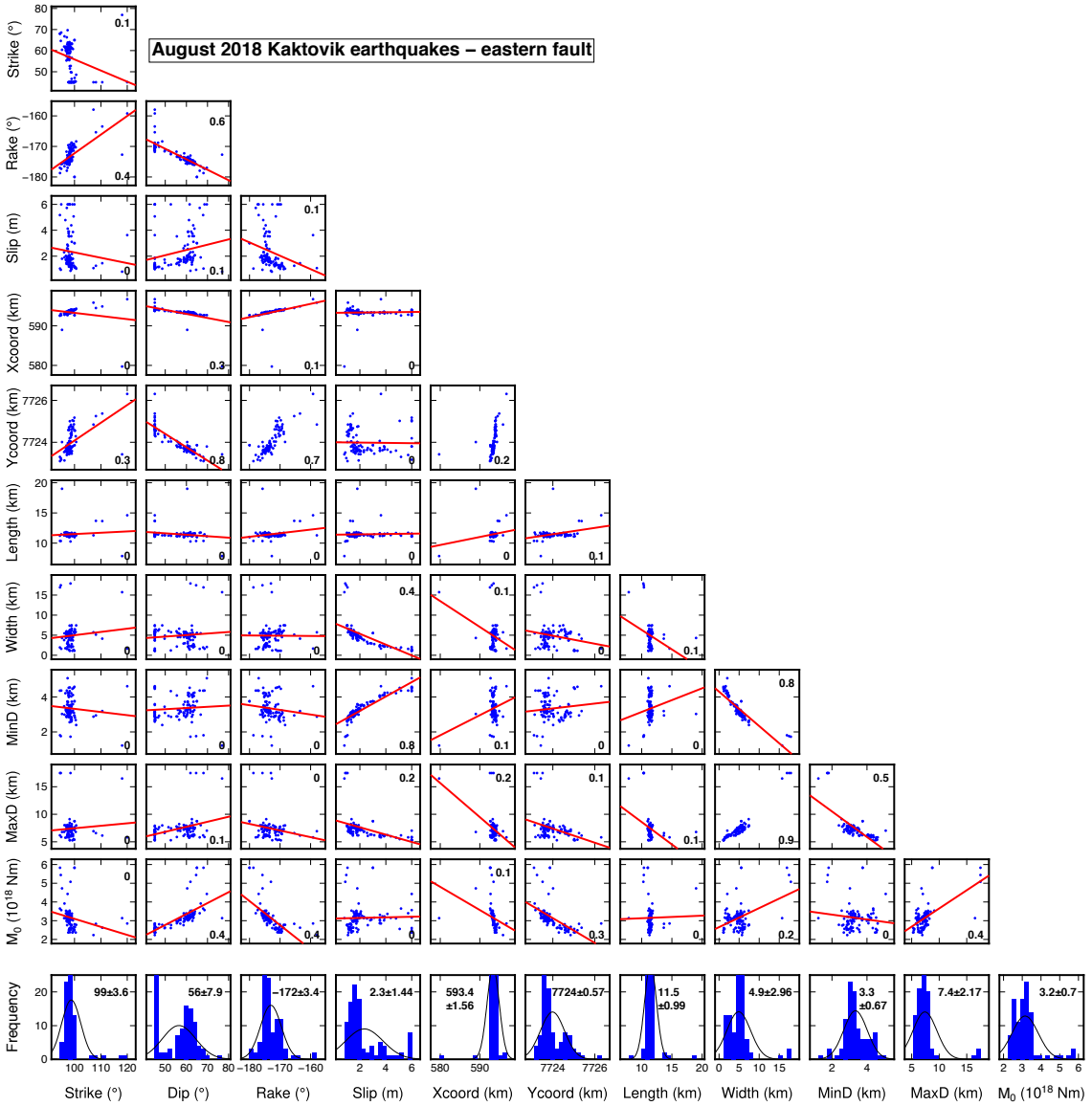


Figure 2.7: Model parameter tradeoffs from a Monte Carlo analysis of a uniform slip model for the eastern fault of the 2018 Kaktovik earthquake. Formatting is the same as Figure 2.6.

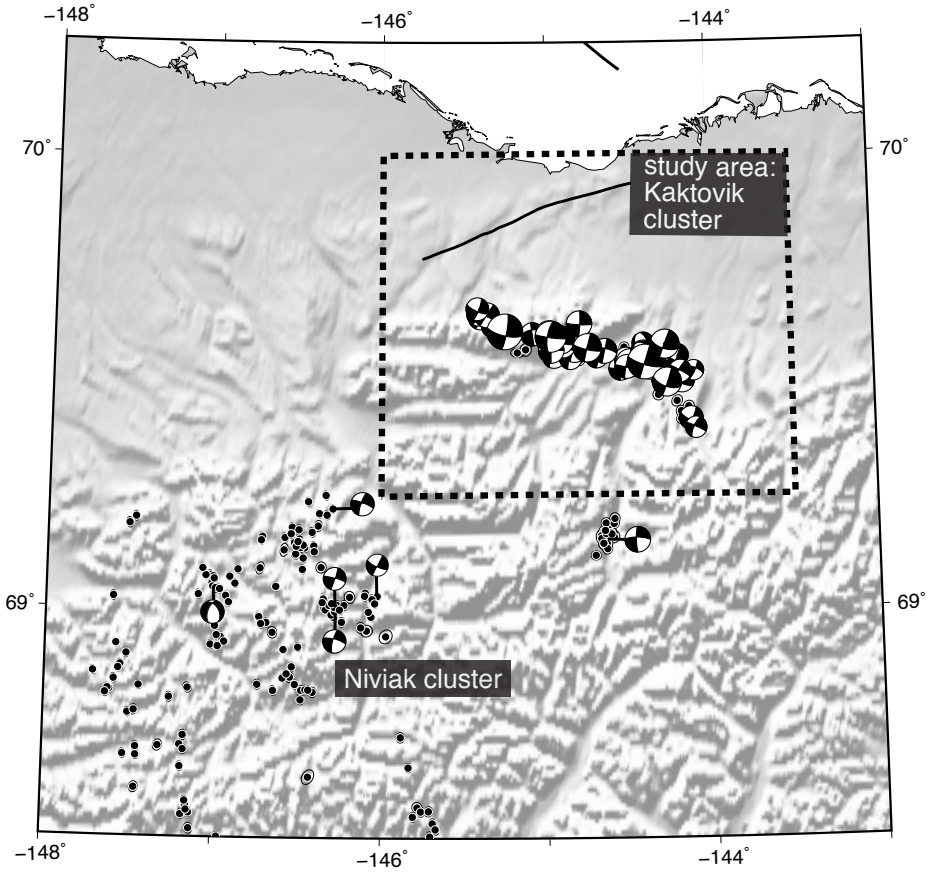


Figure 2.8: Calibrated relocated epicenters for the Kaktovik cluster (indirect calibration) and Niviak cluster (all epicenters outside of dashed box – direct calibration).

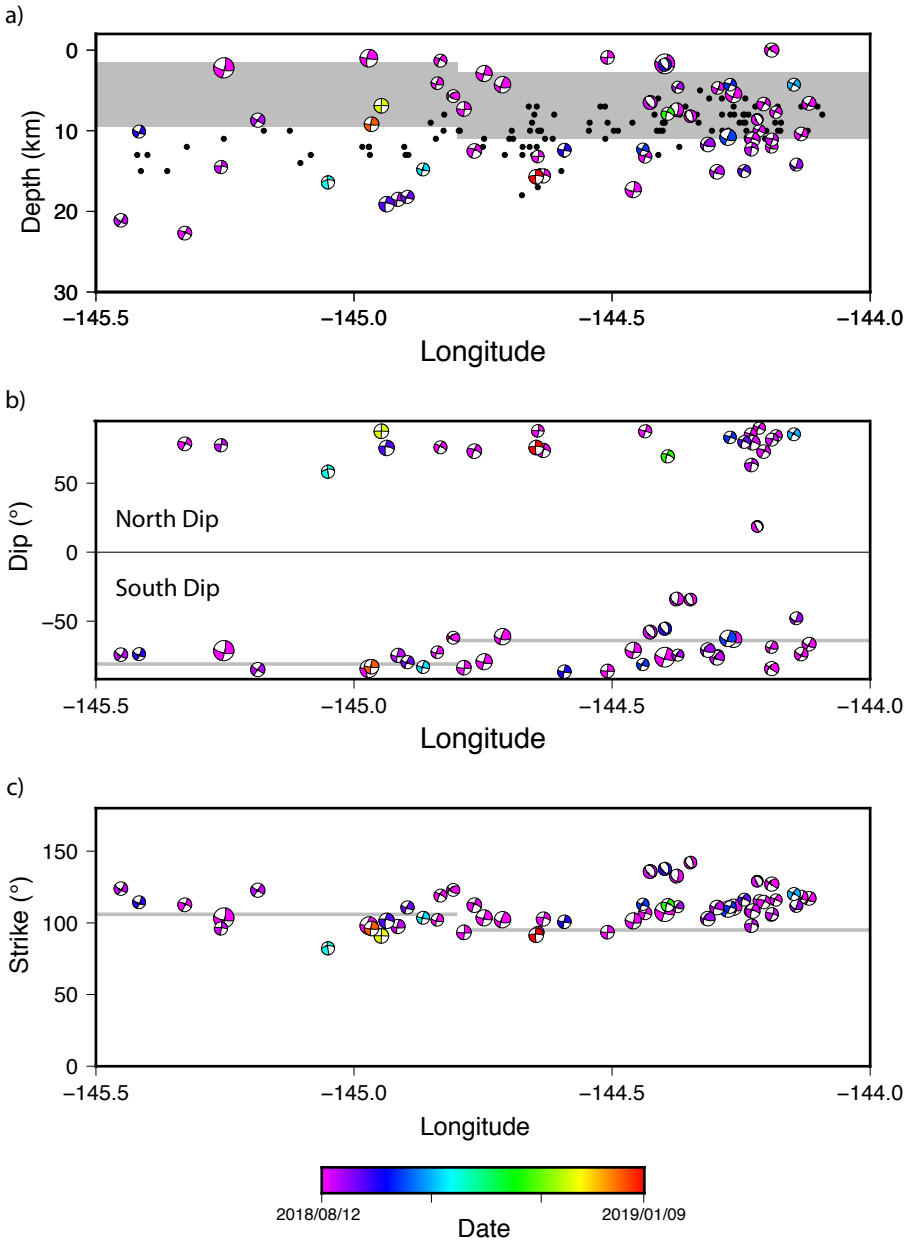


Figure 2.9: Results from the regional moment tensor analysis plotted as a function of longitude. Gray lines represent InSAR model fault planes. a) RMT centroid depths (focal mecanisms) and relocated focal depths (black circles); b) dip of E-W nodal plane; c) strike of E-W nodal plane.

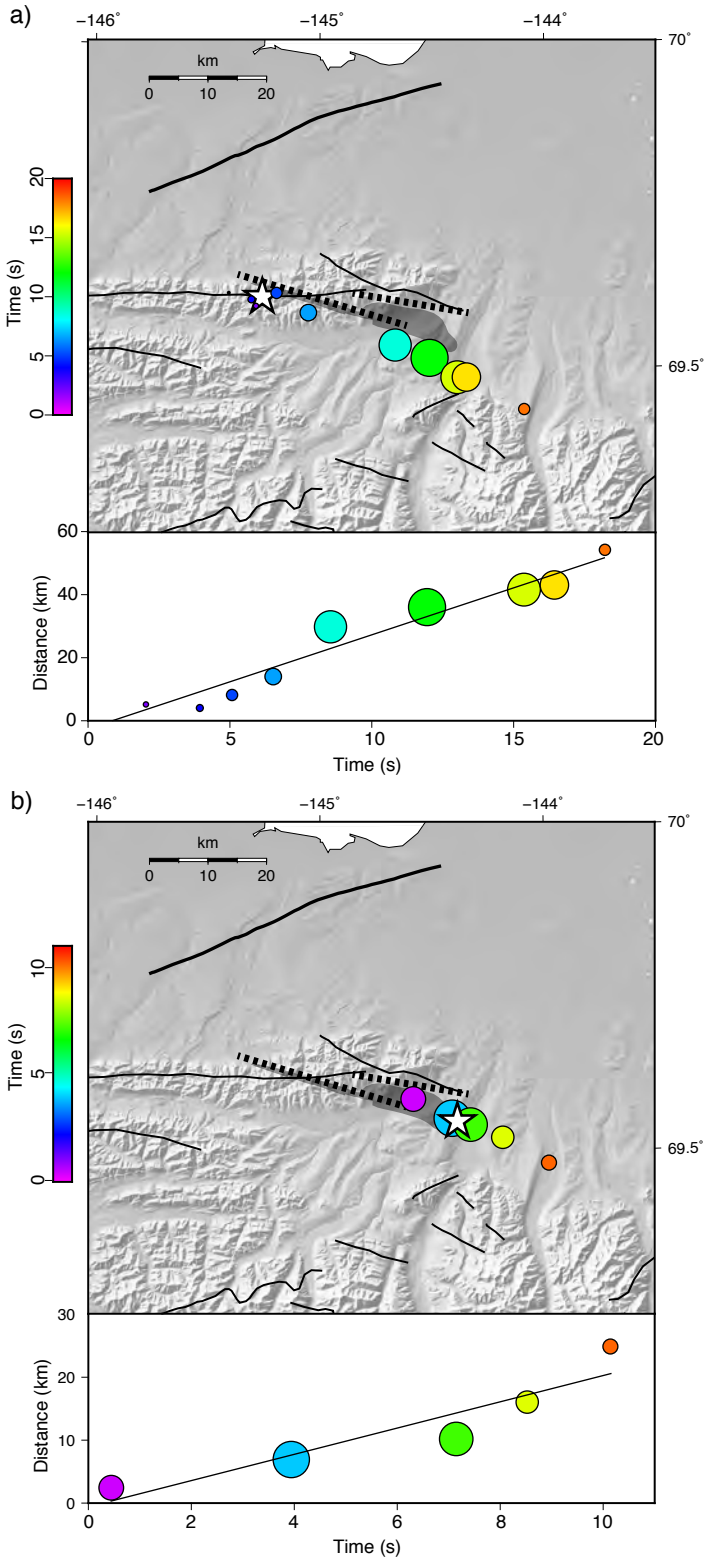


Figure 2.10: Teleseismic back-projection results. (a) The top panel shows back projected 0.2–2 Hz energy for the $M_W$ 6.4 mainshock as circles, colored by time since rupture initiation and scaled by relative energy. Epicenter location designated by the star. The rupture patch from the InSAR model (Figure 2.2b) is the shaded area and the dashed lines are the fault planes. The lower panel shows the same data plotted by distance from epicenter and time since rupture initiation; the straight line denotes an average velocity of 2.6 km/s. (b) Results from the $M_W$ 6.0 event (0.2–2 Hz). Formatting is the same as in Figure 2.9a in Supplementary section 2.11. The average velocity is 2.1 km/s.

Table 2.1: Range allowed in uniform slip modeling

| Parameter | Western Fault | Eastern Fault |
|---|---|---|
| Strike (°) | 95 - 115 | 90 - 110 |
| Dip (°) | 85 - 90 | 40 - 80 |
| Rake (°) | 0 - 360 | 160 - 180 |
| Slip (m) | 0 - 2 | 0 - 2 |
| Easting[a] (km) | 570 - 590 | 583 - 603 |
| Northing[a] (km) | 7713 - 7733 | 7714 - 7734 |
| Minimum depth of dislocation (km) | 0 - 5 | 0 - 5 |
| Maximum depth of dislocation (km) | 0 - 11.5 | 0 - 11.5 |

[a]Of projected center of surface break (UTM zone 6W)

Table 2.2: Best-fit uniform slip fault model parameters for the 2018 Kaktovik earthquakes with uncertainties from the Monte Carlo analysis, compared with RMT, USGS and GCMT solutions.

| Parameter | Western Fault Model | Eastern Fault Model | RMT focal mechanism | USGS focal mechanism | GCMT focal mechanism |
|---|---|---|---|---|---|
| Strike (°) | $106 \pm 0.7$ | $95 \pm 3$ | 103 | 103 | 103 |
| Dip (°) | $81 \pm 4$ | $64 \pm 8$ | 71 | 71 | 77 |
| Rake (°) | $177 \pm 0.8$ | $180 \pm 3$ | -170 | -170 | 175 |
| Slip (m) | $2.00 \pm 1.7$ | $4 \pm 1.80$ | – | – | – |
| Easting[a] (km) | $578.3 \pm 0.7$ | $592.4 \pm 1.6$ | – | – | – |
| Northing[a] (km) | $7723.8 \pm 0.3$ | $7723.6 \pm 0.6$ | – | – | – |
| Length of Scarp (km) | $15.06 \pm 0.89$ | $11.87 \pm 0.99$ | – | – | – |
| Minimum Depth (km) | $3.2 \pm 3$ | $4.2 \pm 0.7$ | 2.2[b] | 11.5[b] | 12.0[b] |
| Maximum Depth (km) | $4.6 \pm 1$ | $6.1 \pm 2.1$ | – | – | – |
| Moment ($10^{18}$ N m) | $3.3 \pm 0.7$ | $2.8 \pm 0.7$ | 5.6 | 5.6 | 5.5 |
| $M_W$ | $6.2 \pm 0.06$ | $6.3 \pm 0.1$ | 6.3 | 6.4 | 6.4 |

[a]Of projected center of surface break (UTM zone 6W)
[b]Depth of centroid

Table 2.3: Best-fit parameters distributed slip fault model with variable rake for the 2018 Kaktovik earthquakes.

| Parameter | Western Fault Model | Eastern Fault Model | RMT focal mechanism | USGS focal mechanism | GCMT focal mechanism |
|---|---|---|---|---|---|
| Strike (°) | 105 | 98 | 103 | 103 | 103 |
| Dip (°) | 84 | 62 | 71 | 71 | 77 |
| Rake (°) | 174[a] | -177[a] | -170 | -170 | 175 |
| Peak Slip (m) | 1.3 | 1.8 | – | – | – |
| Easting[b] (km) | 578 | 593 | – | – | – |
| Northing[b] (km) | 7724 | 7724 | – | – | – |
| Length of Scarp[c] (km) | 26 | 18 | – | – | – |
| Minimum Depth (km) | 1.5[c] | 2.7[c] | 2.2[d] | 11.5[d] | 12.0[d] |
| Maximum Depth (km) | 9.5[c] | 11.0[c] | – | – | – |
| Moment ($10^{18}$ N m) | 11.42 | 2.8 | 5.6 | 5.6 | 5.5 |
| $M_W$ | 6.6 | | 6.3 | 6.4 | 6.4 |

[a]Weighted average
[b]Of projected center of surface break (UTM zone 6W)
[c]Slip $>$ 0.2 m
[d]Depth of centroid

Table 2.4: Fault parameter range allowed in Monte Carlo analysis

| Parameter | Western Fault | Eastern Fault |
|---|---|---|
| Strike (°) | 85 - 115 | 80 - 120 |
| Dip (°) | 65 - 90 | 45 - 90 |
| Rake (°) | 150 - 210 | 150 - 210 |
| Slip (m) | 0 - 6 | 0 - 6 |
| Easting[a] (km) | 570 - 590 | 573 - 613 |
| Northing[a] (km) | 7712 - 7732 | 7704 - 7744 |
| Minimum depth of dislocation (km) | 0 - 7.5 | 0 - 7.5 |
| Maximum depth of dislocation (km) | 0 - 17.5 | 0 - 17.5 |

[a]Of projected center of surface break

Table 2.5: Best-fit uniform slip fault model parameters for a listric fault: western fault segment

| Parameter | Steep Dip Segment | Shallow Dip Segment |
|---|---|---|
| Strike (°) | 105 | 105 |
| Dip (°) | 85 | 30 |
| Rake (°) | 180 | 180 |
| Slip (m) | 4 | 0.12 |
| Easting[a] (km) | 579 | 579 |
| Northing[a] (km) | 7725 | 7729 |
| Length of Scarp (km) | 19 | 11 |
| Minimum Depth of Dislocation (km) | 2.4 | 3.0 |
| Maximum Depth of Dislocation (km) | 3.0 | 13.0 |

[a]Of projected center of surface break

Table 2.6: Best-fit uniform slip fault model parameters for a listric fault: eastern fault segment

| Parameter | Steep Dip Segment | Shallow Dip Segment |
|---|---|---|
| Strike (°) | 100 | 100 |
| Dip (°) | 85 | 30 |
| Rake (°) | -169 | -174 |
| Slip (m) | 4 | 0.5 |
| Easting[a] (km) | 593 | 594 |
| Northing[a] (km) | 7724 | 7729 |
| Length of Scarp (km) | 9 | 12 |
| Minimum Depth of Dislocation (km) | 2.6 | 3.0 |
| Maximum Depth of Dislocation (km) | 3.0 | 10.8 |

[a]Of projected center of surface break

Table 2.7: Calibrated epicenters of earthquakes in the Kaktovik cluster. Az is the azimuth of the 90% confidence ellipse; L1 and L2 are the semi-axis lengths of the long and short axes of the 90% confidence ellipse, respectively. The area of the 90% confidence ellipse is given in the 'Area' column.

| Date | Time (UTC) | Latitude (°) | Longitude (°) | Focal depth (km) | Depth uncertainty (km) | Magnitude | Az (°) | L1 (km) | L2 (km) | Area ($km^2$) |
|---|---|---|---|---|---|---|---|---|---|---|
| 12-08-2018 | 14:58:53 | 69.6139 | -145.2523 | 11.0 | 4.0 | 6.4 Mw | 290 | 2.23 | 2.34 | 16.4 |
| 12-08-2018 | 15:04:06 | 69.5661 | -145.1747 | 10.0 | 4.0 | 4.2 ML | 6 | 2.13 | 3.24 | 21.6 |
| 12-08-2018 | 15:04:48 | 69.5730 | -145.1243 | 10.0 | 4.0 | 4.4 ML | 282 | 2.73 | 3.17 | 27.2 |
| 12-08-2018 | 15:14:20 | 69.5774 | -144.7480 | 11.0 | 4.0 | 5.0 Mw | 304 | 2.2 | 2.21 | 15.3 |
| 12-08-2018 | 15:18:36 | 69.5639 | -144.6943 | 10.0 | 4.0 | 4.7 mb | 296 | 2.19 | 2.28 | 15.7 |
| 12-08-2018 | 15:33:36 | 69.5485 | -144.4018 | 10.0 | 4.0 | 4.1 ML | 292 | 2.49 | 3.05 | 23.9 |
| 12-08-2018 | 15:34:48 | 69.5525 | -144.6991 | 11.0 | 4.0 | 4.7 mb | 296 | 2.26 | 2.42 | 17.2 |
| 12-08-2018 | 15:42:06 | 69.6038 | -144.8253 | 8.0 | 4.0 | 4.4 mb | 282 | 2.38 | 2.68 | 20.1 |
| 12-08-2018 | 15:42:24 | 69.5740 | -144.3697 | 12.0 | 4.0 | 4.6 mb | 301 | 2.48 | 2.66 | 20.8 |
| 12-08-2018 | 16:02:08 | 69.6026 | -144.9712 | 12.0 | 4.0 | 5.1 Mw | 313 | 2.16 | 2.17 | 14.8 |
| 12-08-2018 | 16:11:30 | 69.5489 | -144.7949 | 10.0 | 4.0 | 4.0 ML | 302 | 2.41 | 2.69 | 20.4 |
| 12-08-2018 | 16:44:39 | 69.5315 | -144.5451 | 10.0 | 4.0 | 4.2 Mw | 299 | 2.33 | 2.69 | 19.7 |

| | | | | | | | | | | |
|---|---|---|---|---|---|---|---|---|---|---|
| 12-08-2018 | 16:53:12 | 69.6049 | -145.1040 | 14.0 | 4.0 | 4.0 mb | 291 | 2.24 | 2.39 | 16.9 |
| 12-08-2018 | 17:30:43 | 69.5580 | -144.9516 | 7.0 | 4.0 | 4.1 ML | 297 | 2.41 | 2.84 | 21.5 |
| 12-08-2018 | 17:54:24 | 69.5957 | -144.8415 | 11.0 | 4.0 | 4.1 ML | 293 | 2.22 | 2.41 | 16.8 |
| 12-08-2018 | 18:36:43 | 69.5788 | -144.7501 | 12.0 | 4.0 | 4.7 Mw | 288 | 2.17 | 2.19 | 14.9 |
| 12-08-2018 | 19:38:27 | 69.5542 | -144.8515 | 9.0 | 4.0 | 3.9 Mw | 287 | 2.4 | 2.64 | 19.9 |
| 12-08-2018 | 20:55:39 | 69.5769 | -144.5226 | 7.0 | 4.0 | 4.0 ML | 294 | 2.31 | 2.56 | 18.6 |
| 12-08-2018 | 20:56:43 | 69.5724 | -144.4017 | 9.0 | 4.0 | 4.0 Mw | 293 | 2.24 | 2.47 | 17.4 |
| 12-08-2018 | 21:15:01 | 69.5454 | -144.3980 | 9.0 | 4.0 | 6.0 Mw | 295 | 2.14 | 2.16 | 14.5 |
| 12-08-2018 | 21:22:10 | 69.5474 | -144.4967 | 10.0 | 4.0 | 4.0 ML | 285 | 2.42 | 2.96 | 22.5 |
| 12-08-2018 | 21:24:10 | 69.5449 | -144.4134 | 10.0 | 4.0 | 4.5 mb | 283 | 2.39 | 2.66 | 20 |
| 12-08-2018 | 21:24:27 | 69.4963 | -144.2743 | 10.0 | 4.0 | 4.5 mb | 325 | 2.48 | 2.67 | 20.8 |
| 12-08-2018 | 21:25:47 | 69.5176 | -144.2863 | 10.0 | 4.0 | 4.4 mb | 291 | 2.54 | 3.03 | 24.1 |
| 12-08-2018 | 21:27:21 | 69.4713 | -144.3167 | 12.0 | 4.0 | 4.3 mb | 89 | 2.62 | 2.71 | 22.3 |
| 12-08-2018 | 21:30:20 | 69.4451 | -144.1333 | 7.0 | 4.0 | 4.9 mb | 305 | 2.55 | 2.75 | 22.1 |
| 12-08-2018 | 21:31:04 | 69.5005 | -144.2646 | 7.0 | 4.0 | 5.0 Mw | 324 | 2.27 | 2.28 | 16.3 |
| 12-08-2018 | 21:38:02 | 69.5266 | -144.2359 | 8.0 | 4.0 | 4.3 Mw | 280 | 2.17 | 2.25 | 15.3 |
| 12-08-2018 | 21:44:16 | 69.5447 | -144.4607 | 9.0 | 4.0 | 4.5 mb | 296 | 2.24 | 2.45 | 17.3 |
| 12-08-2018 | 21:47:38 | 69.5314 | -144.2531 | 9.0 | 4.0 | 4.7 mb | 284 | 2.21 | 2.32 | 16.1 |
| 12-08-2018 | 21:49:28 | 69.4931 | -144.1740 | 10.0 | 4.0 | 4.4 mb | 305 | 2.33 | 2.51 | 18.4 |
| 12-08-2018 | 22:00:16 | 69.5397 | -144.5436 | 9.0 | 4.0 | 4.4 mb | 282 | 2.17 | 2.25 | 15.3 |
| 12-08-2018 | 22:09:02 | 69.5462 | -144.3325 | 9.0 | 4.0 | 4.5 mb | 292 | 2.26 | 2.48 | 17.6 |
| 12-08-2018 | 22:11:13 | 69.4347 | -144.1792 | 8.0 | 4.0 | 4.1 mb | 291 | 2.39 | 2.63 | 19.7 |
| 12-08-2018 | 22:20:08 | 69.4574 | -144.2036 | 11.0 | 4.0 | 4.3 mb | 305 | 2.37 | 2.91 | 21.7 |
| 12-08-2018 | 22:46:25 | 69.4179 | -144.1785 | 10.0 | 4.0 | 4.4 mb | 299 | 2.28 | 2.6 | 18.7 |

| | | | | | | | | | | |
|---|---|---|---|---|---|---|---|---|---|---|
| 12-08-2018 | 23:29:38 | 69.5040 | -144.1728 | 9.0 | 4.0 | 4.1 Mw | 302 | 2.25 | 2.53 | 17.9 |
| 12-08-2018 | 23:30:02 | 69.4203 | -144.1211 | 10.0 | 4.0 | 4.1 Mw | 306 | 2.51 | 2.94 | 23.2 |
| 12-08-2018 | 23:59:49 | 69.5375 | -144.2397 | 10.0 | 4.0 | 4.1 Mw | 296 | 2.18 | 2.36 | 16.2 |
| 13-08-2018 | 02:42:33 | 69.5572 | -144.6916 | 11.0 | 4.0 | 3.8 Mw | 293 | 2.2 | 2.39 | 16.6 |
| 13-08-2018 | 05:00:19 | 69.5521 | -144.5131 | 11.0 | 4.0 | 4.0 Mw | 293 | 2.16 | 2.31 | 15.7 |
| 13-08-2018 | 05:22:31 | 69.4000 | -144.0928 | 8.0 | 4.0 | 3.9 Mw | 313 | 2.6 | 2.95 | 24.2 |
| 13-08-2018 | 05:41:47 | 69.5302 | -144.2224 | 7.0 | 4.0 | 3.9 Mw | 293 | 2.18 | 2.35 | 16.1 |
| 13-08-2018 | 05:43:57 | 69.5859 | -144.4071 | 10.0 | 4.0 | 4.1 Mw | 292 | 2.29 | 2.45 | 17.6 |
| 13-08-2018 | 06:37:25 | 69.5518 | -144.2457 | 9.0 | 4.0 | 4.0 Mw | 296 | 2.21 | 2.37 | 16.5 |
| 13-08-2018 | 08:53:12 | 69.5658 | -144.4103 | 13.0 | 4.0 | 4.4 Mw | 294 | 2.24 | 2.38 | 16.8 |
| 13-08-2018 | 09:55:55 | 69.5209 | -144.2418 | 9.0 | 4.0 | 4.5 ML | 295 | 2.2 | 2.35 | 16.2 |
| 13-08-2018 | 09:56:59 | 69.6305 | -144.7971 | 10.0 | 4.0 | 4.4 Mw | 288 | 2.22 | 2.31 | 16.1 |
| 13-08-2018 | 11:05:12 | 69.5702 | -144.6431 | 10.0 | 4.0 | 4.3 Mw | 288 | 2.15 | 2.24 | 15.1 |
| 13-08-2018 | 11:47:26 | 69.5524 | -144.2432 | 8.0 | 4.0 | 3.9 Mw | 291 | 2.18 | 2.33 | 16 |
| 13-08-2018 | 13:35:44 | 69.6454 | -145.4003 | 13.0 | 4.0 | 4.2 Mw | 296 | 2.28 | 2.48 | 17.8 |
| 13-08-2018 | 19:36:08 | 69.5429 | -144.4885 | 10.0 | 4.0 | 4.7 Mw | 290 | 2.17 | 2.21 | 15.1 |
| 13-08-2018 | 23:53:10 | 69.5428 | -144.2457 | 8.0 | 4.0 | 4.1 Mw | 296 | 2.18 | 2.31 | 15.9 |
| 14-08-2018 | 06:31:01 | 69.5212 | -144.2634 | 8.0 | 4.0 | 4.0 Mw | 295 | 2.2 | 2.39 | 16.5 |
| 14-08-2018 | 14:49:58 | 69.5079 | -144.2868 | 8.0 | 4.0 | 4.3 Mw | 299 | 2.2 | 2.41 | 16.6 |
| 14-08-2018 | 16:53:10 | 69.5737 | -144.8265 | 10.0 | 4.0 | 4.4 Mw | 292 | 2.21 | 2.32 | 16.1 |
| 16-08-2018 | 06:32:29 | 69.5633 | -144.4107 | 6.0 | 4.0 | 4.3 Mw | 293 | 2.17 | 2.22 | 15.1 |
| 16-08-2018 | 07:22:39 | 69.5310 | -144.2873 | 6.0 | 4.0 | 4.5 Mw | 291 | 2.15 | 2.23 | 15.1 |
| 17-08-2018 | 13:27:08 | 69.5127 | -144.2419 | 6.0 | 4.0 | 3.9 Mw | 291 | 2.18 | 2.36 | 16.2 |
| 18-08-2018 | 04:39:36 | 69.5391 | -144.3067 | 10.0 | 4.0 | 4.2 Mw | 283 | 2.14 | 2.21 | 14.9 |

| | | | | | | | | | | |
|---|---|---|---|---|---|---|---|---|---|---|
| 18-08-2018 | 04:52:57 | 69.6269 | -145.3240 | 12.0 | 4.0 | 4.0 Mw | 290 | 2.18 | 2.34 | 16.1 |
| 18-08-2018 | 07:06:01 | 69.5346 | -144.3118 | 6.0 | 4.0 | 4.2 Mw | 296 | 2.21 | 2.46 | 17.1 |
| 19-08-2018 | 13:32:23 | 69.5982 | -144.9003 | 13.0 | 4.0 | 4.3 Mw | 292 | 2.2 | 2.35 | 16.3 |
| 19-08-2018 | 19:30:07 | 69.6533 | -145.4129 | 15.0 | 4.0 | 4.1 Mw | 289 | 2.2 | 2.38 | 16.4 |
| 20-08-2018 | 09:33:48 | 69.6506 | -145.3619 | 15.0 | 4.0 | 4.4 Mw | 272 | 2.23 | 2.37 | 16.6 |
| 21-08-2018 | 18:23:43 | 69.5295 | -144.3687 | 8.0 | 4.0 | 3.8 Mw | 295 | 2.24 | 2.41 | 17 |
| 22-08-2018 | 21:09:33 | 69.5477 | -144.3901 | 8.0 | 4.0 | 4.0 ML | 290 | 2.27 | 2.45 | 17.4 |
| 23-08-2018 | 04:30:39 | 69.5400 | -144.3359 | 8.0 | 4.0 | 4.7 mb | 293 | 2.16 | 2.28 | 15.5 |
| 23-08-2018 | 16:11:25 | 69.5587 | -144.2010 | 10.0 | 4.0 | 4.0 Mw | 293 | 2.21 | 2.37 | 16.5 |
| 28-08-2018 | 11:13:21 | 69.5814 | -144.8946 | 13.0 | 4.0 | 4.0 Mw | 292 | 2.3 | 2.56 | 18.5 |
| 30-08-2018 | 22:49:50 | 69.5275 | -144.2709 | 8.0 | 4.0 | 3.9 Mw | 290 | 2.2 | 2.37 | 16.3 |
| 01-09-2018 | 06:41:19 | 69.5913 | -144.9711 | 12.0 | 4.0 | 4.5 Mw | 283 | 2.15 | 2.2 | 14.9 |
| 05-09-2018 | 04:03:50 | 69.5577 | -144.3579 | 7.0 | 4.0 | 4.1 Mw | 286 | 2.17 | 2.3 | 15.7 |
| 06-09-2018 | 04:05:11 | 69.6639 | -145.4201 | 13.0 | 4.0 | 4.0 Mw | 274 | 2.24 | 2.44 | 17.1 |
| 10-09-2018 | 23:37:08 | 69.5351 | -144.5087 | 9.0 | 4.0 | 3.9 Mw | 283 | 2.17 | 2.33 | 15.9 |
| 18-09-2018 | 12:40:57 | 69.5841 | -144.2754 | 10.0 | 4.0 | 5.0 Mw | 291 | 2.33 | 2.6 | 19 |
| 19-09-2018 | 22:12:43 | 69.5378 | -144.3295 | 5.0 | 4.0 | 3.9 Mw | 288 | 2.17 | 2.37 | 16.2 |
| 20-09-2018 | 09:27:59 | 69.5470 | -144.4180 | 8.0 | 4.0 | 3.8 Mw | 286 | 2.15 | 2.28 | 15.4 |
| 21-09-2018 | 04:28:25 | 69.5253 | -144.1021 | 7.0 | 4.0 | 3.9 Mw | 288 | 2.2 | 2.31 | 16 |
| 04-10-2018 | 13:12:57 | 69.5241 | -144.1839 | 9.0 | 4.0 | 4.0 Mw | 294 | 2.17 | 2.34 | 16 |
| 04-10-2018 | 13:12:56 | 69.5275 | -144.1791 | 7.0 | 4.0 | 4.0 Mw | 290 | 2.16 | 2.37 | 16.1 |
| 09-10-2018 | 07:11:21 | 69.5900 | -144.9027 | 12.0 | 4.0 | 4.0 Mw | 292 | 2.17 | 2.32 | 15.9 |
| 12-10-2018 | 14:48:16 | 69.5619 | -144.5138 | 7.0 | 4.0 | 3.1 ML | 290 | 2.28 | 2.68 | 19.2 |
| 16-10-2018 | 16:45:17 | 69.6081 | -145.0838 | 13.0 | 4.0 | 4.0 Mw | 292 | 2.23 | 2.37 | 16.6 |

| | | | | | | | | | | |
|---|---|---|---|---|---|---|---|---|---|---|
| 16-11-2018 | 03:31:15 | 69.5440 | -144.3995 | 9.0 | 4.0 | 3.9 Mw | 292 | 2.18 | 2.34 | 16 |
| 07-12-2018 | 15:22:57 | 69.5724 | -144.9692 | 13.0 | 4.0 | 4.2 Mw | 274 | 2.45 | 2.56 | 19.7 |
| 30-12-2018 | 07:14:11 | 69.6097 | -144.9840 | 12.0 | 4.0 | 4.5 mb | 12 | 2.57 | 2.89 | 23.3 |
| 09-01-2019 | 06:51:40 | 69.1536 | -144.6440 | 17.0 | 4.0 | 4.3 Mw | 290 | 2.2 | 2.29 | 15.9 |
| 09-01-2019 | 15:35:49 | 69.1600 | -144.5982 | 15.0 | 4.0 | 2.5 ML | 292 | 2.57 | 3.02 | 24.4 |
| 10-01-2019 | 10:49:09 | 69.1726 | -144.6598 | 12.0 | 4.0 | 2.7 ML | 277 | 2.41 | 2.57 | 19.4 |
| 10-01-2019 | 11:25:22 | 69.1460 | -144.6385 | 10.0 | 4.0 | 3.9 ML | 276 | 2.44 | 2.6 | 19.9 |
| 10-01-2019 | 19:36:39 | 69.1571 | -144.6746 | 18.0 | 4.0 | 4.0 Mw | 289 | 2.25 | 2.46 | 17.4 |
| 12-01-2019 | 17:14:07 | 69.1752 | -144.6401 | 15.0 | 4.0 | 4.1 Mw | 287 | 2.32 | 2.47 | 18 |
| 12-01-2019 | 18:30:29 | 69.1705 | -144.6530 | 13.0 | 4.0 | 2.9 ML | 86 | 2.35 | 2.5 | 18.5 |
| 12-01-2019 | 21:00:35 | 69.1629 | -144.6738 | 13.0 | 4.0 | 2.8 ML | 288 | 2.62 | 2.98 | 24.5 |
| 13-01-2019 | 06:45:30 | 69.1853 | -144.6298 | 11.0 | 4.0 | 3.1 ML | 288 | 2.54 | 2.79 | 22.2 |
| 21-01-2019 | 04:59:20 | 69.1450 | -144.6550 | 9.0 | 4.0 | 2.6 ML | 280 | 2.48 | 2.72 | 21.2 |
| 07-02-2019 | 01:32:07 | 69.1451 | -144.6407 | 13.0 | 4.0 | 2.9 ML | 282 | 2.28 | 2.46 | 17.6 |
| 08-02-2019 | 10:16:50 | 69.1565 | -144.6732 | 12.0 | 4.0 | 3.2 ML | 278 | 2.29 | 2.49 | 18 |
| 10-02-2019 | 10:34:31 | 69.1906 | -144.6460 | 12.0 | 4.0 | 2.5 ML | 276 | 2.3 | 2.57 | 18.5 |
| 16-03-2019 | 00:29:15 | 69.1696 | -144.6151 | 11.0 | 4.0 | 2.4 ML | 295 | 2.57 | 2.8 | 22.6 |
| 24-03-2019 | 12:44:42 | 69.1892 | -144.5974 | 12.0 | 4.0 | 2.6 ML | 297 | 2.35 | 2.53 | 18.7 |
| 09-04-2019 | 16:25:11 | 69.1672 | -144.6457 | 7.0 | 4.0 | 2.5 ML | 291 | 2.43 | 2.63 | 20.1 |
| 16-04-2019 | 00:27:06 | 69.2004 | -144.5925 | 13.0 | 4.0 | 2.7 ML | 88 | 2.45 | 2.78 | 21.4 |
| 03-07-2019 | 04:38:23 | 69.1199 | -144.7080 | 13.0 | 6.0 | 5.1 Mw | 12 | 2.27 | 2.31 | 16.4 |
| 03-07-2019 | 04:58:54 | 69.1437 | -144.6589 | 10.0 | 4.0 | 4.3 Mw | 290 | 2.23 | 2.36 | 16.5 |
| 05-07-2019 | 05:59:14 | 69.1342 | -144.6380 | 10.0 | 4.0 | 3.3 ML | 289 | 2.3 | 2.73 | 19.7 |
| 08-07-2019 | 23:20:27 | 69.1663 | -144.6120 | 8.0 | 4.0 | 4.1 Mw | 290 | 2.43 | 2.59 | 19.8 |

| | | | | | | | | | | |
|---|---|---|---|---|---|---|---|---|---|---|
| 13-07-2019 | 22:21:52 | 69.1742 | -144.6507 | 8.0 | 4.0 | 3.6 Mw | 294 | 2.25 | 2.43 | 17.2 |
| 16-07-2019 | 21:42:42 | 69.1460 | -144.6614 | 7.0 | 4.0 | 3.6 ML | 276 | 2.56 | 3 | 24.1 |

Table 2.8: Regional moment tensor solutions for the 2018 Kaktovik mainshock and 87 best-recorded aftershocks.

| Event ID | Date, time (UTC) | Latitude (°) | Longitude (°) | Depth (km) | Local magnitude | Strike 1 (°) | Dip 1 (°) | Rake 1 (°) | Strike 2 (°) | Dip 2 (°) | Rake 2 (°) |
|---|---|---|---|---|---|---|---|---|---|---|---|
| ak20076877[a] | 12-08-2018 14:58 | 69.5619 | -145.2998 | 2.2 | 6.3 | 103.45 | 71.35 | -170.47 | 10.37 | 80.98 | -18.90 |
| ak20076944[a] | 12-08-2018 15:14 | 69.5722 | -144.7372 | 2.9 | 5.0 | 103.50 | 79.39 | 178.27 | 193.82 | 88.30 | 10.61 |
| ak20077947[a] | 12-08-2018 16:02 | 69.5493 | -144.9518 | 1.0 | 5.5 | 189.86 | 72.69 | 5.80 | 98.13 | 84.46 | 162.60 |
| ak20079009 | 12-08-2018 16:44 | 69.4709 | -144.5089 | 0.9 | 4.2 | 93.49 | 86.06 | -178.61 | 3.39 | 88.61 | -3.94 |
| ak20079190 | 12-08-2018 17:30 | 69.5265 | -144.8325 | 1.3 | 4.0 | 299.00 | 76.00 | -164.00 | 205.00 | 75.00 | -15.00 |
| ak20080120 | 12-08-2018 17:54 | 69.5429 | -144.8078 | 5.7 | 4.0 | 123.00 | 62.00 | 139.00 | 235.00 | 55.00 | 35.00 |
| ak20080290 | 12-08-2018 18:36 | 69.5347 | -144.7123 | 4.3 | 5.1 | 102.20 | 61.22 | 167.97 | 198.06 | 79.48 | 29.32 |
| ak20081352 | 12-08-2018 19:38 | 69.5339 | -144.8386 | 4.1 | 3.9 | 102.08 | 72.43 | 170.52 | 194.96 | 80.97 | 17.79 |

| | | | | | | | | | | | |
|---|---|---|---|---|---|---|---|---|---|---|---|
| ak20083386 | 12-08-2018 20:56 | 69.4504 | -144.3410 | 4.5 | 4.1 | 103.73 | 75.78 | 176.38 | 194.62 | 86.50 | 14.25 |
| ak20083478[a] | 12-08-2018 21:15 | 69.5205 | -144.3602 | 1.7 | 6.1 | 107.82 | 76.14 | 179.81 | 197.87 | 89.81 | 13.86 |
| ak20083586[a] | 12-08-2018 21:31 | 69.4683 | -144.2440 | 5.5 | 5.1 | 110.90 | 63.16 | -176.22 | 19.19 | 86.63 | -26.89 |
| ak20086036 | 12-08-2018 23:29 | 69.4182 | -144.1184 | 6.6 | 4.3 | 117.07 | 66.67 | -178.14 | 26.33 | 88.29 | -23.34 |
| ak20086064 | 12-08-2018 23:30 | 69.4399 | -144.1337 | 10.4 | 4.2 | 118.04 | 73.86 | -169.65 | 25.13 | 80.06 | -16.40 |
| ak20087083 | 12-08-2018 23:59 | 69.6159 | -144.1907 | 0.0 | 4.4 | 127.05 | 84.38 | 148.29 | 220.51 | 58.47 | 6.60 |
| ak20088613 | 13-08-2018 2:42 | 69.5079 | -144.6439 | 13.2 | 3.9 | 3.65 | 79.21 | 2.12 | 273.25 | 87.92 | 169.20 |
| ak20089887 | 13-08-2018 4:43 | 69.4865 | -144.4680 | 15.5 | 3.8 | 23.00 | 78.25 | 10.36 | 290.87 | 79.86 | 168.06 |
| ak20091069 | 13-08-2018 5:00 | 69.5187 | -144.4359 | 13.2 | 4.1 | 16.92 | 87.59 | 2.39 | 286.82 | 87.62 | 177.59 |
| ak20091105 | 13-08-2018 5:22 | 69.4583 | -144.1824 | 7.7 | 3.8 | 295.96 | 84.35 | -162.66 | 204.20 | 72.74 | -5.92 |
| ak20091133 | 13-08-2018 5:41 | 69.4679 | -144.1909 | 12.0 | 3.9 | 105.45 | 68.77 | 167.51 | 200.04 | 78.37 | 21.70 |
| ak20091142 | 13-08-2018 5:43 | 69.5186 | -144.3482 | 8.2 | 3.9 | 142.06 | 34.35 | -109.65 | 345.44 | 57.90 | -77.06 |

| | | | | | | | | | | | |
|---|---|---|---|---|---|---|---|---|---|---|---|
| ak20092362 | 13-08-2018 6:37 | 69.4732 | -144.2148 | 10.0 | 3.8 | 295.40 | 89.95 | -167.51 | 205.39 | 77.51 | -0.05 |
| ak20094870 | 13-08-2018 8:53 | 69.4703 | -144.3751 | 7.4 | 4.3 | 132.60 | 33.99 | -140.08 | 7.86 | 68.98 | -62.66 |
| ak20094927 | 13-08-2018 9:56 | 69.5355 | -144.7871 | 7.3 | 4.5 | 93.39 | 83.69 | -175.07 | 2.85 | 85.10 | -6.34 |
| ak20096198 | 13-08-2018 11:05 | 69.5344 | -144.6331 | 15.6 | 4.4 | 192.56 | 89.70 | -16.29 | 282.65 | 73.71 | -179.68 |
| ak20097481 | 13-08-2018 11:47 | 69.4277 | -144.2954 | 4.7 | 3.9 | 110.97 | 75.16 | -168.29 | 17.93 | 78.68 | -15.14 |
| ak20097611 | 13-08-2018 13:35 | 69.6505 | -145.3279 | 22.7 | 4.3 | 23.38 | 86.22 | 11.54 | 292.61 | 78.48 | 176.14 |
| ak20100243 | 13-08-2018 16:19 | 69.5196 | -144.4707 | 13.3 | 3.9 | 16.78 | 85.16 | 17.41 | 285.27 | 72.65 | 174.93 |
| ak20101765 | 13-08-2018 19:36 | 69.5469 | -144.4590 | 17.3 | 5.0 | 101.39 | 71.13 | -173.12 | 9.15 | 83.49 | -19.00 |
| ak20101805 | 13-08-2018 20:05 | 69.4766 | -144.4649 | 11.4 | 3.5 | 102.95 | 71.93 | 164.24 | 197.96 | 75.03 | 18.72 |
| ak20101888 | 13-08-2018 21:40 | 69.4796 | -144.2254 | 17.8 | 3.8 | 292.11 | 75.58 | -172.85 | 200.32 | 83.07 | -14.53 |
| ak20101921 | 13-08-2018 21:51 | 69.4298 | -144.1671 | 18.4 | 3.7 | 197.80 | 75.16 | -14.32 | 291.54 | 76.16 | -164.70 |
| ak20102030 | 13-08-2018 23:53 | 69.4823 | -144.2317 | 10.9 | 3.9 | 288.23 | 85.39 | -171.32 | 197.53 | 81.35 | -4.66 |

| | | | | | | | | | | | |
|---|---|---|---|---|---|---|---|---|---|---|---|
| ak20102278 | 14-08-2018 6:31 | 69.4667 | -144.2187 | 8.6 | 3.6 | 153.78 | 72.97 | -82.31 | 309.04 | 18.64 | -113.59 |
| ak20102778 | 14-08-2018 14:49 | 69.4665 | -144.2064 | 6.7 | 4.2 | 25.44 | 87.01 | 17.13 | 294.52 | 72.89 | 176.87 |
| ak20102929 | 14-08-2018 16:53 | 69.5408 | -144.7669 | 12.5 | 4.5 | 200.31 | 83.30 | -16.92 | 292.35 | 73.20 | -173.00 |
| ak20102954 | 14-08-2018 17:04 | 69.5018 | -144.3242 | 5.4 | 3.5 | 123.42 | 85.88 | 153.31 | 215.49 | 63.39 | 4.60 |
| ak20103077 | 14-08-2018 17:45 | 69.4506 | -144.2382 | 3.0 | 3.8 | 25.07 | 55.28 | -19.57 | 126.52 | 74.02 | -143.66 |
| ak20103130 | 14-08-2018 18:20 | 69.5360 | -144.6586 | 14.8 | 3.8 | 107.58 | 81.90 | 168.34 | 199.25 | 78.46 | 8.26 |
| ak20103839 | 15-08-2018 2:47 | 69.5156 | -144.3507 | 9.0 | 3.6 | 23.31 | 64.66 | -6.93 | 116.29 | 83.74 | -154.50 |
| ak20103979 | 15-08-2018 6:08 | 69.5059 | -144.2224 | 10.9 | 3.8 | 9.69 | 72.05 | 2.37 | 278.95 | 87.74 | 162.03 |
| ak20104157 | 15-08-2018 9:19 | 69.5420 | -144.5524 | 13.4 | 3.7 | 333.97 | 63.63 | -75.29 | 123.39 | 29.94 | -117.11 |
| ak20104648 | 15-08-2018 14:52 | 69.4895 | -144.3294 | 12.0 | 3.8 | 312.23 | 89.00 | -177.78 | 222.19 | 87.78 | -1.00 |
| ak20106048 | 16-08-2018 6:32 | 69.4902 | -144.4262 | 6.5 | 4.3 | 340.64 | 34.68 | -69.15 | 135.79 | 57.88 | -103.83 |
| ak20106116 | 16-08-2018 7:22 | 69.5342 | -144.2275 | 11.1 | 4.5 | 195.24 | 74.55 | -11.13 | 288.24 | 79.28 | -164.27 |

| | | | | | | | | | | | |
|---|---|---|---|---|---|---|---|---|---|---|---|
| ak20108236 | 17-08-2018 13:27 | 69.5003 | -144.1905 | 11.1 | 4.0 | 17.80 | 78.63 | 8.64 | 286.09 | 81.53 | 168.51 |
| ak20109930 | 18-08-2018 1:26 | 69.5789 | -144.8002 | 12.6 | 3.6 | 174.96 | 71.61 | -18.27 | 270.90 | 72.70 | -160.71 |
| ak20110107 | 18-08-2018 4:39 | 69.4826 | -144.2966 | 15.1 | 4.5 | 110.71 | 76.58 | 152.74 | 207.53 | 63.55 | 15.02 |
| ak20110135 | 18-08-2018 4:52 | 69.6377 | -145.2578 | 14.5 | 4.1 | 7.12 | 85.18 | 12.61 | 276.05 | 77.44 | 175.06 |
| ak20110237 | 18-08-2018 7:06 | 69.5127 | -144.2300 | 12.3 | 4.2 | 277.99 | 63.16 | -178.32 | 187.24 | 88.50 | -26.85 |
| ak20115069 | 19-08-2018 13:32 | 69.5810 | -144.9148 | 18.5 | 4.4 | 97.49 | 74.76 | 170.18 | 190.10 | 80.53 | 15.46 |
| ak20116787 | 19-08-2018 19:30 | 69.6396 | -145.4517 | 21.1 | 4.2 | 123.88 | 74.25 | -166.34 | 30.10 | 76.87 | -16.19 |
| ak20122189 | 20-08-2018 9:33 | 69.5727 | -145.1864 | 8.7 | 4.4 | 122.79 | 85.04 | 178.37 | 212.93 | 88.38 | 4.96 |
| ak20130297 | 21-08-2018 6:16 | 69.4968 | -144.1559 | 15.6 | 3.6 | 199.11 | 87.54 | 0.35 | 109.09 | 89.65 | 177.54 |
| ak20131399 | 21-08-2018 10:08 | 69.4635 | -144.1095 | 5.8 | 3.7 | 21.26 | 82.76 | 12.25 | 289.69 | 77.84 | 172.60 |
| ak20134170 | 21-08-2018 16:24 | 69.4855 | -144.5310 | 8.2 | 3.5 | 98.38 | 62.00 | -129.21 | 338.46 | 46.83 | -40.06 |
| ak20134753 | 21-08-2018 18:23 | 69.4657 | -144.3726 | 4.6 | 3.7 | 111.33 | 74.62 | 161.07 | 206.52 | 71.77 | 16.21 |

| | | | | | | | | | | | |
|---|---|---|---|---|---|---|---|---|---|---|---|
| ak20156330 | 23-08-2018 4:30 | 69.4957 | -144.3146 | 11.7 | 4.5 | 103.00 | 71.00 | 137.00 | 210.00 | 50.00 | 25.00 |
| ak20159998 | 23-08-2018 8:59 | 69.5181 | -144.4912 | 7.4 | 3.8 | 106.99 | 71.72 | 161.87 | 202.86 | 72.81 | 19.17 |
| ak20166550 | 23-08-2018 16:11 | 69.5234 | -144.1430 | 14.2 | 4.0 | 18.30 | 86.07 | -42.22 | 111.86 | 47.90 | -174.69 |
| ak20196039 | 25-08-2018 10:10 | 69.4991 | -144.2738 | 7.0 | 3.6 | 198.44 | 85.20 | -15.89 | 289.80 | 74.16 | -175.01 |
| ak20227700 | 26-08-2018 23:52 | 69.5948 | -145.2076 | 15.4 | 3.6 | 347.56 | 40.61 | -72.21 | 144.64 | 51.70 | -104.68 |
| ak20237017 | 28-08-2018 11:13 | 69.5602 | -144.8964 | 18.2 | 4.1 | 110.76 | 79.71 | 171.15 | 202.36 | 81.30 | 10.42 |
| ak20238453 | 30-08-2018 22:49 | 69.5052 | -144.2439 | 15.0 | 4.0 | 296.21 | 79.88 | -153.34 | 201.17 | 63.78 | -11.29 |
| ak20238992 | 01-09-2018 6:41 | 69.5759 | -144.9367 | 19.1 | 4.8 | 187.01 | 73.48 | -15.10 | 281.40 | 75.53 | -162.93 |
| ak20240211 | 03-09-2018 0:59 | 69.5964 | -144.1433 | 7.7 | 3.5 | 36.19 | 85.54 | 6.98 | 305.64 | 83.04 | 175.50 |
| ak20240352 | 03-09-2018 7:08 | 69.4574 | -144.4269 | 5.3 | 3.7 | 193.33 | 65.22 | -8.60 | 286.96 | 82.20 | -154.97 |
| ak20241469 | 04-09-2018 17:29 | 69.4217 | -144.1498 | 6.8 | 3.6 | 144.01 | 55.70 | -104.14 | 348.09 | 36.77 | -70.30 |
| ak20241922 | 05-09-2018 4:03 | 69.4720 | -144.3977 | 1.8 | 4.1 | 137.63 | 55.48 | -113.62 | 355.28 | 40.98 | -59.78 |

| | | | | | | | | | | | |
|---|---|---|---|---|---|---|---|---|---|---|---|
| ak20243704 | 06-09-2018 4:05 | 69.5937 | -145.4165 | 10.1 | 4.0 | 114.38 | 73.85 | -167.55 | 20.87 | 78.04 | -16.52 |
| ak20250603 | 10-09-2018 23:37 | 69.5864 | -144.5924 | 12.4 | 4.2 | 191.06 | 84.72 | 3.40 | 100.75 | 86.62 | 174.71 |
| ak20257361[a] | 18-09-2018 12:40 | 69.5136 | -144.1598 | 10.8 | 5.1 | 109.56 | 62.48 | 177.04 | 200.93 | 87.38 | 27.56 |
| ak20258796 | 19-09-2018 22:12 | 69.4831 | -144.2715 | 4.3 | 3.9 | 21.25 | 87.80 | 6.82 | 290.99 | 83.18 | 177.79 |
| ak20259185 | 20-09-2018 9:27 | 69.4976 | -144.4405 | 12.3 | 3.8 | 112.95 | 81.38 | 169.90 | 204.48 | 80.02 | 8.75 |
| ak20259931 | 21-09-2018 4:28 | 69.4556 | -143.9369 | 5.0 | 3.6 | 24.71 | 79.49 | 22.43 | 290.41 | 67.97 | 168.65 |
| ak20263318 | 25-09-2018 20:37 | 69.5027 | -144.4839 | 11.3 | 3.6 | 93.78 | 65.65 | 142.66 | 201.24 | 56.45 | 29.65 |
| ak20270862 | 04-10-2018 13:12 | 69.4139 | -144.1478 | 4.3 | 4.0 | 300.16 | 85.43 | -168.16 | 209.20 | 78.20 | -4.67 |
| ak20274320 | 09-10-2018 7:11 | 69.5496 | -144.8661 | 14.8 | 4.0 | 103.60 | 83.20 | 171.70 | 194.59 | 81.76 | 6.87 |
| ak20284819 | 16-10-2018 16:45 | 69.5833 | -145.0505 | 16.4 | 4.1 | 171.35 | 88.49 | -31.69 | 262.28 | 58.32 | -178.23 |
| ak20288092 | 20-10-2018 11:53 | 69.4741 | -144.1022 | 18.8 | 3.9 | 303.31 | 76.58 | -178.52 | 212.97 | 88.56 | -13.42 |
| ak20364106 | 16-11-2018 3:31 | 69.5355 | -144.3921 | 7.9 | 4.1 | 196.03 | 73.54 | -21.51 | 292.40 | 69.41 | -162.38 |

| | | | | | | | | | | | |
|---|---|---|---|---|---|---|---|---|---|---|---|
| ak20459899 | 07-12-2018 15:22 | 69.5942 | -144.9470 | 6.9 | 4.5 | 270.88 | 87.60 | -179.02 | 180.84 | 89.02 | -2.40 |
| ak20521818 | 18-12-2018 2:31 | 69.6662 | -144.7349 | 10.0 | 4.7 | 185.97 | 89.34 | -22.15 | 276.24 | 67.85 | -179.28 |
| ak20593585 | 30-12-2018 7:14 | 69.5805 | -144.9660 | 9.2 | 4.5 | 187.29 | 80.55 | 7.13 | 96.11 | 82.97 | 170.47 |
| ak019ezpqow | 09-01-2019 6:51 | 69.1382 | -144.6471 | 15.7 | 4.5 | 179.13 | 81.15 | -14.32 | 271.38 | 75.86 | -170.87 |
| ak019k4nmjh | 12-01-2019 17:14 | 69.1308 | -144.6465 | 12.9 | 4.2 | 183.89 | 77.33 | 2.58 | 93.32 | 87.48 | 167.32 |
| ak019n5rosi | 14-01-2019 0:41 | 69.6240 | -145.0273 | 5.6 | 4.9 | 95.92 | 78.70 | -167.98 | 3.53 | 78.21 | -11.54 |
| ak019ngj7hy | 14-01-2019 18:49 | 69.6099 | -145.0847 | 16.7 | 4.0 | 98.69 | 77.10 | -162.51 | 4.67 | 72.97 | -13.50 |
| ak019p2unz7 | 15-01-2019 16:44 | 69.4903 | -144.1918 | 8.4 | 4.2 | 286.35 | 55.91 | 179.75 | 16.49 | 89.79 | 34.09 |

Table 2.9: Phase-weighted relative back-projection of the $M_W$6.4 mainshock in the 2018 Kaktovik sequence.

| Latitude (°) | Longitude (°) | Source time (s) | Relative energy |
|---|---|---|---|
| 69.62 | -145.40 | -0.3112 | 0.0077 |
| 69.60 | -145.28 | 2.0396 | 0.0145 |
| 69.61 | -145.30 | 3.9377 | 0.0174 |
| 69.62 | -145.19 | 5.0741 | 0.0285 |
| 69.59 | -145.05 | 6.5259 | 0.0430 |
| 69.54 | -144.67 | 8.5452 | 0.0901 |
| 69.52 | -144.52 | 11.9484 | 0.0999 |
| 69.49 | -144.40 | 15.3631 | 0.0871 |
| 69.49 | -144.36 | 16.4352 | 0.0736 |
| 69.44 | -144.11 | 18.2161 | 0.0215 |

Table 2.10: Phase-weighted relative back-projection of the $M_W$6.0 aftershock in the 2018 Kaktovik sequence.

| Latitude (°) | Longitude (°) | Source time (s) | Relative energy |
|---|---|---|---|
| 69.58 | -144.59 | 0.4300 | 0.0943 |
| 69.55 | -144.42 | 3.9305 | 0.1358 |
| 69.54 | -144.34 | 7.1389 | 0.1266 |
| 69.52 | -144.20 | 8.5198 | 0.0790 |
| 69.48 | -144.00 | 10.1390 | 0.0459 |

# Chapter 3

# Complex 3-D surface deformation in the 1971 San Fernando, California earthquake reveals static and dynamic controls on off-fault deformation

## 3.1 Article Information

This chapter was published in the American Geophysical Union's Journal of Geophysical Research. I undertook the data curation, formal analysis, created the figures, wrote and edited the text. Dr. Edwin Nissen supervised and provided manuscript edits. Dr. James Hollingsworth supervised, provided some scripts for the data analysis, and minor manuscript edits. Dr. Gareth Funning contributed minor manuscript edits.

### 3.1.1 Citation

Gaudreau, É., Hollingsworth, J., Nissen, E., and Funning, G. (2023). Complex 3-D surface deformation in the 1971 San Fernando, California earthquake reveals static and dynamic controls on off-fault deformation. Journal of Geophysical Research: Solid Earth, 128(3):e2022JB024985.

### 3.1.2 Author Names and Affiliations

É. Gaudreau[1], J. Hollingsworth[2], E. Nissen[1], G.J. Funning[3]

[1]University of Victoria, Victoria, Canada
[2]Université Grenoble Alpes, Université Savoie Mont Blanc, CNRS, IRD, Université Gustave Eiffel, Grenoble, France
[3]University of California Riverside, Riverside, USA

## 3.2 Abstract

The shallow 1971 $M_W$ 6.6 San Fernando, California earthquake involved a complex rupture process on an immature thrust fault with a non-planar geometry, and is notable for having a higher component of left-lateral surface slip than expected from seismic source models. We extract its 3-D coseismic surface displacement field from aerial stereo photographs and document the amount and width of the vertical and fault trace-parallel components of distributed deformation along strike. The results confirm the significant left-lateral surface offsets, suggesting a slip vector rotation at shallow depths. Comparing our offsets against field measurements of fault slip, we observe that most of the offset was accommodated in the damage zone, with off-fault deformation averaging 69% in both the fault trace-parallel and vertical components. However, the magnitude and width of off-fault deformation behave differently between the vertical and fault trace-parallel components, which, along with the rotation in rake near the surface, can be explained by dynamic rupture effects.

## 3.3 Plain Language Summary

The 1971 San Fernando, California earthquake is infamous for its strong ground motions and large lateral fault offsets measured in the field, despite the compressional tectonic stresses that triggered the earthquake. We produce maps of the 3-D surface deformation that occurred during the earthquake by comparing pre-earthquake and post-earthquake aerial photographs of this area. The results confirm the presence of important lateral and compression-driven deformation at the surface. This surface deformation was distributed over a wide zone, and as such, previously reported field measurements did not capture the total slip that occurred at the surface. Understanding controls on the width of the deformation zone provides insight into earthquake behavior and helps improve our estimates

of seismic hazard. Our results show that during the San Fernando earthquake, lateral and compression-driven deformation behaved differently within the fault zone, which may suggest that the two slip components were affected by different factors and damage generation mechanisms.

## 3.4 Introduction

As a fault zone accumulates damage during many earthquake cycles, its geometrical and material properties change, which may in turn play a significant role in earthquake rupture behavior (e.g., Bürgmann et al., 1994; Manighetti et al., 2007; Perrin et al., 2016; Thakur and Huang, 2021; Wesnousky, 1990). Although there is no single metric for the maturity of a fault due to the many factors that affect fault evolution (e.g., cumulative slip, varying fault healing rates), faults are generally considered immature if they have not hosted many earthquakes and as a result have not yet developed an efficient system for localizing deformation (Ben-Zion and Sammis, 2003; Dolan and Haravitch, 2014). A fault zone's elastic moduli weaken as it matures, resulting in a zone of low seismic velocities in which deformation becomes progressively more localized (e.g., Cochran et al., 2009; Dolan and Haravitch, 2014). As faults accrue more slip, fault traces become straighter, and separate fault segments coalesce (Manighetti et al., 2007; Manighetti et al., 2021; Wesnousky, 1988, 1990). Fault step-overs and other geometric complexities may limit earthquake rupture propagation, and thus earthquakes are perhaps more likely to rupture over a larger area on mature faults than on immature faults (Huang, 2018; Manighetti et al., 2007; Wesnousky, 1988, 1990). The segmentation and roughness of immature faults produce heterogeneities in stress and fault strength and may be an important factor in triggering supershear rupture velocities (Bruhat et al., 2016). However, smoother, more mature fault segments are otherwise more likely to sustain fast rupture velocities, while immature faults are typically associated with slower rupture velocities and a more irregular slip distribution (Bürgmann et al., 1994; Bruhat et al., 2016, 2020; Perrin et al., 2016; Pousse-Beltran et al., 2020). The progressive development of the damage zone and simplification of the fault geometry is associated with lower stress drops, more regular recurrence intervals, and influences hypocenter depths (Berryman et al., 2012; Harrington and Brodsky, 2009; Radiguet et al., 2009; Thakur et al., 2020; Thakur and Huang, 2021; Wesnousky, 1990; Zielke et al., 2017). The complexity of the fault geometry also seems to be an important factor controlling the delocalization of seismic slip (Antoine et al., 2021; Dolan and Haravitch, 2014; Milliner et al., 2015). Since immature faults are associated with deformation distributed tens of me-

ters to kilometers beyond the main slip surfaces, primary fault offsets observed in the field in the fault core fall short of the total coseismic offset, which may result in an underestimation of the fault slip rate and seismic hazard (e.g., Cheng and Barnhart, 2021; Milliner et al., 2015). Furthermore, geodetic modeling that simplifies the fault zone to a planar feature in a purely elastic medium often overlooks near-surface displacements and inelastic deformation (e.g., Cheng and Barnhart, 2021; Dolan and Haravitch, 2014; Milliner et al., 2021). Studying the behavior of immature faults is important for seismic hazard assessments as the hazard around these faults is often underestimated until a strong and potentially damaging earthquake occurs (e.g., Gaudreau et al., 2019; Jackson et al., 2006; Quigley et al., 2012).

In this study, we use the term "off-fault deformation" (OFD) to refer to the deformation that occurs in the wide (tens of meters to kilometers) zone of damaged rock around the high-strain fault core. This includes deformation accommodated by micro- and macrofracturing, warping, granular flow, and block rotation, and consists of both elastic and inelastic deformation (e.g., Cheng and Barnhart, 2021; Milliner et al., 2015; Scott et al., 2018). Distributed deformation in the shallow crust is thought to be one of the factors causing apparent shallow slip deficits, the systematic reduction in shallow crustal slip compared to greater slip at depth based on geodetic elastic dislocation models (e.g., Fialko et al., 2005; Kaneko and Fialko, 2011; Xu et al., 2016a). Different mechanisms contribute toward OFD generation during an earthquake, such as the formation of a cloud of microcracks around the rupture tip as it propagates (Lockner et al., 1991; Lyakhovsky et al., 1997; Martel et al., 1988), seismic waves propagating ahead of the rupture front (Jara et al., 2021; Ma, 2008; Thomas and Bhat, 2018) and the zone of high strain rate around the dynamically-propagating rupture front (Andrews, 1976; Poliakov et al., 2002; Rice et al., 2005). Moreover, stress heterogeneities caused by continued slip on a rough fault surface after the passage of the rupture front generate additional off-fault damage (Chester and Chester, 2000; Dieterich and Smith, 2009).

We assess the role of structural complexity, fault maturity and near-surface geological material on the distribution of OFD. Straighter, structurally simpler and more mature fault segments, as well as stronger near-surface materials tend to promote more uniform slip and localized deformation, and thick, undeformed sediments and partially indurated sedimentary rocks are thought to delocalize deformation (Dolan and Haravitch, 2014; Milliner et al., 2015; Roten et al., 2017; Zinke et al., 2014). Other factors commonly affecting OFD distribution include damage inherited from previous earthquakes (e.g., Cochran et al., 2009; Fialko et al., 2002; Zinke et al., 2014). Most of the aforementioned studies focus on

strike-slip earthquakes, and OFD in thrust earthquakes is relatively poorly studied, in part because surface-rupturing thrust earthquakes are relatively uncommon. The oblique 1971 San Fernando, California earthquake is a well-known case study of a destructive rupture on a thrust fault that was poorly studied prior to the earthquake and featured strong ground motions (Wentworth et al., 1971). The San Fernando Fault is immature based on several factors including its relatively low slip rate of 2–3 mm/year, its relatively short 16 km fault length within the ∼140-km-long Sierra Madre Fault System, and its relatively high density of step-overs with widths >1% of the fault length (∼3 wide step-overs within 16 km; Burgette et al., 2020; Lindvall and Rubin, 2008; Manighetti et al., 2007; Manighetti et al., 2021; Wells and Coppersmith, 1994). Here, we extract the complex 3-D coseismic deformation field from high-resolution stereo aerial photographs, and assess the factors controlling the width and amount of distributed deformation in an earthquake with a significant thrust component. Offsets and OFD magnitude and width are measured by profiling the displacement field at regular intervals along strike. Their distribution along with changes in fault geometry and geology allow us to explore which factors may control the surface expression of near-fault coseismic deformation. Notably, spatial patterns of OFD magnitude and deformation zone widths are different in the fault trace-parallel and vertical components, which may reflect the complexity of the rupture and the combination of static and dynamic processes affecting the distribution of deformation.

## 3.5 Tectonic Setting and Fault Structure

The WNW-striking, north-dipping San Fernando Fault is located in the Transverse Ranges of California, USA, in the transpressional region south of the San Andreas Fault's "big bend" (Figure 3.1). The Transverse Ranges are characterized by substantial late Cenozoic north-south shortening and numerous east-west strike-slip and thrust faults (Wentworth et al., 1971). The surface ruptures from the 1971 earthquake are situated in the San Fernando Valley of the Greater Los Angeles area, which is bounded to the north by the Santa Susana and San Gabriel Mountains, and to the south by the Santa Monica Mountains. The compressional axis of the regional stress field is oriented N-S to NNE-SSW (e.g., Stein et al., 1994). The San Gabriel Mountains are the result of 5–10 million years of thrusting on structures such as the Sierra Madre and Santa Susana Faults (Figure 3.1). Despite the presence of many young faults in the San Gabriel Mountains, the San Fernando area was characterized by scarce seismicity prior to the 1971 earthquake (Wentworth et al., 1971), with fewer than 10 earthquakes larger than magnitude

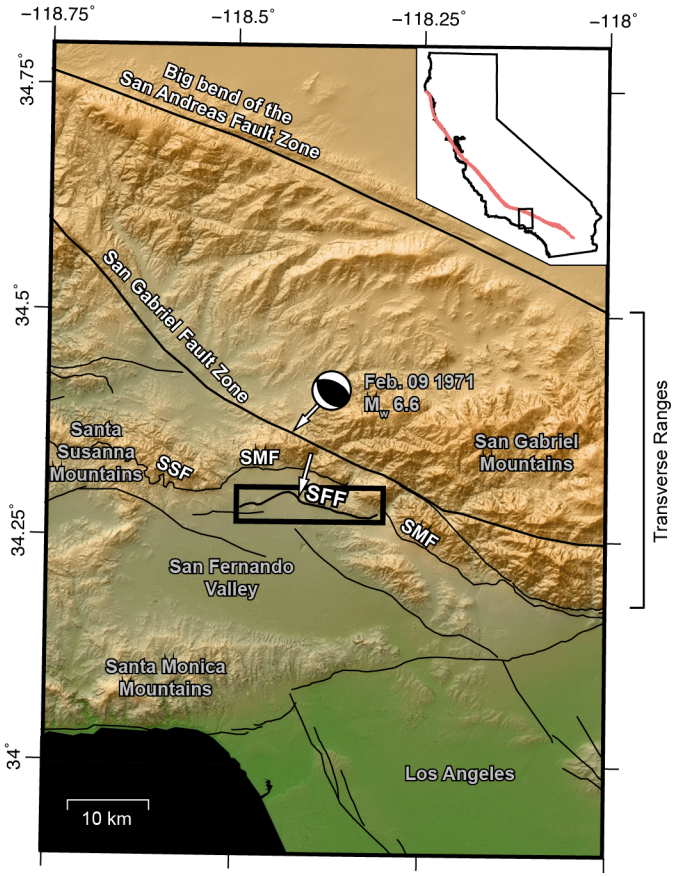


Figure 3.1: Active fault map around the San Fernando area. Thin black lines are surface fault traces from the U.S. Geological Survey Quaternary Fault and Fold Database (`https://doi.org/10.5066/F7S75FJM`) and Whitcomb et al. (1973) determined the focal mechanism from P-wave first motions. White arrows show slip vector azimuths for the deeper and shallower portions of the rupture based on local and teleseismic waveform modeling (Heaton, Thomas H, 1982). Rectangle shows location of Figure 3.2a. SSF: Santa Susana Fault; SMF: Sierra Madre Fault; SFF: San Fernando Fault. Inset shows the location of the main figure (black rectangle) and San Andreas Fault (red line) within the state of California.

4.0 recorded in and around the San Fernando Valley (USGS COMCAT catalog; https://earthquake.usgs.gov/earthquakes/search/). Before 1971, the most notable event in the region is the historical Pico Canyon earthquake of 1893, for which there were reports of strong shaking and multiple landslides (Townley and Allen, 1939). As a result, the San Fernando Fault and many others in the San Gabriel Mountains were either unknown or not widely considered to be active at the time (Weber, 1975; Wentworth et al., 1971, and references therein).

The 1971 surface rupture consists of two north-dipping main segments offset by a 1.3 km right step: the west-striking Sylmar segment cross-cutting the San Fernando Valley, and to the east, the WNW-striking Tujunga segment, a valley-bounding fault south of the San Gabriel Mountains (Figure 3.2a; Wentworth et al., 1971). Secondary surface ruptures identified after the earthquake include the Sylmar Basin secondary fault in the footwall which is sub-parallel to the main strand's Sylmar segment, and the Kagel Canyon secondary fault that cuts across the San Gabriel Mountains at a 30° angle from the main Tujunga segment. Farther east is the Little Tujunga Canyon secondary fault, sub-parallel to the main fault (Figure 3.2a). These fault segments are thought to represent an increase in fault complexity near the surface (e.g., Carena and Suppe, 2002; Savage et al., 1975). At depth, the San Fernando Fault cuts through dense, crystalline basement (Langenheim et al., 2011; Tsutsumi and Yeats, 1999; Wentworth et al., 1971). Near the surface, the Sylmar segment cuts through ∼4–5 km of sedimentary rocks, including moderately indurated Late Miocene and Early Pliocene sandy siltstone, sandstone and shale overlain by undeformed and partially indurated Pleistocene conglomerate, and alluvium (Langenheim et al., 2011; Wentworth et al., 1971). The Tujunga segment cuts through crystalline basement and ∼1–1.5 km of the Late Miocene siltstone and sandstone formation (Langenheim et al., 2011). Field and seismic reflection data have suggested that the fault follow bedding planes near the surface, with the Sylmar segment dipping 55°–60° and the Tujunga segment ∼25° (Barrows, 1975; Kamb et al., 1971; Sharp, 1975; Tsutsumi and Yeats, 1999; Weber, 1975). The Sylmar segment coincides with a >8 m-high pre-existing fault scarp, but paleoseismic offset could not be determined (Heath and Leighton, 1973; Weber, 1975). In the Tujunga segment, paleoseismic trenches uncovered slip surfaces indicative of prior faulting including >3.5 m of reverse slip in one location, and in another, >13 m of Late Miocene sedimentary rocks overlying undated alluvium and highly deformed hanging wall rocks near the slip surface (Barrows, 1975; Heath and Leighton, 1973). Further, a trench that was excavated across the Lopez Canyon secondary fault (see Figure 3.2a) showed evidence of ∼1 m of slip prior to the San Fernando earthquake, which occurred between 100 and 300 years ago

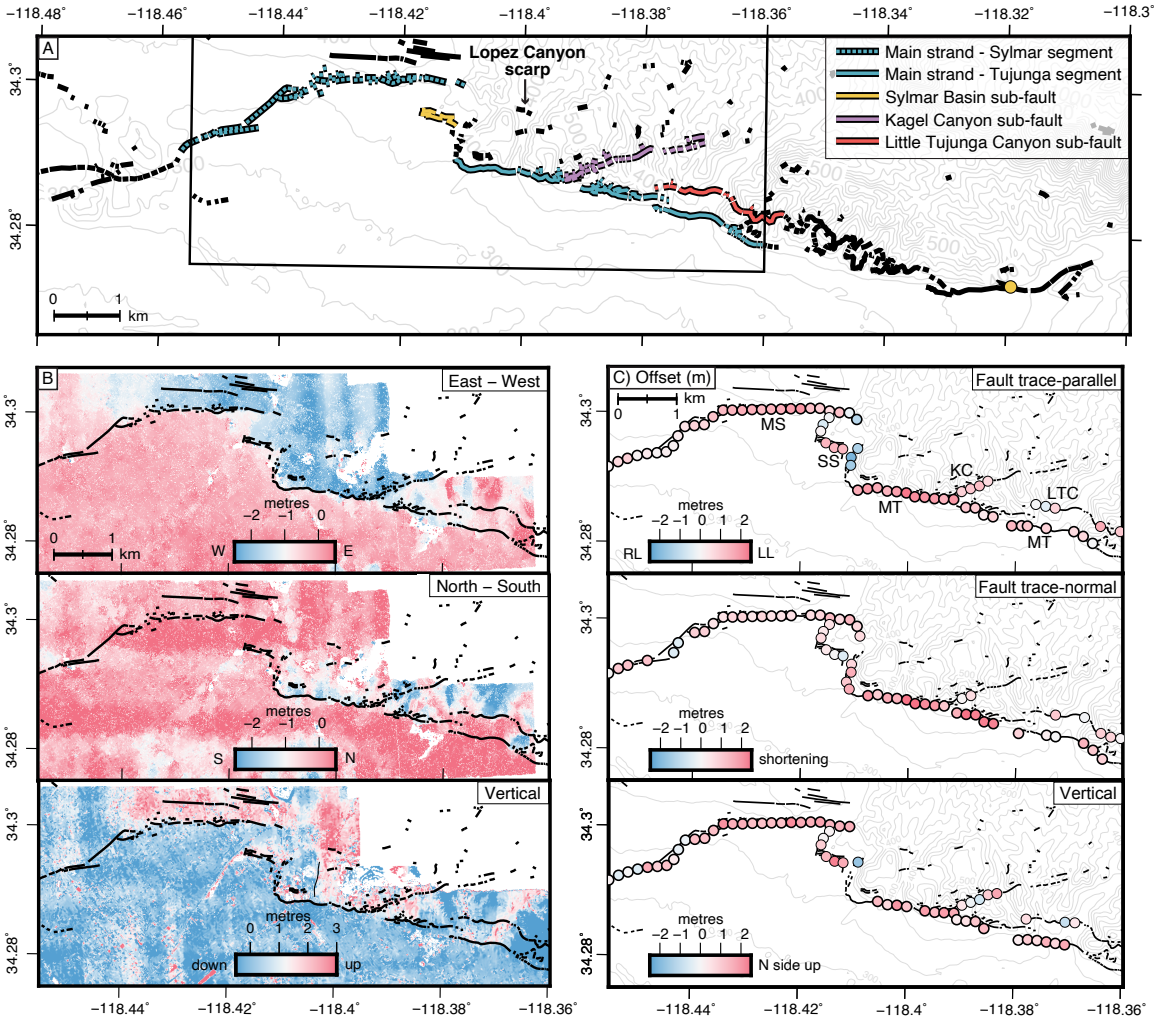


Figure 3.2: (a) Surface rupture of the 1971 San Fernando earthquake (USGS Quaternary fault and fold database of the United States; `https://www.usgs.gov/programs/earthquake-hazards/faults`; Bonilla et al., 1971; Kahle, 1975; Proctor et al., 1972; Wentworth et al., 1971). Rectangle corresponds to the area analyzed using aerial photographs. Gray contour lines show the topography in meters: the Sylmar segment in the west cuts through the San Fernando basin, while the Tujunga segment intersects the surface at the foothills of the San Gabriel Mountains. Yellow circle: location in Kahle (1975) where curved slickenlines recorded initial left-lateral slip then thrust-oriented slip. Curved slickenlines were also found by Bonilla et al. (1971) at the Lopez Canyon scarp although no interpretation was reported. (b) Coseismic displacement field of the 1971 San Fernando earthquake from optical image correlation and DEM differencing. Thin north-south-oriented line in the vertical panel traces the zone of vertical offset mapped by Barrows (1975, see Section 3.7.1). (c) Offset measurements from fault trace-perpendicular displacement profiles. Circles with thick outlines correspond to measurements on main fault strands used for averages in Sections 3.7 and 3.8.

and is thought to have involved rupture of the entire San Fernando fault system (Bonilla, 1973). While there is a scarcity of information on the slip history of the San Fernando Fault, the greater density of macroscopic undulations in the Sylmar segment compared to the Tujunga segment may imply that the Tujunga segment is more mature (Figure 3.2a; Manighetti et al., 2021).

The 1971 San Fernando earthquake ruptured one of multiple splays off a north-dipping decollement that continues further south (Fuis et al., 2003). The focal mechanism in Figure 3.1 was determined by Whitcomb et al. (1973) using P-wave first motions, and thus only represents the initial slip. It is generally agreed upon that the down-dip structure must be more complex than a single fault plane (e.g., Whitcomb et al., 1973), as the surface projections of such models are not consistent with the location of the observed surface rupture trace. Furthermore, teleseismic waveform modeling studies have demonstrated the complexity of the rupture with moment tensor solutions that have high compensated linear vector dipole components for a single point source (Barker and Langston, 1982; Kim, 1989). Multiple studies propose an evolving seismic source where the deeper slip has an oblique rake of 76°–84° and the slip shallower than ∼5–8 km has a rake of 89° or 90° (Figure 3.1 Heaton and Helmberger, 1979; Heaton, Thomas H, 1982; Kim, 1989; Langston, 1978). These models include either (A) a fault where the dip changes with depth (e.g., Carena and Suppe, 2002; Heaton and Helmberger, 1979; Langston, 1978), or (B) two subparallel faults, one surface rupturing and the other a deeper and buried rupture (Heaton, Thomas H, 1982; Kim, 1989). Aftershock relocations form a plane that dips ∼40° (Mori et al., 1995) and nodal planes from moment tensor solutions of the deeper segments dip between 29° and 54° (Heaton, Thomas H, 1982; Kim, 1989; Langston, 1978).

Contrary to the seismic data indicating that the bulk of the slip style was thrust, field data and horizontal control geodetic surveys collected in the 1960s and 1970s indicate left-lateral coseismic surface offsets that are roughly equivalent in amplitude to the vertical offsets, reaching ∼1.9 m on the Sylmar segment (e.g., Barrows et al., 1973; Bonilla et al., 1971; Kamb et al., 1971; Meade and Miller, 1973; Savage et al., 1975). The surface rupture traces were discontinuous but well-defined, although fault surface exposures were rare and thus most slip measurements were made using offset surface features and visual projection of scarp heights (e.g., Bonilla et al., 1971; Kamb et al., 1971; Sharp, 1975). Field teams noted much more slip variability over short distances along the Tujunga segment than the Sylmar segment. Offset measurement challenges included landsliding, roadwork, lack of exposure because of vegetation and buildings, and streets and sidewalks accommodating deformation differently than the underlying geology (Barrows et al., 1973; Bonilla et al.,

1971; Kamb et al., 1971; Sharp, 1975). These difficulties further motivate the application of novel remote sensing techniques to better characterize the surface deformation.

## 3.6 Methods

### 3.6.1 Digital Elevation Model Generation and Image Orthorectification

We obtained high-resolution scans of historical stereo aerial photographs of the study area acquired in 1969 and 1972 from the United States Geological Survey's Center for Earth Resources Observation and Science (EROS; `http://earthexplorer.usgs.gov`). Image identifiers and acquisition dates are listed in Table 3.1 in Supporting Information section 3.12. The scope of the pre-earthquake aerial survey was to image the San Fernando Valley, therefore providing limited coverage of the hanging wall: other pre-earthquake datasets that had broader coverage suffered greatly in terms of striping artifacts and other sources of noise. We reduced errors created by scanning by first rotating and cropping the photographs such that the corner fiducials were located at the corners of the scan. We enhanced the image contrast using contrast-limited adaptive histogram equalization, and applied a Gaussian blur ($\sigma$ = 0.5) to reduce speckle. To orthorectify the photographs, we produced pre-earthquake and post-earthquake DEMs using the open-source photogrammetry software Ames Stereo Pipeline (ASP), which has extensive documentation and applications in digital Earth observation datasets, historical (scanned film) datasets as well as Lunar and Martian images (Beyer et al., 2018). Orthorectification accuracy depends on the accuracy of the area of interest's topography, the position and orientation of the camera, as well as the camera's intrinsic parameters including focal length, principal point and distortion coefficients. Since historical imagery usually has very limited metadata, the ASP workflow for processing historical imagery begins by computing estimates for each camera's extrinsic parameters. This is done using the THEIA Structure from Motion library (`http://www.theia-sfm.org/index.html`) invoked from ASP, given initial intrinsic parameter values which are fixed in this step (in this study, the U.S. Geological Survey [USGS] provided the initial estimates for focal lengths, and we assumed the optical center to be in the center of the cropped and rotated image). We then use ASP to perform a bundle adjustment with ground control points collected using SRTM as a reference DEM to estimate absolute camera positions (Ajorlou et al., 2021).

We further refine the intrinsic and extrinsic parameters of each camera by collect-

ing dense and uniformly distributed match points between overlapping images, and using these in subsequent bundle adjustments where intrinsic and extrinsic parameters for multiple cameras in the dataset are jointly optimized. The stereo reconstruction (i.e., DEM-creation) process is performed using images that are projected onto a reference DEM, and ASP's MGM Final stereo matching algorithm. Normally the reference DEM has a much coarser resolution than the aerial photographs, which supplies the stereo reconstruction with the long-wavelength topography of the area of interest; however, due to the highly varied topography of the study region, we use a 1-m lidar DEM (USGS 3D Elevation Program; `https://www.usgs.gov/core-science-systems/ngp/3dep`) since lower resolution reference DEMs lead to great inaccuracies in the stereo reconstruction. The use of a high-resolution reference DEM may add to the high-frequency noise of the DEMs generated. The resulting point clouds may be shifted in space from the reference DEM, and therefore are then aligned to the reference DEM using an iterative closest point algorithm (using the libpointmatcher library, invoked from ASP; `https://github.com/ethz-asl/libpointmatcher`). We obtained optimal results when we aligned the point clouds from each stereo pair independently to the reference DEM, and a subsequent bundle adjustment jointly optimized the camera parameters for all cameras. Bundle adjustments are most successful in jointly optimizing multiple cameras when there is large (e.g., 60%) overlap between adjacent photographs. However, a joint optimization may be performed over multiple flight lines by collecting interest points in the side lap. This optimization may suffer due to errors introduced by the large perpendicular baseline between flight lines resulting in greater stereoscopic differences, and by illumination differences due to the passage of time between flight lines. Moreover, the overlap area is small (e.g., $<$30%), and scanning artifacts introduce additional errors (the latter also affect bundle adjustments of 60% overlap stereo pairs). In this case, we find bundle adjustment is most successful when the joint optimization of the cameras is performed initially for each flight line separately, then a subsequent bundle adjustment is invoked to jointly refine the cameras in all flight lines, improving the co-registration accuracy between the flight lines. We orthorectified the photographs using the optimized camera parameters and the pre-earthquake and post-earthquake DEMs produced using the photographs themselves. The final ground resolution of the orthophotos and DEMs is 1 m.

### 3.6.2 Extraction of Horizontal and Vertical Displacement Field Components

Once the pre-earthquake and post-earthquake orthomosaics are created using ASP, we measured the lateral coseismic displacements using COSI-Corr (Ajorlou et al., 2021; Leprince et al., 2007; Milliner et al., 2015). We used a multiscale sliding correlation window of 256 by 256 pixels to 32 by 32 pixels for the correlation, with a step size of eight pixels, resulting in 8 m-resolution images that represent the eastward and northward components of displacement.

We measured the vertical coseismic displacement field using the pre-earthquake and post-earthquake DEMs created using ASP; however, simply differencing the DEMs does not isolate the vertical component of displacement when there is also a horizontal component (e.g., Barnhart et al., 2019; Delorme et al., 2020; Oskin et al., 2012). In this study, we measured the vertical component by (a) downsampling the pre-earthquake and post-earthquake DEMs to the same grid as the COSI-Corr displacement maps. Using a MATLAB code, we then calculated the vertical displacement for each pixel by (b) resampling and (c) warping the pre-earthquake DEM such that the pre-earthquake topography is shifted based on the amount of lateral coseismic displacement from our COSI-Corr displacement maps, then (d) subtracting this grid from the post-earthquake DEM.

We masked outliers and pixels where the optical image correlation signal-to-noise ratio is $< 0.97$ (Leprince et al., 2007). We used the detrending tool in COSI-Corr to remove a second-order polynomial trend which does not impact the near-field offset estimate, and corrected undulating artifacts by sampling the undulations away from the rupture and subtracting the average from the displacement field. We used the Non-Local Means tool in COSI-Corr to denoise the displacement field using a noise parameter of $\sim$0.7, a search area dimension of 21 $\times$ 21 pixels (168 $\times$ 168 m), and a patch size of 5 $\times$ 5 pixels (40 $\times$ 40 m). We estimate the precision of the resulting displacement field from the standard deviation in a stable area of the displacement maps as 0.16 m for the east-west component, 0.27 m for the north-south component, and 0.64 m for the vertical component.

### 3.6.3 Coseismic Offset and Distributed Deformation Measurements

To quantify offsets along the length of the main fault and secondary strands, we extract fault trace-parallel, normal and vertical displacement profiles oriented perpendicular to the simplified fault traces at regular intervals along strike. For each profile, we first rotated

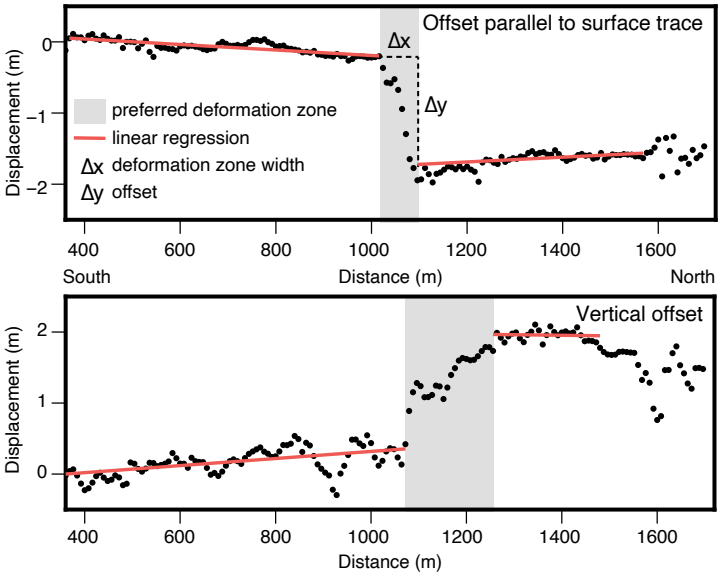


Figure 3.3: Example strike-perpendicular profile showing the fault trace-parallel and vertical components of the preferred deformation zone, linear regressions and offset (profile 16: see Figure 3.6 in Supporting Information section 3.12).

the E-W and N-S displacements into components parallel and normal to the local fault strike. We consider secondary fault ruptures mapped in the field in the San Fernando area as separate, discrete fault strands rather than distributed deformation around the main fault strand (e.g., USGS Quaternary Fault and Fold Database, `https://doi.org/10.5066/F7S75FJM`; Barrows, 1975). The profiles are 2 km-long, are regularly-spaced 21 pixels (168 m) apart and are the average of 21 pixel-wide swaths such that each measurement is independent from its neighbors. We discarded the profiles for which the displacement trends are obscured by decorrelation or noise. In some areas that are decorrelated near the surface rupture, we use 25 pixel-wide swaths.

The offsets were measured by fitting linear regressions to the trends in displacement on either side of the fault (Figure 3.3 and Figure 3.7 in Supporting Information section 3.12) and differencing the linear regression values at the near-fault extremities of the regression lines. Offset error was estimated by propagating the standard error of the regression on either side of the fault. The regression line boundaries were picked manually, since displacement maps produced from historical optical imagery often have more noise than those produced with modern imaging systems including long wavelength trends and topographic artifacts, particularly for the vertical component in areas of variable topography (Ajorlou et al., 2021). The displacement maps were also assessed for non-tectonic noise when choosing the trends used in the linear regressions. When it was unclear whether a

signal is tectonic or noise, adjacent profiles were checked to confirm whether the feature is continuous. In some cases, the linear regressions end where the displacements start to deviate from their far-field trends. However, some profiles exhibit clear near-field inelastic deformation, and to better capture the full displacement in these cases, the linear regression sampled this trend only where continuous across at least five adjacent pixels. Secondary surface ruptures mapped in the field are considered to be discrete faults, and their offsets are measured separately, even where manifest on the same profile (the target fault is located approximately in the middle of each profile).

Preferred deformation zone widths were defined as the distance between the two regression line end-points on either side of the fault. Though we treat these measurements as rough approximations, they do show that some deformation zones are wider than others by an order of magnitude (Figure 3.3 and Figure 3.7 in Supporting Information section 3.12). Preferred deformation zone widths were not determined in profiles with excessive decorrelation near the fault zone or where displacement trends on either side of the fault were too gradual to choose a preferred width.

We measured the magnitude of OFD at each profile by subtracting the maximum localized offsets measured in the field located within one profile swath from the total offset measured by profiling the displacement field either side of the fault zone. We normalized the OFD value to the total offset to obtain the percentage of off-fault deformation (%OFD). The OFD measurements presented in Figures 3.4b and 3.4c and Tables 3.2 and 3.3 in Supporting Information section 3.12 include elastic and inelastic OFD (e.g., Milliner et al., 2015; Scott et al., 2018; Zinke et al., 2019). We did not attempt to isolate the inelastic component of deformation because the noise level and resolution of the data preclude us from reliably quantifying strain within the fault zone (e.g., Barnhart et al., 2019; Milliner et al., 2015; Scott et al., 2018). We used localized near-fault measurements taken from detailed field surveys conducted in the days following the earthquake that measured shortening, fault trace-parallel and vertical offsets (Baize et al., 2020; Barrows et al., 1973; Bonilla et al., 1971; Kamb et al., 1971; Sharp, 1975). In areas of highly distributed deformation, the field offset measurements reported are the cumulative displacement over a 50 m-wide (Kamb et al., 1971) or 200 m-wide zone (Bonilla et al., 1971), whereas elsewhere discrete offsets were measured on well-defined fault scarps. For the purpose of measuring %OFD, we chose field offset measurements within a 50 m-wide zone centered upon the primary fault break (e.g., Scott et al., 2018). The component of lateral offset perpendicular to the profile swath orientation is taken when calculating fault-trace parallel OFD. When only one or two of the three slip components were recorded in the field within a swath, we assumed

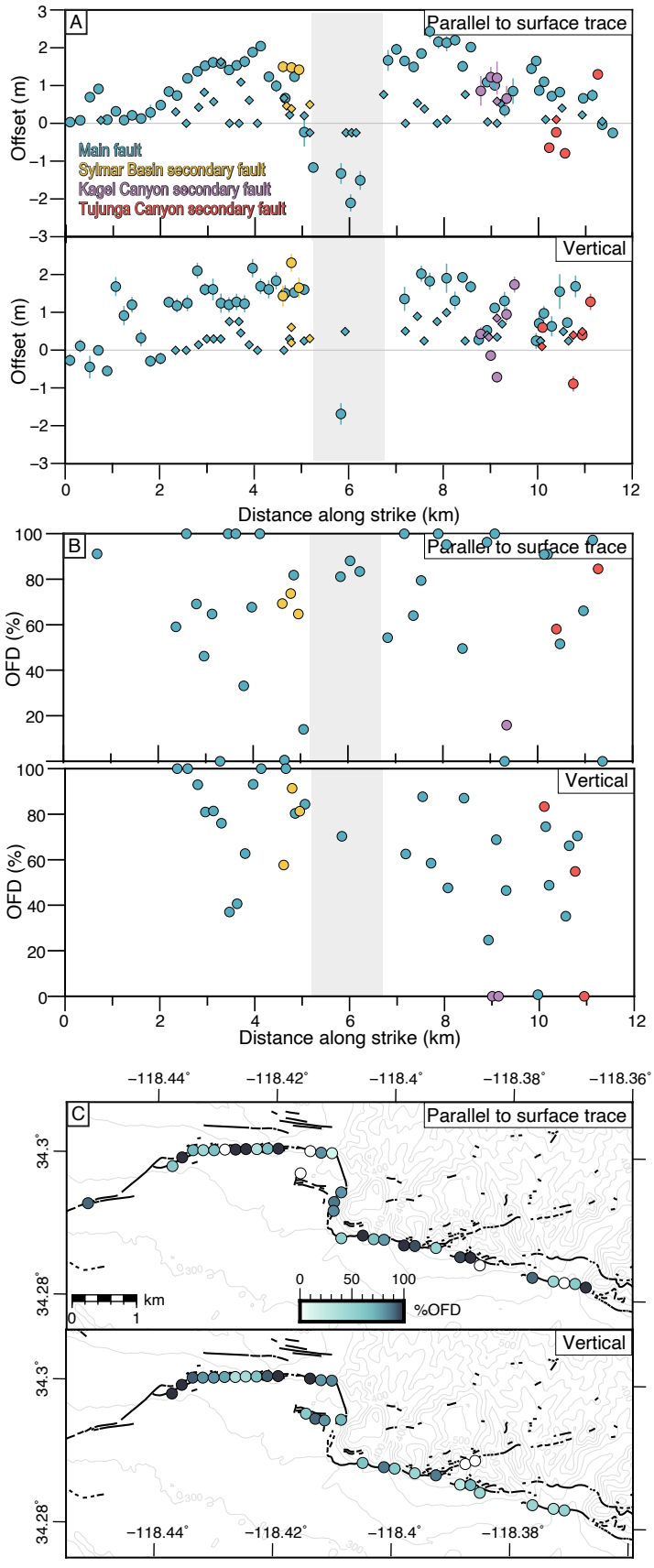


Figure 3.4: A) Offset measurements plotted as a function of distance along the fault trace: left-lateral slip and hanging wall uplift are positive. Circles are offsets measured from displacement fields in Figure 3.2a and diamonds are field measurements (see Supplementary Tables 3.2 and 3.3 in Supporting Information section 3.12 for references). Shaded area represents the tear fault separating the Sylmar and Tujunga sections of the main fault. B) %OFD estimates as a function of distance along strike, where there are field offset measurements located within profile swaths of image correlation and DEM differencing displacement fields. C) %OFD estimates plotted over fault trace.

that the remaining slip component(s) were imperceptible in the field within this swath and were given a value of 0.

## 3.7 Results

### 3.7.1 3-D Coseismic Displacements

While seismic source models described shallow slip as pure reverse (Heaton and Helmberger, 1979; Heaton, Thomas H, 1982; Langston, 1978), the 3-D coseismic displacement results (Figure 3.2b) reveal a large component of left-lateral offset, consistent with previously published field and trilateration data (Bonilla et al., 1971; Kamb et al., 1971; Meade and Miller, 1973; Savage et al., 1975), but the higher spatial resolution obtained from image correlation and DEM differencing is indispensable for assessing the spatial distribution of near-field deformation and estimating the amount of OFD (Section 3.7.3). Precise measurements of postseismic deformation from repeat leveling and trilateration surveys indicate that afterslip was negligible compared to total slip, and below the detection threshold of the method used in this study (Savage and Church, 1975; Savage et al., 1975; Sylvester and Pollard, 1975). Some of the limitations of processing of historical aerial photographs are noticeable in Figure 3.2b; striping artifacts (north-south-oriented stripes in the east-west and vertical displacement components, east-west-oriented stripes in the north-south displacement component) were significantly, although not completely reduced. The north-south component of the tectonic signal is particularly affected by long-wavelength noise since the striping artifacts are roughly parallel to the fault rupture trace and difficult to reduce. This has a very limited impact on the vertical component of displacement since the topography in much of the study area is muted, and in the area of varied topography (in the San Gabriel Mountains), using the lateral displacements to extract the vertical component still reduces topographic noise. In all three dimensions, noise is much greater in the hanging wall of the Tujunga segment, likely introduced by the varied topography of the San Gabriel Mountains and anthropogenic changes that occurred between aerial photograph and reference DEM data acquisitions affecting the DEM generation and orthorectification steps. This heavily affected the region between longitudes $-118.365$ and $-118.342$ in the vertical component, and thus offsets were not measured in this area (Figure 3.8 in Supporting Information section 3.12). The section of the San Fernando Fault shown in Figure 3.2b (the area used in this study) hosted the most slip and has a higher density of field measurements.

### 3.7.2 Near-Field Coseismic Offsets

All fault trace-perpendicular profiles with their deformation zone picks and linear regressions are included in Figure 3.7 in Supporting Information 3.12. While shortening is evident in the north-south displacement field, there are stripe artifacts near the fault (particularly in the footwall of the Tujunga segment). They introduce a gradual, long-wavelength signal to the fault-normal displacement profiles where long-wavelength OFD signals are expected and interferes with our ability to measure the total offset. Therefore, we focus on the fault-parallel and vertical components of displacement. Surface offsets on the Sylmar segment of the main fault rupture have roughly equal left-lateral and vertical components, reaching a maximum of 2.0 and 2.2 m, respectively, and 2.2 and 2.0 m in the Tujunga segment. The north-south tear fault connecting the two segments is dominated by right-lateral slip; however, a north-south zone of diffuse deformation $\sim$800 m to the east is accommodating most of the vertical component of deformation at the bend connecting the Sylmar and Tujunga segments (Figure 3.2b). Barrows (1975) mapped vertical deformation at this location but were unable to determine whether it occurred during the earthquake and most subsequent surface rupture maps do not include this detail (e.g., USGS Quaternary Fault and Fold Database, `https://doi.org/10.5066/F7S75FJM`). Determining that this deformation did occur during the 1971 earthquake demonstrates the effectiveness of historical image correlation in mapping complex coseismic surface deformation in greater detail. The largest left-lateral and vertical offsets in the Sylmar and Tujunga segments occur on the relatively straight parts of the fault where slip is not distributed onto secondary faults (Figures 3.2c and 3.4a). The Sylmar Basin secondary fault accommodates up to 1.5 and 2.3 m of left-lateral and vertical slip, respectively. The Kagel Canyon and Little Tujunga Canyon secondary fault offsets are irregular, with the former dominated by left-lateral slip while the latter is dominated by shortening.

The offsets increase gradually from the extremities of the study area toward the tear fault, plateauing for 1–2 km on either side of it, though in the Sylmar segment, the offset parallel to surface trace is distributed between the main fault and Sylmar Basin secondary fault (Figures 3.2c and 3.4a). The vertical offset at the Sylmar Basin secondary fault is a near-fault feature. The pattern of offsets along the fault trace is asymmetrical, with offsets tapering more gradually in the Tujunga segment, and according to field, leveling and trilateration surveys, continues to taper for $\sim$6 km beyond the study area (Barrows et al., 1973; Bonilla et al., 1971; Meade and Miller, 1973; Savage et al., 1975).

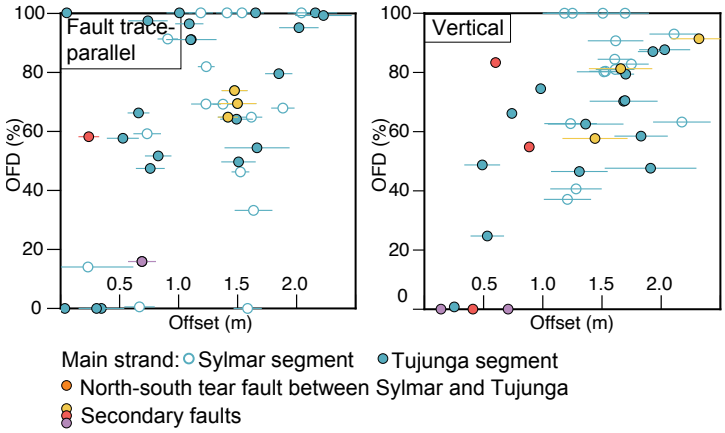


Figure 3.5: Comparison of %OFD and surface offset derived from fault-perpendicular profiles. Colours correspond to fault segments in Figure 1.

### 3.7.3 Off-Fault Deformation

The average %OFD ($\pm$ standard deviations) for the fault trace-parallel and vertical components are 69 $\pm$ 33%, and 69 $\pm$ 29%, respectively (Figure 3.4b). Since the Sylmar and Tujunga segments differ in terms of near-surface fault geometry, near-surface geological material, and surrounding topography, we assess the %OFD for the two segments separately. Fault trace-parallel %OFD is 65 $\pm$ 34% for the Sylmar segment and 70 $\pm$ 34% for the Tujunga segment. For the vertical component, average %OFD is larger for the Sylmar segment at 80 $\pm$ 20%, with 53 $\pm$ 29% OFD for the Tujunga segment. The irregularity of %OFD measured in the fault trace-parallel orientation may reflect the challenges in measuring offsets in the field in an urban environment. On the geometrically simpler, straighter parts of the surface rupture where slip is not distributed onto secondary faults, %OFD in the fault trace-parallel orientation is still generally higher in the Tujunga segment than the Sylmar segment. Many of the offsets shown in the fault-perpendicular profiles are nonlinear, and have a different shape and width in the three dimensions at the same location, suggesting that different off-fault structures are accommodating different proportions of deformation in the dip slip and strike-slip orientations (Figure 3.3; Figure 3.7 in Supporting Information section 3.12).

In the fault-parallel component, there is little correlation between %OFD and total (profile-derived) offset; however, there is a weak positive correlation between %OFD and offset in the vertical component (Figure 3.5).

### 3.7.4 Width of Deformation Zone

In this section we present the average width of the zone of distributed deformation for the main rupture trace (using the "preferred" width measurement), then the averages and standard deviations of the Sylmar and Tujunga segments of the main rupture trace separately. This additional step is taken because the width of diffuse deformation may be affected by attributes that differ between the two segments including near-surface fault geometry, near-surface geological material, surrounding topography. The average deformation zone width and standard deviations for the main rupture is 101 $\pm$ 70 m in the fault trace-parallel component, and 131 $\pm$ 79 m in the vertical component (Figure 3.9 in Supporting Information section 3.12). Although there is a lot of scatter, the average width of the deformation zone of the fault trace-parallel component is narrower in the Sylmar segment than the Tujunga segment (87 $\pm$ 54 m and 112 $\pm$ 82 m respectively). The Sylmar segment has a wider deformation zone on average in the vertical component (143 $\pm$ 76 m) compared to the Tujunga

segment (120 $\pm$ 84 m). While there is little correlation between %OFD and deformation width (Figure 3.10a in Supporting Information section 3.12), there is a weak positive correlation between deformation width and offset (Figure 3.10b in Supporting Information section 3.12).

The portion of offset accommodated by the hanging wall side of the field surface trace is generally distributed over a wider zone than the offset accommodated by the footwall side (Figure 3.7 in Supporting Information section 3.12). However, there are a few areas where footwall deformation is more broadly distributed than hanging wall deformation over multiple consecutive profiles, in either parallel or vertical component, and these are located in areas of structural complexity. This occurs in main fault profiles 22 and 23 where the Sylmar segment deviates from its relatively straight trace over $\sim$400 m, accommodated by multiple small structures at a high angle from the main fault (Figures 3.6 and 3.7 in Supporting Information section 3.12; Barrows, 1975). The footwall deformation is wider in main fault profiles 46 and 47 where the Kagel secondary fault meets the main fault (Figures 3.6 and 3.7 in Supporting Information section 3.12). The vertical displacements along nearby profile 44 also has a wider footwall deformation zone than most profiles, being approximately equal to the hanging wall deformation width. Profiles 57 to 61, located near a step-over, have approximately equal or wider hanging wall deformation widths (3.6 and 3.7 in Supporting Information section 3.12; Barrows, 1975).

## 3.8 Discussion

We focus here on the vertical and fault trace-parallel components of deformation, since the striping artifacts in some areas obscure the horizontal shortening component, with particular attention given to the main fault strand.

### 3.8.1 Near-Surface Slip Distribution and Rotation of Rake Away From Pre-Stress Direction

Our results are consistent with previous studies in that offset measurements are generally highest and vary more smoothly on simpler, straighter segments of the main fault, and lower and more heterogeneous where there are small wavelength variations in fault trace orientation and where slip is partitioned onto secondary faults (Figures 3.2c et 3.4a; e.g., Ajorlou et al., 2021; Bruhat et al., 2020; Klinger et al., 2006; Manighetti et al., 2007;

Milliner et al., 2015; Perrin et al., 2016). This suggests that structural complexity has a primary control on slip distribution.

Similar to field observations, fault trace-parallel and vertical surface offsets on the western half of the San Fernando rupture are roughly equal, however, those measured in this study are larger (Barrows et al., 1973; Bonilla et al., 1971; Kamb et al., 1971; Sharp, 1975). Trilateration data indicated similarly large coseismic offsets, and the higher-resolution coseismic displacement fields presented in this paper confirm that much of this offset occurred on structures within hundreds of meters from the mapped surface rupture trace (Burford et al., 1971; Meade and Miller, 1973; Morrison, 1973; Savage et al., 1975). The left-lateral offset component contrasts with seismic source models that indicate that slip at depth was dominated by thrust faulting (e.g., Heaton, Thomas H, 1982; Langston, 1978). Furthermore, regional stress field estimations are inconsistent with the left-lateral surface slip, with the average compression axis oriented 16° from north, approximately perpendicular to the San Fernando fault strike (Stein et al., 1994, and references therein). Dynamic rupture modeling of pure thrust earthquakes reveals a small, temporary component of strike-slip motion induced near the edges of the rupture at shallow depths associated with the passage of the rupture front; however, the dip-slip component still dominates (Hampel et al., 2013; Kearse and Kaneko, 2020). According to these models, the north-dipping San Fernando Fault would see a slight increase in left-lateral slip toward the western rupture termination and a slight increase in right-lateral slip toward the eastern rupture termination. The fault trace-parallel surface offset pattern of the San Fernando earthquake tells a different story, with left-lateral offset roughly equal to vertical offset in the western half, and on the eastern half, a left-lateral component that decreases toward the eastern termination (Figure 3.8 in Supporting Information section 3.12; Barrows et al., 1973; Kahle, 1975).

This asymmetry may be partly due to the oblique (thrust/left-lateral) rake suggested by focal mechanisms determined by P-wave first motions (e.g., Whitcomb et al., 1973); however, the left-lateral component of slip is large enough at the eastern end that there may be an additional factor amplifying the left-lateral motion (Figure 3.8 in Supporting Information section 3.12; Barrows et al., 1973). Additionally, Heaton and Helmberger (1979); Heaton, Thomas H (1982); Kim (1989); Langston (1978) showed that the rupture evolving from oblique slip at depth to pure thrust in the shallower portion of the crust, aligning with the regional stress field (Stein et al., 1994), was more compatible with local and teleseismic data, suggesting that the left-lateral component of slip measured at the surface is too shallow to be resolved using seismic data (Figure 3.1). Guatteri and Spudich (1998) showed that the local slip direction can change when dynamic stresses radiated from

elsewhere on the fault differ from the static prestress. This change is most likely when the prestress is heterogeneous, as expected for ruptures of geometrically-complex, immature faults like in the 1971 San Fernando earthquake Bouchon (1978). This can result in a temporal and spatial rotation in rake if the dynamic stresses are amplified enough near the free surface (Guatteri and Spudich, 1998; Oglesby, 2000).

In a surface-rupturing thrust earthquake such as this one, the dipping geometry of the fault amplifies the dynamic stresses in the hanging wall near the free surface and also enhances near-surface slip (Gabuchian et al., 2017; Oglesby, 2000). This amplification is consistent with the models proposed by Allen et al. (1998) and Brune (2001) for the San Fernando earthquake, which explain observations such as (a) the intense hanging wall ground shaking that launched a 50 m long piece of asphalt into the air during the earthquake (Boore, 1972; Maley and Cloud, 1971), (b) shattered earth on the hanging wall (Maley and Cloud, 1971; Nason, 1973), and 3) asymmetric static displacements measured by leveling surveys (Burford et al., 1971). The ground motion amplification in the hanging wall of a surface-rupturing thrust fault is due to geometric and dynamic effects, such as seismic waves propagating ahead of the rupture, reflecting off the free surface and back onto the fault (Oglesby, 2000; Oglesby and Day, 2001a). If the dynamic stresses near the surface did have a different direction than the static prestress, we would expect a temporal rotation in rake away from the static prestress direction due to the high ratio of dynamic to static stress magnitudes, until the dynamic stresses wane after the passage of the rupture front (Guatteri and Spudich, 1998; Kearse and Kaneko, 2020; Oglesby and Day, 2001b). The temporal rotation in rake is consistent with reports of curved slickenlines found on some 1971 fault plane exposures, including ones near the eastern end of the surface rupture that recorded initial left-lateral slip then a rotation toward the prestress (thrust) slip direction (Kahle, 1975). Nevertheless, we cannot exactly account for the large-left-lateral component. Comparisons between static and dynamic rupture models may help determine whether increased slip on the western side of the study area occurred due to amplified dynamic stresses (e.g., Oglesby and Day, 2001a).

### 3.8.2 Factors Affecting % Off-Fault Deformation

Relatively immature faults are often associated with proportionally more distributed deformation (Dolan and Haravitch, 2014; Milliner et al., 2015; Perrin et al., 2016; Zinke et al., 2015), which is consistent with the generally high %OFD of the San Fernando Fault. However, the distribution of %OFD is different between the vertical and fault trace-parallel

components (Figures 3.3; 3.4b,c). The fault trace-parallel %OFD of the main fault is similar between the Sylmar and Tujunga segments while there is more of a difference in vertical %OFD between the two segments. Along the Sylmar segment, fault trace-parallel %OFD is 65%, compared to 80% for the vertical component, and along the Tujunga segment, the fault trace-parallel component's %OFD is 70%, compared to 53% for the vertical component. The increased scatter in %OFD measurements compared to the offsets measured from the optical image correlation and DEM differencing displacement fields is due to scatter in the field measurements, reflecting the increasing irregularity of offsets near the fault (e.g., Gold et al., 2019, 2021; Milliner et al., 2015; Scott et al., 2018) and uncertainties related to field data collection. For instance, greater fault trace-parallel offsets may be measured where there are features cross-cutting the fault such as roads, sidewalks and fences. The surface trace of the Sylmar segment is centered in the neighborhood of Sylmar, but the surface trace of the Tujunga segment is located at the edge of the urban area. Lateral offsets were likely less perceptible and more prone to underestimation in areas where the surface trace is located in the foothills of the San Gabriel Mountains. In the following paragraphs we discuss other possibilities that may have further impacted the fault trace-parallel and vertical components of %OFD.

Near-surface geology may have a primary control over the vertical component of %OFD, with greater average %OFD in the Sylmar segment of the main fault where it cuts through a thick package of sediments including partially indurated Pliocene-Pleistocene formations, based on studies integrating of geologic, geophysical, and oil well data (Langenheim et al., 2011). Vertical %OFD is lower in the Tujunga segment, which cuts through an older, stronger and thinner package of sedimentary rock than the Sylmar segment (Langenheim et al., 2011; Levi and Yeats, 1993). Structural complexity may also be a factor in the distribution of %OFD in the vertical component particularly along the Sylmar segment, with higher %OFD on the main fault near the segment boundaries and near macroscopic bends (Figures 3.4b and 3.4c). The difference in hanging wall topography between the Sylmar and Tujunga segment may imply a difference in slip rate, which is sometimes used as a metric for fault maturity which in turn may impact the %OFD as well (Dolan and Haravitch, 2014). Unlike for the vertical component of %OFD, near-surface geology and macroscopic fault corrugations do not appear to be primary controls in the fault trace-parallel component, with the Tujunga segment %OFD slightly higher than that of the Sylmar segment and no clear correlation with fault trace complexity (Figures 3.4b and 3.4c). Moreover, %OFD does not seem to scale with offset magnitude in the fault-parallel component, while there is a positive correlation in the vertical component (Figure 3.5).

A zone of broadly distributed deformation mapped in the hanging wall of the Sylmar segment possibly due to fold-related secondary faults may have affected the vertical component of %OFD (e.g., Allmendinger, 1998; Barrows, 1975; Gold et al., 2019). The strong dynamic stresses may have influenced the distribution of deformation as well, and may explain some of the differences between the vertical and fault trace-parallel components. The short-lived dynamic effects include damage due to seismic waves propagating ahead of the rupture front (Ma, 2008; Thomas and Bhat, 2018) and sudden and short-lived increases in normal stress, shear stress, strain rate, slip rate and rupture velocity around the rupture front (Andrews, 1976; Poliakov et al., 2002; Rice et al., 2005). After the passage of the rupture front, generation of OFD continues at generally lower stresses and strains (Thomas and Bhat, 2018) as slip progresses on the fault, since geometric complexities will locally increase the stress field enough to initiate cracking in the damage zone (Chester and Chester, 2000; Dieterich and Smith, 2009). The previously mentioned temporal rake rotation may explain the different OFD behaviors in the fault trace-parallel and vertical components. If most of the left-lateral near-surface offset resulted from transient dynamic effects, most of the fault trace-parallel OFD would have been generated as a result of the high stress and strain rates associated with the passage of the rupture front. Compared to the Sylmar segment, the left-lateral %OFD in the Tujunga segment may have been enhanced by greater ground motion amplification due its much shallower dip and greater hanging wall topography (Boore, 1973; Oglesby, 2000). While some of the vertical component of OFD would have likely been generated during the very short dynamic stress stage, some of the OFD will have accumulated as the slip vector rotated toward the prestress (thrust) direction and continued slipping. These very different conditions under which %OFD develops result in different micro- and macrocrack orientations, spatial patterns and magnitudes of %OFD. As a result, much of the left-lateral and vertical components of OFD may have been accommodated on separate structures, as suggested by differing shapes and gradients of the fault trace-parallel and vertical displacement profiles (e.g., Figure 3.3; Figure 3.7 in Supporting Information section 3.12; Aben et al., 2020; Chester and Chester, 2000; Griffith et al., 2010; Templeton and Rice, 2008; Yamashita, 2000). Dynamic rupture models suggest that OFD generated by dynamic stresses is influenced by fault roughness (and by extension fault maturity) and by the strength of near-surface materials (Roten et al., 2017; Wollherr et al., 2019). However, comparison between the different components of slip is limited by the unreliable fault trace-perpendicular offsets in the optical image correlation displacement field.

The poor correlation between %OFD and deformation zone width suggests that these

measures have different controls resulting in OFD that can be distributed over different deformation zone widths (Figure 3.10a in Supporting Information section 3.12). For example, the density of off-fault microfractures near the fault core may influence the deformation zone width for a given %OFD. Localized, near-fault offsets are also more irregular than farther-field offsets, affecting the %OFD estimation and introducing some of the scatter into Figure 3.10a in Supporting Information section 3.12 (e.g., Gold et al., 2019, 2021; Milliner et al., 2015; Scott et al., 2018). This scatter may reflect the increase in complexity near the fault core and the challenges in measuring offsets in the field. The Sylmar segment deformation zone measured from the fault trace-parallel displacement field is generally wider than that of the Tujunga segment, suggesting that near-surface materials may have a primary control on deformation zone width in the fault trace-parallel orientation, while this does not seem to be the case for %OFD. The wider deformation zone in the vertical orientation may be due to greater noise level of the DEMs than the optical image correlations, wider deformation caused by progressive slip on a rough surface, more cumulative slip in the thrust than fault trace-parallel direction (Faulkner et al., 2011; Mitchell and Faulkner, 2009), or perhaps a reduction in the thrust component of slip near the surface (Gold et al., 2019).

## 3.9 Conclusions

While most studies on slip localization focus on strike-slip earthquakes, stereo photographs and advances in image processing enabled the production of displacement maps capturing the fault-trace parallel and vertical components of coseismic deformation from the 1971 San Fernando oblique thrust earthquake. The results have important implications for the characterization of the fault for seismic hazard assessments, with some offsets distributed over a wide zone ($>$200 m) and a greater component of left-lateral surface offset than expected from moment tensor inversions and finite fault modeling (e.g., Heaton, Thomas H, 1982; Kim, 1989; Langston, 1978). The rotation of the slip vector near the surface may have occurred as a transient dynamic effect based on the amplification of dynamic stresses associated with surface-rupturing thrust faults (Guatteri and Spudich, 1998; Oglesby, 2000), consistent both with the presence of curved slickenlines (Kahle, 1975; Kearse and Kaneko, 2020) and with previous models that attempted to explain the intense ground motions of the San Fernando earthquake (Allen et al., 1998; Boore, 1973). Furthermore, the displacement maps show that dip slip and strike slip were partitioned on different secondary structures, some of which are not present in most rupture maps of this area. This study suggests that

in oblique thrust/reverse faults, the fault-trace parallel and vertical components of OFD can be partitioned. For surface-rupturing dip-slip faults, it is worth considering near-surface dip and topography as factors that can amplify hanging wall ground motions and OFD. However, further work is needed to investigate the OFD patterns caused by processes such as the amplification of dynamic stresses and slip on a rough surface and whether they are more strongly influenced by different factors.

## 3.10 Acknowledgments

E. G. was funded through an Alexander Graham Bell Canada Graduate Scholarship and Michael Smith Foreign Study Supplement from the Natural Sciences and Engineering Research Council of Canada, and a Montalbano Scholars Fellowship and President's Research Scholarship, both from University of Victoria. E. N. was supported by a Canada Research Chair and grants from the Natural Sciences and Engineering Research Council of Canada (NSERC Discovery Grant 2017-04029), the Canada Foundation for Innovation, and the BC Knowledge Development Fund. J.H. was supported by grants from CNES and BQR. G.F. was supported by SCEC Award 21128. We are grateful for thorough reviews from Katherine Scharer and an anonymous reviewer, which greatly improved the manuscript. We also thank Editor in Chief Isabelle Manighetti and an associate editor for their valuable and constructive comments.

## 3.11 Data Availability

Scanned aerial photographs were obtained from the United States Geological Survey's Center for Earth Resources Observation and Science (EROS; `http://earthexplorer.usgs.gov`). Ames Stereo Pipeline (Beyer et al., 2018) and COSI-Corr (Leprince et al., 2007) were used for data processing. The digital elevation models and displacement maps produced are available at `https://doi.org/10.5281/zenodo.7327824`. The figures in this paper were generated using Generic Mapping Tools (Wessell et al., 2013). Offsets measured in the field used to calculate off-fault deformation are from Baize et al. (2020); Barrows et al. (1973); Bonilla et al. (1971); Kamb et al. (1971).

## 3.12 Supporting Information for "Complex 3-D surface deformation in the 1971 San Fernando, California earthquake reveals static and dynamic controls on off-fault deformation"

The supporting information provides more information on the full 3-D displacement field, strike-perpendicular profiles used to measure offsets, fault zone deformation and fault zone widths.

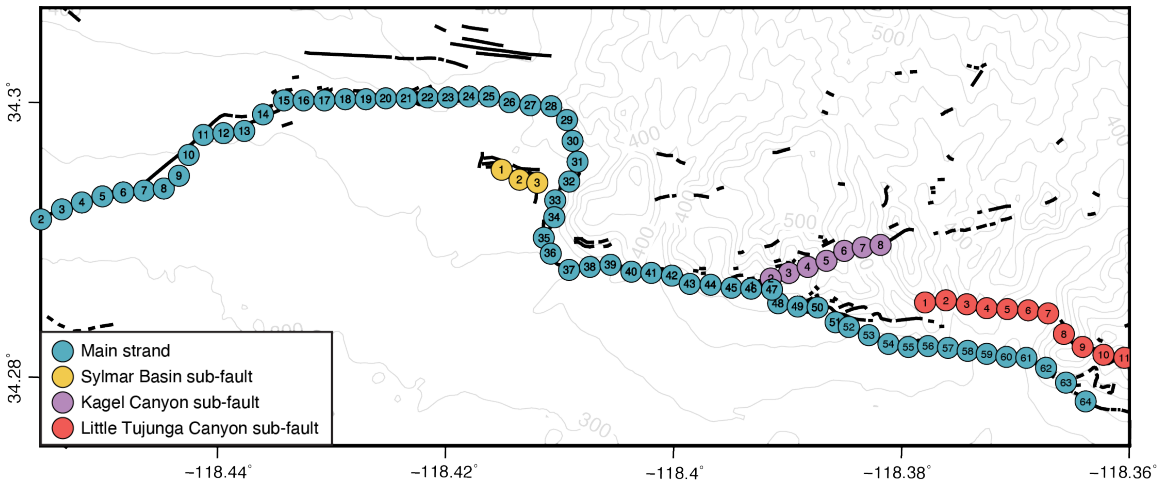


Figure 3.6: Map showing location of profiles in Figure 3.7.

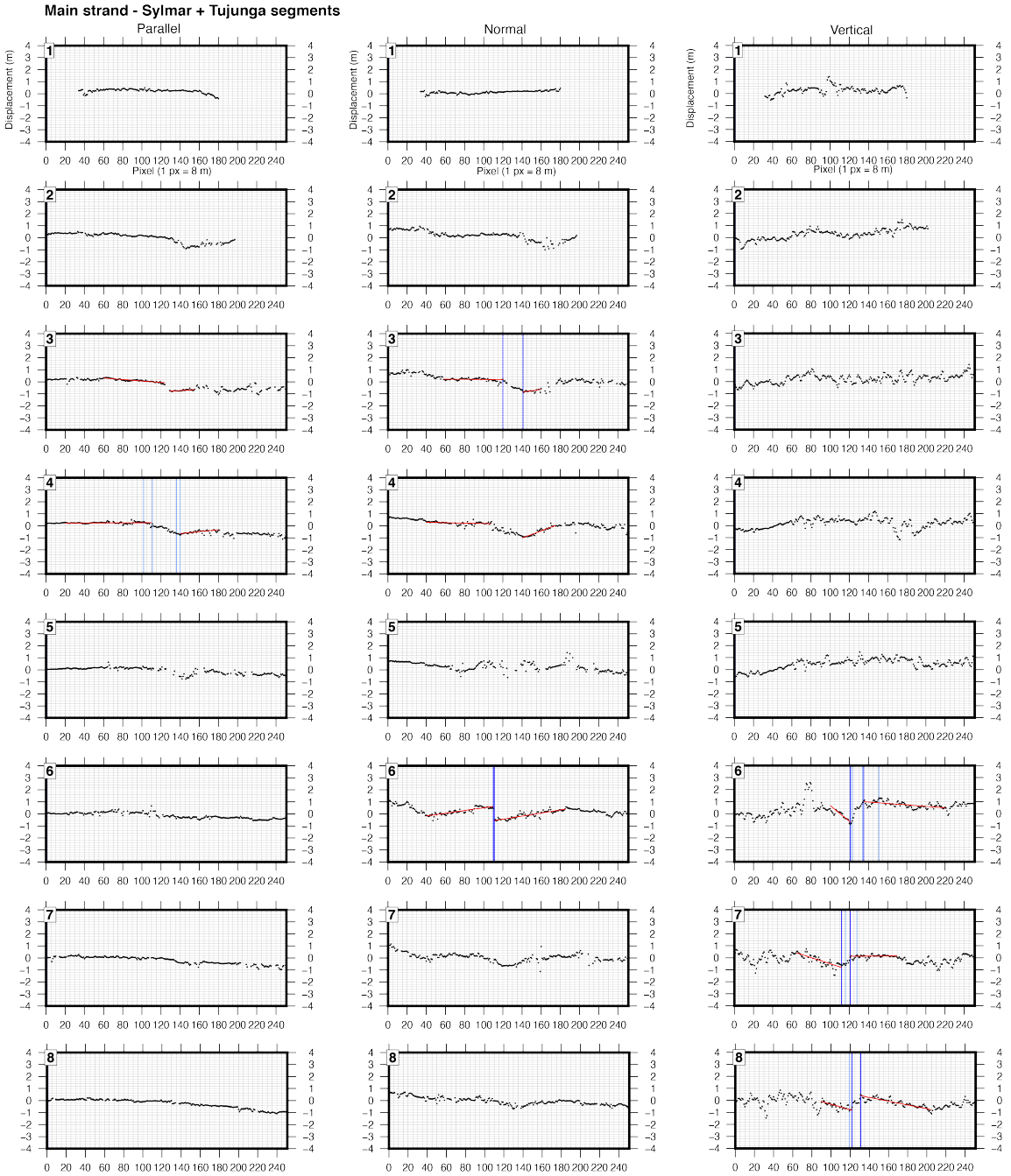


Figure 3.7: Rupture trace-perpendicular coseismic displacement profiles from an averaged swath of a 21 pixel width. All profiles are as labeled on the first row of each page; displacement (m) as a function of fault-perpendicular distance (px). Numbers correspond to locations in Figure 3.6. Red lines represent linear regression and dark blue lines are placed at the boundaries of the preferred deformation zone. Light blue lines represent minimum and maximum deformation zone where different than preferred location. The mapped fault trace is located in the centre of each profile at pixel 126. In a few locations the fault trace is displaced by a few pixels from the centre due to small-scale fault trace variations, in which case the location of the surface trace is identified by a red arrow above the profile.

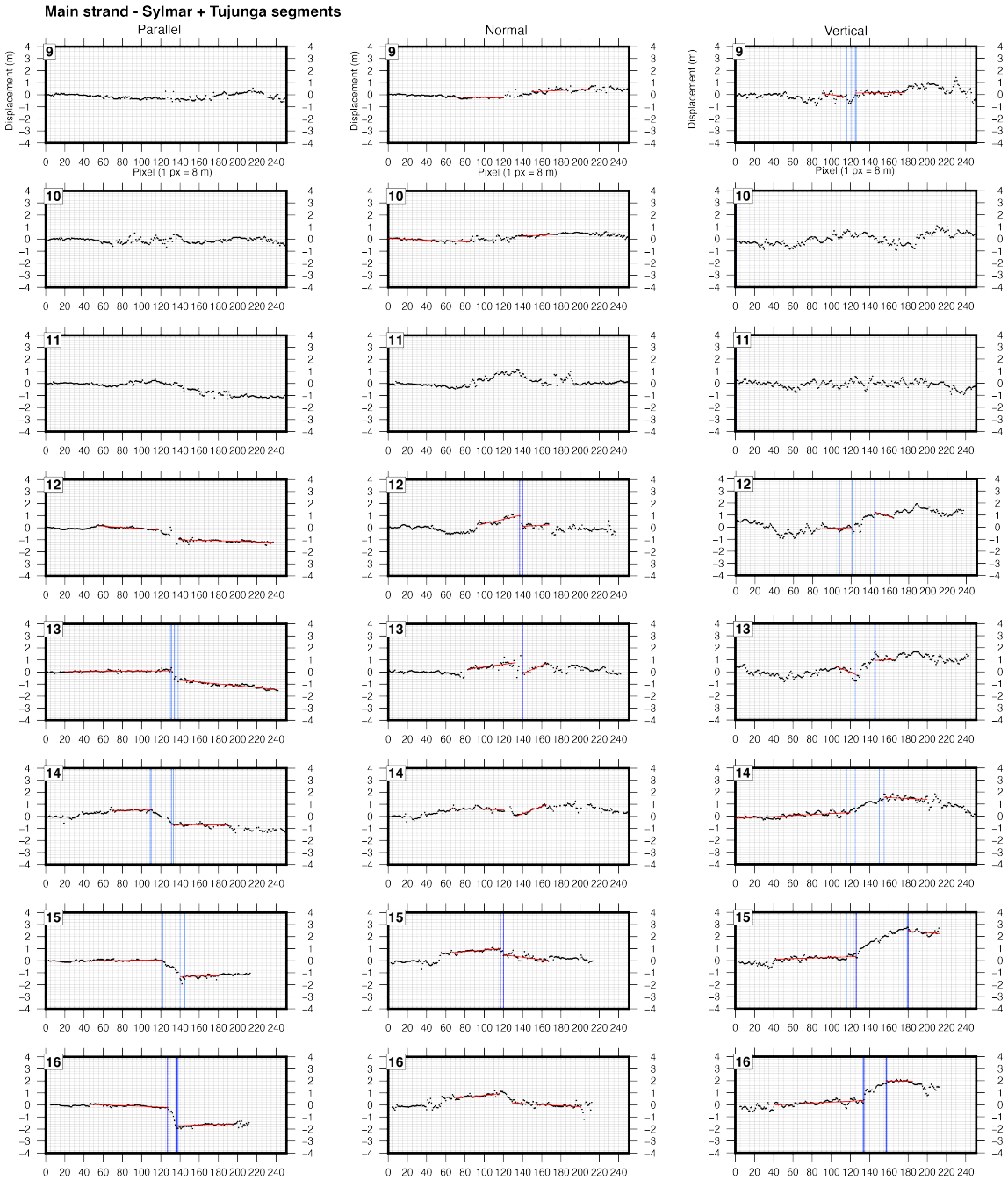
Main strand - Sylmar + Tujunga segments
Parallel
Normal
Vertical
Displacement (m)
Pixel (1 px = 8 m)
9
10
11
12
13
14
15
16

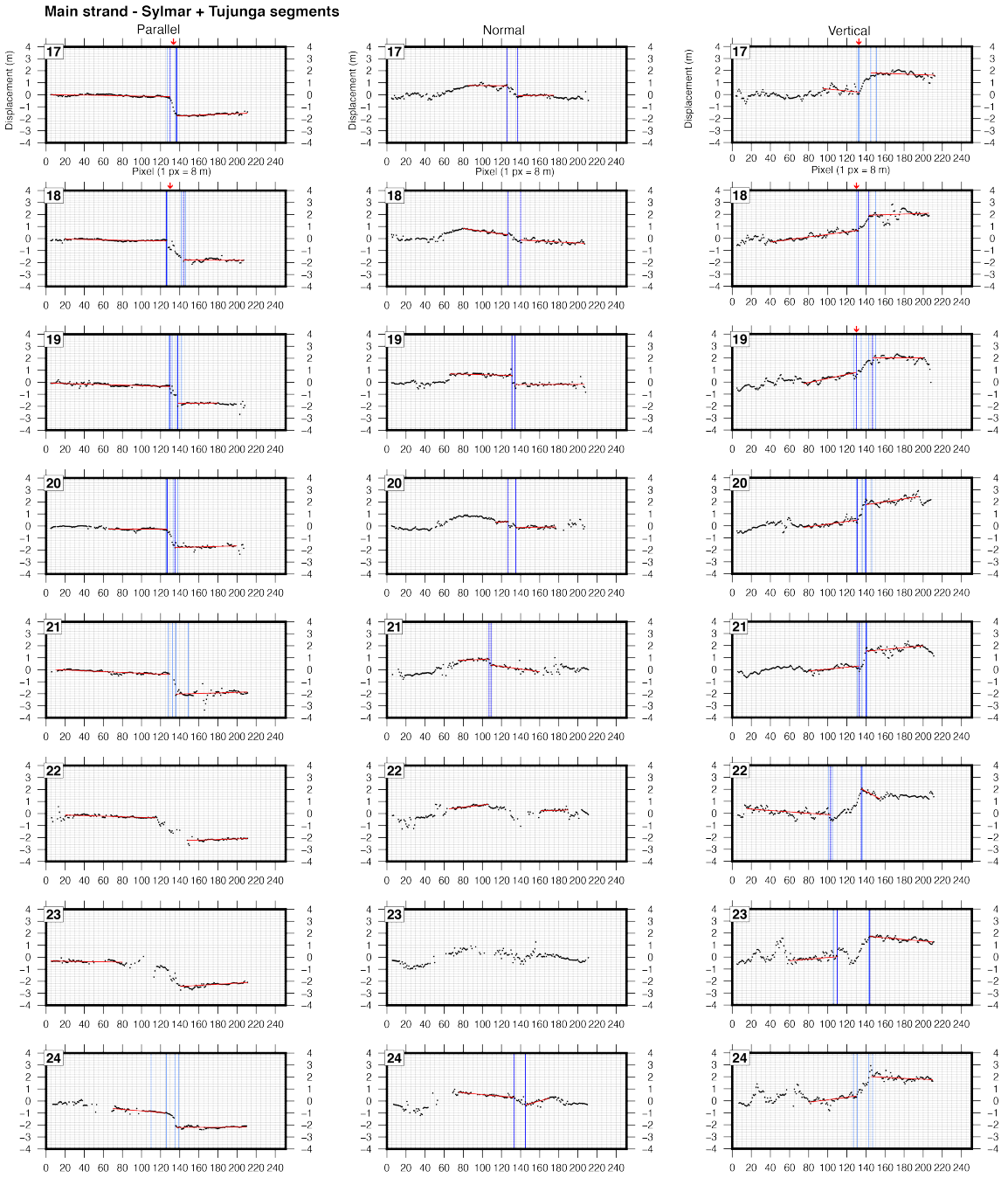
Main strand - Sylmar + Tujunga segments
Parallel
Normal
Vertical
Displacement (m)
Pixel (1 px = 8 m)
17
18
19
20
21
22
23
24

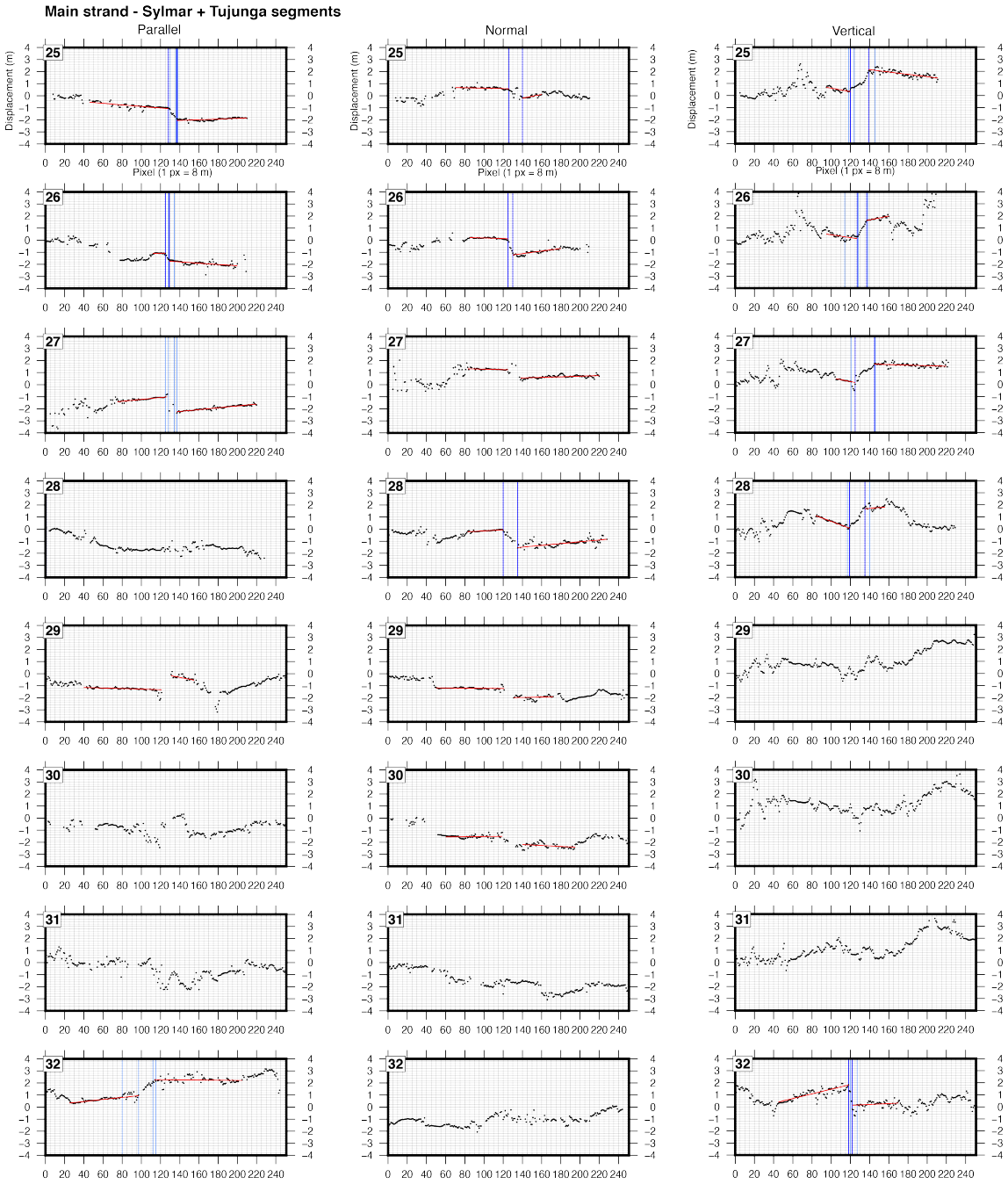
Main strand - Sylmar + Tujunga segments
Parallel
Normal
Vertical
Displacement (m)
Pixel (1 px = 8 m)
25
26
27
28
29
30
31
32

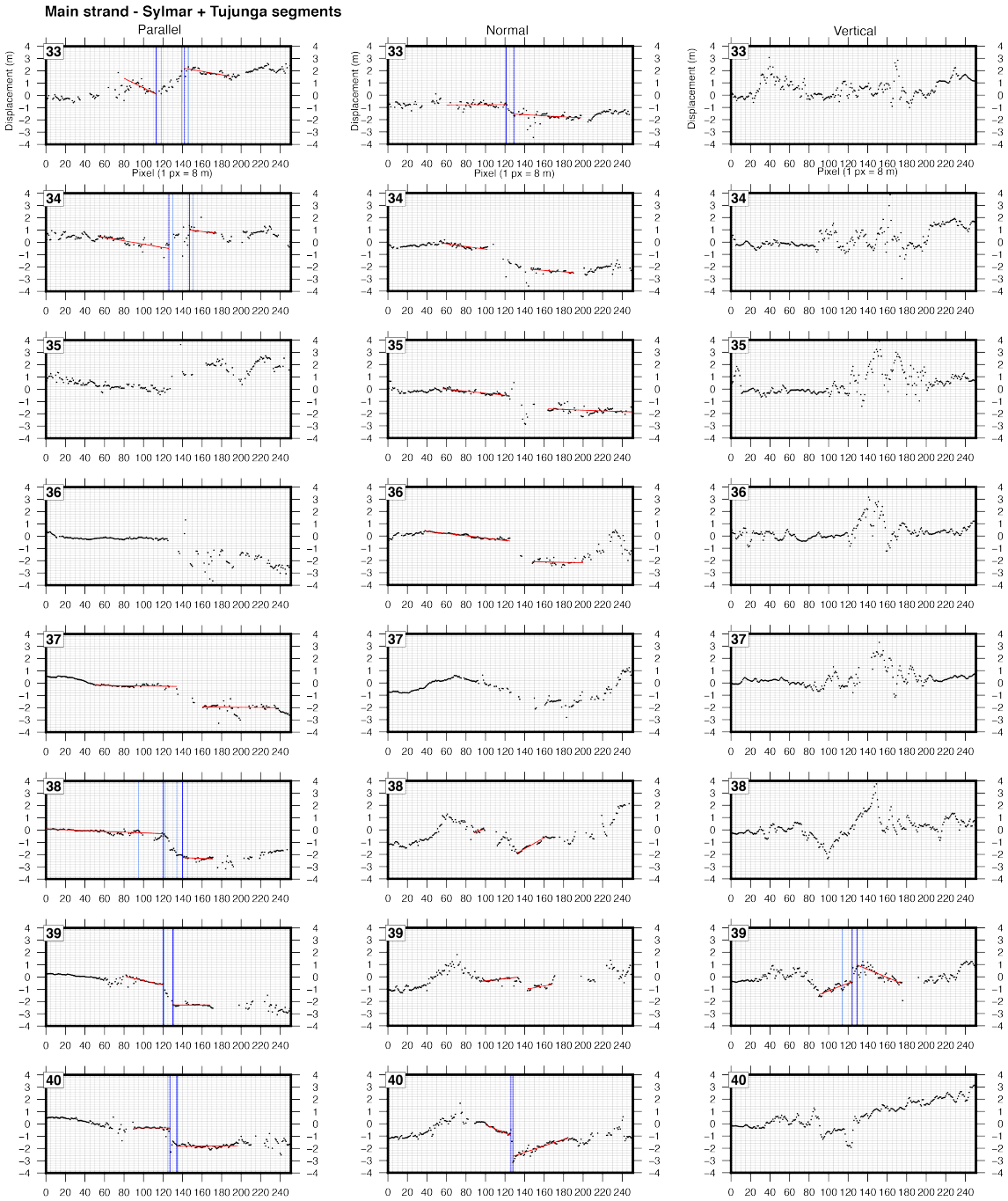
Main strand - Sylmar + Tujunga segments
Parallel
Normal
Vertical
Displacement (m)
Pixel (1 px = 8 m)
33
34
35
36
37
38
39
40

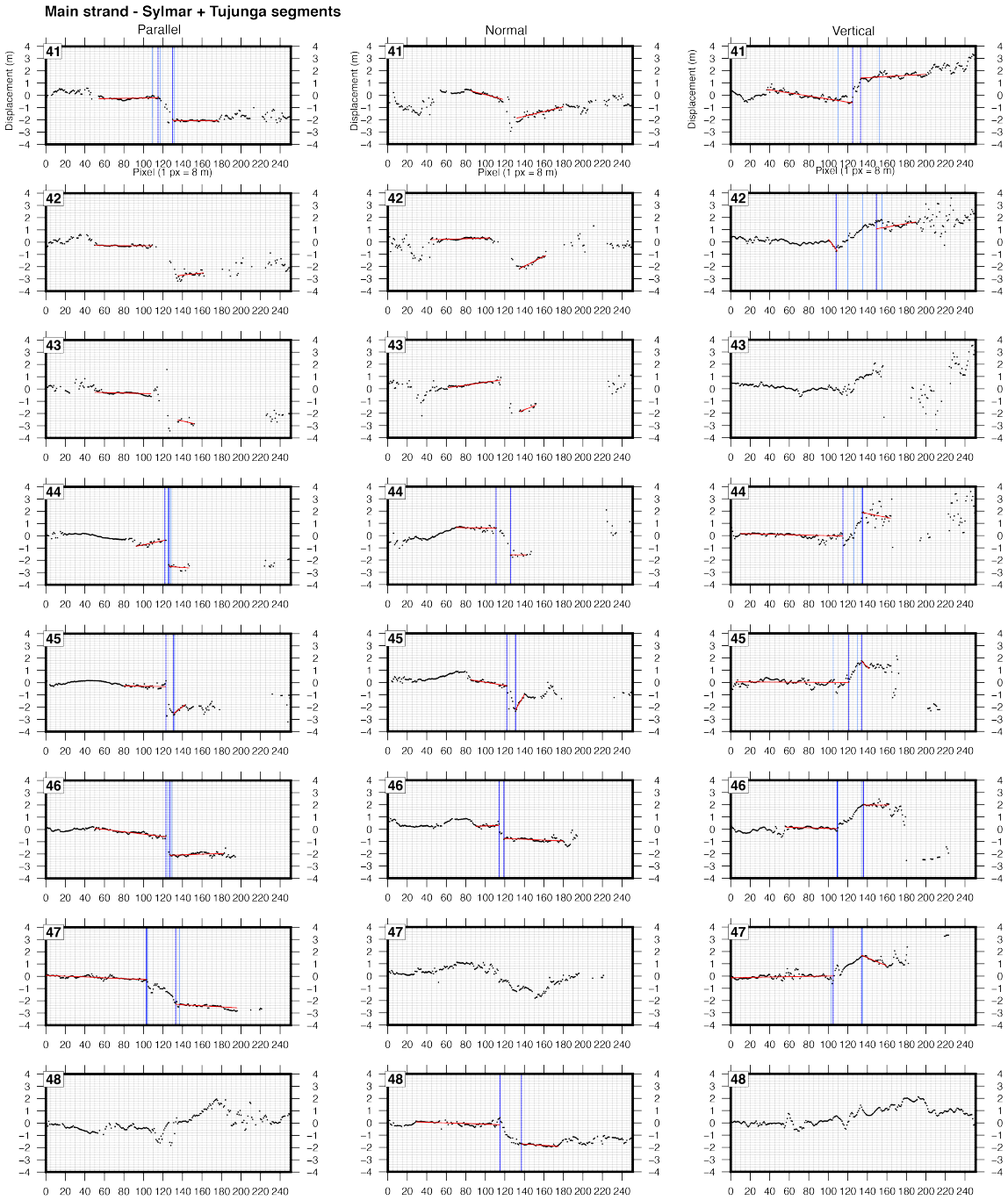
Main strand - Sylmar + Tujunga segments
Parallel
Normal
Vertical
Displacement (m)
Pixel (1 px = 8 m)
41
42
43
44
45
46
47
48

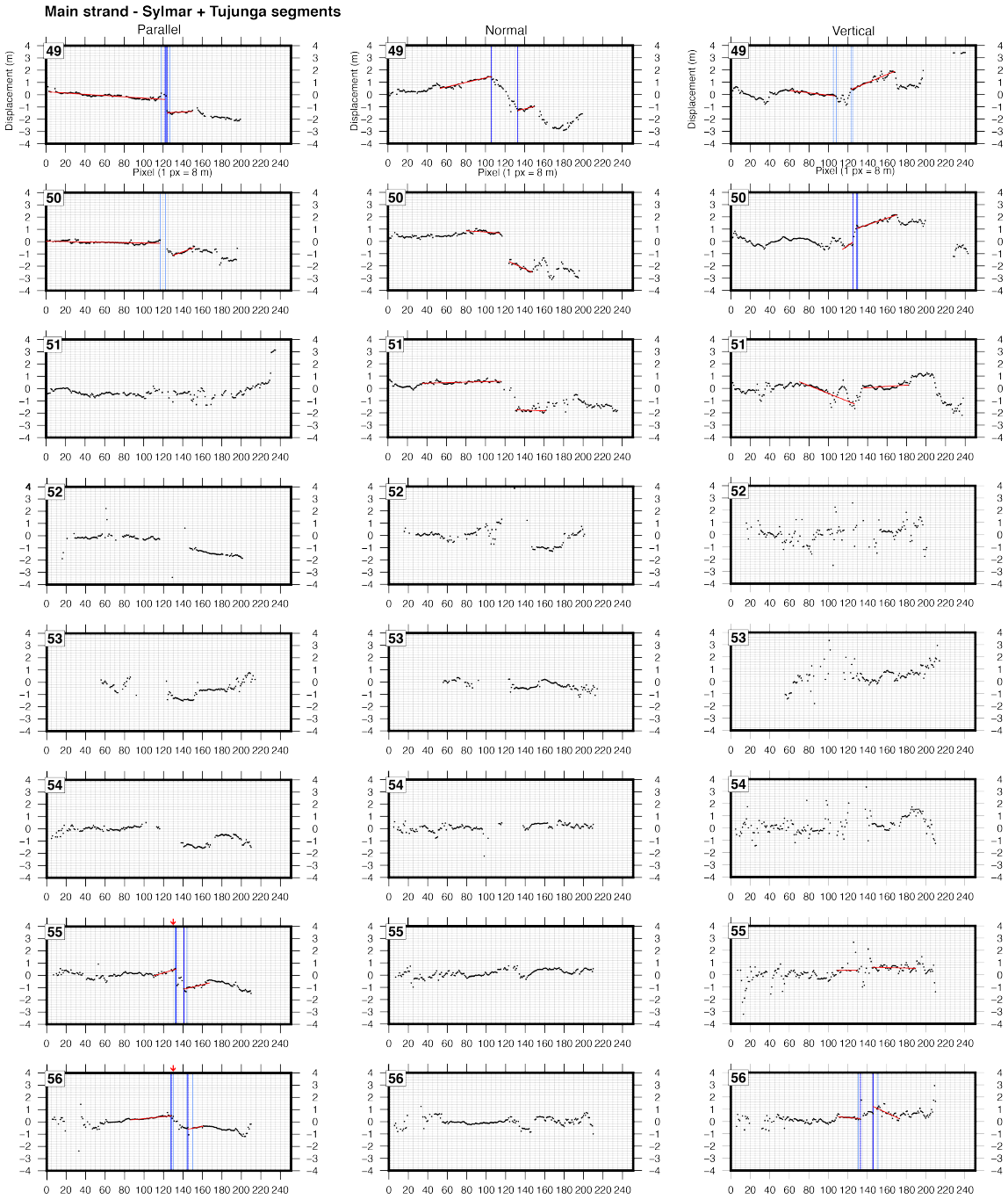
Main strand - Sylmar + Tujunga segments
Parallel
Normal
Vertical
Displacement (m)
Pixel (1 px = 8 m)
49
50
51
52
53
54
55
56

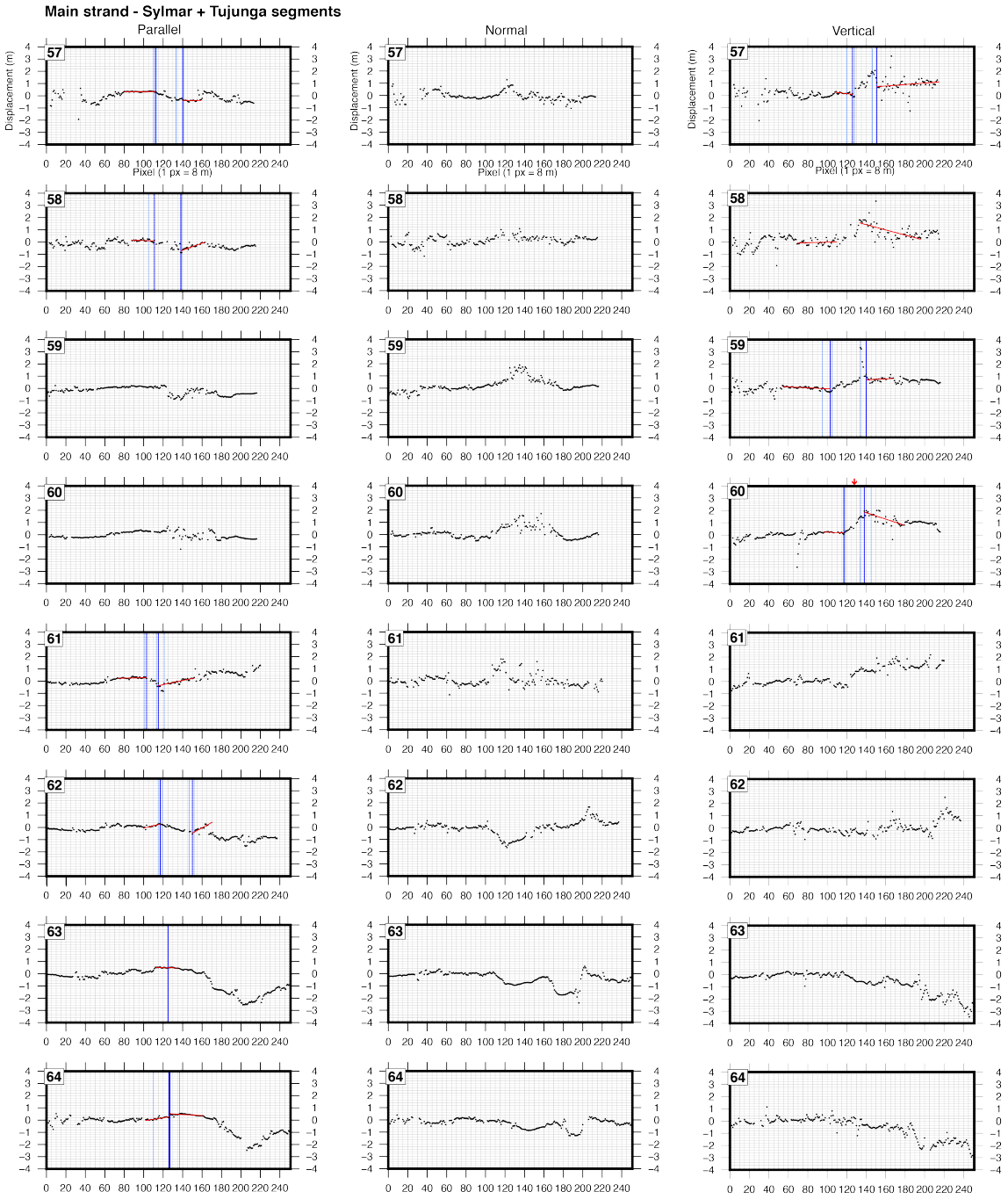
Main strand - Sylmar + Tujunga segments
Parallel
Normal
Vertical
Displacement (m)
Pixel (1 px = 8 m)
57
58
59
60
61
62
63
64

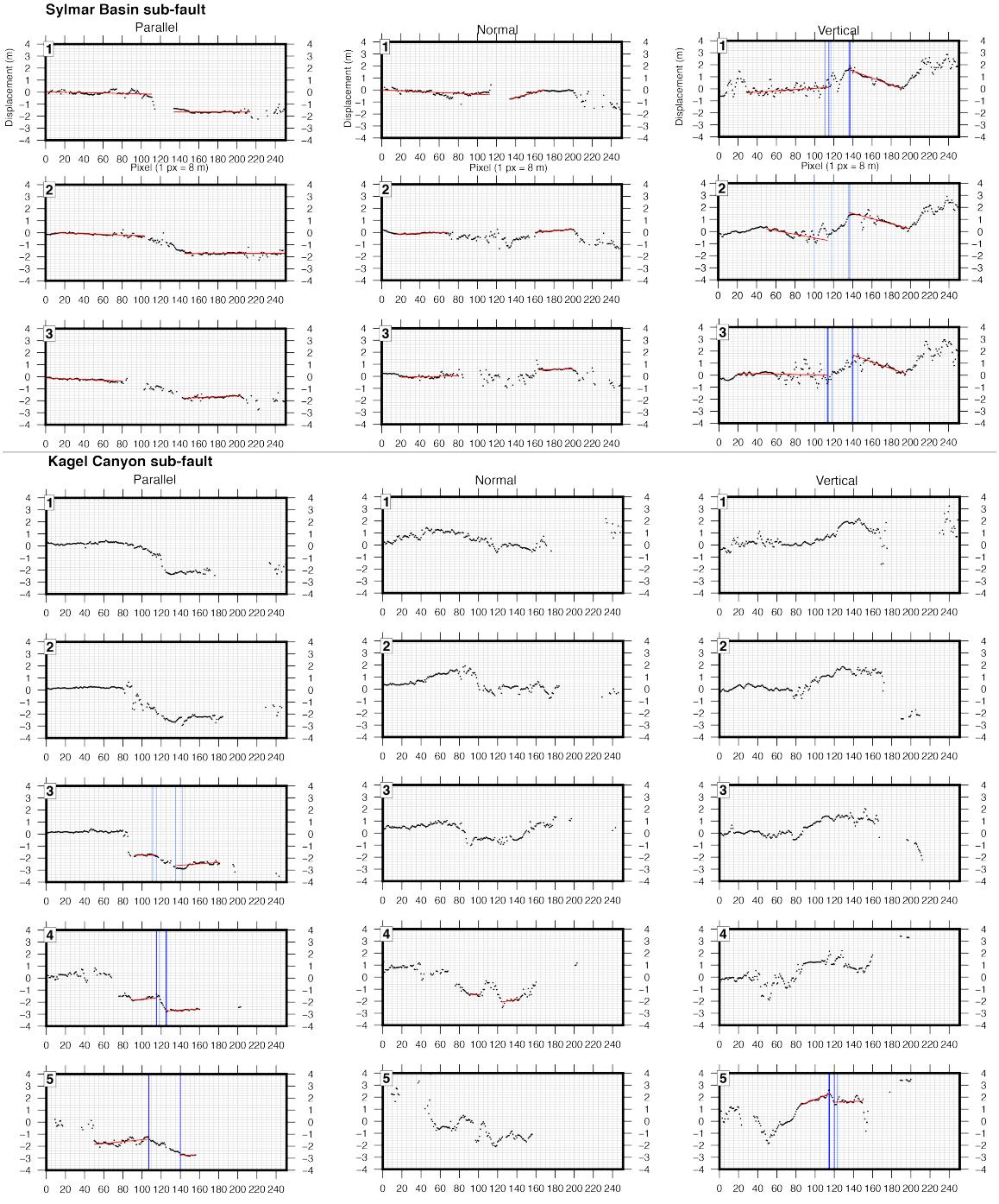
Sylmar Basin sub-fault
Parallel
Normal
Vertical
Displacement (m)
Pixel (1 px = 8 m)
Kagel Canyon sub-fault
Parallel
Normal
Vertical

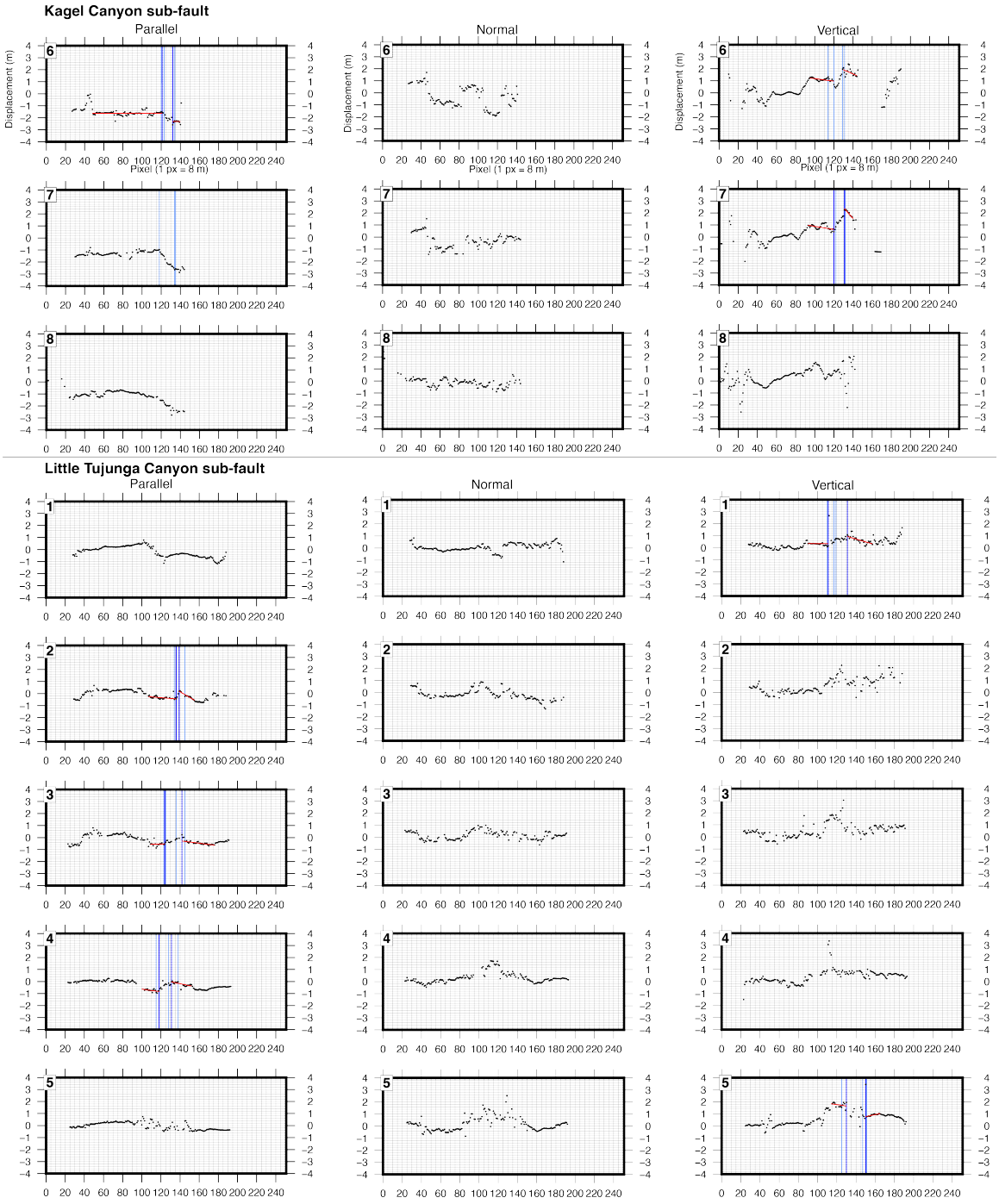
Kagel Canyon sub-fault
Parallel
Normal
Vertical
Displacement (m)
Pixel (1 px = 8 m)
Little Tujunga Canyon sub-fault
Parallel
Normal
Vertical

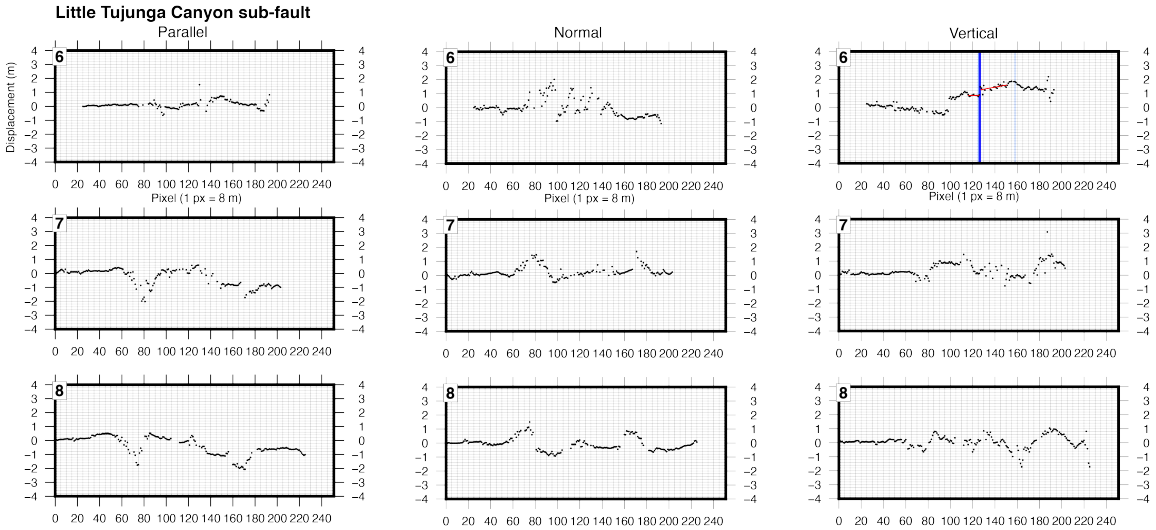
Little Tujunga Canyon sub-fault
Parallel
Normal
Vertical
Displacement (m)
Pixel (1 px = 8 m)
6
7
8

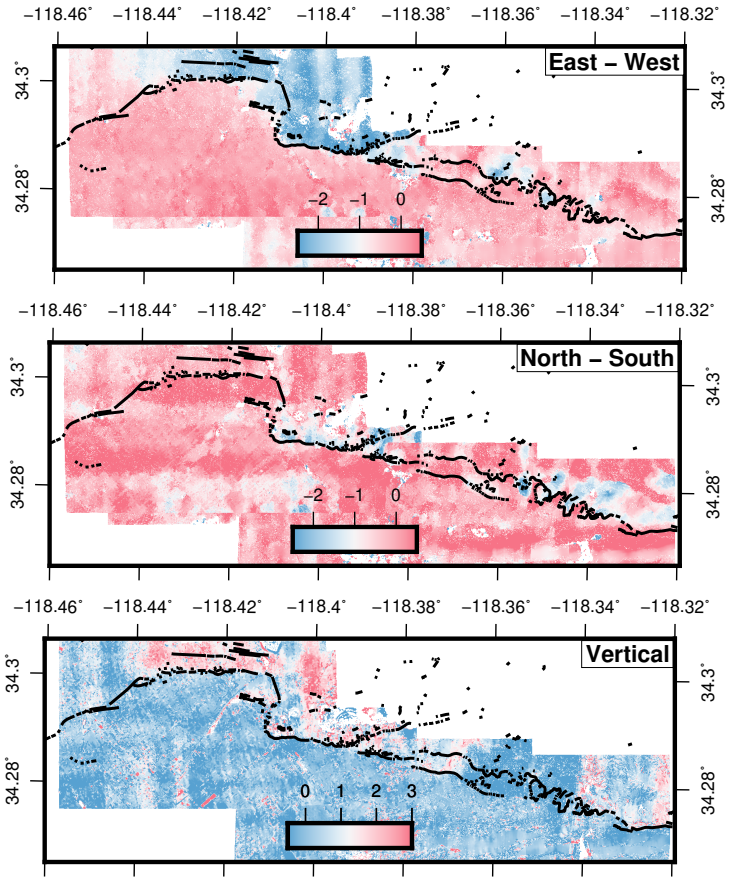


Figure 3.8: Full 3-D displacement field in meters.

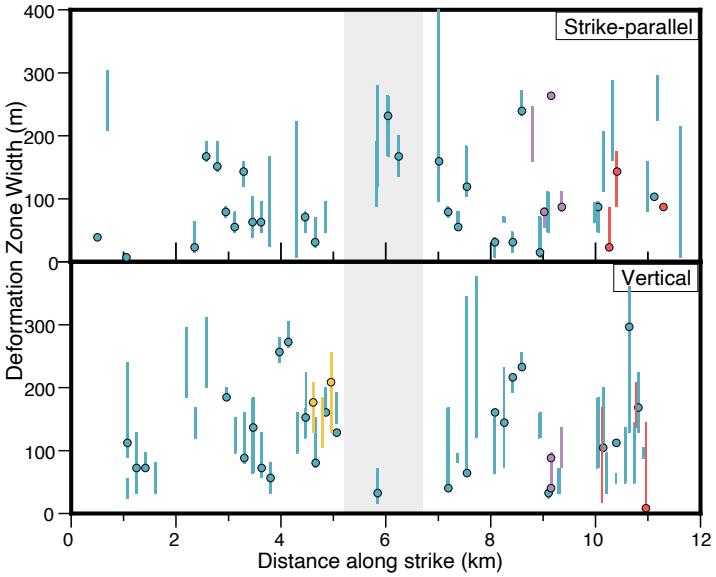


Figure 3.9: Preferred deformation zone widths plotted as a function of distance along fault trace. Vertical lines span the minimum and maximum deformation widths.

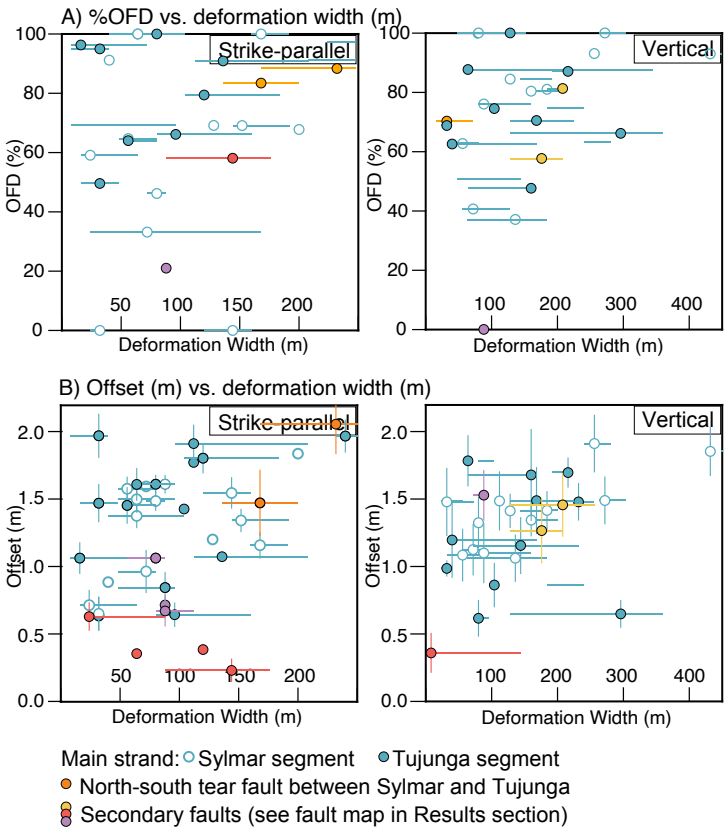


Figure 3.10: A) Comparison of %OFD and deformation zone width. B) Comparison of surface offset and deformation zone width.

Table 3.1: Images from USGS EarthExplorer used in the analysis

| Sensing Period | Image Identifier | Acquisition Date |
|---|---|---|
| Pre-earthquake | 1VCHC00010175 | 1969-07-25 |
| Pre-earthquake | 1VCHC0001131A | 1969-07-25 |
| Pre-earthquake | 1VCHC0001131B | 1969-07-25 |
| Pre-earthquake | 1VCHC0001X160 | 1969-07-25 |
| Pre-earthquake | 1VCHC0001X208 | 1969-07-25 |
| Pre-earthquake | 1VCHC0001X209 | 1969-07-25 |
| Post-earthquake | 1VCYY00020004 | 1972-10-25 |
| Post-earthquake | 1VCYY00020005 | 1972-10-25 |
| Post-earthquake | 1VCYY00020006 | 1972-10-25 |
| Post-earthquake | 1VCYY00020007 | 1972-10-25 |
| Post-earthquake | 1VCYY00020008 | 1972-10-25 |
| Post-earthquake | 1VCYY00020009 | 1972-10-25 |

Table 3.2: Rupture trace-parallel offsets, field measurements used in OFD estimation and OFD from strike-perpendicular profiles. Some field measurements have been projected to be perpendicular to each profile. Fault ID corresponds to the different fault segments mentioned in the text: MS: main rupture strand – Sylmar segment. MT: main strand – Tujunga segment. SS: Sylmar secondary fault. KS: Kagel Canyon secondary fault. TS: Little Tujunga Canyon secondary fault. Field offset references: (1) Bonilla et al. (1971); (2) Kamb et al. (1971); (3) Baize et al. (2020); (4) Barrows et al. (1973).

| Fault ID | Lon | Lat | Offset (m) | Offset error (m) | Field offset longitude | Field offset latitude | Field offset (m) | OFD (m) | %OFD | Deformation zone width (m) | Field offset reference |
|---|---|---|---|---|---|---|---|---|---|---|---|
| MS | -118.4568 | 34.2902 | 0.0320 | 0.0594 | 0.0000 | 0.0000 | 0.0000 | 0.0000 | 0 | 0 | 0 |
| MS | -118.4552 | 34.2915 | 0.0792 | 0.1162 | 0.0000 | 0.0000 | 0.0000 | 0.0000 | 0 | 0 | 0 |
| MS | -118.4534 | 34.2922 | 0.6928 | 0.0584 | 0.0000 | 0.0000 | 0.0000 | 0.0000 | 0 | 40 | 0 |
| MS | -118.4517 | 34.2928 | 0.9081 | 0.0863 | -118.4514 | 34.2933 | 0.0800 | 0.8281 | 91 | 0 | 1 |
| MS | -118.4499 | 34.2932 | 0.0951 | 0.0972 | 0.0000 | 0.0000 | 0.0000 | 0.0000 | 0 | 0 | 0 |
| MS | -118.4481 | 34.2935 | 0.3164 | 0.1123 | 0.0000 | 0.0000 | 0.0000 | 0.0000 | 0 | 8 | 0 |
| MS | -118.4462 | 34.2937 | 0.0848 | 0.0514 | 0.0000 | 0.0000 | 0.0000 | 0.0000 | 0 | 0 | 0 |

| | | | | | | | | | | | |
|---|---|---|---|---|---|---|---|---|---|---|---|
| MS | -118.4445 | 34.2939 | 0.2105 | 0.0329 | 0.0000 | 0.0000 | 0.0000 | 0.0000 | 0 | 0 | 0 |
| MS | -118.4432 | 34.2948 | 0.1283 | 0.1036 | 0.0000 | 0.0000 | 0.0000 | 0.0000 | 0 | 0 | 0 |
| MS | -118.4424 | 34.2963 | 0.2886 | 0.2020 | 0.0000 | 0.0000 | 0.0000 | 0.0000 | 0 | 0 | 0 |
| MS | -118.4411 | 34.2978 | 0.4799 | 0.0871 | 0.0000 | 0.0000 | 0.0000 | 0.0000 | 0 | 0 | 0 |
| MS | -118.4394 | 34.2980 | 0.8396 | 0.0951 | 0.0000 | 0.0000 | 0.0000 | 0.0000 | 0 | 0 | 0 |
| MS | -118.4375 | 34.2981 | 0.7334 | 0.1166 | -118.4379 | 34.2983 | 0.3000 | 0.4334 | 59 | 24 | 2 |
| MS | -118.4359 | 34.2994 | 1.1885 | 0.1022 | -118.4357 | 34.2989 | 0.0000 | 1.1885 | 100 | 168 | 2 |
| MS | -118.4341 | 34.3004 | 1.3761 | 0.0886 | -118.4339 | 34.2995 | 0.4248 | 0.9513 | 69 | 152 | 2 |
| MS | -118.4324 | 34.3004 | 1.5240 | 0.0748 | -118.4325 | 34.3000 | 0.8197 | 0.7043 | 46 | 80 | 2 |
| MS | -118.4305 | 34.3005 | 1.6166 | 0.0931 | -118.4304 | 34.3009 | 0.5700 | 1.0466 | 65 | 56 | 2 |
| MS | -118.4287 | 34.3005 | 1.5851 | 0.1197 | -118.4288 | 34.3010 | 1.6280 | -0.0430 | 0 | 144 | 2 |
| MS | -118.4269 | 34.3006 | 1.4108 | 0.0928 | -118.4268 | 34.3004 | 0.0000 | 1.4108 | 100 | 64 | 2 |
| MS | -118.4252 | 34.3007 | 1.5368 | 0.1018 | -118.4246 | 34.3003 | 0.0000 | 1.5368 | 100 | 64 | 2 |
| MS | -118.4233 | 34.3007 | 1.6348 | 0.1601 | -118.4242 | 34.3007 | 1.0920 | 0.5428 | 33 | 0 | 2 |
| MS | -118.4215 | 34.3008 | 1.8841 | 0.0995 | -118.4218 | 34.2997 | 0.6074 | 1.2767 | 68 | 0 | 1 |
| MS | -118.4197 | 34.3008 | 2.0411 | 0.1181 | -118.4204 | 34.3007 | -0.0100 | 2.0511 | 100 | 0 | 3 |
| MS | -118.4179 | 34.3009 | 1.2322 | 0.1268 | 0.0000 | 0.0000 | 0.0000 | 0.0000 | 0 | 0 | 0 |
| MS | -118.4161 | 34.3009 | 0.9889 | 0.1636 | 0.0000 | 0.0000 | 0.0000 | 0.0000 | 0 | 72 | 0 |
| MS | -118.4143 | 34.3005 | 0.6685 | 0.1292 | -118.4144 | 34.3007 | 0.6650 | 0.0035 | 0 | 32 | 2 |
| MS | -118.4125 | 34.3003 | 1.2343 | 0.0721 | -118.4133 | 34.3005 | 0.2246 | 1.0097 | 82 | 0 | 2 |
| MS | -118.4106 | 34.3002 | -0.2316 | 0.3844 | 0.0000 | 0.0000 | 0.0000 | 0.0000 | 0 | 0 | 0 |
| MS | -118.4092 | 34.2993 | -1.1672 | 0.1176 | 0.0000 | 0.0000 | 0.0000 | 0.0000 | 0 | 0 | 0 |

| | | | | | | | | | | | |
|---|---|---|---|---|---|---|---|---|---|---|---|
| MS | -118.4090 | 34.2948 | -1.3276 | 0.2755 | -118.4099 | 34.2944 | 0.2500 | 1.0776 | 81 | 0 | 3 |
| MT | -118.4102 | 34.2934 | -2.1073 | 0.2268 | -118.4113 | 34.2938 | 0.2500 | 1.8573 | 88 | 232 | 3 |
| MT | -118.4102 | 34.2922 | -1.5095 | 0.2517 | -118.4112 | 34.2928 | 0.2500 | 1.2595 | 83 | 168 | 3 |
| MT | -118.4089 | 34.2884 | 1.6648 | 0.2761 | -118.4099 | 34.2887 | 0.7600 | 0.9048 | 54 | 0 | 3 |
| MT | -118.4070 | 34.2886 | 1.9597 | 0.1447 | 0.0000 | 0.0000 | 0.0000 | 0.0000 | 0 | 160 | 0 |
| MT | -118.4052 | 34.2888 | 1.6519 | 0.0713 | -118.4050 | 34.2890 | 0.0000 | 1.6519 | 100 | 80 | 3 |
| MT | -118.4034 | 34.2883 | 1.4912 | 0.1393 | -118.4026 | 34.2883 | 0.5362 | 0.9550 | 64 | 56 | 3 |
| MT | -118.4017 | 34.2882 | 1.8488 | 0.1153 | -118.4007 | 34.2886 | 0.3800 | 1.4688 | 79 | 120 | 4 |
| MT | -118.3998 | 34.2880 | 2.4364 | 0.1851 | 0.0000 | 0.0000 | 0.0000 | 0.0000 | 0 | 0 | 0 |
| MT | -118.3983 | 34.2875 | 2.1589 | 0.1857 | -118.3985 | 34.2878 | 0.0000 | 2.1589 | 100 | 3 | 0 |
| MT | -118.3964 | 34.2874 | 2.1336 | 0.2282 | -118.3962 | 34.2876 | 0.1017 | 2.0319 | 95 | 32 | 1 |
| MT | -118.3946 | 34.2872 | 2.2040 | 0.1341 | 0.0000 | 0.0000 | 0.0000 | 0.0000 | 0 | 0 | 0 |
| MT | -118.3929 | 34.2872 | 1.5079 | 0.1462 | -118.3923 | 34.2868 | 0.7600 | 0.7479 | 50 | 32 | 3 |
| MT | -118.3910 | 34.2871 | 2.0170 | 0.1251 | 0.0000 | 0.0000 | 0.0000 | 0.0000 | 0 | 240 | 0 |
| MT | -118.3888 | 34.2859 | 1.0907 | 0.1203 | -118.3886 | 34.2865 | 0.0400 | 1.0507 | 96 | 16 | 4 |
| MT | -118.3870 | 34.2859 | 1.0071 | 0.1098 | -118.3864 | 34.2859 | 0.0000 | 1.0071 | 100 | 0 | 2 |
| MT | -118.3854 | 34.2848 | 0.3455 | 0.1937 | -118.3855 | 34.2857 | 0.5253 | -0.1798 | 0 | 0 | 1 |
| MT | -118.3773 | 34.2832 | 1.1017 | 0.0329 | -118.3770 | 34.2835 | 0.1000 | 1.0017 | 91 | 136 | 3 |
| MT | -118.3738 | 34.2829 | 0.8268 | 0.1124 | -118.3734 | 34.2827 | 0.4000 | 0.4268 | 52 | 0 | 4 |
| MT | -118.3687 | 34.2824 | 0.6605 | 0.0927 | -118.3690 | 34.2826 | 0.2237 | 0.4368 | 66 | 96 | 2 |
| MT | -118.3669 | 34.2817 | 0.7399 | 0.1676 | -118.4004 | 34.2921 | 0.0200 | 0.7199 | 97 | 264 | 3 |
| MT | -118.3651 | 34.2807 | -0.0361 | 0.0261 | -118.3654 | 34.2805 | 0.0518 | -0.0157 | 0 | 0 | 2 |

| | | | | | | | | | | | |
|---|---|---|---|---|---|---|---|---|---|---|---|
| SS | -118.4149 | 34.2956 | 1.4991 | 0.1595 | -118.4159 | 34.2960 | 0.4600 | 1.0391 | 69 | 0 | 3 |
| SS | -118.4133 | 34.2949 | 1.4741 | 0.1090 | -118.4141 | 34.2953 | 0.3875 | 1.0866 | 74 | 0 | 2 |
| SS | -118.4118 | 34.2947 | 1.4180 | 0.0852 | -118.4117 | 34.2945 | 0.5000 | 0.9180 | 65 | 0 | 3 |
| KS | -118.3896 | 34.2884 | 0.8791 | 0.1356 | 0.0000 | 0.0000 | 0.0000 | 0.0000 | 0 | 0 | 0 |
| KS | -118.3879 | 34.2888 | 1.0908 | 0.0448 | 0.0000 | 0.0000 | 0.0000 | 0.0000 | 0 | 80 | 0 |
| KS | -118.3863 | 34.2893 | 1.3037 | 0.2033 | 0.0000 | 0.0000 | 0.0000 | 0.0000 | 0 | 264 | 0 |
| KS | -118.3847 | 34.2900 | 0.6896 | 0.1181 | -118.3844 | 34.2904 | 0.5800 | 0.1096 | 15 | 88 | 3 |
| TS | -118.3758 | 34.2865 | -0.0285 | 0.1301 | 0.0000 | 0.0000 | 0.0000 | 0.0000 | 0 | 24 | 0 |
| TS | -118.3739 | 34.2863 | -0.2387 | 0.0883 | -118.3735 | 34.2859 | 0.1000 | 0.1387 | 58 | 144 | 4 |
| TS | -118.3722 | 34.2860 | 0.8118 | 0.1186 | 0.0000 | 0.0000 | 0.0000 | 0.0000 | 0 | 0 | 0 |

Table 3.3: Vertical offsets, field measurements used in OFD estimation and OFD from strike-perpendicular profiles. See Table 3.1 for fault ID explanation and field offset references.

| Fault ID | Lon | Lat | Offset (m) | Offset error (m) | Field offset longitude | Field offset latitude | Field offset (m) | OFD (m) | %OFD | Deformation zone width (m) | Field offset reference |
|---|---|---|---|---|---|---|---|---|---|---|---|
| MS | -118.4481 | 34.2935 | -1.6909 | 0.2491 | 0.0000 | 0.0000 | 0.0000 | 0.0000 | 0 | 0 | 0 |
| MS | -118.4462 | 34.2937 | -0.9191 | 0.2563 | 0.0000 | 0.0000 | 0.0000 | 0.0000 | 0 | 0 | 0 |
| MS | -118.4445 | 34.2939 | -1.2079 | 0.2067 | 0.0000 | 0.0000 | 0.0000 | 0.0000 | 0 | 0 | 0 |
| MS | -118.4432 | 34.2948 | -0.3283 | 0.2246 | 0.0000 | 0.0000 | 0.0000 | 0.0000 | 0 | 0 | 0 |
| MS | -118.4394 | 34.2980 | -1.2774 | 0.1334 | 0.0000 | 0.0000 | 0.0000 | 0.0000 | 0 | 0 | 0 |
| MS | -118.4375 | 34.2981 | -1.1824 | 0.1838 | -118.4379 | 34.2983 | 0.0000 | 1.1824 | 100 | 0 | 1 |
| MS | -118.4359 | 34.2994 | -1.2496 | 0.2135 | -118.4357 | 34.2989 | 0.0000 | 1.2496 | 100 | 0 | 2 |
| MS | -118.4341 | 34.3004 | -2.1085 | 0.2076 | -118.4345 | 34.3006 | 0.1500 | 1.9585 | 93 | 432 | 2 |
| MS | -118.4324 | 34.3004 | -1.6107 | 0.1633 | -118.4316 | 34.3020 | 0.3000 | 1.3108 | 81 | 184 | 2 |
| MS | -118.4305 | 34.3005 | -1.6127 | 0.2884 | -118.4304 | 34.3009 | 0.3000 | 1.3127 | 81 | 2 | 0 |
| MS | -118.4287 | 34.3005 | -1.2509 | 0.2531 | -118.4288 | 34.3010 | 0.3000 | 0.9509 | 76 | 88 | 2 |
| MS | -118.4269 | 34.3006 | -1.2077 | 0.1997 | -118.4268 | 34.3004 | 0.7600 | 0.4477 | 37 | 136 | 2 |
| MS | -118.4252 | 34.3007 | -1.2801 | 0.2174 | -118.4246 | 34.3003 | 0.7600 | 0.5201 | 41 | 72 | 2 |
| MS | -118.4233 | 34.3007 | -1.2342 | 0.2228 | -118.4242 | 34.3007 | 0.4600 | 0.7742 | 63 | 56 | 2 |
| MS | -118.4215 | 34.3008 | -2.1745 | 0.2434 | -118.4218 | 34.2997 | 0.1500 | 2.0245 | 93 | 256 | 1 |

| | | | | | | | | | | | |
|---|---|---|---|---|---|---|---|---|---|---|---|
| MS | -118.4197 | 34.3008 | -1.6950 | 0.2017 | -118.4204 | 34.3007 | 0.0000 | 1.6950 | 100 | 272 | 1 |
| MS | -118.4143 | 34.3005 | -1.5068 | 0.2175 | -118.4144 | 34.3007 | 0.0000 | 1.5068 | 100 | 80 | 2 |
| MS | -118.4179 | 34.3009 | -1.6149 | 0.2345 | 0.0000 | 0.0000 | 0.0000 | 0.0000 | 0 | 152 | 0 |
| MS | -118.4161 | 34.3009 | -1.8413 | 0.2288 | 0.0000 | 0.0000 | 0.0000 | 0.0000 | 0 | 160 | 0 |
| MS | -118.4125 | 34.3003 | -1.5292 | 0.1371 | -118.4133 | 34.3005 | 0.3000 | 1.2292 | 80 | 160 | 2 |
| MS | -118.4106 | 34.3002 | -1.6072 | 0.1439 | -118.4106 | 34.3003 | 0.2500 | 1.3572 | 84 | 128 | 2 |
| MT | -118.4090 | 34.2948 | 1.6833 | 0.2870 | -118.4095 | 34.2947 | 0.5000 | 1.1833 | 70 | 32 | 2 |
| MT | -118.4052 | 34.2888 | -1.3615 | 0.3195 | -118.4050 | 34.2890 | 0.5100 | 0.8515 | 62 | 40 | 3 |
| MT | -118.4017 | 34.2882 | -2.0291 | 0.2155 | -118.4010 | 34.2886 | 0.2500 | 1.7791 | 88 | 64 | 3 |
| MT | -118.3998 | 34.2880 | -1.8297 | 0.2255 | -118.3985 | 34.2878 | 0.7600 | 1.0697 | 58 | 0 | 3 |
| MT | -118.3964 | 34.2874 | -1.9101 | 0.3874 | -118.3962 | 34.2876 | 1.0000 | 0.9100 | 48 | 160 | 3 |
| MT | -118.3946 | 34.2872 | -1.3147 | 0.2399 | 0.0000 | 0.0000 | 0.0000 | 0.0000 | 0 | 104 | 0 |
| MT | -118.3929 | 34.2872 | -1.9304 | 0.1271 | -118.3923 | 34.2868 | 0.2500 | 1.6804 | 87 | 216 | 3 |
| MT | -118.3910 | 34.2871 | -1.6828 | 0.1580 | 0.0000 | 0.0000 | 0.0000 | 0.0000 | 0 | 232 | 0 |
| MT | -118.3888 | 34.2859 | -0.5310 | 0.1415 | -118.3887 | 34.2858 | 0.4000 | 0.1310 | 25 | 0 | 4 |
| MT | -118.3870 | 34.2859 | -1.1221 | 0.0690 | -118.3863 | 34.2860 | 0.3500 | 0.7721 | 69 | 32 | 4 |
| MT | -118.3854 | 34.2848 | -1.3087 | 0.2394 | -118.3853 | 34.2855 | 0.7000 | 0.6087 | 47 | 0 | 4 |
| MT | -118.3790 | 34.2831 | -0.2518 | 0.2097 | -118.3781 | 34.2836 | 0.2500 | 0.0018 | 0 | 0 | 4 |
| MT | -118.3773 | 34.2832 | -0.9813 | 0.1873 | -118.3781 | 34.2836 | 0.2500 | 0.7313 | 75 | 104 | 4 |
| MT | -118.3755 | 34.2831 | -0.6364 | 0.2662 | 0.0000 | 0.0000 | 0.0000 | 0.0000 | 0 | 0 | 0 |
| MT | -118.3738 | 34.2829 | -1.5547 | 0.4605 | 0.0000 | 0.0000 | 0.0000 | 0.0000 | 0 | 0 | 0 |
| MT | -118.3721 | 34.2827 | -0.7384 | 0.1175 | -118.3720 | 34.2825 | 0.2500 | 0.4884 | 66 | 296 | 4 |
| MT | -118.3704 | 34.2825 | -1.6933 | 0.2837 | -118.3731 | 34.2826 | 0.5000 | 1.1933 | 70 | 168 | 4 |
| SS | -118.4149 | 34.2956 | -1.4408 | 0.2753 | -118.4149 | 34.2954 | 0.6100 | 0.8308 | 58 | 176 | 3 |

| | | | | | | | | | | | |
|---|---|---|---|---|---|---|---|---|---|---|---|
| SS | -118.4133 | 34.2949 | -2.3195 | 0.2376 | -118.4141 | 34.2953 | 0.2000 | 2.1195 | 91 | 0 | 3 |
| SS | -118.4118 | 34.2947 | -1.6574 | 0.2677 | -118.4117 | 34.2945 | 0.3100 | 1.3474 | 81 | 208 | 3 |
| KS | -118.3896 | 34.2884 | -0.4347 | 0.1814 | 0.0000 | 0.0000 | 0.0000 | 0.0000 | 0 | 0 | 0 |
| KS | -118.3879 | 34.2888 | 0.1395 | 0.1333 | -118.3884 | 34.2898 | 0.3500 | -0.2100 | 0 | 0 | 4 |
| KS | -118.3863 | 34.2893 | 0.7067 | 0.1452 | -118.3860 | 34.2897 | 0.8500 | -0.7000 | 0 | 40 | 4 |
| KS | -118.3847 | 34.2900 | -0.9532 | 0.2030 | 0.0000 | 0.0000 | 0.0000 | 0.0000 | 0 | 0 | 0 |
| KS | -118.3831 | 34.2902 | -1.7401 | 0.2130 | 0.0000 | 0.0000 | 0.0000 | 0.0000 | 0 | 88 | 0 |
| TS | -118.3776 | 34.2864 | -0.6010 | 0.1158 | -118.3778 | 34.2863 | 0.1000 | 0.5010 | 83 | 0 | 4 |
| TS | -118.3704 | 34.2859 | 0.8853 | 0.2041 | -118.3703 | 34.2858 | 0.4000 | 0.4853 | 55 | 0 | 4 |
| TS | -118.3685 | 34.2859 | -0.4093 | 0.1685 | -118.3687 | 34.2863 | 0.5000 | -0.0907 | 0 | 8 | 4 |
| TS | -118.3368 | 34.2755 | -0.5618 | 0.2896 | 0.0000 | 0.0000 | 0.0000 | 0.0000 | 0 | 16 | 0 |

# Chapter 4

# Consequences of distributed surface deformation and fault structural maturity on shallow slip deficit in the Tibetan Plateau

## 4.1 Article Information

This chapter will be submitted to a journal. I undertook the data curation, formal analysis, created the figures, wrote and edited the text. Dr. Edwin Nissen supervised and provided manuscript edits. Jinrui Liu helped with the literature review and measured cumulative fault offsets from geological maps.

### 4.1.1 Author Names and Affiliations

É. Gaudreau[1], J. Liu[2], E. Nissen[1]

[1]University of Victoria, Victoria, Canada
[2]State Key Laboratory of Earthquake Dynamics, Institute of Geology, China Earthquake Administration, Beijing, China

## 4.2 Abstract

InSAR-constrained elastic dislocation models are often used to characterize large earthquakes and their slip distributions. A common feature of these models is a decrease in slip near the surface, that does not seem to be accommodated interseismically. The source of this shallow slip deficit and its significance for seismic hazard are still debated, with some studies suggesting that it is a manifestation of fault structural immaturity, exclusive to faults with small cumulative offsets that have not yet developed a single dominant, through-going slip surface. We explore this possibility through a survey of 10 recent (1997 to 2022) strike-slip earthquakes from the Tibetan Plateau that are well-documented with InSAR-derived slip models and which occurred on faults that sample a wide spectrum of structural maturity. We compare independently modeled slip distributions with each other and, where available, with surface offsets measured in the field or derived from horizontal displacement maps produced using SAR amplitude or optical imagery. We find that there is a large range in shallow slip deficits between InSAR models of the same earthquake, in some cases greater than 50%. Analysis of thirteen slip models of the 2021 $M_w$7.4 Maduo earthquake and ten slip models of the 2022 $M_w$ 6.9 Menyuan earthquake indicate that the models are not robust in the upper 1 km of the crust, nor at greater depths near the highest slip areas, and in regions of fault bends and other segmentation. Furthermore, we find that fault structural maturity has at most a secondary control on shallow slip deficit and rupture length on the largest recent strike-slip earthquakes in the Tibetan Plateau.

## 4.3 Introduction

Elastic dislocation models constrained by Interferometric Synthetic Aperture Radar (InSAR) surface displacements are widely used to characterize large continental earthquakes, providing important information on the fault geometry and rupture length, the distribution of slip at depth, and the geodetic moment magnitude (e.g., Wright et al., 2013). This has been a significant development in the characterization of earthquakes and seismic hazard, particularly in remote regions (e.g., Funning et al., 2007; Gaudreau et al., 2019). These models systematically exhibit greater coseismic slip at depths of several kilometers than at the surface, a pattern termed the shallow slip deficit (SSD; Fialko et al., 2005; Marchandon et al., 2021; Xu et al., 2016b). This deficit is often reported in publications, and is estimated from slip distributions by comparing the weighted sum of slip at the surface and at depth, along the length of the fault (Dolan and Haravitch, 2014; Fialko et al., 2005;

Marchandon et al., 2021; Xu et al., 2016b). While the elastic rebound model of crustal deformation requires slip rates to be uniform across the seismogenic layer, the "missing" near-surface slip is not usually significantly accommodated through postseismic slip or interseismic creep (e.g., Fialko et al., 2005; Hussain et al., 2018; Kaneko and Fialko, 2011). Elastic models are poorly representative of the rheology of fault zones near the free surface, since the upper few kilometers of the crust are mechanically distinct from the rest of the seismogenic zone (Marone, 1998). Furthermore, fault zones develop bands of damaged rock hundreds of meters to kilometers in width near the surface over which coseismic deformation may be distributed, often with an inner zone of inelastic deformation (Barnhart et al., 2020; Bartlett et al., 1981; Ma and Andrews, 2010). The likely velocity-strengthening region of the shallow crust impedes coseismic rupture near the surface, and may deform via distributed inelastic deformation during the interseismic period, thus accumulating little elastic strain (Fialko et al., 2005). Thick sediments near the surface can promote this velocity-strengthening behavior (Marone et al., 1991; Zhao et al., 2023).

Fault structural maturity (Manighetti et al., 2007) is also thought to impact damage zone material properties and therefore SSD. This is related to how fault zone properties evolve incrementally through successive earthquakes (e.g., Bürgmann et al., 1994; Li et al., 2020b; Manighetti et al., 2007; Wesnousky, 1990), including the widening and intensification of the damage zone (Faulkner et al., 2011; Lyakhovsky and Ben-Zion, 2009; Shipton and Cowie, 2003). For relatively immature faults, coseismic deformation tends to be distributed over the entire width of the damage zone, whereas more mature faults are associated with more localized coseismic deformation, once the fault core and innermost damage zone become sufficiently damaged that strain is more efficiently accommodated there (Cowie and Scholz, 1992; Dolan and Haravitch, 2014). Furthermore, relatively immature faults typically have a greater density of bends, steps and secondary faulting, which promotes distributed deformation (e.g., Dolan and Haravitch, 2014; Manighetti et al., 2007; Milliner et al., 2015; Wesnousky, 1988). As a fault accrues slip over many earthquake cycles, separate fault segments coalesce, eventually becoming a smoother and geometrically simpler through-going fault (Cooke and Madden, 2014; Hatem et al., 2017; Shipton and Cowie, 2003). Other than potentially affecting the amount of SSD, the maturity of a fault may impact other aspects of earthquake behavior such as rupture length (Manighetti et al., 2007; Wesnousky, 1988, 1990), ground motion amplitude (Radiguet et al., 2009), rupture velocity (Bruhat et al., 2016; Perrin et al., 2016), stress drop, slip magnitude and heterogeneity (Bruhat et al., 2020; Manighetti et al., 2007), and the likelihood of characteristic earthquakes (Ben-Zion and Sammis, 2003; Wesnousky, 1994). Consequently, a variety of proxies for the maturity

of a fault have been proposed that could potentially improve characterization of seismic hazard (Manighetti et al., 2007). Due to the wide range of factors that may influence fault zone evolution, the structural maturity of a fault is usually qualitatively estimated using these proxies, including cumulative offset, long-term or geodetic slip rate, fault length, and fault surface trace complexity (Manighetti et al., 2021; Perrin et al., 2016). For example, faults that have a cumulative offset of $<$10 km are generally considered immature, and faults that have a cumulative offset of $>$100 km are generally considered mature (e.g., Manighetti et al., 2007).

The common model approximation of a fault as a planar feature embedded in a homogeneous elastic medium may more successfully reproduce coseismic deformation on mature fault zones where deformation is localized on a narrow, structurally simpler structure than their immature counterparts. Therefore, fault structural maturity is potentially important in assessing the reliability of certain aspects of these models, since common modeling choices may artificially alter near-surface slip. These include modeling the crust as a homogeneous elastic halfspace without a compliant fault zone, changes in mechanical properties with depth, or variable topography (Kaneko and Fialko, 2011; Marchandon et al., 2021; Roten et al., 2017; Xu et al., 2016b). Simplifying the fault geometry can also introduce spurious model slip or slip deficit at shallow depths, especially around segment boundaries (Xu et al., 2016b). Furthermore, a regularization is usually applied such that the resulting slip distribution is deemed realistic, but the degree of smoothing is a subjective choice and a small difference in smoothing factor may result in very different SSD values (Gombert et al., 2018). The data and data downsampling used in the slip inversions are also thought to be important contributors to modeled SSD: InSAR fringes decorrelate near surface ruptures due to the high displacement gradients, and the lack of near-fault constraints and/or errors introduced during aggressive phase unwrapping may lead to a change in modeled near-surface slip. This can be mitigated with joint inversions that include near-fault horizontal pixel displacement fields from the correlation of SAR amplitude or optical images (Gombert et al., 2018; Marchandon et al., 2021; Vallage et al., 2015; Xu et al., 2016b). However, near-fault data may cause problems in the inversion since elastic models cannot solve for inelastic deformation (Kaneko and Fialko, 2011; Gombert et al., 2018). Marchandon et al. (2021) also demonstrated that correlated noise in the input data may increase SSD, while downsampling the data using a quadtree algorithm (giving more weight to near-field data) reduces SSD.

In this paper we reassess the significance of the SSD by compiling 41 InSAR-constrained coseismic slip models from ten large ($M_w$ 6.5–7.8) predominantly strike-slip earthquakes

that occurred in the Tibetan Plateau from 1997 to 2022 (Figure 4.1 and Table 4.1). Our geographic focus is motivated firstly by the larger number of Tibetan earthquakes well-documented with InSAR compared to other continental earthquake belts, and secondly by the fact that these earthquakes occurred on well-studied faults of various maturities and tectonic settings. These include block-bounding and lithospheric-scale fault systems, intra-block faults, and complex fault networks accommodating the convergence between the weaker laterally escaping plateau and the stronger surrounding blocks. We explore the variation between InSAR models of the same earthquake to assess where model slip is relatively consistent between models, despite having been inverted completely independently in most cases. The goal of this study is not to determine which coseismic slip models are superior, particularly since differences between models are expected due to the non-uniqueness of the problem, the necessary approximations involved, and the vast combination of valid modeling choices that are possible. Rather, our aim is to assess whether SSD is a reliable metric, and the roles of fault structural maturity on SSD, on the amount of distributed surface slip measured by SAR or optical pixel displacements or inferred from field measurements, and on other aspects of earthquake behavior such as rupture length. Since faults grow laterally over many earthquake cycles, there are expected to be differences in structural maturity along a fault or fault system. However, previous studies that estimate fault structural maturity in order to assess its impacts on earthquake behavior sometimes use maximum maturity proxies of the entire fault system, potentially overestimating the maturity of the segment that actually ruptured (Dolan and Haravitch, 2014; Manighetti et al., 2007; Perrin et al., 2016). Therefore, we are careful to use cumulative offset and slip rate measurements taken as close as possible to each rupture. Where nearby cumulative offset measurements were not found in the literature, we estimated them ourselves from geological and topographic maps.

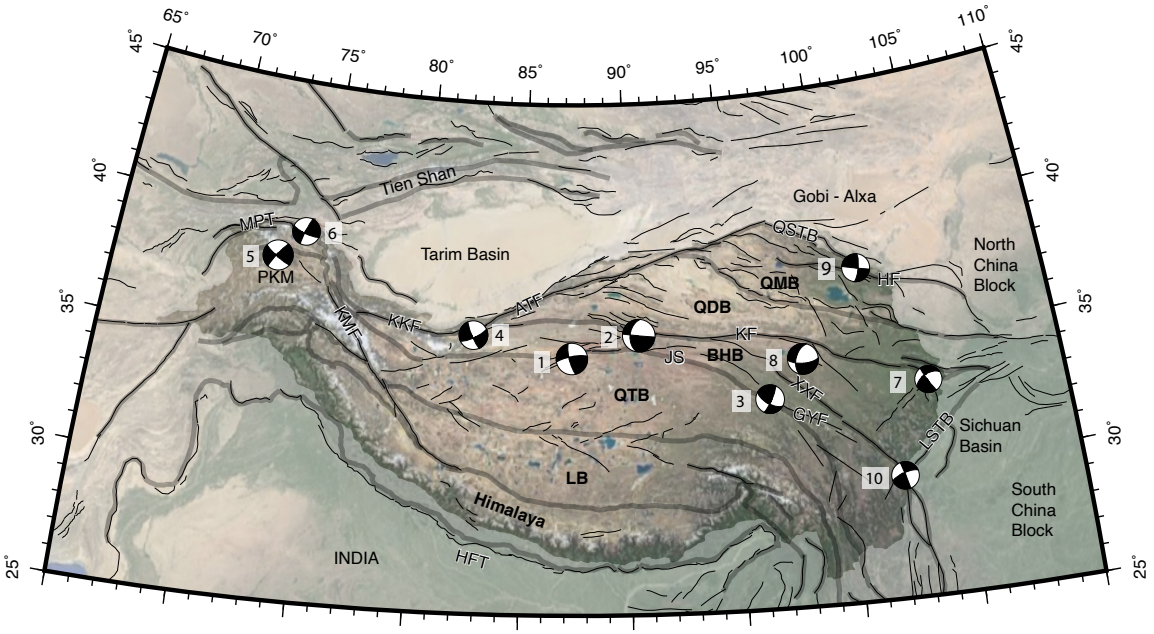


Figure 4.1: U.S. Geological Survey focal mechanisms of the ten earthquakes in this study with transparency applied to surrounding areas to outline the Tibetan Plateau. Thin black lines are major active faults from Taylor and Yin (2009) and thick gray lines are major tectonic boundaries from Liu et al. (2022b). Earthquakes are labelled as follows: 1) 1997 $M_W$ 7.5 Manyi, 2) 2001 $M_W$ 7.8 Kunlun, 3) 2010 $M_W$ 6.9 Yushu, 4) 2014 $M_W$ 6.9 Yutian, 5) 2015 $M_W$ 7.2 Murghab, 6) 2016 $M_W$ 6.6 Aketao, 7) 2017 $M_W$ 6.5 Jiuzhaigou, 8) 2021 $M_W$ 7.4 Maduo, 9) 2022 $M_W$ 6.9 Menyuan, 10) 2022 $M_W$ 6.6 Luding earthquake. Tectonic features are labelled as follows: MPT: Main Pamir thrust system, PKM: Pamir-Karakorum mountains, KMF: Karakorum fault system, KKF: Karakax fault system, ATF: Altyn Tagh fault system, JS: Jinsha suture, KF: Kunlun fault system, QSTB: Qilian Shan thrust belt, XXF: Xianshuihe-Xiaojiang fault system, GYF: Ganzi-Yushu fault system, HF: Haiyuan fault system, LSTB: Longmen Shan thrust belt, LB: Lhasa block, QTB: Qiangtang block, QDB: Qaidam block, BHB: Bayan Har block, QMB: Qilian Mountain block.

## 4.4 Tectonic setting

The Tibetan Plateau is a region of thickened continental crust where uplift and eastward extrusion of the lithosphere are ongoing due to the collision of the Indian and Eurasian plates (e.g., Molnar and Tapponnier, 1975). The plateau is separated into what can be described as "blocks", with deformation concentrated around their boundaries but some residual strain occurring internally (Zheng et al., 2017). Some of these blocks include an amalgamation of terranes separated by lithospheric-scale sutures, including the Lhasa and Qangtang blocks in the south near the main Himalayan frontal thust, the Bayan Har and Qaidam blocks in the central plateau and the Qilian Mountain block in the northeast (Figure 4.1).

The Tibetan Plateau has a longer geologic history of deformation than many other earthquake belts, which in the context of this study helps explain why it exhibits such a wide range of fault structural maturities. Collision of the Indian and Eurasian plates commenced at ∼50 Ma following northward subduction of the Tethys Ocean beneath Eurasia (e.g., Rowley, 1998; Royden et al., 2008; Searle et al., 1987). Shortening, crustal thickening and surface uplift initially concentrated in southern and central Tibet before progressing northwards to reach the north Qaidam Basin and the East Kunlun-West Qinling mountain range at ∼30 Ma (Li et al., 2021; Wang et al., 2017, 2022b; Yu et al., 2023). Eastward extrusion and crustal-scale dextral transpressive thrusting of central Tibet also started around this time, eventually reaching eastern Tibet. The extrusion was accommodated by eastward crustal flow within the plateau and regional clockwise rotation around the eastern Himalayan Syntaxis (Gan et al., 2007; Tapponnier et al., 2001; Zhang et al., 2004a). Major east-west-striking left-lateral fault systems in the east-central and northeastern plateau that accommodate present-day lateral growth initiated in the Eocene to Miocene, namely the Altyn Tagh (initiation age of left-lateral slip poorly constrained; Eocene to Miocene), the Haiyuan (∼10–17 Ma), Kunlun (∼10–20 Ma), Xianshuihe-Xiaojiang (∼5–13 Ma) and Ganzi-Yushu (∼13 Ma) fault systems (Dai et al., 2017; Duvall et al., 2013; Fu and Awata, 2007; Roger et al., 1995; Wang et al., 2009b; Zhang et al., 2004b, and references therein). Accelerated and synchronous crustal deformation also occurred across the plateau in the Miocene (Gan et al., 2021; Molnar and Stock, 2009; Wang et al., 2022b). At the western margin of the Tibetan Plateau, the Pamirs were characterized by alternating periods of N-S shortening/lateral extrusion and extension since the Paleogene (Rutte et al., 2017). Here, India-Eurasia convergence has been accommodated by the NW-SE right-lateral Karakorum fault system, displacing material northwest towards the Pamirs (Fan et al., 1994). Since the

initiation of the major strike-slip fault systems, the central and southern Plateau have been characterized by north-south shortening, east-west extension and continued eastward extrusion of lithosphere on dextral and oblique fault systems, while overthrusting north of the Kunlun fault resulted in ongoing rapid uplift and shortening in the northeastern part of the Plateau (Meyer et al., 1998; Tapponnier et al., 1990; Wang et al., 2017; Zheng et al., 2017).

Current orogen-scale deformation patterns are well characterized, having been measured using seismic and GNSS data for several decades (Chen et al., 2004; Larson et al., 1999; Molnar and Lyon-Caen, 1989; Priestley et al., 2008; Wang et al., 2001). More recent densification of GNSS networks and improvements to InSAR data coverage have allowed for a more complete picture of crustal velocities throughout the Tibetan Plateau (e.g., Garthwaite et al., 2013; Huang et al., 2022b; Ou et al., 2022; Wang et al., 2019; Wang and Shen, 2020; Zheng et al., 2017). Certain areas of high shear strain coincide with major fault systems including the east-west to northwest-southwest Xianshuihe-Xiaojiang, Kunlun and Haiyuan fault systems, though it is unclear whether these represent long-term deformation rates or transient earthquake cycle effects (Wang et al., 2021; Zheng et al., 2017). Geodetic strain maps also clearly delineate zones of high strain that extend away from mapped major faults such as the Yutian-Zhongba strain rate zone in the western plateau (Wang et al., 2019) and unmapped faults south of the Haiyuan fault system (Ou et al., 2022). Material contrasts also induce high strain in areas such as around the Altyn Tagh fault system, which marks the boundary between the stronger Tarim Basin and the weaker Tibetan Plateau (Zheng et al., 2017). Based on crustal velocity inversions derived from InSAR and GPS data, the Altyn Tagh, Kunlun, Ganzi-Yushu and Xianshuihe-Xiaojiang strike slip fault systems slip at rates of 10–12 mm/yr (Garthwaite et al., 2013; Liu et al., 2022c; Loveless and Meade, 2011; Wang et al., 2009a), which is fairly consistent with long-term slip rates estimated from Quaternary dating of offset landforms (Gold et al., 2009, 2011; Harkins et al., 2010; Kirby et al., 2007; Kirby and Harkins, 2013; Shi et al., 2013; Wang et al., 2009b; Wu et al., 2017). The Haiyuan fault system at the northeastern margin of the plateau currently slips up to 6.4 mm/yr (Huang et al., 2022b), similar to long-term slip rates that cluster around 5 mm/yr (Huang et al., 2022b; Li et al., 2009, 2016; Ou et al., 2022). While much of the strain ($\sim$40 nanostrain/year) and seismicity are concentrated in wide areas around the major fault systems, GNSS and InSAR data indicate that the Tibetan Plateau is deforming diffusely at $\sim$18 nanostrain/year between major faults (Loveless and Meade, 2011; Zheng et al., 2017). This is supported by seismicity distributed on conjugate faults throughout central Tibet that accommodate some of the north-south shortening and east-west extension in this region (Zhu et al., 2017). Stable, undeforming regions surround the Tibetan

Plateau, including the Tarim Basin, which bounds the plateau in the northwest, Gobi-Alxa platform in the northeast, and the Sichuan and Ordos Basins in the east (Zheng et al., 2017).

## 4.5 Surface and Subsurface Deformation in the 2021 Maduo and 2022 Menyuan Earthquakes

In this section we focus on two of the most thoroughly documented Tibetan earthquakes: the 2021 $M_w$ 7.4 Maduo and 2022 $M_w$ 6.6 Menyuan events. Both are surface-rupturing earthquakes with high quality surface deformation data including Sentinel-1 InSAR line-of-sight displacements, SAR and optical pixel displacements, and field offsets, and both have at least ten published and accessible InSAR slip models. In each case, we are interested firstly in whether SSD estimates are relatively consistent (and therefore reliable estimates of modeled slip deficit, whether due to modeling choices or true slip deficit), and secondly in whether they can be explained by distributed coseismic surface deformation. We begin by comparing InSAR-derived slip distributions and SSD estimates in what to our knowledge are some of the most comprehensive such InSAR model inter-comparisons yet attempted.

For each coseismic slip model, a normalized slip profile was generated in the conventional way, by calculating the weighted sum of slip along the model fault (weighted by slip patch length, e.g., Fialko et al., 2005) for each depth increment of the original model. The summed slip values were then normalized against the maximum value. Profiles were plotted such that the nodes correspond to the center of each patch. The profiles are step functions (since model slip is uniform across each patch) but plotting the profiles as lines connecting the center depths of the slip patches is visually simpler. For multi-segment models that have different dips, the segments had fault patches at different depths, but the depth increments across the length of the fault were similar since the dips were similar. For each model, the increments used for sampling the modeled slip and plotting the slip profiles were that of the first fault segment (since the dips were similar, these depth increments always sampled the same "row" of slip patches along the entire fault). The SSD was also calculated in the conventional way, by subtracting the normalized weighted sum of the shallowest (surficial) row of slip patches from 1. This is expressed as a percentage: an SSD of 0% means the shallowest row has the highest slip of all model rows, and an SSD of 100% means that the shallowest row has no slip.

For a description of how the modeled slip distributions were compared, see Appendix section 4.9.1.

Next, we investigate distributed surface deformation from fault trace-parallel offsets measured over ∼1 km fault zone widths from optical pixel displacements, to then compare against InSAR-derived surface and maximum model slip values. More details on the displacement data, profiling and offset measurements are in Appendix 4.9.2. Comparing these offsets with modeled slip values to get a value comparable to SSD (here named distributed shallow slip deficit; DSSD) involves matching the offsets to the nearest model surficial slip patch. In most cases, there were multiple offsets per slip patch, so the average value was used. To better characterize the average slip deficit, we normalize each distributed surface offset to the maximum InSAR model slip value downdip, then average these normalized surface slip values. This is similar to the local surface slip ratio (LSSR) value in Dolan and Haravitch (2014), though their metric utilizes field offset measurements rather than those obtained from near-field displacement field. We calculate DSSD by subtracting this value from 1, expressing it as a percentage that is readily comparable to SSD. This gives an estimate of the remaining slip deficit once distributed deformation is taken into account.

### 4.5.1 The 2021 $M_w$ 7.4 Maduo Earthquake

The $M_w$ 7.4 Maduo earthquake occurred on May 22, 2021 on the ∼370 km-long left-lateral Jiangcuo fault (Deng et al., 2003). The ∼161 km-long rupture is located within the Bayan-Har block, sub-parallel to and ∼80 km south of the block-bounding Kunlun fault system (Figures 4.1,4.2a). The Jiangcuo fault was not widely known prior to this earthquake (Yuan et al., 2022, and references therein). Li et al. (2022a) identified a long-lived linear trough in pre-earthquake topography data and geomorphic markers offset by a maximum of 4–5 km. The exact cumulative offset is uncertain as these markers may be much younger than the fault, but the lack of obvious geologic offsets and low geologic and current slip rates (0.35 mm/yr and 1.2 mm/yr, respectively) support the interpretation that this fault is immature (Ren et al., 2022; Zhu et al., 2021). The 2021 Maduo earthquake surface rupture is composed of many discontinuous segments, but most are sub-parallel (e.g., Li et al., 2022a) and line up along strike such that the overall trace of the rupture is conspicuously linear. This pattern is disrupted by a bend near its eastern end. There is also a secondary fault south of the eastern end of the main strand (Figure 4.2a). Field surveys measured left-lateral offsets mostly of $<$2 m and up to a maximum of 3.6 m (Pan et al., 2022; Ren et al., 2022; Yuan et al., 2022). There are two $>$20 km long surface rupture gaps around complex areas and where there are soft sediments (see gaps in field measurements in Figure 4.4b and Yuan et al., 2022).

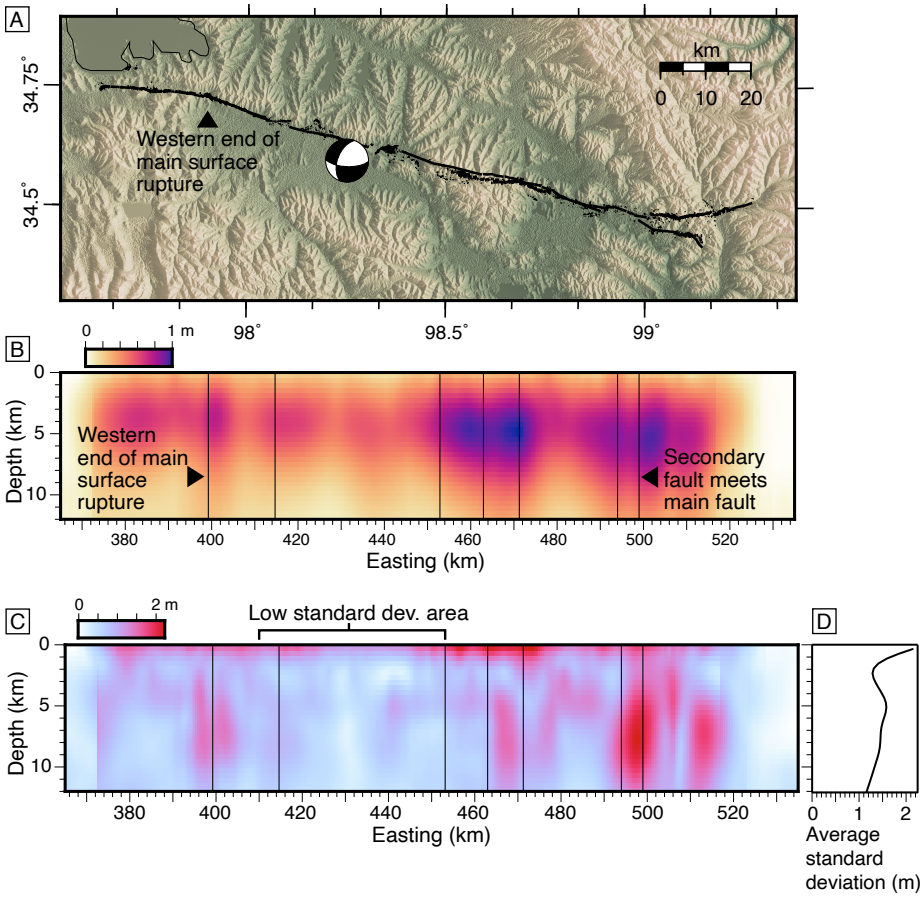


Figure 4.2: A) Surface rupture of the 2021 $M_w$ 7.4 Maduo earthquake (Liu et al., 2022a; Ren et al., 2022). B) Summed and normalized main fault slip distribution from 13 slip models (see (Table 4.1), geographically aligned with map in A), showing areas of high and low model slip. Models were interpolated and oversampled so they have the same raster grid (see Appendix 4.9.1). Vertical lines denote major bends in fault trace as mapped from SAR pixel displacements. C) Standard deviation of the 12 slip models as a function of depth and easting. D) Average standard deviation as a function of depth.

We have compiled thirteen published InSAR-derived coseismic slip models of the 2021 Maduo earthquake (Figure 4.3; details in Table 4.1). We compare the main fault between models. Not all models included a segment for the secondary fault south of the eastern end (Figure 4.2a) and differences in segmentation between models is shown in Figure 4.3: some have a very detailed main fault geometry (>10 segments) while others are much simpler, with ∼3 segments. Slip magnitudes vary significantly between models but slip is mainly left-lateral in all of them. The normalized slip profiles are in Figure 4.4a. Also plotted in Figure 4.4a are the SSD values, which range from 0% to 88% and have a bimodal distribution, with four models having a very low (<20%) SSD and four models having a much higher value of 60–80% (Figure 4.4a).

Untangling the myriad of combinations of parameters and procedures chosen for each model is challenging, particularly since they are not always disclosed. Still, some modeling choices that are thought to impact SSD can easily be explored. Near-fault decorrelation of InSAR data is suggested as a source of the systematic SSD (Marchandon et al., 2021; Xu et al., 2016b), and 5 of the 13 models include horizontal pixel displacements from SAR azimuth and range displacements and/or optical image correlation to better resolve shallow slip (Table 4.9.1). Such pixel displacements can also capture north-south-oriented deformation which InSAR is insensitive to. However, the amount of smoothing done when processing the displacements may affect SSD, as this can result in an artificially gradual near-fault offset. Some authors also choose to remove some SAR pixel displacement data within hundreds of meters to kilometers from the fault where inelastic deformation is expected, as the models can only resolve elastic deformation. Many authors also use the pixel displacements to help constrain the fault geometry, as this has been suggested to improve results (e.g., Luo and Wang, 2022; Xu et al., 2016b). However, Figure 4.4a demonstrates that inversions that exploit near-fault pixel displacements have as wide a range of SSDs (0–81%) as those that only invert InSAR data (0–79%), without the anticipated bias towards having more shallow model slip (Gombert et al., 2018; Marchandon et al., 2021; Xu et al., 2016b). Marchandon et al. (2021) demonstrated that wider near-fault displacement map data gaps can induce a SSD, but of the three models that use only InSAR data, the lowest estimate of SSD (0%) is from the model that has the widest fault zone data gap (based on visual comparison) and the fewest InSAR data points (∼2000 per interferogram; Xu et al., 2021), while larger estimates of 69–79% are derived from models with smaller data gaps and that use more data points (∼3000–6000 per interferogram) (Table 4.1; Zhao et al., 2022b; Fang et al., 2022). Of the models constrained also by SAR range and azimuth displacements, Yue et al. (2022) yield the outlier SSD value of 0%, and their near-field data

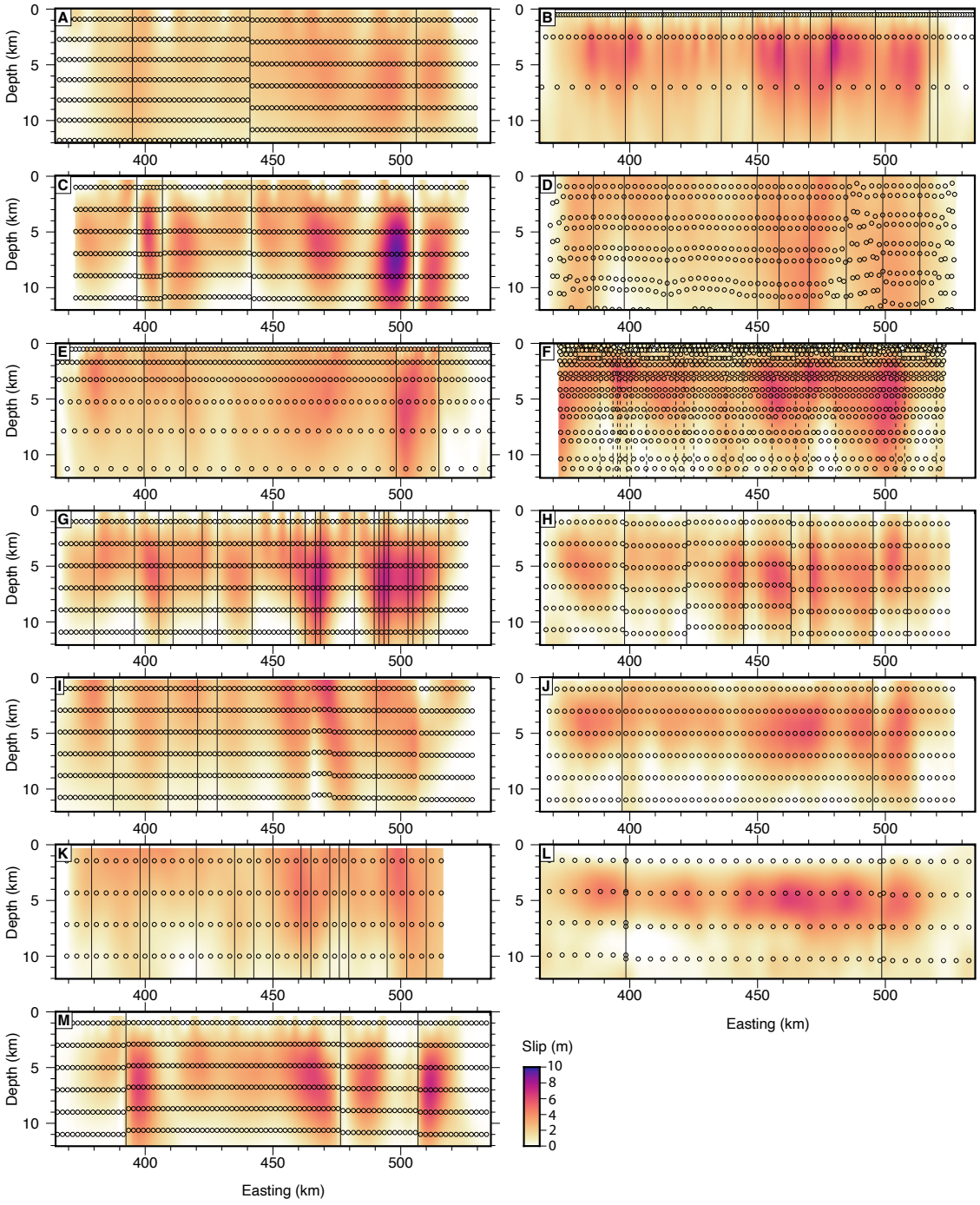


Figure 4.3: Interpolated and resampled geodetic slip models of the 2021 Maduo earthquake (main fault only). Circles mark center points of each slip patch and their fill color corresponds to the model slip in that patch. Vertical lines separate model fault segments. a) Chen et al. (2021) b) Fang et al. (2022) c) Guo et al. (2021) d) He et al. (2022) e) Jin and Fialko (2021) f) Liu et al. (2022a) g) Wang et al. (2022a) h) Wei et al. (2022) i) Xu et al. (2021) j) Xu et al. (2023) k) Yue et al. (2022) l) Zhang et al. (2022) m) Zhao et al. (2022b).

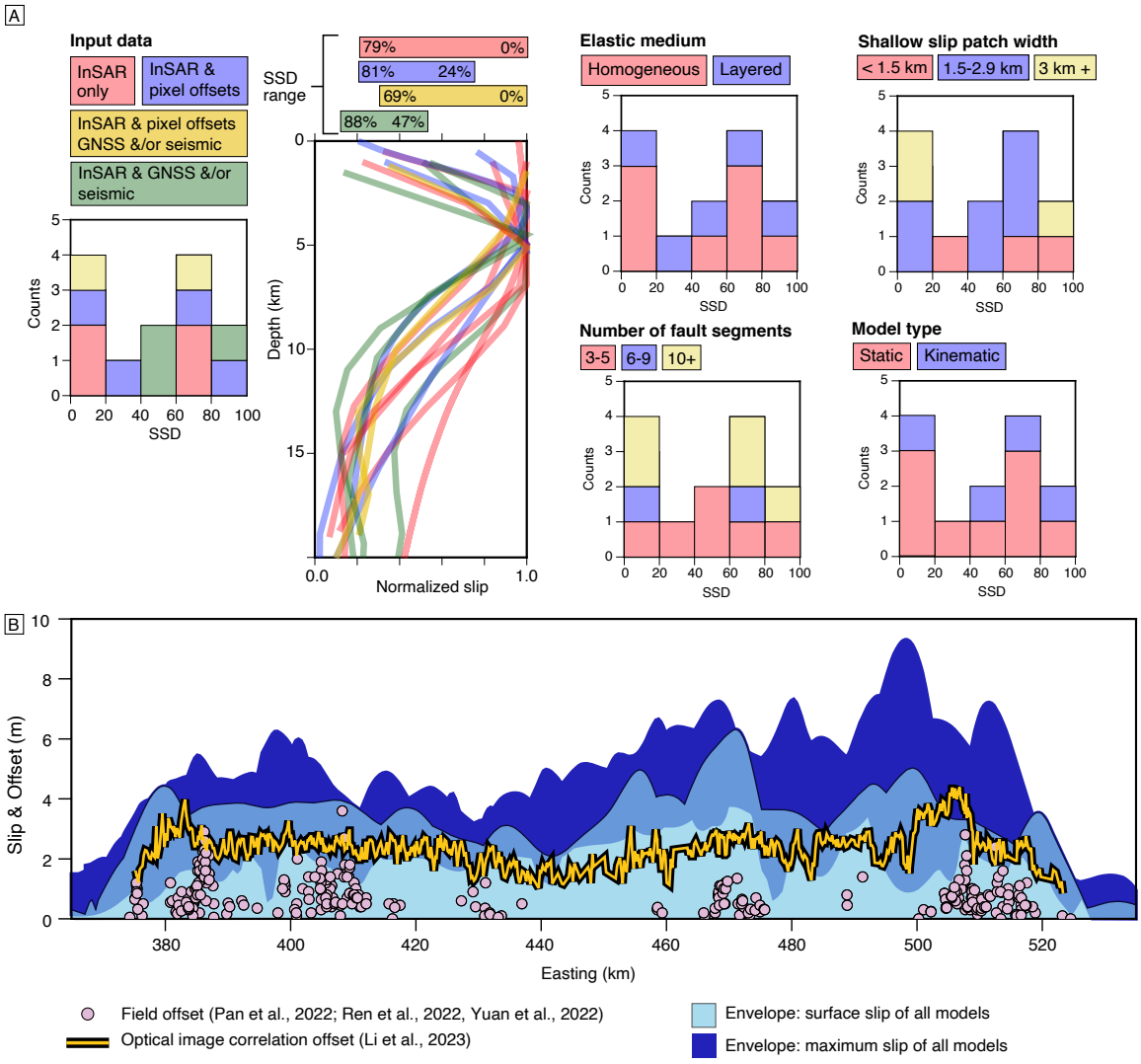


Figure 4.4: A) Normalized slip profiles of thirteen geodetic models of the 2021 Maduo earthquake (center), colored according to input data type (see figure legend) and histograms showing modeled SSD values as a function of the data types used (left) and other modeling choices (right). B) Range of shallowest (light blue transparent envelope) and maximum (dark blue envelope) slip vs. easting amongst the thirteen main fault slip models, overlain by main fault surface offsets measured in the field (pink circles) and estimated by profiling Sentinel-2 optical image correlation displacements (yellow line; from Li et al., 2022a).

sampling (4 km spacing) is sparser than most other models. For example, the 250 m InSAR data sampling nearest to the fault used by Jin and Fialko (2021) resulted in 21% SSD, although they masked points within 2 km of the fault to avoid issues caused by inelastic deformation. The SSD in Jin and Fialko (2021) may have been influenced by the visibly smoother coseismic displacements that are resolved by the greater sampling rate near the fault. The models that jointly invert InSAR and GNSS and/or seismic data have a narrower, although still significant SSD range of 47–88% (Figure 4.4a). While choosing a layered elastic model over a homogeneous halfspace may reduce the SSD in a controlled setting where all other parameters are the same (e.g., Gombert et al., 2018; Marchandon et al., 2021), this does not result in systematically lower SSD when comparing independent models in our survey (Figure 4.4a). Similarly, neither slip patch size, geometric complexity of the modeled fault (i.e. the number of segments), near-fault data gap size, nor choice of regularization scheme (Laplacian or otherwise) appears to have a clear, systematic influence on SSD. Unfortunately, since there is no standardized way of quantifying the smoothing of model slip distributions (Jónsson et al., 2002), we found it impossible to assess this potential influence on SSD.

These model comparisons suggest that as well as the type and distribution of input data and the medium used in the inversion, other choices such as the data weighting, the inversion method, and the degree of model slip smoothing also impact SSD in a significant way. Collectively, combinations of these typical data and modeling choices cause SSD to vary more significantly than any particular factor does, and models that use multiple factors explored in this section that are meant to reduce SSD (e.g., using both SAR pixel displacements and a more detailed fault geometry) still do not bias models to a lower SSD value.

To visualize where significant variations between slip models occur, we first resampled and interpolated each model slip distribution to give them a consistent grid spacing and gradual transition between modeled slip values (Figure 4.3; see Appendix 4.9.1 for interpolation details). This in turn allowed us to map the standard deviation in slip of all models onto a regular grid of depth and easting (Figure 4.2c), given the mostly WNW-ESE-oriented fault segments. The standard deviation in model slip is especially high in the upper 1 km, consistent with the large range in SSD between models, and particularly around fault bends, implying sensitivity of model slip to the representation of the fault surface trace and its segmentation. There is a reduction in standard deviation at $\sim$2 km depth, indicating relative consistency between models here (Figure 4.2d). At depths greater than 2 km, the standard deviation is high around bends and other geometric complexities such as

where the secondary fault meets the main fault near the eastern end of the rupture (Figure 4.2c). As with at $<$1 km depths, this may be due to differences in how fault segmentation is represented in the models and whether or not model slip is constrained to vary smoothly across these boundaries.

As an additional constraint on how much slip reached the surface, we use fault trace-parallel surface offsets from Li et al. (2022a), measured from a displacement field derived from the correlation of Sentinel-2 panchromatic imagery (see Appendix section 4.9.2 for more details). These represent the total offset within an aperture of $\sim$1 km, therefore they account for distributed off-fault deformation as well as primary fault slip, but may also capture the elastic response of a steep decrease in slip in the very shallow ($<$ 1 km) crust, i.e. a slip gradient that is concentrated in a much shallower part of the crust than what is resolved in most InSAR models (Figure 4.3, Supporting Information Figure 4.10).

The distribution of optical image-derived fault offsets along strike lacks symmetry, with relatively low values west of the surface trace centerpoint and the greatest values near the eastern termination (Figure 4.4b). Most of these kilometer-aperture offsets are significantly greater than colocated offsets measured in the field, and many are equal to or greater than the local surface slip values derived by InSAR models (light blue envelope in Figure 4.4b). This suggests either that much of the SSD is caused by distributed slip in the shallow crust that is not captured by the InSAR models, or that the SSD is concentrated within the shallowest hundreds of meters of the crust. When comparing the optical image-derived fault offsets with modeled slip, we obtain DSSD values that range from -1 to 38%. The generally lower values suggest that distributed near fault surface slip may partly account for the modeled SSD. The range of DSSD between models is much narrower than that of SSD, since the maximum slip at depth is more consistent between InSAR models than surface slip is.

### 4.5.2 The 2022 $M_w$ 6.6 Menyuan Earthquake

The left-lateral $M_w$ 6.6 Menyuan earthquake occurred on 8 January 2022. It generated a $\sim$35 km-long rupture along the $\sim$1000 km-long Haiyuan fault system on the bend linking the Tuolaishan and Lenglongling fault segments (Figures 4.1, 4.5a), where it partially filled an apparent seismic gap between the 1927 $M$ 8 Gulang and 1932 $M$ 7.6 Changma earthquakes (Guo et al., 2019, 2020; Yuan et al., 2008; Xu et al., 2010). The Haiyuan fault system is a major strike-slip structure at the northeastern boundary of the Tibetan Plateau, separating it from the Gobi-Alxa platform (Figure 4.1). Its Holocene slip rate is 4.4 to

6.6 mm/yr (Jiang et al., 2017; Zheng et al., 2013) and its geodetic strain accumulation rate is ∼5 mm/yr (Huang et al., 2022b; Li et al., 2016; Ou et al., 2022). Multiple offset geologic units near the 2022 rupture suggest that the cumulative offset of this section is closer to 14 km (Burchfiel et al., 1991), making this a relatively immature section of the Haiyuan fault system. However, this segment still has greater slip rates, cumulative offset and more developed topography than the Jiangcuo fault which suggests that the 2022 Menyuan earthquake occurred on a more mature fault than the 2021 Maduo earthquake.

The 2022 earthquake surface rupture has a ∼30 km-long and relatively straight main strand (Figure 4.5). West of its western termination, an additional ∼5 km-long segment also ruptured: they are separated by a ∼3 km-wide left-step. Offsets measured in the field reach 3 m and are predominantly left-lateral (Niu et al., 2023).

We have compiled ten published InSAR-derived slip models of the 2022 Menyuan earthquake (Figure 4.6; Table 4.9.1). We compare the main fault segments (some models had a secondary fault for the smaller fault south of the step). The model geometries were fairly simple due to the relatively straight rupture: 4 main fault models consist of a single segment and the maximum number of main fault segments is 4 (Figure 4.6). Their SSD values range from 0% to 51% (Figure 4.7a). Similar to the 2021 Maduo earthquake, incorporation of larger slip patch sizes, a more complex fault trace, or a layered elastic half space do not systematically reduce SSD. However, the three models that use SAR displacements in the inversion have a SSD <=25%, and the models that only invert InSAR data have a SSD that ranges from 19 to 49% (Figure 4.7a). Only some studies that inverted SAR range displacements masked data from near the fault to remove any signal that may be inelastic and which elastic models cannot solve for. This may partly explain the range in SSD; for example, the Han et al. (2023b) model has a data gap within 1 km of the fault trace has and a SSD of 0%, whereas the Luo and Wang (2022) model has no data gap and 22% SSD. The models that jointly invert InSAR and seismic and/or GNSS data range from 33 to 51%. However, it is not necessarily the case that the inclusion of these data result in greater SSD than InSAR-only inversions; for example, the InSAR-only inversion by Huang et al. (2022a) resulted in a SSD of 45% while their joint inversion with accelerogram data resulted in a SSD of 33% (Table 4.1). The standard deviation of modeled slip in the shallowest 1 km is high yet not as uniformly so as for the 2021 Maduo earthquake, being conspicuously high near the bend on the main segment (Figure 4.5c). The average standard deviation of all slip models is lower between 1 and 2 km, similar to results from the 2021 Maduo earthquake, then increases between 2 and 4 km due to model variability around the maximum slip area (which is also near the fault bend) and near the eastern

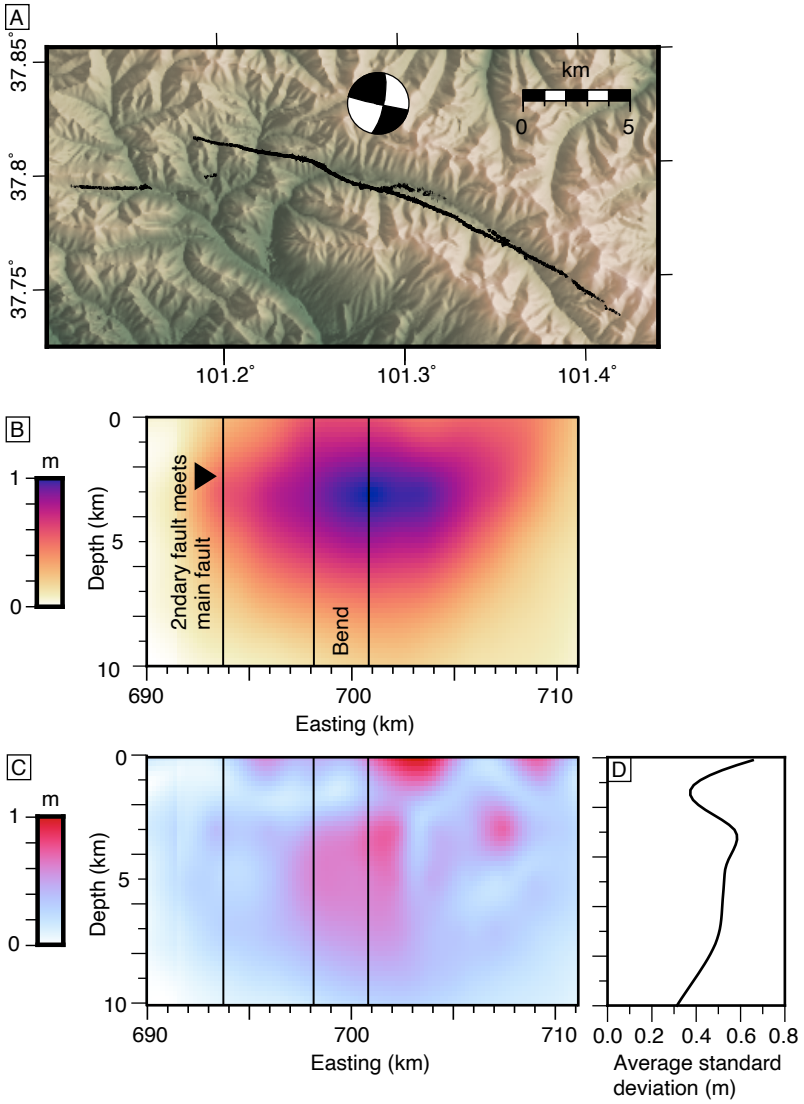


Figure 4.5: A) Surface rupture of the 2022 $M_w$ 6.6 Menyuan earthquake (Niu et al., 2023). B) Summed and normalized map of ten main fault slip models (see Table 4.1) showing high and low slip areas, geographically aligned with map in A). Vertical lines denote major bends in the fault trace as mapped with SAR pixel displacements. C) Standard deviation of the ten slip models as a function of depth and easting. D) Average standard deviation as a function of depth.

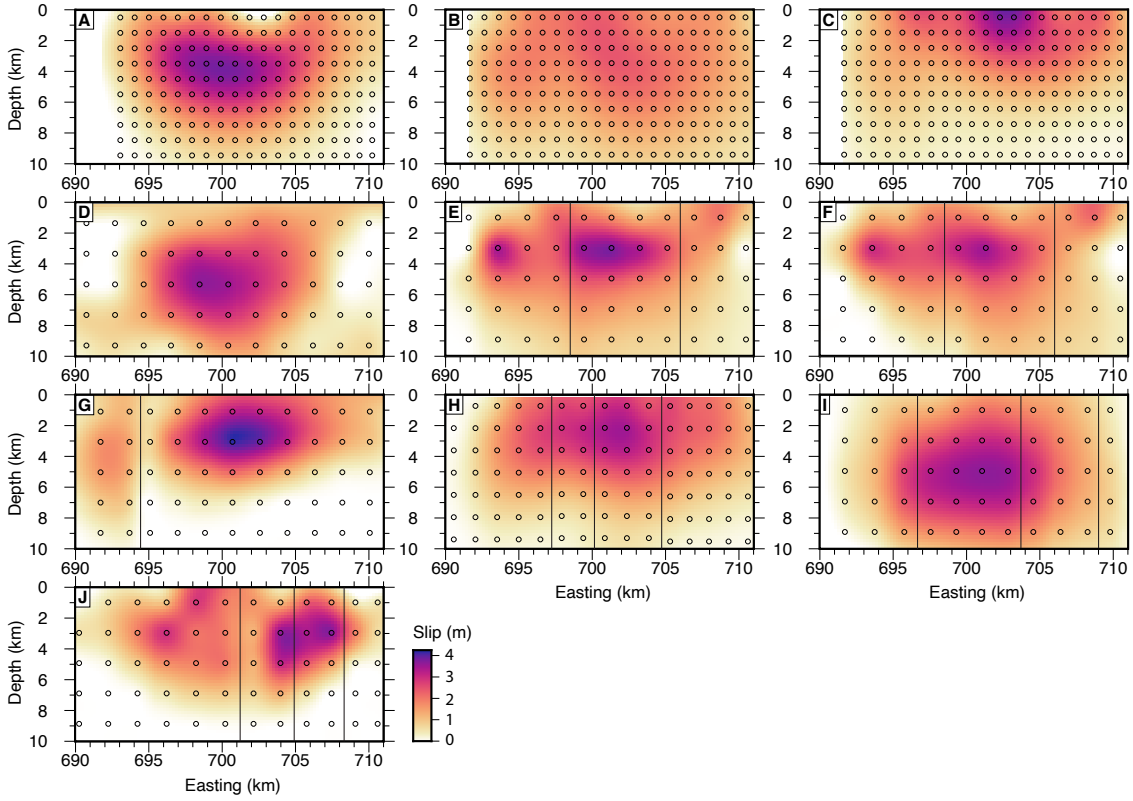


Figure 4.6: Interpolated and resampled geodetic slip models of the 2022 Menyuan earthquake (main fault only). Circles mark center points of each slip patch and their fill color corresponds to the model slip in that patch. Vertical lines separate model fault segments. a) Guo et al. (2022) b) Han et al. (2023b) (InSAR only) c) Han et al. (2023b) (joint inversion: InSAR and E-W lateral deformation from pixel offsets) d) He et al. (2023) e) Huang et al. (2022a) (InSAR only) f) Huang et al. (2022a) (joint inversion: InSAR and accelerogram data) g) Lü et al. (2022) h) Luo and Wang (2022) i) Yang et al. (2022) j) Zhang et al. (2023).

rupture termination (Figure 4.5d).

Han et al. (2023b) measured fault trace-parallel surface offsets within a ∼kilometer-wide aperture, from fault-perpendicular profiles of the horizontal displacement field as calculated from GaoFen-2 and GaoFen-7 panchromatic imagery. Within this aperture, these offsets account for both on- and off-fault deformation. The offsets have a fairly symmetric shape along strike and reach 4 m near the center of the rupture (Figure 4.7b). In many locations, peaks in offset measured in the field by Niu et al. (2023) and (Yuan et al., 2022) are more than 50% of the profile offsets measured from the GaoFen-2/7-derived displacement field, and a few field offsets are almost identical to nearby profile offsets, suggesting that surface deformation was fairly localized in some areas (Figure 4.7b; Dolan and Haravitch, 2014; Milliner et al., 2015). The offsets measured from the GaoFen-2/7 displacement field

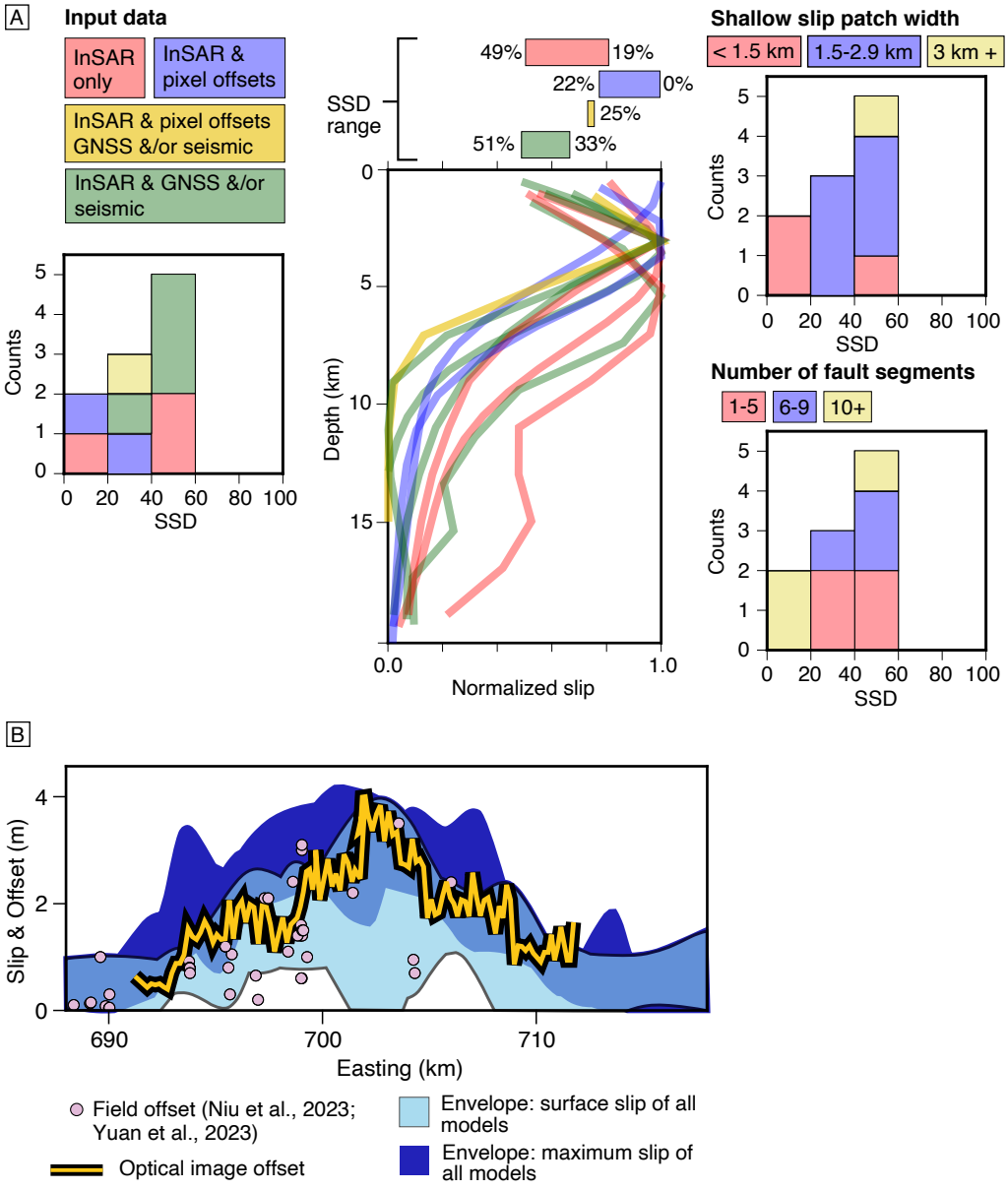


Figure 4.7: A) Normalized slip profiles of ten main fault geodetic models of the 2022 Menyuan earthquake (center), colored according to input data type (see figure legend), and histograms showing modeled SSD values as a function of the data types inverted for (left) and other modeling choices (right). B) Range of shallowest (light blue transparent envelope) and maximum (dark blue envelope) slip vs. easting amongst the ten slip models, overlain by main fault surface offsets measured in the field (pink circles) and estimated by profiling GaoFen-2/7 optical image correlation displacements (yellow line; from Han et al., 2023b).

are similar to the maximum modeled surface slip from the ten InSAR studies, although this model is an outlier with most other models yielding smaller surface slip than our profiled surface offsets. Our DSSD values range from -25% to 9%, suggesting that near fault surface displacements (or a steep tapering of slip in the very shallow crust; Supporting Information Figure 4.10) account for SSD and are greater than the maximum modeled slip.

### 4.5.3 Summary

Coseismic slip models derived from InSAR and other geodetic data are often used to interpret what proportion of slip at depth reaches the surface (Fialko et al., 2005; Pousse-Beltran et al., 2020; Wang et al., 2020), but thirteen slip models of the Maduo earthquake yield a large range of SSD (0–88%) without a clear peak value, while half of the ten Menyuan earthquake slip models have an SSD of 40–51% and the rest are distributed between 0–33%. For both earthquakes, the standard deviation between models is high in the upper 1 km, in high slip areas, and near fault segment boundaries. Of the model parameterization choices analyzed, there is no single one that affects SSD above all others for the 2021 Maduo earthquake but 2022 Menyuan earthquake models tended to have lower SSDs if they inverted near-fault displacements, possibly due to its simpler fault trace. Also, the joint inversions of InSAR, GNSS and/or seismic data are in the higher SSD range; however, for any input data category, the range in SSD is still high. Interestingly, we observe no systematic decrease in SSD with decreasing near-fault data gap size, in models that used a more complex (and perhaps more accurate) modeled fault, or in those which embed those faults within a layered half space (Figures 4.4a,4.7a). The large range in SSD despite the use of sometimes multiple SSD-reducing parameters cautions that inferring the structural maturity of a fault or its susceptibility to SSD (e.g., Li et al., 2020b) from modeled slip distributions must be done with care, because of the non-uniqueness of models, how vastly different near-surface slip distributions are depending on the combination of model parameterization choices, and the challenge in reproducing near-fault displacements measured from optical image or SAR pixel correlation using elastic dislocation models (Figure 4.4,4.7, Supporting Information Figure 4.10).

## 4.6 Surface Slip Comparison of Ten Tibetan Plateau Earthquakes

In this section, we compare InSAR models and surface offsets (when available) of ten previously-studied earthquakes that occurred on well-characterized faults from across the Tibetan Plateau (Figure 4.1). The causative faults range from very immature (negligible cumulative offsets and slip rates) to very mature (tens of kilometers in cumulative offsets and slip rates of several millimeters per year), allowing for the qualitative assessment of the influence of fault maturity on SSD and distributed surface deformation. As mentioned in Section 4.3, we have reviewed geological and geomorphic offsets reported in the literature, to ensure that we take the closest possible cumulative offset to the earthquake rupture as our principal maturity proxy. We also consider Holocene and geodetic slip rates, which are well-determined for most of the faults in this study. Furthermore, whereas most previous fault maturity and SSD studies focus on earthquakes greater than $M_w$ 7 (Dolan and Haravitch, 2014; Manighetti et al., 2021; Perrin et al., 2016), we include in our study six earthquakes smaller than $M_w$ 7, allowing us to assess relations between SSD and earthquake magnitude.

The ten earthquakes include the 2021 Maduo and 2022 Menyuan earthquakes described in the previous section. The remaining eight earthquakes and the data and InSAR models we have compiled for them are described below. For each earthquake, we calculate SSD values for one to thirteen InSAR-derived models. For surface-rupturing earthquakes, we also measured surface offsets using our own standardized profiling procedure (as described in Appendix 4.9.2), where SAR or optical image displacement fields were available, or we use already-published offsets measured in a similar way (6 earthquakes: 2001 Kunlun, 2010 Yushu, 2014 Yutian, 2015 Murghab, 2021 Maduo and 2022 Menyuan earthquakes). We normalize the surface offsets to the local maximum slip values of each InSAR model to assess the validity of the modeled SSD. This value provides information on the amount of distributed surface deformation and/or near-fault inelastic deformation.

### 4.6.1 Measurements and Models of Coseismic Slip

**The November 8 1997 $M_w$ 7.5 Manyi earthquake** ruptured a ∼185 km-long segment of the ∼385 km-long Manyi fault in north-central Tibet (Figure 4.1; Ren and Zhang, 2019). The Manyi fault is itself part of a larger, ∼560 km-long fault system (Manighetti et al., 2021). The Manyi fault is a reactivated segment of the ancient Jinsha suture, which bounds

the Bayan Har block in the north and the Qangtang block in the south, and has been interpreted as a splay off of the western end of the Kunlun fault system (Figure 4.1; Tapponnier and Molnar, 1977). The 1997 earthquake was mostly left-lateral, with coseismic offsets measured in the field by Xu (1999) reaching 4.5 m and offsets to landforms mapped from high-resolution WorldView and SPOT-5 imagery reaching 7.5 m (Ren and Zhang, 2019). We estimate a local cumulative offset of 70–80 km based on offset geologic units (Li et al., 2019a). Geodetic slip rate estimates range from 3–6 mm/yr (Bell et al., 2011; Zhao et al., 2022a). By either measure, this is one of the more mature faults in this study. We calculate a SSD of 19% from an InSAR-only slip model by Funning et al. (2007) based on their inversion of three adjacent, descending track ESA European Remote Sensing (ERS-2) interferograms (Figure 4.8a,d,g, Table 4.1). The model incorporates eleven adjoining planar segments, each with a slip patch dimension of 4 km. Funning et al. (2007) used SAR azimuth displacements to constrain the surface trace of the model fault, which was fixed in the inversion, but did not invert for these SAR data. We were unable to acquire these SAR pixel displacements ourselves and therefore do not estimate DSSD for this event.

**The November 14 2001 $M_w$ 7.8 Kunlun (Kokoxili) earthquake** occurred along a $\sim$450 km-long segment of the $\sim$1700 km-long Kunlun fault in north-central Tibet (Figure 4.1; Klinger et al., 2005; Manighetti et al., 2021). The rupture initiated on a splay in the western horsetail system of the Kunlun fault system, before migrating eastward and transferring onto one of the principal Kunlun fault segments where supershear speeds were attained (Supporting Information Figure 4.11; Bouchon and Vallée, 2003; Lasserre et al., 2005). Coseismic landform offsets measured from 1 m-resolution Ikonos imagery reached 7.6 m (Xu et al., 2006). The maximum cumulative offset estimate for the Kunlun fault of 100 km lies east of the 2001 rupture, and an estimate much closer to it based on offset geologic units yields a value of 45–50 km (Fu and Awata, 2007). Geologic and geodetic slip rate estimates range from 10–12 mm/yr (Harkins et al., 2010; Kirby et al., 2007; Kirby and Harkins, 2013; Zhao et al., 2022a; Zheng et al., 2017). By either proxy, the Kunlun fault is one of the more mature faults in this study. Lasserre et al. (2005); Wan et al. (2008) inverted descending track ERS-1 and ERS-2 data to obtain the slip distribution and the SSD estimated from both InSAR-only models is 0% (Table 4.1). We measured surface offsets from optical image correlation of SPOT-1 and SPOT-4 data by Rosu et al. (2015). Our DSSD values are -9% and 13% for the Wan et al. (2008) and Lasserre et al. (2005) models respectively, meaning that the near-fault offsets are greater than the maximum modeled slip in Wan et al. (2008) and a bit less than the maximum slip in Lasserre et al. (2005) (Figure 4.8a,b).

**The April 14 2010 $M_w$ 6.9 Yushu earthquake** ruptured a ∼60 km-long section of the Yushu fault segment of the ∼400 km-long NW-SE-oriented Ganzi-Yushu fault in the eastern Tibetan Plateau (Figures 4.1, Supporting Information Figure 4.11). The mapped surface rupture is only about 37 km long (Guo et al., 2012; Manighetti et al., 2021), significantly shorter than the >60 km-long subsurface rupture length inferred from geodetic studies (Supporting Information Figure 4.11). The Ganzi-Yushu fault connects with the major Xianshuihe-Xiaojiang fault system to the southeast and forms the strike-slip boundary between the Bayan Har and and Qiangtang blocks (Wang et al., 2008). Coseismic offsets measured in the field by Guo et al. (2012) reach 2.1 m. Wang et al. (2008) estimate a cumulative offset of the Yushu fault segment of ∼25 km based on an offset river channel. Slip on this fault started at 13 Ma and geologic slip rate estimates range from 7–10 mm/yr (Wang et al., 2009b). This marks the fault as of intermediate maturity in this study. We estimate SSD from two published models that inverted downsampled ALOS (PALSAR) and ENVISAT (ASAR) interferograms; one of them (Li et al., 2011) inverted ascending and descending track data jointly with teleseismic waveforms, while Jiang et al. (2013) inverted ascending track data only (Table 4.1). We obtain SSD values of 35% and 6% from these two models, respectively (Figure 4.8a,d,g). We measured surface offsets from ALOS PALSAR pixel displacements processed by Liu et al. (2011). Our DSSD values are 45% for both models, which therefore both appear to have overestimated shallow slip (Figure 4.8b,e,h). The SSD difference between the two models disappeared with the DSSD estimation since the maximum slip is similar.

**The February 12 2014 $M_w$ 6.9 Yutian earthquake** ruptured for ∼37 km along the South Xor Kol and Ashikule faults in northwestern Tibet (Supporting Information Figure 4.11). These are parallel fault splays connected by a relay fault, near the southwestern end of the ∼1600 km-long Altyn Tagh fault system (ATFS), where the ATFS converges with the Karakax fault system that continues to the southwest (Figure 4.1). The ATFS and the Karakax fault system form the northwestern boundary between the Tibetan Plateau and Tarim basin. Coseismic offsets measured in the field by Li et al. (2016) reach 1 m and we estimate a cumulative offset of ∼18 km based on offset geologic units immediately east of the 2014 surface rupture (Li et al., 2019a), suggesting an intermediate maturity relative to the other faults in this study. There are no published geodetic or long-term slip rates on either the South Xor Kol or Ashikule fault. We estimate SSD from a single slip model (from Li et al., 2020a), constrained by TANDEM-X interferograms, SAR range displacements and SPOT-6/7 optical image correlation displacements, obtaining a value of 45% (Figure 4.8a,g). We measured surface offsets from the correlation of SPOT-6 images, processed by

Li et al. (2020a) (Table 4.1). This yields a DSSD value of 62%, suggesting that the InSAR model overestimated the surface slip (Figure 4.8b,h).

**The December 7 2015 $M_w$ 7.2 Murghab (Sarez) earthquake** broke a ∼48 km-long section of the ∼200 km-long Sarez-Karakul fault in the central Pamir mountains of Tajikistan, at the far western end of the Tibetan Plateau (Figures 4.1, Supporting Information Figure 4.11). This area is characterized by a network of conjugate strike-slip faults, including the NE–SW-oriented, sinistral transtensional Sarez-Karakul fault. This fault cuts across a number of approximately E–W-oriented terrane-bounding sutures and thrust faults (Supporting Information Figure 4.11; Elliott et al., 2020). Coseismic offsets measured in the field by Metzger et al. (2017) reach 2 m. Zubovich et al. (2022) infers that the current slip rate on this fault ranges from 3–4 mm/yr. We do not find obvious geologic or geomorphic offsets, suggesting that this is a very immature section of the fault. We calculate normalized slip profiles from three geodetic slip models that used either Sentinel-1 interferograms, Sentinel-1 SAR pixel displacements and GNSS measurements (Metzger et al., 2017) or Sentinel-1 and ALOS-2 interferograms (Jin et al., 2022; Sangha et al., 2017) as input data. This yields SSD values that range from 0 to 20%.

**The November 16 2016 $M_w$ 6.6 Aketao earthquake** ruptured a ∼45 km-long section of the ∼80 km-long Muji fault in the northern Pamir mountains of China, at the far western end of the Tibetan Plateau (Figures 4.1, Supporting Information Figure 4.11). Field surveys and InSAR interferograms suggest that this was a left-lateral, buried rupture (Chen et al., 2016; Feng et al., 2017). The Muji fault seems to be a secondary structure off of the Main Pamir Thrust, which is the major boundary between the Pamir and Tien Shan. We estimate a cumulative offset of 30–35 km based on offset geologic units (Li et al., 2019b). Slip on this fault started at ∼7–8 Ma (Li et al., 2019b) and geologic slip rate estimates range from 6–9 mm/yr (Deng et al., 2020; Li et al., 2019b). We estimate SSD from four models that used either Sentinel-1 interferograms (Feng et al., 2017), Sentinel-1 and ALOS-2 interferograms (Bie et al., 2018; He et al., 2018), or Sentinel-1 interferograms and teleseismic data (Zhang et al., 2019) as input data, obtaining values that range from 28 to 98% (Table 4.1).

**The August 8 2017 $M_w$ 6.5 Jiuzhaigou earthquake** occurred along a ∼25 km-long buried section of the Huya fault in the far eastern Tibetan Plateau (Zhao et al., 2018). This left-lateral fault is located in a complex network of strike-slip and thrust faults near the edge of the Bayan-Har block where the Kunlun fault system approaches the eastern edge of the Tibetan Plateau (Figures 4.1, Supporting Information Figure 4.11). The fault network accommodates the E–W convergence of the east-central Tibetan Plateau with rigid material beneath the Sichuan basin and South China block (Figure 4.1; Avouac and Tapponnier,

1993). We estimate a cumulative offset of 3.5–4 km based on an offset river (Li et al., 2019a), and suggest that this fault is relatively immature. We estimate SSD from four geodetic slip models that inverted Sentinel-1 and RADARSAT-2 interferograms and GNSS data (Hong et al., 2018; Li et al., 2020b), Sentinel-1 interferograms and seismic data (Zheng et al., 2020) or Sentinel-1 interferograms alone (Tang et al., 2021). We obtain SSD values that range from 45 to 72%.

**The September 5 2022 $M_w$ 6.6 Luding earthquake** ruptured a ∼35 km-long buried section of the Moxi segment of the ∼320 km-long left-lateral Xianshuihe-Xiaojiang fault system in the northeastern Tibetan Plateau. The rupture is located in the eastern part of the fault system where its orientation rotates from NW-SE to N-S (Figure 4.1). The southern end of the rupture coincides with the junction between the Xianshuihe-Xiaojiang fault and the Longmen Shan Thrust belt, and where the Xianshuihe-Xiaojiang fault system splits into multiple splays (Figure Supporting Information 4.11). This corresponds to the southeastern corner of the Bayan-Har block, at the boundary between the Tibetan Plateau and stronger South China block. Yan and Lin (2015) estimate a cumulative offset of ∼60 km based on geologic and geomorphic features. Geologic slip rate estimates for this fault range from 10–13 mm/yr (Bai et al., 2021) and geodetic slip rate estimates range from 16–20 mm/yr (Qiao and Zhou, 2021). We estimate SSD from two models that either inverted Sentinel-1 and ALOS-2 interferograms (Han et al., 2023a) or jointly inverted Sentinel-1, GNSS and strong motion seismic data (Li et al., 2022b), obtaining values that range from 48 to 100% (Figure 4.8, Table 4.1).

### 4.6.2 Summary

Similar to the 2021 Maduo earthquake, InSAR modeling of the 2016 Aketao and 2022 Luding earthquakes yields a range of SSD that exceeds 50%, demonstrating the non-uniqueness of slip models particularly within the shallowest portion of the fault.

We find no clear correlations between SSD and cumulative offset, nor between DSSD and cumulative offset (Figure 4.8a,b). Likewise, there is no clear correlation between SSD, DSSD and Holocene slip rate (Figure 4.8d,e). This may simply reflect the large uncertainty in shallow model slip that is evident from the wide range of SSD values obtained for some of the earthquakes. We also acknowledge that there may be large uncertainties in cumulative offset, particularly for geomorphic markers such as rivers or younger sedimentary units that might postdate the initiation of the fault. Similarly, for some faults there is much debate on slip initiation ages that can result in very different slip rate estimates (e.g., Dai

et al., 2017, and references therein). However, the lack of any clear correlations does at least suggest that cumulative slip and slip rate are not the dominant factors governing SSD and DSSD, and/or that other factors such as moment magnitude and near-surface geology may be just as important.

In general, SSD decreases with increasing magnitude, with proportionally more shallow slip in larger earthquakes than in smaller ones (Figure 4.8g, Antoine et al., 2023; Sethanant et al., 2023). There is a clear negative correlation between DSSD and magnitude for earthquakes equal or greater than $M_w$ 6.9, though interpretation is limited by the low number of DSSD data points (Figure 4.8h). In many cases, DSSD is less than the SSD estimate. However, rather than make up for SSD, the surface offset measured from the near-fault displacement field is less than modeled surface slip (i.e. DSSD $>$ SSD) for one model of the 2001 Kunlun earthquake, three models of the 2021 Maduo earthquake, and all models of the 2010 Yushu and 2014 Yutian earthquakes.

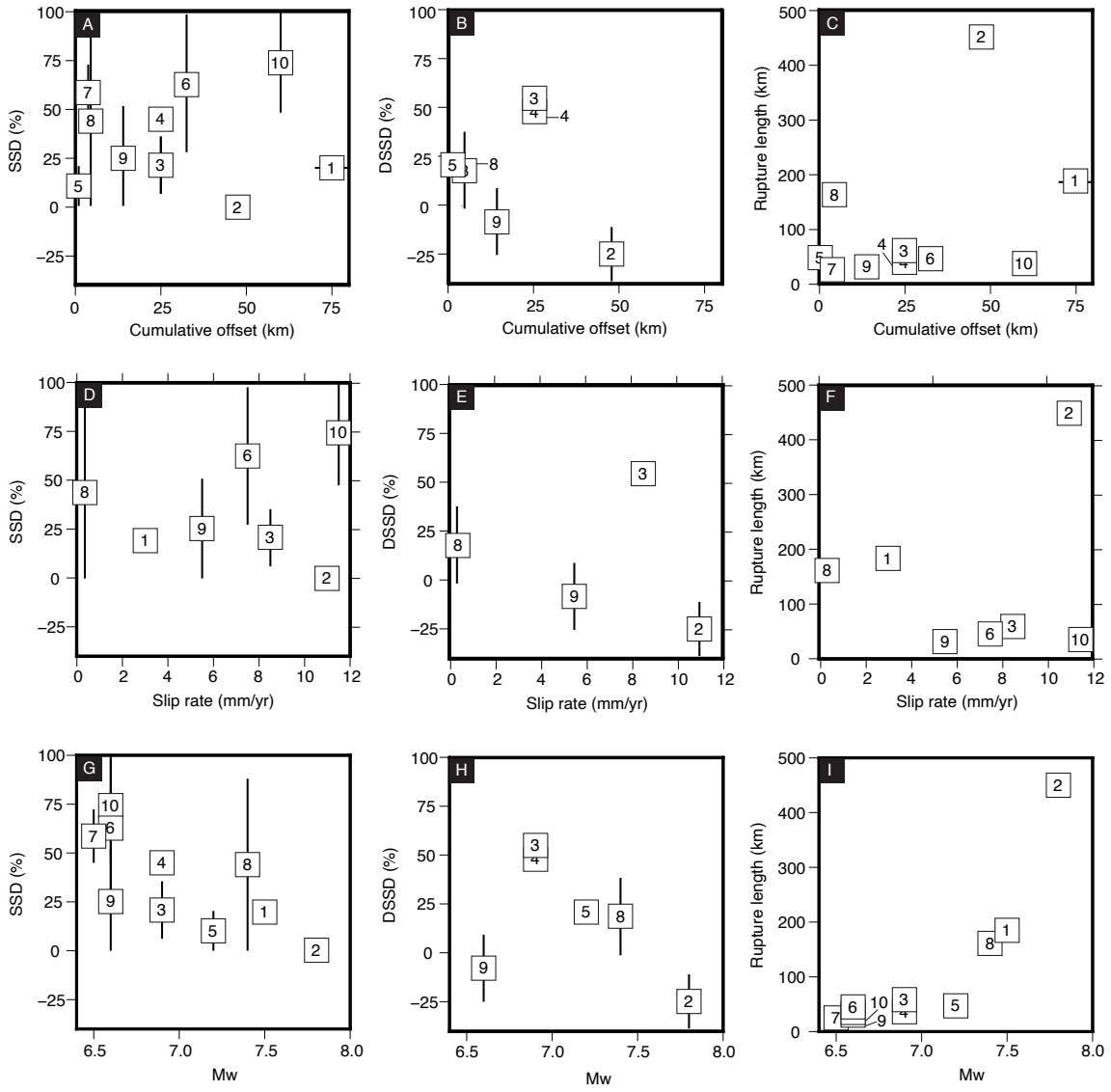


Figure 4.8: Scatter plots comparing shallow slip deficit (SSD), distributed shallow slip deficit (DSSD), and rupture length as a function of cumulative offset, geologic slip rate and moment magnitude. Data points are labelled by earthquake number as on Figure 4.1: 1) 1997 Manyi, 2) 2001 Kunlun, 3) 2010 Yushu, 4) 2014 Yutian, 5) 2015 Murghab, 6) 2016 Aketao, 7) 2017 Jiuzhaigou, 8) 2021 Maduo, 9) 2022 Menyuan, 10) 2022 Luding. Vertical bars represent the ranges of SSD and DSSD obtained from all available InSAR slip models. A) SSD, B) DSSD and C) rupture length as a function of cumulative offset. D) SSD, E) DSSD and F) rupture length as a function of geologic slip rate (geodetic slip rate for Manyi). See sections 4.5 and 4.6 for references. G) SSD, H) DSSD and I) rupture length as a function of magnitude.

## 4.7 Discussion

### 4.7.1 On the Reliability of Shallow Slip Deficit Estimates

Many InSAR studies of earthquakes calculate the shallow slip deficit, some using it to interpret the maturity of the causative fault (e.g., Dolan and Haravitch, 2014; Li et al., 2020b). However, our analysis shows that the SSD estimated from models of the same earthquake can vary by more than 50%, implying that it may be an unreliable metric (particularly when calculated from a single slip model, like in most studies) and a poor indication for the maturity of a fault. As previously mentioned, our goal is not to determine which models are superior as many modeling choices are subjective with different approaches equally justifiable. The variation between models may be greater in immature faults that have a higher density of bends, steps and secondary faults, since this is where we show model slip to vary the most (Figures 4.2c, 4.5c). Conversely, the variation between models may be lower in mature faults that have a simple geometry. However, this is difficult to assess with the models presented in this study because of the wide range in the number of available models per earthquake. It should therefore be noted that a smaller range in SSD does not mean that the SSD values are accurate. Furthermore, the standard deviation of models of the 2021 Maduo and 2022 Menyuan earthquakes show that models are the most consistent at a depth of $\sim$1–2 km (Figures 4.2d, 4.5d). High standard deviation areas are located within the upper 1 km of the crust and at the location of maximum slip, the exact depths used in SSD estimations.

Surprisingly, jointly inverting InSAR with SAR range displacements does not systematically yield lower SSD for the 2021 Maduo earthquake, and models constrained only by InSAR data span almost the full range of SSD estimates (Figure 4.4a). Controlled tests in which most inversion parameters are kept constant show that using near-fault pixel displacement data, increased near-fault sampling and using a layered elastic medium reduces SSD (Marchandon et al., 2021; Xu et al., 2016b), but those modeling choices do not seem significant when comparing completely independently modeled slip distributions (Figure 4.4a, 4.7a). In their modeling of the Menyuan earthquake, Han et al. (2023b) did eliminate SSD altogether (a reduction of 19%) when constraining the near-fault displacement with optical image correlation displacement field and InSAR instead of InSAR only. SSD values from joint inversions with seismic and/or GNSS data (both more sensitive to deeper slip than InSAR) are concentrated in the higher SSD range, but in their study of the Menyuan earthquake Huang et al. (2022a) found that jointly inverting InSAR and accelerogram data

decreased the SSD by 12%, despite seismic data being more sensitive to deeper slip. Therefore, the higher average SSD of these joint models may be misleading. In controlled tests, Gombert et al. (2018), Marchandon et al. (2021) and Xu et al. (2016b) found important reductions in SSD when using a heterogeneous rather than a homogenous elastic medium and when using near-field displacement fields as additional input data to InSAR. In contrast, Jin and Fialko (2021) and He et al. (2022) found that using a heterogeneous medium did not significantly change the model. The lack of systematic SSD reduction and large SSD range of the models that choose one or a combination of these parameters, particularly when comparing slip models of the same earthquake, suggests that other modeling choices have a larger impact on the slip distribution, such as the smoothing of near-field input data, the weighting of the datasets used in the inversion, the inversion method itself, the number of discrete model faults used to represent the earthquake, and the degree of slip smoothing across the model fault plane.

### 4.7.2 On the Scaling Relationship of Shallow Slip Deficit and Earthquake Magnitude

The negative correlation between SSD and magnitude supports the findings of Antoine et al. (2023) and Sethanant et al. (2023) that larger surface-rupturing earthquakes produce proportionally more surface slip than smaller ones (Figure 4.8g). However, our assessment of the 2021 Maduo and 2022 Menyuan earthquakes suggests that there may be a larger range of modeled SSD values for well-studied earthquakes (such as the 2019 Ridgecrest and 2013 Balochistan earthquakes) than many published SSD comparisons show, so the relationship between SSD and magnitude is not necessarily as straightforward as portrayed. Furthermore, differences between SSD and DSSD values suggest that the source of the SSD may vary between earthquakes, complicating the interpretation of this scaling relationship (Figure 4.8h). For instance, a positive DSSD value may mean that the slip deficit is real, caused either by distributed inelastic deformation during the interseismic cycle (i.e. accumulating little elastic strain) or near-surface velocity strengthening behavior impeding rupture (Fialko et al., 2005; Marone, 1998), or that modeling choices such as the degree of smoothing are affecting the maximum slip at depth. In certain cases such as for the 2022 Menyuan earthquake, modeled SSD can be completely explained by near-surface deformation, yielding a DSSD that is negative in some cases (Figure 4.8b), whether it be through widely distributed deformation or a narrow zone of inelastic (coseismic) deformation. Many of the fault-perpendicular profiles through optical image displacements of the

Menyuan earthquake do exhibit gradual offsets accommodated over a few hundred meters (Supporting Information Figure 4.10a; Han et al., 2023b). These could also be caused by a very near-surface reduction in slip, but elastic dislocation forward models show that this reduction would need to be extremely shallow ($<$0.3 km from the surface) for the gradual offset to be contained within a few hundred meters of the fault (Supporting Information Figure 4.10). However, for other events such as the 2010 Yushu and 2014 Yutian earthquakes, modeled surface slip exceeded the distributed surface offset measurement (DSSD $>$ SSD; Figure 4.8a,b). This may be due to model uncertainties and the small number of available models (two for Yushu, one for Yutian) resulting in a narrow range of SSD values. Of the thirteen 2021 Maduo earthquake models, two overestimated surface slip (DSSD $>$ SSD; Figure 4.8a,b). The scatter in the DSSD scatter plots may also be due to differences such as thick sedimentary material near the surface promoting velocity-strengthening behavior and/or distributed surface deformation, and variations in the depth of the hypocenter (e.g., Zhao et al., 2023; Zinke et al., 2014). Since DSSD is estimated by comparing measurements of true surface offset (with caveats related to aspects such as displacement field resolution and precision and the profile swath width) with maximum local modeled slip, and generally has a smaller range than SSD, DSSD may provide a better estimate of the slip deficit.

The negative correlation between SSD and magnitude may be a combination of two factors. Firstly, smaller magnitude earthquakes have smaller rupture areas and are thus less likely to rupture to the surface with more dependence on the hypocenter depth (Lauer et al., 2020; Sethanant et al., 2023; Yao and Yang, 2022). Secondly, the surface displacements generated in earthquakes that rupture over larger areas with greater surface slip may be better characterized by dislocations in a homogeneous elastic medium.

### 4.7.3 On the Importance of Fault Structural Maturity on Seismic Hazard in the Tibetan Plateau

While there may be a scaling relationship globally (Dolan and Haravitch, 2014), and while maturity may still have important implications for seismic hazard such as influencing the earthquake magnitude and slip distribution, a scaling relationship between cumulative offset and SSD or DSSD is not representative of the most important strike-slip earthquakes of the last few decades in the Tibetan Plateau. This is likely partly because cumulative offset measurements are challenging as they often rely on geomorphic features such as rivers and streams that may postdate fault incipience. More importantly, the variability in shal-

low (0–1 km) modeled slip in the 2021 Maduo and 2022 Menyuan earthquake, with no clear cause of the variability other than the myriad of possible combinations of modeling choices, cautions against drawing strong conclusions from near-surface slip distributions.

Similarly, while there may be a relationship between rupture length and area and cumulative offset globally (Manighetti et al., 2007), it is not apparent in the most important recent strike-slip earthquakes of the Tibetan Plateau (Figure 4.8c). Our results do not support the hypothesis that more mature faults generate longer ruptures, which stems from the idea that incipient faults are more segmented with softer, disconnected linkages, and that as faults mature, earthquakes weaken these segments barriers to produce hard-linked segments and eventually through-going faults (Manighetti et al., 2007). Instead, there may be other factors that explain the range of rupture lengths observed in the Tibetan Plateau earthquakes studied here. These earthquakes seem to fall in two distinct categories. In the first category, seven of the earthquakes were limited to rupture lengths of 25–60 km, yet the cumulative offsets of the faults that hosted them vary from near zero (the very immature Huya fault) to 60 km (the mature Moxi fault). In the second category, the Manyi, Kunlun and Maduo earthquakes each occurred on or close to major sutures in the central Tibetan Plateau and managed to grow laterally to rupture lengths of 161–450 km (Figures 4.1, 4.8i, Supporting Information Figure 4.11).

We consider this second category of earthquake first. The Manyi fault is located on the Jinsha suture at the southwestern boundary of the Bayan Har block, exhibits 70–80 km of cumulative offset, has a relatively low Holocene slip rate of 3–6 mm/yr and the 1997 Manyi rupture reached a length of 185 km (Bell et al., 2011; Li et al., 2019a; Ren and Zhang, 2019; Zhao et al., 2022a). Near the 2001 Kunlun rupture, the cumulative offset on the Kunlun suture (the northern margin of the Bayan Har block) is 45–50 km, and therefore 15–35 km less than faults hosting the 1997 Manyi and 2022 Luding earthquakes, yet the 2001 earthquake grew to a length of 450 km. The Kunlun fault system does have a high slip rate, at 10–12 mm/yr (Harkins et al., 2010; Kirby et al., 2007; Kirby and Harkins, 2013; Zhao et al., 2022a; Zheng et al., 2017). Finally, the 2021 Maduo earthquake occurred on a previously barely recognized intra-block fault dozens of kilometers south of the Kunlun suture, and sub-parallel to it. It only has 4–5 km of cumulative offset (Li et al., 2022a), a very low Holocene slip rate of 0.35 mm/yr–1.2 mm/yr (Ren et al., 2022; Zhu et al., 2021) and exhibits a high density of steps $>$1 km in width that is similar to other immature faults (Wesnousky, 1990), yet its surface rupture grew to a length of 160 km. That these three ruptures that are an order of magnitude longer than the other earthquakes are on or near and sub-parallel to major sutures in the central Tibetan Plateau — despite them

exhibiting important differences in maturity, geometric complexity, and involvement of intrablock and block-bounding faults — may have important implications for the likelihood of large-magnitude earthquakes and thus seismic hazard (Figure 4.8i; Wells and Coppersmith, 1994). Therefore there are other more important factors than structural maturity that allowed ruptures to grow laterally in the central Tibetan Plateau while limiting rupture size in other areas. The Bayan Har block (or Songpan Ganzi terrane) is a fold belt with a long history of N-S convergence resulting in many roughly E-W structures parallel to its northern boundary, the Kunlun suture (Figure 4.1; e.g., Yue et al., 2022). The 161 to 450 km-long 1997 Manyi, 2001 Kunlun and 2021 Maduo earthquakes occurred near the central part of the Kunlun and Jinsha sutures, away from major fault system junctions and plateau boundaries with protracted tectonic histories governed by the competition between outward extrusion of the Tibetan Plateau and the stronger, stable blocks surrounding it.

In contrast with the central Tibetan suture zones, the plateau margins exhibit more complex fault zones involving sets of faults and inherited structures at high angles from each other that may inhibit rupture growth (e.g., Elliott et al., 2020). For instance, the 35 km-long 2022 Luding earthquake occurred on a fault segment with more cumulative offset and a similar slip rate to that of the 450 km-long 2001 Kunlun earthquake, but was located in a complex fault network at the intersection of the Xianshuihe-Xiaojiang fault system and the Longmen Shan thrust belt, on the eastern margin of the Tibetan Plateau (Figure 4.1). It was bounded by seismic gaps and areas of geometric complexity: the western termination of the rupture is where the fault separates into different strands, and where estimated $M_W$ 6–7 earthquakes have happened regularly (Wen et al., 2008), while the eastern rupture termination is where the Xianshuihe-Xiaojiang fault splits into splays (Supporting Information Figure 4.11). Multiple ruptures have stopped at this location, suggesting that this is a long-term rupture propagation barrier (Wen et al., 2008). The 2014 Yutian, 2015 Murghab, 2016 Aketao, 2017 Jiuzhaigou and 2022 Menyuan earthquakes were short in length (25–48 km) and ruptured low to intermediate maturity faults. Similar to the 2022 Luding earthquake, they occurred near the boundaries of the Tibetan Plateau, where interactions between the outward extrusion of the weaker plateau against stronger stable bounding blocks resulted in complex interacting fault networks and inherited structures at very different angles from each other, acting as rupture barriers (Figure 4.1, Supporting Information Figure 4.11; e.g., Elliott et al., 2020). Many of these ruptures are also bounded by important geometric complexities such as bends, steps and the splitting of the fault into multiple segments (Supporting Information Figure 4.11). Similar to the long rupture earthquakes though, the 2010 Yushu earthquake occurred in the central Tibetan Plateau, on a structure of intermediate

maturity very near and sub-parallel to the Jinsha suture, yet the rupture is only 60 km long (Figure 4.1, Supporting Information Figure 4.11). However, its eastern and western rupture terminations coincide with major segment boundaries, and the eastern termination (where the Yushu and Dengke segments meet) coincides with the western termination of an 1896 event (Supporting Information Figure 4.11; Wang et al., 2008; Zhao et al., 2019). A cluster of historic earthquakes on the same fault east of the 2010 Yushu event may have had similar rupture lengths to the 2010 earthquake (Zhao et al., 2019).

This is not to say that long (>150 km) ruptures and large-magnitude ($M_w$ >7) strike-slip earthquakes are impossible on the faults mentioned in the previous paragraph (the instrumental and historical records attest to this; Niu et al., 2023; Wen et al., 2008), but longer ruptures may be more favorable in the central Tibetan Plateau where active faults and older pervasive geologic structures have similar and optimal orientations. Therefore, in these areas, even immature and intra-block faults may pose an elevated seismic hazard.

## 4.8 Conclusions

Persistent shallow slip deficits in geodetic models may be explained by a number of factors, and whether the deficit is real or caused by model assumptions has important implications for seismic hazard assessments. Based on InSAR-constrained coseismic slip models of ten of the most significant strike-slip earthquakes in the Tibetan Plateau since 1997, we find that SSD estimates can be unreliable. SSD from models of the same earthquake vary by up to 88%, largely because modeled slip distributions vary greatly both in the shallowest 1 km and in maximum slip areas, which are the very depths considered in SSD estimations. Furthermore, while other studies performing controlled tests of a single earthquake have shown that adding near-fault constraints from pixel tracking, modeling the crust as a heterogeneous elastic material, and using a more accurate fault geometry can reduce SSD (Huang et al., 2022a; Luo and Wang, 2022; Xu et al., 2016b), our comparison of independently inverted slip models for the two best-studied Tibetan earthquakes shows that such models are not necessarily biased towards lower SSD values. These observations caution against over-interpreting near-surface modeled slip and SSD. Straighter, more mature faults may yield more consistent SSD estimates, but in-depth investigations of different inversion methods, data weighting and near-fault data smoothing is needed to isolate the sources of the variability of shallow modeled slip.

Comparing deeper modeled slip to distributed surface offsets measured from near-field pixel tracking displacements — a relation we term the distributed shallow slip deficit

(DSSD) — may provide more information on the source of the SSD, including whether the SSD is due to coseismic distributed deformation, or a real deficit caused by velocity strengthening behavior or an accumulation of inelastic strain in the interseismic period. In some cases, SSD and DSSD are similar, while in other cases DSSD is significantly reduced compared to SSD, suggesting that much (or all) of the slip reached the surface coseismically but was not modeled as such. These observations, i.e., assessing whether or not SSD may be real and as systematic as it has seemed are important to consider when interpreting the seismic hazard of an area. For instance, underestimating shallow slip leads to an underestimation of seismic hazard. Furthermore, these observations may have safety and building code implications when it comes to how widespread coseismic damage may be if at least some of the slip deficit can be explained by distributed surface slip rather than entirely by modeling choices. Mature faults have been associated with less SSD, and while there may be a global trend, this appears to be obscured in our study of Tibetan Plateau earthquakes due to factors such as model uncertainties, inherited structures affecting rupture propagation, and differences in near surface geology. There is a clearer relationship between SSD and magnitude, with larger earthquakes having proportionally more surface slip than smaller events. The SSD obtained from an earthquake slip model is therefore not a useful proxy for the maturity of the host fault in the Tibetan Plateau. Furthermore, maturity does not explain why a minority of ruptures, all within the central Tibetan Plateau, grew past a length of $\sim$160 km. This may instead be explained by favorably-oriented inherited structures. Fault structural maturity may play only a secondary role in earthquake behavior in the Tibetan Plateau, and the regional tectonic history may be more significant.

## 4.9 Appendix

### 4.9.1 Data manipulation

#### Maps of slip distribution standard deviation

Direct, quantitative comparisons of coseismic slip distributions requires reducing some of the information, since independently modeled fault planes do not directly overlie one another and have different lengths, fault end coordinates and geometries. We therefore cannot plot and compare slip distributions vs. distance along strike, as the slip at a certain distance along strike in one model will not correspond to the same section of the fault at that same distance for another model. We undertook slip model comparisons for the 2021 Maduo

and 2022 Menyuan earthquakes only (Figures 4.2c, 4.5c). Since they occurred on approximately ENE–WSW-striking faults, we compared the slip of all models for each earthquake at regular increments of depth and easting, the latter being a rough but convenient approximation for distance along strike. The eastings values of our grid are those of the surface projection of the slip patch coordinates, since the deeper slip patches of a dipping fault that is not striking E-W will have eastings that progressively drift either eastward or westward with depth (although this effect is minor as the fault segments are sub-vertical). Plotting the slip distributions at regular increments of easting more easily allows us to compare slip magnitude at distinct sections along the rupture (for example, sections where the surface displacements are greatest, where high shallow slip magnitudes are expected, sections where there is a clear segmentation in the surface rupture, and sections where slip is distributed over the main fault and secondary faults). This involves disregarding that the models have variable strikes, dips and segmentation. However, these parameters likely control aspects of the slip distribution; therefore a large variation in slip magnitude between models at a particular section of the fault (which we can map) can be indicative of how different the model geometries are at that location. In other words, our standard deviation maps illustrate differences in slip magnitudes, but also differences in model fault segment geometry, indirectly: we do see increased standard deviations in certain areas of fault complexity for example near the fault bend of the Menyuan earthquake (Figure 4.5c).

Since slip patch sizes and shapes varied between models, each model was interpolated and oversampled using a spline interpolation, such that every slip distribution had an identical grid of easting and depth. We used increments of 400 m and otherwise default parameters in the Generic Mapping Tools software, as this gave a reasonable interpolation. This resulted in a gradual slip distribution without steps in model slip at each slip patch boundary. This interpolation did not significantly change the slip at model boundaries — most importantly near the surface — but provides a realistic gradient based on the surrounding data points. The standard deviation between the different models was then calculated at each grid point (Figure 4.2c, 4.5c).

### 4.9.2 Surface displacement profiles

For 6 of the ten earthquakes surveyed, surface displacement data from SAR or optical image pixel displacements were used to estimate along-strike variations in the total near-fault offset accommodated across a $\sim$1 km aperture centered upon the rupture trace. The data type used varied based on availability and quality. For the 2001 Kunlun earthquake,

the optical image correlation displacement fields from Rosu et al. (2015) were used. The data are 160 m-resolution, E-W and N-S components of the displacement field produced from SPOT-1 and SPOT-4 panchromatic images. For the 2010 Yushu earthquake, we used 50 m-resolution range and azimuth displacement fields derived from ALOS PALSAR data, provided by Liu et al. (2011). The images were acquired from the ascending track (satellite heading vector is 350°, and average fault strike is 310° – the range and azimuth displacements provide displacement components perpendicular to each other though). For the 2014 Yutian earthquake, 9 m-resolution E-W and N-S displacement fields produced from the correlation of SPOT-6 and SPOT-7 panchromatic images provided by Li et al. (2020a) were used. For the 2015 Murghab earthquake, we used offsets measured by Elliott et al. (2020). They profiled the 30 m-resolution E-W and N-S components of the displacement field derived from 15-m resolution Landsat-8 panchromatic imagery and measured total fault-parallel offsets within a 1 km aperture. For the 2021 Maduo earthquake, we used offsets measured by Li et al. (2022a). They profiled the 10 m-resolution E-W and N-S components of the displacement field derived from 10-m resolution Sentinel-2 panchromatic imagery and measured total fault-parallel offsets within a $\sim$1 km aperture. For the 2022 Menyuan earthquake, we used offsets measured by Han et al. (2023b). They profiled the E-W and N-S components of the displacement field derived from 0.65–0.8-m resolution GaoFen-2 and GaoFen-7 panchromatic imagery and measured fault-parallel total offsets within a $\sim$1 km aperture. There are differences in displacement map resolution and profile swath width, however as explained later in this section, the DSSD value is calculated by averaging the offset values within a region the length of a model slip patch (therefore getting rid of smaller-wavelength variations in offset measured by the narrower profile swaths).

For the 2001 Kunlun, 2010 Yushu and 2014 Yutian earthquakes, profiles were extracted from the perpendicular components of the displacement fields using the COSI-Corr profiling tool (Leprince et al., 2007), averaging pixel values over a 450–480 m-wide swath (variation in profile widths depended on the displacement map resolution). The displacement components were projected such that they represented displacement parallel to the local fault strike. To measure the offset for a given profile, linear regressions were performed on carefully selected subsets of displacement data on either side of the fault. Profile subsets used for the linear regressions were chosen manually as a representative near-fault sample of the total coseismic slip (elastic and inelastic). Offsets were measured by subtracting the offset value on the regression line boundary closest to the fault on either side of the fault. Profiles that had a low signal-noise ratio near the fault were discounted from the analysis.

Table 4.1: Slip models used in this study

| Earthquake | Model reference | Inversion data | SSD |
|---|---|---|---|
| 1997 Manyi | Funning et al. (2007) | InSAR, SAR displacements | 19% |
| 2001 Kunlun | Lasserre et al. (2005) | InSAR | 0% |
| 2001 Kunlun | Wan et al. (2008) | InSAR, GNSS | 0% |
| 2010 Yushu | Li et al. (2011) | InSAR | 35% |
| 2010 Yushu | Jiang et al. (2013) | InSAR | 6% |
| 2014 Yutian | Li et al. (2020a) | InSAR, SAR & optical image displacements | 45% |
| 2015 Murghab | Metzger et al. (2017) | InSAR, SAR displacements, GNSS | 0% |
| 2015 Murghab | Sangha et al. (2017) | InSAR | 7% |
| 2015 Murghab | Jin et al. (2022) | InSAR | 20% |
| 2016 Aketao | Feng et al. (2017) | InSAR | 98% |
| 2016 Aketao | He et al. (2018) | InSAR, GNSS | 70% |
| 2016 Aketao | Bie et al. (2018) | InSAR | 83% |
| 2016 Aketao | Zhang et al. (2019) | InSAR, near-field seismic, teleseismic | 28% |
| 2017 Jiuzhaigou | Hong et al. (2018) | InSAR, GNSS | 72% |
| 2017 Jiuzhaigou | Li et al. (2020b) | InSAR, GNSS | 47% |
| 2017 Jiuzhaigou | Zheng et al. (2020) | InSAR, teleseismic, strong motion | 45% |
| 2017 Jiuzhaigou | Tang et al. (2021) | InSAR | 67% |
| 2021 Maduo | Chen et al. (2021) | InSAR | 17% |
| 2021 Maduo | Fang et al. (2022) | InSAR | 69% |
| 2021 Maduo | He et al. (2022) | InSAR | 4% |
| 2021 Maduo | Jin and Fialko (2021) | InSAR, SAR range | 24% |
| 2021 Maduo | Liu et al. (2022a) | InSAR, SAR displacements | 81% |
| 2021 Maduo | Wang et al. (2022a) | InSAR, SAR displacements | 68% |

| | | | |
|---|---|---|---|
| 2021 Maduo | Wei et al. (2022) | InSAR, SAR displacements, high rate GNSS, regional & teleseismic waveforms | 66% |
| 2021 Maduo | Xu et al. (2021) | InSAR, burst overlap interferometry | 0% |
| 2021 Maduo | Xu et al. (2023) | InSAR, teleseismic | 47% |
| 2021 Maduo | Yue et al. (2022) | InSAR, SAR displacements, GNSS, telesismic | 0% |
| 2021 Maduo | Zhang et al. (2022) | InSAR, strong motion, regional & teleseismic | 88% |
| 2021 Maduo | Zhao et al. (2022b) | InSAR | 79% |
| 2022 Menyuan | Guo et al. (2022) | InSAR, GNSS | 51% |
| 2022 Menyuan | Han et al. (2023b) | InSAR | 19% |
| 2022 Menyuan | Han et al. (2023b) | InSAR, optical image displacements | 0% |
| 2022 Menyuan | He et al. (2023) | InSAR, teleseismic | 48% |
| 2022 Menyuan | Huang et al. (2022a) | InSAR | 45% |
| 2022 Menyuan | Huang et al. (2022a) | InSAR, accelerogram | 33% |
| 2022 Menyuan | Lü et al. (2022) | InSAR, SAR displacements, high-rate GNSS | 25% |
| 2022 Menyuan | Luo and Wang (2022) | InSAR, SAR displacements | 22% |
| 2022 Menyuan | Yang et al. (2022) | InSAR | 49% |
| 2022 Menyuan | Zhang et al. (2023) | InSAR, GNSS | 43% |
| 2022 Luding | Han et al. (2023a) | InSAR | 100% |
| 2022 Luding | Li et al. (2022b) | InSAR | 48% |

## 4.10 Supporting Information

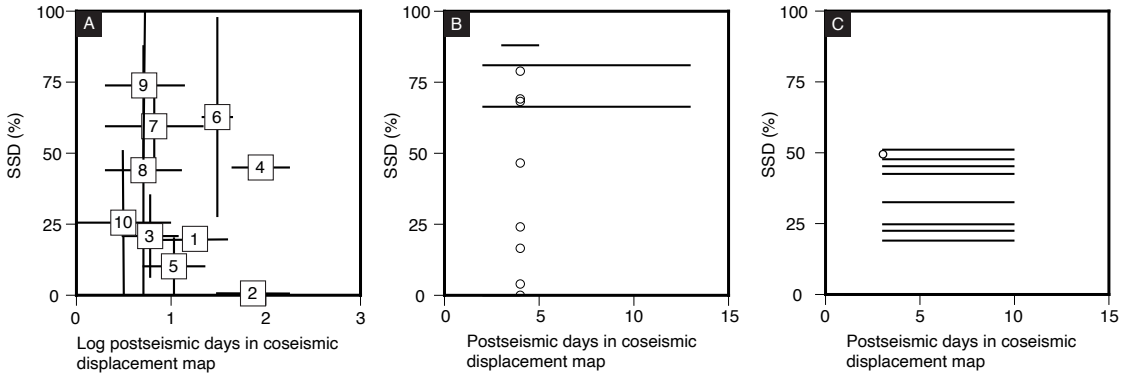


Figure 4.9: SSD as a function of the number of postseismic days captured in the displacement maps used in the coseismic slip inversions for (a) all earthquakes: 1) 1997 Manyi, 2) 2001 Kunlun, 3) 2010 Yushu, 4) 2014 Yutian, 5) 2015 Murghab, 6) 2016 Aketao, 7) 2017 Jiuzhaigou, 8) 2021 Maduo, 9) 2022 Menyuan, 10) 2022 Luding; b) individual slip models of the 2021 Maduo earthquake; c) individual slip models of the 2022 Menyuan earthquake.

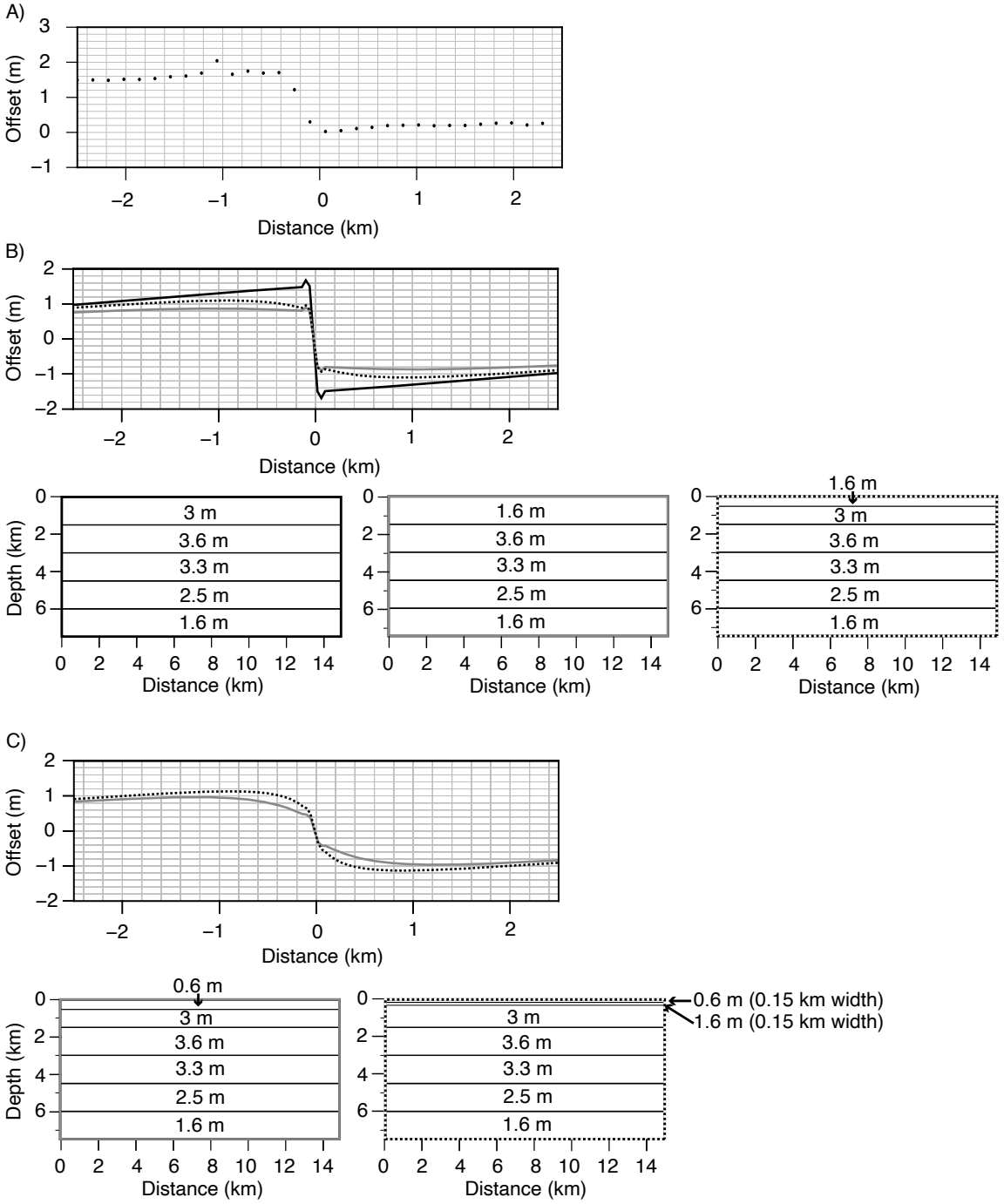


Figure 4.10: a) Example of a typical Sentinel-2 profile across the displacement field of the 2022 Menyuan earthquake. Here, the minimum width over which the offset is distributed is 160 m (distance between two circles) and the maximum is 480 m (3 pixels-wide). b) Profiles across the surface displacements resulting from elastic dislocation forward modeling (Okada, 1985; Wright et al., 1999), independent of profile in a) showing the effect of different SSD amounts and gradients: none can replicate a gradual offset contained within a 480 m zone like in a) (slip distributions for the different tests are shown below: slip values are written on the fault). c) Extremely shallow SSD still cannot replicate a gradual offset within a 480 m-wide zone only (slip distributions for the different tests are shown below: slip values are written on the fault).

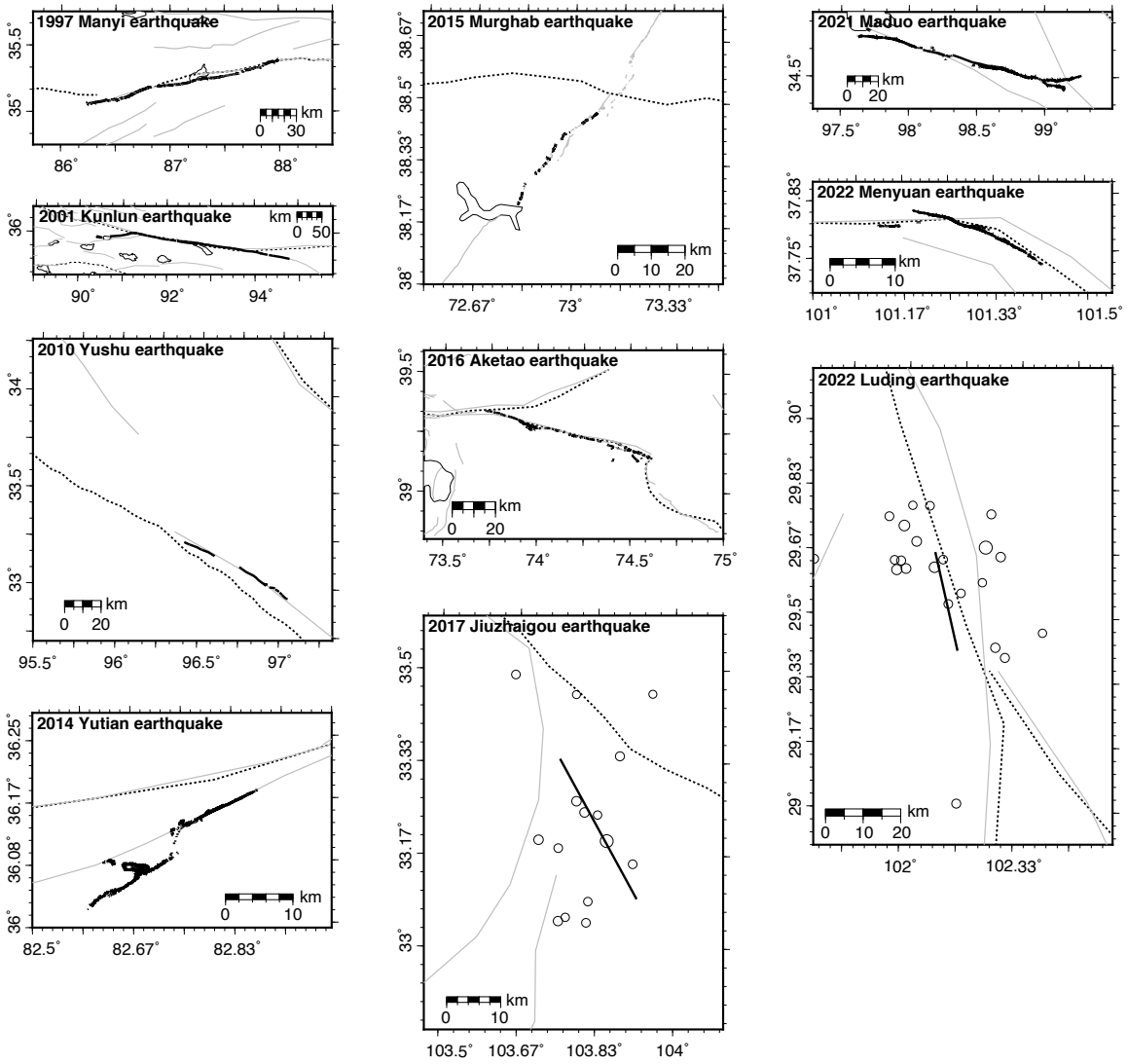


Figure 4.11: Black lines: surface ruptures. For buried faults: black lines are surface projection of InSAR models and circles show main shock and aftershock locations (U.S. Geological Survey ComCat, `https://earthquake.usgs.gov/earthquakes/search/`). Gray lines: major active faults. Dashed line: major suture zones.

Table 4.2: 2001 Kunlun earthquake: fault trace-parallel offsets measured from SPOT-1/4 optical image correlation profiles (error estimated by propagating the standard error of the regression)

| Longitude | Latitude | Offset (m) | Error (m) |
|---|---|---|---|
| 91.6846026002 | 35.95782258 | 3.92829 | 0.30264 |
| 91.6899479688 | 35.9564386139 | 6.23844 | 0.552536 |
| 91.6952931575 | 35.9550544056 | 2.52891 | 0.635227 |
| 91.7006145437 | 35.955112145 | 3.48937 | 0.344625 |
| 91.705959471 | 35.9537274554 | 4.97055 | 0.874614 |
| 91.7113042183 | 35.9523425236 | 3.24889 | 0.348368 |
| 91.7166254563 | 35.9523995494 | 3.93012 | 1.04082 |
| 91.7219699419 | 35.9510141365 | 6.52911 | 0.0825677 |
| 91.7272911129 | 35.9510706877 | 3.53499 | 0.879469 |
| 91.7326353365 | 35.9496847939 | 5.46886 | 1.4037 |
| 91.7433004018 | 35.9483544957 | 2.79571 | 0.378015 |
| 91.7486214384 | 35.9484100977 | 2.73221 | 0.173442 |
| 91.7539651373 | 35.9470232422 | 4.28947 | 0.308265 |
| 91.7592861063 | 35.9470783696 | 4.14741 | 0.332531 |
| 91.7646295426 | 35.9456910335 | 3.21839 | 0.142865 |
| 91.807327194 | 35.9374681445 | 2.97732 | 0.274415 |
| 91.8126692002 | 35.9360786386 | 2.40754 | 0.278786 |
| 91.8179895513 | 35.9361311499 | 3.62538 | 0.272914 |
| 91.8233312938 | 35.934741164 | 3.49281 | 0 |
| 91.8446754674 | 35.9306210786 | 7.352 | 0.75537 |
| 91.8500164022 | 35.9292298881 | 3.71447 | 0.679054 |
| 91.8553363652 | 35.9292807359 | 3.46887 | 0 |
| 91.8820176003 | 35.9237622661 | 2.36167 | 1.08273 |
| 91.8873372558 | 35.9238116894 | 1.79768 | 0 |
| 92.020528318 | 35.9091047258 | 7.69113 | 0 |
| 92.041821415 | 35.9078340252 | 4.70031 | 0.404864 |
| 92.0471575665 | 35.9064339782 | 6.71079 | 0.256722 |
| 92.0524763389 | 35.9064760669 | 4.83766 | 0.226008 |
| 92.0578122217 | 35.9050755419 | 4.14506 | 0.200694 |

| | | | |
|---|---|---|---|
| 92.0631309196 | 35.9051171573 | 3.85471 | 0.293557 |
| 92.0684665336 | 35.9037161543 | 3.2201 | 0 |
| 92.0791205015 | 35.9023558156 | 4.5268 | 0.0717997 |
| 92.0844390496 | 35.9023964846 | 4.70727 | 0.154353 |
| 92.0897741251 | 35.900994526 | 4.63199 | 0.26317 |
| 92.0950925979 | 35.9010347219 | 3.66066 | 0.365166 |
| 92.1057458011 | 35.8996720083 | 4.88938 | 0.131565 |
| 92.1110642087 | 35.8997114956 | 5.37015 | 0.305444 |
| 92.1163986589 | 35.8983083441 | 4.08978 | 0.300643 |
| 92.1270511706 | 35.8969437294 | 4.44637 | 0.102047 |
| 92.1323694262 | 35.8969822706 | 4.11376 | 0.0400028 |
| 92.1376876919 | 35.8970205765 | 4.75063 | 0.0736967 |
| 92.1430059675 | 35.8970586468 | 5.4689 | 0.155704 |
| 92.1483397043 | 35.8956540655 | 5.62094 | 0.246078 |
| 92.1536579033 | 35.8956916629 | 4.49578 | 0.44306 |
| 92.1589913694 | 35.8942866044 | 4.98419 | 0.131955 |
| 92.1643246512 | 35.8928813061 | 5.57955 | 0.00847409 |
| 92.1696426866 | 35.8929181933 | 4.75271 | 0 |
| 92.1749756973 | 35.8915124179 | 5.82297 | 0 |
| 92.1803085237 | 35.8901064029 | 4.5063 | 0.0261552 |
| 92.1856263949 | 35.89014258 | 5.41848 | 0.0275306 |
| 92.1909442756 | 35.8901785215 | 5.06125 | 0.128438 |
| 92.1962767436 | 35.8887717924 | 4.87121 | 0.141706 |
| 92.2015945465 | 35.8888072612 | 4.44373 | 0.291568 |
| 92.2228799451 | 35.8875043376 | 5.94231 | 0.403841 |
| 92.2335154585 | 35.8875726822 | 4.44098 | 0.262445 |
| 92.2388470331 | 35.8861640507 | 4.25289 | 0.0868382 |
| 92.2441647156 | 35.8861976327 | 4.37785 | 0.138085 |
| 92.2494960175 | 35.8847885248 | 4.28627 | 0.3209 |
| 92.2548271343 | 35.8833791776 | 4.14937 | 0 |
| 92.260158066 | 35.8819695912 | 4.31485 | 0.406634 |
| 92.2654888126 | 35.8805597657 | 5.64605 | 0.117302 |
| 92.2708193739 | 35.879149701 | 2.73715 | 0 |
| 92.276136626 | 35.8791818621 | 2.55282 | 0 |

Table 4.3: 2010 Yushu earthquake: fault trace-parallel offsets measured from Sentinel-1 SAR range and azimuth displacement profiles (error estimated by propagating the standard error of the regression)

| Longitude | Latitude | Offset (m) | Error (m) |
|---|---|---|---|
| 96.4170425657 | 33.2298677765 | 3.91384 | 0.211906 |
| 96.4219335251 | 33.2277152035 | 2.50376 | 0.10024 |
| 96.4268110535 | 33.226012972 | 0.592973 | 0.433073 |
| 96.4316884034 | 33.2243105394 | 8.00988 | 0.680355 |
| 96.4365524257 | 33.2230584558 | 8.46714 | 0.411444 |
| 96.4414294447 | 33.2213556231 | 9.99844 | 0.586366 |
| 96.4463062852 | 33.2196525894 | 5.12856 | 0.443621 |
| 96.4511698753 | 33.2183999102 | 18.5317 | 1.01093 |
| 96.4560333382 | 33.2171470338 | 12.4621 | 0.295799 |
| 96.4608966739 | 33.2158939602 | 12.7618 | 1.11959 |
| 96.4657728779 | 33.2141901285 | -4.69728 | 0.250163 |
| 96.4803745822 | 33.2099785615 | 6.68515 | 0.44018 |
| 96.4852501233 | 33.2082739306 | 5.7739 | 0.0248004 |
| 96.4901254858 | 33.206569099 | 3.88398 | 0.467869 |
| 96.5096506747 | 33.1988466127 | 1.17825 | 0.929369 |
| 96.5145250918 | 33.1971407748 | 1.11056 | 0.737198 |
| 96.5193993301 | 33.1954347365 | 5.96062 | 0.540926 |
| 96.5242733896 | 33.1937284979 | 2.88944 | 0.223633 |
| 96.5291346102 | 33.1924726431 | -0.582215 | 0.869253 |
| 96.5340083377 | 33.1907660056 | 0.674274 | 0.187322 |
| 96.5388692776 | 33.1895097556 | 1.27241 | 0.175957 |
| 96.5437426729 | 33.1878027193 | -1.30202 | 0.328954 |
| 96.5486033319 | 33.1865460741 | 0.805462 | 0.585034 |
| 96.5534638632 | 33.1852892322 | 6.59384 | 0.564026 |
| 96.5583367731 | 33.1835815989 | 0.551967 | 0.720782 |
| 96.5681069649 | 33.1792645352 | -1.08125 | 0.583569 |
| 96.5730041426 | 33.1766550978 | 1.43942 | 0.741597 |
| 96.5778886353 | 33.1744960553 | 2.44993 | 0.38834 |
| 96.582785273 | 33.1718862055 | 1.03589 | 0.575271 |

| | | | |
|---|---|---|---|
| 96.5925653755 | 33.1671164922 | 3.14198 | 0.555483 |
| 96.5974488927 | 33.1649566324 | 0.87768 | 0.421566 |
| 96.7548847198 | 33.1083815784 | 3.75457 | 0.747329 |
| 96.7597841841 | 33.1053136854 | 5.41792 | 0.365602 |
| 96.7646833126 | 33.1022455839 | 10.7786 | 0.0701041 |
| 96.7695707171 | 33.0996279426 | 6.0587 | 0.201066 |
| 96.7744578384 | 33.0970100963 | 4.07616 | 0.232836 |
| 96.7793446764 | 33.0943920449 | 10.8236 | 0.5407 |
| 96.7842312312 | 33.0917737885 | 13.3505 | 0.139975 |
| 96.7891287868 | 33.0887046515 | 10.8877 | 0.170222 |
| 96.7940147491 | 33.0860859837 | 11.9084 | 0.399816 |
| 96.7989004281 | 33.083467111 | 8.06659 | 0.4914 |
| 96.8037634119 | 33.0817493948 | 6.52053 | 0.196184 |
| 96.8086373962 | 33.0795807983 | 14.9318 | 0.0425255 |
| 96.8134999942 | 33.0778626842 | 18.4085 | 0.28471 |
| 96.8183735416 | 33.0756936866 | 18.3438 | 0.4999 |
| 96.8232357539 | 33.0739751748 | 18.4719 | 0.379356 |
| 96.832959638 | 33.0705375571 | 9.61647 | 0.271068 |
| 96.8378323368 | 33.0683677595 | 17.2156 | 0.571131 |
| 96.8427158053 | 33.0657470674 | 10.086 | 0.807774 |
| 96.8476099654 | 33.0626754759 | 11.1161 | 0.449851 |
| 96.8525037902 | 33.0596036769 | 14.9815 | 0.382028 |
| 96.8573972795 | 33.0565316704 | 16.3967 | 0.446924 |
| 96.8623122252 | 33.0525580562 | 10.8991 | 0.124282 |
| 96.8666915672 | 33.0485750731 | 17.9876 | 0.112623 |
| 96.8716056531 | 33.0446010527 | 20.4637 | 0.717515 |
| 96.8765192981 | 33.0406268183 | 8.80881 | 0.52804 |
| 96.8814001263 | 33.0380044908 | 20.7093 | 0.374062 |
| 96.8862914378 | 33.034931251 | 16.0231 | 0.175113 |
| 96.8911716739 | 33.0323085143 | 11.954 | 1.00154 |
| 96.8960516271 | 33.0296855739 | 11.9962 | 0.497079 |
| 96.9009419856 | 33.0266117166 | 13.6175 | 0.36954 |
| 96.9058213469 | 33.0239883674 | 12.277 | 0.193814 |
| 96.9107110615 | 33.0209140982 | 10.3932 | 0.415318 |
| 96.9150654477 | 33.0178306824 | 6.88327 | 0.242659 |

| | | | |
|---|---|---|---|
| 96.9247904302 | 33.0139347602 | 4.56441 | 0.0434528 |
| 96.9345250998 | 33.0095873194 | 13.427 | 0.536305 |
| 96.9393920875 | 33.0074132989 | 13.3136 | 0.0214026 |
| 96.944227465 | 33.00659126 | 8.06487 | 0.366855 |
| 96.9490731975 | 33.0053183015 | 4.60003 | 0.683394 |
| 96.9539188001 | 33.004045149 | 7.77332 | 0.350143 |
| 96.9587642726 | 33.0027718025 | 13.6466 | 0.562079 |
| 96.9636096151 | 33.0014982622 | 1.16917 | 0.602674 |
| 96.9684548275 | 33.000224528 | 1.99656 | 0.215935 |
| 96.978144862 | 32.997676478 | 9.98019 | 0.562852 |
| 96.9830204593 | 32.9950499457 | 11.3721 | 0.804459 |
| 96.9878957735 | 32.9924232108 | 8.95093 | 0.945614 |
| 96.9927912173 | 32.9888947891 | 8.82441 | 0.0583445 |
| 96.997676094 | 32.9858169022 | 3.08078 | 0.373788 |
| 97.0025707898 | 32.9822880644 | 4.29403 | 0.194896 |
| 97.0074650987 | 32.9787590179 | 3.16811 | 0.219407 |
| 97.0172525555 | 32.9717002989 | -0.352974 | 1.17294 |
| 97.0216210259 | 32.9677114033 | 7.96241 | 0.676018 |
| 97.0259891019 | 32.9637223375 | 8.21966 | 0.097177 |
| 97.0357834136 | 32.9562112756 | 1.58054 | 0 |

Table 4.4: 2014 Yutian earthquake: fault trace-parallel offsets measured from SPOT-6/7 optical image correlation profiles (error estimated by propagating the standard error of the regression)

| Longitude | Latitude | Offset (m) | Error (m) |
|---|---|---|---|
| 82.7050473527 | 36.0772580915 | 0.611622 | 0.0822778 |
| 82.7000063635 | 36.075220302 | 0.414082 | 0.0497573 |
| 82.6949708504 | 36.0734256133 | 0.671551 | 0.0684739 |
| 82.6899338238 | 36.0715495993 | 0.537603 | 0.0818974 |
| 82.6850090452 | 36.0702397133 | 0.476015 | 0.0642079 |
| 82.6799827953 | 36.0688499133 | 0.654184 | 0.0683997 |
| 82.6755337535 | 36.0663971165 | 0.610951 | 0.0568573 |

| | | | |
|---|---|---|---|
| 82.6713572191 | 36.0626422386 | 0.56966 | 0.0476503 |
| 82.6663990661 | 36.0597093991 | 0.825898 | 0.0271885 |
| 82.6613447999 | 36.0569399451 | 0.673663 | 0.0702776 |
| 82.6562942832 | 36.0543324848 | 1.14909 | 0.071671 |
| 82.6512440949 | 36.0517248019 | 1.56626 | 0.0283762 |
| 82.6463076287 | 36.0497643985 | 1.19681 | 0.0634475 |
| 82.6412765759 | 36.0480484808 | 1.48318 | 0.0739336 |
| 82.6362474137 | 36.0464134553 | 1.31144 | 0.0682415 |
| 82.6312184526 | 36.0447782131 | 0.845972 | 0.069256 |
| 82.6262912336 | 36.0432225092 | 0.993223 | 0.0781369 |
| 82.6212626678 | 36.0415868377 | 1.26954 | 0.0566578 |
| 82.6162359612 | 36.0400320601 | 1.05375 | 0.0863344 |
| 82.6113043543 | 36.0382323915 | 1.20756 | 0.0799341 |
| 82.6062632159 | 36.0359471857 | 0.629287 | 0.0659168 |
| 82.6019966133 | 36.0324344178 | 0.793129 | 0.0782371 |
| 82.5652627764 | 36.023589281 | 0.405503 | 0.0630959 |
| 82.5603108972 | 36.0206518733 | 1.087 | 0.078275 |
| 82.555288233 | 36.0191755846 | 0.834855 | 0.0762507 |
| 82.5502800504 | 36.0184291016 | 0.799973 | 0.0750959 |
| 82.5453781349 | 36.0180055749 | 0.631186 | 0.0605328 |
| 82.5406127928 | 36.0143347263 | 0.920949 | 0.0568995 |
| 82.5355767083 | 36.012127565 | 0.747936 | 0.0998349 |
| 82.5305440358 | 36.0100824132 | 0.717307 | 0.119844 |
| 82.5256114507 | 36.0080357732 | 0.662817 | 0.0842349 |
| 82.5205792845 | 36.0059901893 | 0.553319 | 0.112279 |
| 82.5155520304 | 36.0041877322 | 0.292883 | 0.100668 |
| 82.5105249992 | 36.0023850582 | 0.587162 | 0.0757984 |
| 82.5055980153 | 36.0005809144 | 0.587566 | 0.0866301 |
| 82.8549365576 | 36.171734034 | 0.278171 | 0.0840246 |
| 82.8498820003 | 36.1695406721 | 0.305156 | 0.0562666 |
| 82.8449296377 | 36.1674266452 | 0.284433 | 0.0643193 |
| 82.8398794148 | 36.1653950417 | 0.337377 | 0.0576575 |
| 82.8348313362 | 36.1634443163 | 0.462619 | 0.0571228 |
| 82.8297835008 | 36.1614933702 | 0.403383 | 0.0905969 |
| 82.8248471983 | 36.1600272793 | 0.430863 | 0.08243 |

| | | | |
|---|---|---|---|
| 82.8198298121 | 36.1593735024 | 0.410969 | 0.0635151 |
| 82.8147900648 | 36.1577463064 | 0.390639 | 0.0784729 |
| 82.8097430612 | 36.1557944886 | 0.193415 | 0.0769509 |
| 82.7997479312 | 36.1518075867 | -0.244815 | 0.0514455 |
| 82.7946998121 | 36.1497740098 | -0.255896 | 0.0657801 |
| 82.7896519469 | 36.147740212 | -0.303579 | 0.0863364 |
| 82.7495231423 | 36.133486555 | 0.252023 | 0.046393 |

# Chapter 5

# Conclusions

Understanding how fault physical properties affect earthquake behavior and accurately characterizing fault zones are key to mitigating earthquake-related damage. This dissertation sheds light on the poorly understood tectonic settings of immature faults that hosted unexpectedly large earthquakes, advances the understanding of the widely distributed surface deformation associated with immature faulting, and demonstrates that typical coseismic slip models that overlook wide damage zones and distributed deformation are not always reliable.

The earthquakes analyzed in this dissertation, particularly the 1971 $M_w$ 6.6 San Fernando, Califonia, 2018 $M_w$ 6.4 and $M_w$ 6.0 Kaktovik, Alaska, and 2021 $M_w$ 7.4 Maduo, Tibet earthquakes, indicate that immature faults can pose a significant seismic hazard. These faults are often worryingly overlooked and challenging to characterize, as they typically occur in regions of relatively low strain and seismicity, have not developed a clear expression in the topography or in offset geomorphic features, and do not typically host characteristic earthquakes with consistent rupture extents and magnitudes across successive earthquake cycles (Ben-Zion and Sammis, 2003). Ancient convergence-related structures seem to have influenced the location and geometry of both the 2018 Kaktovik and 2021 Maduo earthquakes, and may have enabled the latter to grow to an unusual length for such an immature fault, suggesting that inherited fabric is important for seismic hazard. As for the destructive 1971 San Fernando, California earthquake, the 3-D coseismic displacement field derived from historical aerial photographs reveals a more complex rupture pattern than was previously mapped. Furthermore, the results confirm that there was an important oblique left-lateral component of slip near the surface in contrast to the pure thrust slip direction at deeper depths inferred by previous seismological studies. This illustrates how rupture kinematics can change significantly near the surface and, more broadly, how accurately

characterizing the active tectonics of an area benefits greatly from combining multiple data types (geodetic, field, and seismological).

In general, surface slip in the 1971 San Fernando earthquake was distributed over a broad zone of variable width, and surface slip was greatly underestimated by offsets measured in the field. The amount of vertical and lateral distributed deformation were not always correlated, and may be influenced by different factors. An analysis of some of the most significant recent strike-slip earthquakes in the Tibetan plateau similarly reveals that deformation was distributed over wide fault zones, in keeping with recent studies that question the validity of geodetic slip models based upon rectangular dislocations within a homogeneous elastic medium, and in particular the shallow slip deficits that such models so often produce.

An analysis comparing independently modeled slip distributions indicates that the models vary greatly in the shallowest 1 km, even between models that impose an intricate fault geometry and jointly invert InSAR and near-fault optical or SAR pixel displacement fields. Many recent studies presenting coseismic slip models of an earthquake of interest will interpret it in terms of the shallow slip deficit, and some will draw conclusions from this about the maturity of the host fault. I suggest that this value is not always robust and should not be over-interpreted, and that comparing distributed surface slip measured from optical or SAR pixel offsets with deeper modeled slip may be more valuable and informative. Because earthquake magnitude also appears to impact the shallow slip deficit (with larger events typically having proportionally more surface slip), such analyses should be applied to the full magnitude range of surface-rupturing events. These studies could also leverage improvements in the spatial and temporal resolutions of satellite optical and airborne lidar datasets, which may allow mapping of near-field displacement fields for smaller earthquakes than is currently possible.

When characterizing fault maturity or seismic hazard of an area, it is important to remember the scatter in scaling relationships, caused by the many factors that influence earthquake behavior such as the tectonic history, mechanical properties of the host rock, how favorably aligned a fault is with respect to both the ambient stress field and the presence of seemingly inactive inherited structures. Additional studies are needed to establish whether there is a global scaling relationship between distributed near-surface slip and fault maturity, and should involve comprehensive testing of the various combinations of modeling choices such as input data, degree of smoothing of input data, data set weights and slip roughness. This is important since coseismic slip models are ubiquitous, shallow slip deficits are so often estimated, and these slip distributions inform our understanding of the

seismic hazard of a given area.

# Bibliography

Aben, F. M., Brantut, N., and Mitchell, T. M. (2020). Off-Fault Damage Characterization During and After Experimental Quasi-Static and Dynamic Rupture in Crustal Rock From Laboratory P Wave Tomography and Microstructures. *Journal of Geophysical Research: Solid Earth*, 125(8):e2020JB019860.

Ajorlou, N., Hollingsworth, J., Mousavi, Z., Ghods, A., and Masoumi, Z. (2021). Characterizing Near-Field Surface Deformation in the 1990 Rudbar Earthquake (Iran) Using Optical Image Correlation. *Geochemistry, Geophysics, Geosystems*, 22(6):e2021GC009704.

Allen, C. R., Brune, J. N., Cluff, L. S., and Barrows Jr, A. G. (1998). Evidence for unusually strong near-field ground motion on the hanging wall of the San Fernando fault during the 1971 earthquake. *Seismological Research Letters*, 69(6):524–531.

Allmendinger, R. W. (1998). Inverse and forward numerical modeling of trishear fault-propagation folds. *Tectonics*, 17(4):640–656.

Amato, J. and Miller, E. (2004). Geologic map and summary of the evolution of the Kigluiak Mountains gneiss dome, Seward Peninsula, Alaska. In Whitney, D., Teyssier, C., and Siddoway, C., editors, *Gneiss domes in orogeny*, pages 295–306. Geological Society of America. Special Paper 380.

Andrews, D. (1976). Rupture velocity of plane strain shear cracks. *Journal of Geophysical Research*, 81(32):5679–5687.

Antoine, S., Klinger, Y., Wang, K., and Bürgmann, R. (under revision, 2023). Diffuse deformation explains the magnitude-dependent coseismic shallow slip deficit.

Antoine, S. L., Klinger, Y., Delorme, A., Wang, K., Bürgmann, R., and Gold, R. D. (2021). Diffuse deformation and surface faulting distribution from submetric image correlation

along the 2019 Ridgecrest, California, ruptures. *Bulletin of the Seismological Society of America*, 111(5):2275–2302.

Avouac, J.-P. and Tapponnier, P. (1993). Kinematic model of active deformation in central Asia. *Geophysical Research Letters*, 20(10):895–898.

Ayoub, F., Leprince, S., and Avouac, J.-P. (2009). Co-registration and correlation of aerial photographs for ground deformation measurements. *ISPRS Journal of Photogrammetry and Remote Sensing*, 64:551–560.

Ayoub, F., Leprince, S., and Keene, L. (2017). *User's guide to COSI-CORR co-registration of optically sensed images and correlation*. California Institute of Technology, Pasadena, CA, USA.

Bai, M., Chevalier, M.-L., Leloup, P. H., Li, H., Pan, J., Replumaz, A., Wang, S., Li, K., Wu, Q., Liu, F., et al. (2021). Spatial slip rate distribution along the SE Xianshuihe fault, eastern Tibet, and earthquake hazard assessment. *Tectonics*, 40(11):e2021TC006985.

Baize, S., Nurminen, F., Sarmiento, A., Dawson, T., Takao, M., Scotti, O., Azuma, T., Boncio, P., Champenois, J., Cinti, F. R., et al. (2020). A worldwide and unified database of surface ruptures (SURE) for fault displacement hazard analyses. *Seismological Research Letters*, 91(1):499–520.

Barker, J. S. and Langston, C. A. (1982). Moment tensor inversion of complex earthquakes. *Geophysical Journal International*, 68(3):777–803.

Barnhart, W. D., Gold, R. D., and Hollingsworth, J. (2020). Localized fault-zone dilatancy and surface inelasticity of the 2019 Ridgecrest earthquakes. *Nature Geoscience*, 13(10):699–704.

Barnhart, W. D., Gold, R. D., Shea, H. N., Peterson, K. E., Briggs, R. W., and Harbor, D. J. (2019). Vertical Coseismic Offsets Derived From High-Resolution Stereogrammetric DSM Differencing: The 2013 Baluchistan, Pakistan Earthquake. *Journal of Geophysical Research: Solid Earth*, 124(6):6039–6055.

Barrows, A. G. (1975). Surface Effects and Related Geology of the San Fernando Earthquake in the Foothill Region Between Little Tujunga and Wilson Canyons. In Oakeshott, G., editor, *San Fernando Earthquake of 9 February 1971*, volume 196, pages 97–117. California Division of Mines and Geology, Sacramento, CA.

Barrows, A. G., Kahle, J. E., Weber, F. H., and Saul, R. (1973). Map of surface breaks resulting from the San Fernando, California, earthquake. In Murphy, L., editor, *San Fernando, California, Earthquake of February 9, 1971*, volume 3, pages 127 – 134. U.S. Department of Commerce, National Oceanic and Atmospheric Administration, Washington, D.C., USA.

Bartlett, W., Friedman, M., and Logan, J. (1981). Experimental folding and faulting of rocks under confining pressure Part IX. Wrench faults in limestone layers. *Tectonophysics*, 79(3-4):255–277.

Bell, M., Elliott, J., and Parsons, B. (2011). Interseismic strain accumulation across the Manyi fault (Tibet) prior to the 1997 Mw 7.6 earthquake. *Geophysical Research Letters*, 38(24).

Ben-Zion, Y. and Sammis, C. G. (2003). Characterization of Fault Zones. *Pure and Applied Geophysics*, 160(3-4):677–715.

Bergman, E. A. and Solomon, S. C. (1990). Earthquake swarms on the Mid-Atlantic Ridge: Products of magmatism or extensional tectonics? *Journal of Geophysical Research*, 95(B4):4943–4965.

Berryman, K. R., Cochran, U. A., Clark, K. J., Biasi, G. P., Langridge, R. M., and Villamor, P. (2012). Major earthquakes occur regularly on an isolated plate boundary fault. *Science*, 336(6089):1690–1693.

Beyer, R. A., Alexandrov, O., and McMichael, S. (2018). The Ames Stereo Pipeline: NASA's open source software for deriving and processing terrain data. *Earth and Space Science*, 5(9):537–548.

Bie, L., Hicks, S., Garth, T., Gonzalez, P., and Rietbrock, A. (2018). 'Two go together': Near-simultaneous moment release of two asperities during the 2016 Mw 6.6 Muji, China earthquake. *Earth and Planetary Science Letters*, 491:34–42.

Bonilla, M. (1973). Trench Exposures Across Surface Fault Ruptures Associated With San Fernando Earthquake. In Murphy, L., editor, *San Fernando, California, Earthquake of February 9, 1971*, volume 3, pages 173 – 182. U.S. Department of Commerce, National Oceanic and Atmospheric Administration, Washington, D.C., USA.

Bonilla, M. G., Buchanan, J. M., Castle, R. ., Clark, M. M., Frizzell, V. A., Gulliver, R. M., Miller, F. K., Pinkerton, J., Ross, D. C., Sharp, R. V., Yerkes, R. F., and I., Z. J. (1971). Surface Faulting. In *The San Fernando, California Earthquake of February 9th, 1971*, pages 56 – 76. U.S. Geological Survey Professional Paper 733.

Boore, D. M. (1972). A note on the effect of simple topography on seismic SH waves. *Bulletin of the Seismological Society of America*, 62(1):275–284.

Boore, D. M. (1973). The effect of simple topography on seismic waves: implications for the accelerations recorded at Pacoima Dam, San Fernando Valley, California. *Bulletin of the Seismological Society of America*, 63(5):1603–1609.

Bouchon, M. (1978). A dynamic source model for the San Fernando earthquake. *Bulletin of the Seismological Society of America*, 68(6):1555–1576.

Bouchon, M. and Vallée, M. (2003). Observation of long supershear rupture during the magnitude 8.1 Kunlunshan earthquake. *Science*, 301(5634):824–826.

Bruhat, L., Fang, Z., and Dunham, E. M. (2016). Rupture complexity and the supershear transition on rough faults. *Journal of Geophysical Research: Solid Earth*, 121(1):210–224.

Bruhat, L., Klinger, Y., Vallage, A., and Dunham, E. M. (2020). Influence of fault roughness on surface displacement: from numerical simulations to coseismic slip distributions. *Geophysical Journal International*, 220(3):1857–1877.

Brune, J. N. (2001). Shattered rock and precarious rock evidence for strong asymmetry in ground motions during thrust faulting. *Bulletin of the Seismological Society of America*, 91(3):441–447.

Burchfiel, B., Zhang, P., Wang, Y., Zhang, W., Song, F., Deng, Q., Molnar, P., and Royden, L. (1991). Geology of the Haiyuan fault zone, Ningxia-Hui Autonomous Region, China, and its relation to the evolution of the northeastern margin of the Tibetan Plateau. *Tectonics*, 10(6):1091–1110.

Burford, R., Castle, R., Church, J., Kinoshita, S., Kirby, S., Ruthven, R., and Savage, J. (1971). Preliminary measurements of tectonic movement. In *The San Fernando, California Earthquake of February 9th, 1971*, pages 80 – 85. U.S. Geological Survey Professional Paper 733.

Burgette, R. J., Hanson, A. M., Scharer, K. M., Rittenour, T. M., and McPhillips, D. (2020). Late Quaternary slip rate of the Central Sierra Madre fault, southern California: Implications for slip partitioning and earthquake hazard. *Earth and Planetary Science Letters*, 530:115907.

Bürgmann, R., Pollard, D. D., and Martel, S. J. (1994). Slip distributions on faults: effects of stress gradients, inelastic deformation, heterogeneous host-rock stiffness, and fault interaction. *Journal of Structural Geology*, 16(12):1675–1690.

Carena, S. and Suppe, J. (2002). Three-dimensional imaging of active structures using earthquake aftershocks: the Northridge thrust, California. *Journal of Structural Geology*, 24(4):887–904.

Chen, H., Qu, C., Zhao, D., Ma, C., and Shan, X. (2021). Rupture kinematics and coseismic slip model of the 2021 Mw 7.3 Maduo (China) earthquake: Implications for the seismic hazard of the Kunlun fault. *Remote Sensing*, 13(16):3327.

Chen, J., Li, T., Sun, J., Fang, L., Yao, Y., Li, Y., Wang, H., and Fu, B. (2016). Coseismic surface ruptures and seismogenic Muji fault of the 25 November 2016 Arketao Mw 6.6 earthquake in northern Pamir. *seismology and Geology*, 38(4):1160–1174.

Chen, Q., Freymueller, J. T., Wang, Q., Yang, Z., Xu, C., and Liu, J. (2004). A deforming block model for the present-day tectonics of Tibet. *Journal of Geophysical Research: Solid Earth*, 109(B1).

Cheng, G. and Barnhart, W. D. (2021). Permanent co-seismic deformation of the 2013 Mw7. 7 Baluchistan, Pakistan earthquake from high-resolution surface strain analysis. *Journal of Geophysical Research: Solid Earth*, 126(3):e2020JB020622.

Chester, F. M. and Chester, J. S. (2000). Stress and deformation along wavy frictional faults. *Journal of Geophysical Research: Solid Earth*, 105(B10):23421–23430.

Cochran, E. S., Li, Y. G., Shearer, P. M., Barbot, S., Fialko, Y., and Vidale, J. E. (2009). Seismic and geodetic evidence for extensive, long-lived fault damage zones. *Geology*, 37(4):315–318.

Cooke, M. L. and Madden, E. H. (2014). Is the Earth lazy? A review of work minimization in fault evolution. *Journal of Structural Geology*, 66:334–346.

Cowie, P. A. and Scholz, C. H. (1992). Physical explanation for the displacement-length relationship of faults using a post-yield fracture mechanics model. *Journal of Structural Geology*, 14(10):1133–1148.

Cunningham, D. (2005). Active intracontinental transpressional mountain building in the Mongolian Altai: Defining a new class of orogen. *Earth and Planetary Science Letters*, 240:436–444.

Dai, S., Dai, W., Zhao, Z., Luo, J., Qiang, L., Ma, X., Zhang, X., and Xu, J. (2017). Timing, displacement and growth pattern of the Altyn Tagh Fault: a review. *Acta Geologica Sinica-English Edition*, 91(2):669–687.

Delorme, A., Grandin, R., Klinger, Y., Pierrot-Deseilligny, M., Feuillet, N., Jacques, E., Rupnik, E., and Morishita, Y. (2020). Complex deformation at shallow depth during the 30 October 2016 Mw6. 5 Norcia earthquake: interference between tectonic and gravity processes? *Tectonics*, 39(2):e2019TC005596.

Deng, J., Han, F., Li, T., Zhang, B., Xu, J., and Yao, Y. (2020). Late Quaternary slip sense and rate of the Muji fault, northeastern Pamir. *Quaternary Sciences*, 40(1):114r123.

Deng, Q.-D., Zhang, P., Ran, Y., Yang, X., Min, W., and Chen, L. (2003). Active tectonics and earthquake activities in China. *Earth Science Frontiers*.

Dieterich, J. H. and Smith, D. E. (2009). Nonplanar faults: Mechanics of slip and off-fault damage. In *Mechanics, structure and evolution of fault zones*, pages 1799–1815. Springer.

Dolan, J. F. and Haravitch, B. D. (2014). How well do surface slip measurements track slip at depth in large strike-slip earthquakes? The importance of fault structural maturity in controlling on-fault slip versus off-fault surface deformation. *Earth and Planetary Science Letters*, 388:38–47.

Duvall, A. R., Clark, M. K., Kirby, E., Farley, K. A., Craddock, W. H., Li, C., and Yuan, D.-Y. (2013). Low-temperature thermochronometry along the Kunlun and Haiyuan Faults, NE Tibetan Plateau: Evidence for kinematic change during late-stage orogenesis. *Tectonics*, 32(5):1190–1211.

Elliott, A., Elliott, J., Hollingsworth, J., Kulikova, G., Parsons, B., and Walker, R. (2020). Satellite imaging of the 2015 M 7.2 earthquake in the Central Pamir, Tajikistan, eluci-

dates a sequence of shallow strike-slip ruptures of the Sarez-Karakul fault. *Geophysical Journal International*, 221(3):1696–1718.

Elliott, J., Copley, A. C., Holley, R., Scharer, K., and Parsons, B. (2013). The 2011 Mw 7.1 Van (eastern Turkey) earthquake. *Journal of Geophysical Research: Solid Earth*, 118(4):1619–1637.

Elliott, J. R., Nissen, E. K., England, P. C., Jackson, J. A., Lamb, S., Li, Z., Oehlers, M., and Parsons, B. (2012). Slip in the 2010-2011 Canterbury earthquakes, New Zealand. *Journal of Geophysical Research: Solid Earth*, 117(B3):B03401.

Fan, G., Ni, J. F., and Wallace, T. C. (1994). Active tectonics of the Pamirs and Karakorum. *Journal of Geophysical Research: Solid Earth*, 99(B4):7131–7160.

Fan, W. and Shearer, P. M. (2016). Local near instantaneously dynamically triggered aftershocks of large earthquakes. *Science*, 353:1133–1136.

Fang, J., Ou, Q., Wright, T. J., Okuwaki, R., Amey, R. M., Craig, T. J., Elliott, J. R., Hooper, A., Lazeckỳ, M., and Maghsoudi, Y. (2022). Earthquake Cycle Deformation Associated With the 2021 MW 7.4 Maduo (Eastern Tibet) Earthquake: An Intrablock Rupture Event on a Slow-Slipping Fault From Sentinel-1 InSAR and Teleseismic Data. *Journal of Geophysical Research: Solid Earth*, 127(11):e2022JB024268.

Faulkner, D., Mitchell, T., Jensen, E., and Cembrano, J. (2011). Scaling of fault damage zones with displacement and the implications for fault growth processes. *Journal of Geophysical Research: Solid Earth*, 116(B5).

Feng, W., Tian, Y., Zhang, Y., Samsonov, S., Almeida, R., and Liu, P. (2017). A slip gap of the 2016 Mw 6.6 Muji, Xinjiang, China, earthquake inferred from Sentinel-1 TOPS interferometry. *Seismological Research Letters*, 88(4):1054–1064.

Fialko, Y., Sandwell, D., Agnew, D., Simons, M., Shearer, P., and Minster, B. (2002). Deformation on Nearby Faults Induced by the 1999 Hector Mine Earthquake. *Science*, 297(5588):1858–1862.

Fialko, Y., Sandwell, D., Simons, M., and Rosen, P. (2005). Three-dimensional deformation caused by the Bam, Iran, earthquake and the origin of shallow slip deficit. *Nature*, 435(7040):295–299.

Finzel, E. S., Flesch, L. M., Ridgway, K. D., Holt, W. E., and Ghosh, A. (2015). Surface motions and intraplate continental deformation in Alaska driven by mantle flow. *Geophysical Research Letters*, 42:4350–4358.

Fu, B. and Awata, Y. (2007). Displacement and timing of left-lateral faulting in the Kunlun Fault Zone, northern Tibet, inferred from geologic and geomorphic features. *Journal of Asian Earth Sciences*, 29(2-3):253–265.

Fuis, G. S., Clayton, R. W., Davis, P. M., Ryberg, T., Lutter, W. J., Okaya, D. A., Hauksson, E., Prodehl, C., Murphy, J. M., Benthien, M. L., Baher, S. A., Kohler, M. D., Thygesen, K., Simila, G., and Keller, G. R. (2003). Fault systems of the 1971 San Fernando and 1994 Northridge earthquakes, southern California: Relocated aftershocks and seismic images from LARSE II. *Geology*, 31(2):171.

Fuis, G. S., Moore, T. E., Plafker, G., Brocher, T. M., Fisher, M. A., Mooney, W. D., Nokleberg, W. J., Page, R. A., Beaudoin, B. C., and Christensen, N. I. (2008). Trans-Alaska Crustal Transect and continental evolution involving subduction underplating and synchronous foreland thrusting. *Geology*, 36(3):267–270.

Fuis, G. S., Murphy, J. M., Lutter, W. J., Moore, T. E., Bird, K. J., and Christensen, N. I. (1997). Deep seismic structure and tectonics of northern Alaska: Crustal-scale duplexing with deformation extending into the upper mantle. *Journal of Geophysical Research*, 102(B9):20,873–20,896.

Funning, G. (2005). *Source parameters of large shallow earthquakes in the Alpine-Himalayan belt from InSAR and waveform modelling*. PhD thesis, University of Oxford.

Funning, G. J., Parsons, B., and Wright, T. J. (2007). Fault slip in the 1997 Manyi, Tibet earthquake from linear elastic modelling of InSAR displacements. *Geophysical Journal International*, 169(3):988–1008.

Funning, G. J., Parsons, B., Wright, T. J., Jackson, J. A., and Fielding, E. J. (2005). Surface displacements and source parameters of the 2003 Bam (Iran) earthquake from Envisat advanced synthetic aperture radar imagery. *Journal of Geophysical Research: Solid Earth*, 110(B9):B09406.

Gabriel, A. K., Goldstein, R. M., and Zebker, H. A. (1989). Mapping small elevation changes over large areas: Differential radar interferometry. *Journal of Geophysical Research: Solid Earth*, 94(B7):9183–9191.

Gabuchian, V., Rosakis, A. J., Bhat, H. S., Madariaga, R., and Kanamori, H. (2017). Experimental evidence that thrust earthquake ruptures might open faults. *Nature*, 545(7654):336–339.

Gan, W., Molnar, P., Zhang, P., Xiao, G., Liang, S., Zhang, K., Li, Z., Xu, K., and Zhang, L. (2021). Initiation of clockwise rotation and eastward transport of southeastern Tibet inferred from deflected fault traces and GPS observations. *GSA Bulletin*, 134(5-6):1129–1142.

Gan, W., Zhang, P., Shen, Z.-K., Niu, Z., Wang, M., Wan, Y., Zhou, D., and Cheng, J. (2007). Present-day crustal motion within the Tibetan Plateau inferred from GPS measurements. *Journal of Geophysical Research: Solid Earth*, 112(B8).

Garthwaite, M. C., Wang, H., and Wright, T. J. (2013). Broadscale interseismic deformation and fault slip rates in the central Tibetan Plateau observed using InSAR. *Journal of Geophysical Research: Solid Earth*, 118(9):5071–5083.

Gaudreau, É., Nissen, E. K., Bergman, E. A., Benz, H. M., Tan, F., and Karasözen, E. (2019). The August 2018 Kaktovik Earthquakes: Active Tectonics in Northeastern Alaska Revealed With InSAR and Seismology. *Geophysical Research Letters*, 46(24):14,412–14,420.

Ghods, A., Shabanian, E., Bergman, E., Faridi, M., Donner, S., Mortezanejad, G., and Aziz-Zanjani, A. (2015). The Varzaghan-Ahar, Iran, Earthquake Doublet ($M_w$ 6.4, 6.2): implications for the geodynamics of northwest Iran. *Geophysical Journal International*, 203(1):522–540.

Gold, R. D., Clark, D., Barnhart, W. D., King, T., Quigley, M., and Briggs, R. W. (2019). Surface Rupture and Distributed Deformation Revealed by Optical Satellite Imagery: The Intraplate 2016 $M_w$ 6.0 Petermann Ranges Earthquake, Australia. *Geophysical Research Letters*, 46(10394):10,394–10,403.

Gold, R. D., Cowgill, E., Arrowsmith, J. R., Chen, X., Sharp, W. D., Cooper, K. M., and Wang, X.-F. (2011). Faulted terrace risers place new constraints on the late Quaternary slip rate for the central Altyn Tagh fault, northwest Tibet. *GSA Bulletin*, 123(5-6):958–978.

Gold, R. D., Cowgill, E., Arrowsmith, J. R., Gosse, J., Chen, X., and Wang, X.-F. (2009). Riser diachroneity, lateral erosion, and uncertainty in rates of strike-slip faulting: A case

study from Tuzidun along the Altyn Tagh Fault, NW China. *Journal of Geophysical Research: Solid Earth*, 114(B4).

Gold, R. D., DuRoss, C. B., and Barnhart, W. D. (2021). Coseismic Surface Displacement in the 2019 Ridgecrest Earthquakes: Comparison of Field Measurements and Optical Image Correlation Results. *Geochemistry, Geophysics, Geosystems*, 22(3):e09326.

Goldstein, R. M., Engelhardt, H., Kamb, B., and Frolich, R. M. (1993). Satellite Radar Interferometry for Monitoring Ice Sheet Motion: Application to an Antarctic Ice Stream. *Science*, 262(5139):1525–1530.

Gomberg, J., Bodin, P., and Reasenberg, P. A. (2003). Observing Earthquakes Triggered in the Near Field by Dynamic Deformations. *Bulletin of the Seismological Society of America*, 93:118–138.

Gombert, B., Duputel, Z., Jolivet, R., Doubre, C., Rivera, L., and Simons, M. (2018). Revisiting the 1992 Landers earthquake: a Bayesian exploration of co-seismic slip and off-fault damage. *Geophysical Journal International*, 212(2):839–852.

Grandin, R., Klein, E., Métois, M., and Vigny, C. (2016). Three-dimensional displacement field of the 2015 Mw8.3 Illapel earthquake (Chile) from across-and along-track Sentinel-1 TOPS interferometry. *Geophysical Research Letters*, 43(6):2552–2561.

Grantz, A., Dinter, D. A., and Biswas, N. N. (1983). Map, cross sections, and chart showing late Quaternary faults, folds, and earthquake epicenters on the Alaskan Beaufort Shelf, Map I-1182-C, 1:500,000 scale. In *Miscellaneous Investigations Series*. U.S. Geological Survey.

Griffith, W. A., Nielsen, S., Di Toro, G., and Smith, S. A. (2010). Rough faults, distributed weakening, and off-fault deformation. *Journal of Geophysical Research: Solid Earth*, 115(B8).

Guatteri, M. and Spudich, P. (1998). Coseismic temporal changes of slip direction: the effect of absolute stress on dynamic rupture. *Bulletin of the Seismological Society of America*, 88(3):777–789.

Guo, J., Zheng, J., Guan, B., Fu, B., Shi, P., Du, J., Xie, C., and Liu, L. (2012). Coseismic surface rupture structures associated with 2010 Ms 7.1 Yushu earthquake, China. *Seismological Research Letters*, 83(1):109–118.

Guo, N., Wu, Y., and Zhang, Q. (2022). Coseismic and Pre-seismic Deformation Characteristics of the 2022 MS 6.9 Menyuan Earthquake, China. *Pure and Applied Geophysics*, 179(9):3177–3190.

Guo, P., Han, Z., Gao, F., Zhu, C., and Gai, H. (2020). A new tectonic model for the 1927 M8. 0 Gulang earthquake on the NE Tibetan Plateau. *Tectonics*, 39(9):e2020TC006064.

Guo, P., Han, Z., Mao, Z., Xie, Z., Dong, S., Gao, F., and Gai, H. (2019). Paleoearthquakes and rupture behavior of the Lenglongling fault: Implications for seismic hazards of the northeastern margin of the Tibetan Plateau. *Journal of Geophysical Research: Solid Earth*, 124(2):1520–1543.

Guo, R., Yang, H., Li, Y., Zheng, Y., and Zhang, L. (2021). Complex slip distribution of the 2021 Mw 7.4 Maduo, China, earthquake: An event occurring on the slowly slipping fault. *Seismological Research Letters*, 93(2A):653–665.

Haeussler, P. J. (2008). An overview of the neotectonics of interior Alaska: Far-field deformation from the Yakutat Microplate collision. *Washington DC American Geophysical Union Geophysical Monograph Series*, 179:83–108.

Hampel, A., Li, T., and Maniatis, G. (2013). Contrasting strike-slip motions on thrust and normal faults: Implications for space-geodetic monitoring of surface deformation. *Geology*, 41(3):299–302.

Han, B., Liu, Z., Chen, B., Li, Z., Yu, C., Zhang, Y., and Peng, J. (2023a). Coseismic deformation and slip distribution of the 2022 Luding Mw 6.6 earthquake revealed by InSAR observations. *Geomatics and Information Science of Wuhan University*, 48(1):36–46.

Han, N., Zhang, G., Shan, X., Zhang, Y., Hetland, E., Qu, C., Gong, W., Sun, G., Li, C., Fan, X., et al. (2023b). Coseismic Surface Horizontal Deformation of the 2022 Mw 6.6 Menyuan, Qinghai, China, Earthquake from Optical Pixel Correlation of GF-7 Stereo Satellite Images. *Seismological Society of America*.

Hanks, C., Parker, M., and Jemison, E. (2000). Borehole breakouts and implications for regional in situ stress patterns of the northeastern North Slope, Alaska. In Pinney, D. and Davis, P., editors, *Short notes on Alaska geology 1999*. Alaska Division of Geological & Geophysical Surveys Professional Report 119C.

Hannula, K. A., Miller, E. L., Dumitru, T. A., Lee, J., and Rubin, C. M. (1995). Structural and metamorphic relations in the southwest Seward Peninsula, Alaska: Crustal extension and the unroofing of blueschists. *Geological Society of America Bulletin*, 107(5):536–553.

Harkins, N., Kirby, E., Shi, X., Wang, E., Burbank, D., and Chun, F. (2010). Millennial slip rates along the eastern Kunlun fault: Implications for the dynamics of intracontinental deformation in Asia. *Lithosphere*, 2(4):247–266.

Harrington, R. M. and Brodsky, E. E. (2009). Source duration scales with magnitude differently for earthquakes on the San Andreas Fault and on secondary faults in Parkfield, California. *Bulletin of the Seismological Society of America*, 99(4):2323–2334.

Hatem, A. E., Cooke, M. L., and Toeneboehn, K. (2017). Strain localization and evolving kinematic efficiency of initiating strike-slip faults within wet kaolin experiments. *Journal of Structural Geology*, 101:96–108.

He, K., Wen, Y., Xu, C., and Zhao, Y. (2022). Fault geometry and slip distribution of the 2021 Mw 7.4 Maduo, China, earthquake inferred from InSAR measurements and relocated aftershocks. *Seismological Research Letters*, 93(1):8–20.

He, P., Ding, K., and Xu, C. (2018). The 2016 Mw 6.7 Aketao earthquake in Muji range, northern Pamir: rupture on a strike-slip fault constrained by Sentinel-1 radar interferometry and GPS. *International Journal of Applied Earth Observation and Geoinformation*, 73:99–106.

He, P., Liu, C., Wen, Y., Hu, X., Ding, K., and Xu, C. (2023). The 2022 Mw 6.6 Menyuan Earthquake in the Northwest Margin of Tibet: Geodetic and Seismic Evidence of the Fault Structure and Slip Behavior of the Qilian–Haiyuan Strike-Slip Fault. *Seismological Society of America*, 94(1):26–38.

Heath, E. G. and Leighton, F. B. (1973). Subsurface Investigation of Ground Rupturing During San Fernando Earthquake. In Murphy, L., editor, *San Fernando, California, Earthquake of February 9, 1971*, volume 3, pages 165 – 172. U.S. Department of Commerce, National Oceanic and Atmospheric Administration, Washington, D.C., USA.

Heaton, T. H. and Helmberger, D. V. (1979). Generalized ray models of the San Fernando earthquake. *Bulletin of the Seismological Society of America*, 69(5):1311–1341.

Heaton, Thomas H (1982). The 1971 San Fernando earthquake: A double event? *Bulletin of the Seismological Society of America*, 72(6A):2037–2062.

Herman, M. W., Herrmann, R. B., Benz, H. M., and Furlong, K. P. (2014). Using regional moment tensors to constrain the kinematics and stress evolution of the 2010–2013 Canterbury earthquake sequence, South Island, New Zealand. *Tectonophysics*, 633:1–15.

Herrmann, R. B., Benz, H., and Ammon, C. J. (2011). Monitoring the earthquake source process in North America. *Bulletin of the Seismological Society of America*, 101(6):2609–2625.

Hong, S., Zhou, X., Zhang, K., Meng, G., Dong, Y., Su, X., Zhang, L., Li, S., and Ding, K. (2018). Source model and stress disturbance of the 2017 Jiuzhaigou Mw 6.5 earthquake constrained by InSAR and GPS measurements. *Remote Sensing*, 10(9):1400.

Huang, C., Zhang, G., Zhao, D., Shan, X., Xie, C., Tu, H., Qu, C., Zhu, C., Han, N., and Chen, J. (2022a). Rupture Process of the 2022 Mw6.6 Menyuan, China, Earthquake from Joint Inversion of Accelerogram Data and InSAR Measurements. *Remote Sensing*, 14(20):5104.

Huang, Y. (2018). Earthquake rupture in fault zones with along-strike material heterogeneity. *Journal of Geophysical Research: Solid Earth*, 123(11):9884–9898.

Huang, Z., Zhou, Y., Qiao, X., Zhang, P., and Cheng, X. (2022b). Kinematics of the 1000 km Haiyuan fault system in northeastern Tibet from high-resolution Sentinel-1 InSAR velocities: Fault architecture, slip rates, and partitioning. *Earth and Planetary Science Letters*, 583:117450.

Hussain, E., Wright, T. J., Walters, R. J., Bekaert, D. P., Lloyd, R., and Hooper, A. (2018). Constant strain accumulation rate between major earthquakes on the North Anatolian Fault. *Nature Communications*, 9(1):1392.

Jackson, J., Bouchon, M., Fielding, E., Funning, G., Ghorashi, M., Hatzfeld, D., Nazari, H., Parsons, B., Priestley, K., Talebian, M., et al. (2006). Seismotectonic, rupture process, and earthquake-hazard aspects of the 2003 December 26 Bam, Iran, earthquake. *Geophysical Journal International*, 166(3):1270–1292.

Jara, J., Bruhat, L., Thomas, M. Y., Antoine, S. L., Okubo, K., Rougier, E., Rosakis, A. J., Sammis, C. G., Klinger, Y., Jolivet, R., et al. (2021). Signature of transition to supershear

rupture speed in the coseismic off-fault damage zone. *Proceedings of the Royal Society A*, 477(2255):20210364.

Jiang, C., Schmandt, B., Ward, K. M., Lin, F.-C., and Worthington, L. L. (2018). Upper Mantle Seismic Structure of Alaska From Rayleigh and S Wave Tomography. *Geophysical Research Letters*, 45(19):10,350–10,359.

Jiang, G., Xu, C., Wen, Y., Liu, Y., Yin, Z., and Wang, J. (2013). Inversion for coseismic slip distribution of the 2010 Mw 6.9 Yushu Earthquake from InSAR data using angular dislocations. *Geophysical Journal International*, 194(2):1011–1022.

Jiang, W., Han, Z., Guo, P., Zhang, J., Jiao, Q., Kang, S., and Tian, Y. (2017). Slip rate and recurrence intervals of the east Lenglongling fault constrained by morphotectonics: Tectonic implications for the northeastern Tibetan Plateau. *Lithosphere*, 9(3):417–430.

Jin, Z. and Fialko, Y. (2021). Coseismic and early postseismic deformation due to the 2021 M7.4 Maduo (China) earthquake. *Geophysical Research Letters*, 48(21):e2021GL095213.

Jin, Z., Fialko, Y., Zubovich, A., and Schöne, T. (2022). Lithospheric deformation due to the 2015 M7. 2 Sarez (Pamir) earthquake constrained by 5 years of space geodetic observations. *Journal of Geophysical Research: Solid Earth*, 127(4).

Jónsson, S., Zebker, H., Segall, P., and Amelung, F. (2002). Fault slip distribution of the 1999 $M_w$ 7.1 Hector Mine, California, earthquake, estimated from satellite radar and GPS measurements. *Bulletin of the Seismological Society of America*, 92(4):1377–1389.

Jordan, T. H. and Sverdrup, K. A. (1981). Teleseismic location techniques and their application to earthquake clusters in the south-central Pacific. *Bulletin of the Seismological Society of America*, 71(4):1105–1130.

Kahle, J. E. (1975). Surface Effects and Related Geology of the Lakeview Fault Segment of the San Fernando Fault Zone. In Oakeshott, G., editor, *San Fernando Earthquake of 9 February 1971*, volume 196, pages 119–135. California Division of Mines and Geology, Sacramento, CA.

Kamb, B., Silver, L., Abrams, L., Carter, B., Jordan, T., and Minster, J. (1971). Pattern of faulting and nature of fault movement in the San Fernando earthquake. In *The San Fernando, California Earthquake of February 9th, 1971*, pages 41 – 55. U.S. Geological Survey Professional Paper 733.

Kaneko, Y. and Fialko, Y. (2011). Shallow slip deficit due to large strike-slip earthquakes in dynamic rupture simulations with elasto-plastic off-fault response. *Geophysical Journal International*, 186(3):1389–1403.

Karasözen, E., Nissen, E., Bergman, E. A., Johnson, K. L., and Walters, R. J. (2016). Normal faulting in the Simav graben of western Turkey reassessed with calibrated earthquake relocations. *Journal of Geophysical Research: Solid Earth*, 121(6):4553–4574.

Kearse, J. and Kaneko, Y. (2020). On-Fault Geological Fingerprint of Earthquake Rupture Direction. *Journal of Geophysical Research: Solid Earth*, 125(9):e19863.

Kennett, B. L. N. and Engdahl, E. R. (1991). Traveltimes for Global Earthquake Location and Phase Identification. *Geophysical Journal International*, 105:429–465.

Kim, J. (1989). *Complex seismic sources and time-dependent moment tensor inversion*. PhD thesis, University of Arizona.

Kim, Y.-S., Peacock, D. C. P., and Sanderson, D. J. (2004). Fault damage zones. *Journal of Structural Geology*, 26(3):503–517.

Kirby, E. and Harkins, N. (2013). Distributed deformation around the eastern tip of the Kunlun fault. *International Journal of Earth Sciences*, 102:1759–1772.

Kirby, E., Harkins, N., Wang, E., Shi, X., Fan, C., and Burbank, D. (2007). Slip rate gradients along the eastern Kunlun fault. *Tectonics*, 26(2).

Klinger, Y., Michel, R., and King, G. (2006). Evidence for an earthquake barrier model from Mw 7.8 Kokoxili (Tibet) earthquake slip-distribution. *Earth and Planetary Science Letters*, 242(3-4):354–364.

Klinger, Y., Xu, X., Tapponnier, P., Van der Woerd, J., Lasserre, C., and King, G. (2005). High-resolution satellite imagery mapping of the surface rupture and slip distribution of the Mw 7.8, 14 November 2001 Kokoxili earthquake, Kunlun fault, northern Tibet, China. *Bulletin of the Seismological Society of America*, 95(5):1970–1987.

Koehler, R. (2013). Quaternary faults and folds (QFF). http://maps.dggs.alaska.gov/qff. http://doi.org/10.14509/24956.

Koper, K. D., Hutko, A. R., Lay, T., and Sufri, O. (2012). Imaging short-period seismic radiation from the 27 February 2010 Chile ($M_w$ 8.8) earthquake by back-projection of P, PP, and PKIKP waves. *Journal of Geophysical Research: Solid Earth*, 117(B2):B02308.

Langenheim, V. E., Wright, T. L., Okaya, D. A., Yeats, R. S., Fuis, G. S., Thygesen, K., and Thybo, H. (2011). Structure of the San Fernando Valley region, California: Implications for seismic hazard and tectonic history. *Geosphere*, 7(2):528–572.

Langston, C. A. (1978). The February 9, 1971 San Fernando earthquake: a study of source finiteness in teleseismic body waves. *Bulletin of the Seismological Society of America*, 68(1):1–29.

Larson, K. M., Bürgmann, R., Bilham, R., and Freymueller, J. T. (1999). Kinematics of the India-Eurasia collision zone from GPS measurements. *Journal of Geophysical Research: Solid Earth*, 104(B1):1077–1093.

Lasserre, C., Peltzer, G., Crampé, F., Klinger, Y., van Der Woerd, J., and Tapponnier, P. (2005). Coseismic deformation of the 2001 Mw= 7.8 Kokoxili earthquake in Tibet, measured by synthetic aperture radar interferometry. *Journal of Geophysical Research: Solid Earth*, 110(B12).

Lauer, B., Grandin, R., and Klinger, Y. (2020). Fault geometry and slip distribution of the 2013 Mw 7.7 Balochistan earthquake from inversions of SAR and optical data. *Journal of Geophysical Research: Solid Earth*, 125(7):e2019JB018380.

Leonard, L. J., Mazzotti, S., and Hyndman, R. D. (2008). Deformation rates estimated from earthquakes in the northern Cordillera of Canada and eastern Alaska. *Journal of Geophysical Research: Solid Earth*, 113(B8):B08406.

Leprince, S., Barbot, S., Ayoub, F., and Avouac, J.-P. (2007). Automatic and Precise Orthorectification, Coregistration, and Subpixel Correlation of Satellite Images, Application to Ground Deformation Measurements. *IEEE Transactions on Geoscience and Remote Sensing*, 45:1529–1558.

Levi, S. and Yeats, R. S. (1993). Paleomagnetic constraints on the initiation of uplift on the Santa Susana Fault, Western Transverse Ranges, California. *Tectonics*, 12(3):688–702.

Li, C., Li, T., Shan, X., and Zhang, G. (2022a). Extremely Large Off-Fault Deformation during the 2021 Mw 7.4 Maduo, Tibetan Plateau, Earthquake. *Seismological Society of America*, 94(1):39–51.

Li, C., Wang, X., He, C., Wu, X., Kong, Z., and Li, X. (2019a). China National Digital Geological Map (Public Version at 1:200 000 Scale) Spatial Database[J]. *Geology in China*, 46(S1):1–10.

Li, C., Zhang, P.-Z., Yin, J., and Min, W. (2009). Late Quaternary left-lateral slip rate of the Haiyuan fault, northeastern margin of the Tibetan Plateau. *Tectonics*, 28(5).

Li, C., Zheng, D., Zhou, R., Yu, J., Wang, Y., Pang, J., Wang, Y., Hao, Y., and Li, Y. (2021). Late Oligocene tectonic uplift of the East Kunlun Shan: expansion of the northeastern Tibetan Plateau. *Geophysical Research Letters*, 48(3):e2020GL091281.

Li, T., Schoenbohm, L. M., Chen, J., Yuan, Z., Feng, W., Li, W., Xu, J., Owen, L. A., Sobel, E. R., Zhang, B., et al. (2019b). Cumulative and coseismic (during the 2016 Mw 6.6 Aketao earthquake) deformation of the dextral-slip Muji Fault, northeastern Pamir orogen. *Tectonics*, 38(11):3975–3989.

Li, X., Xu, W., Jónsson, S., Klinger, Y., and Zhang, G. (2020a). Source model of the 2014 Mw 6.9 Yutian earthquake at the southwestern end of the Altyn Tagh fault in Tibet estimated from satellite images. *Seismological Research Letters*, 91(6):3161–3170.

Li, Y., Bürgmann, R., and Zhao, B. (2020b). Evidence of Fault Immaturity from Shallow Slip Deficit and Lack of Postseismic Deformation of the 2017 Mw 6.5 Jiuzhaigou Earthquake. *Bulletin of the Seismological Society of America*, 110(1):154–165.

Li, Y., Shan, X., Qu, C., and Wang, Z. (2016). Fault locking and slip rate deficit of the Haiyuan-Liupanshan fault zone in the northeastern margin of the Tibetan Plateau. *Journal of Geodynamics*, 102:47–57.

Li, Y., Zhao, D., Shan, X., Gao, Z., Huang, X., and Gong, W. (2022b). Coseismic Slip Model of the 2022 Mw 6.7 Luding (Tibet) Earthquake: Pre-and Post-Earthquake Interactions With Surrounding Major Faults. *Geophysical Research Letters*, 49(24):e2022GL102043.

Li, Z., Elliott, J. R., Feng, W., Jackson, J. A., Parsons, B. E., and Walters, R. J. (2011). The 2010 Mw 6.8 Yushu (Qinghai, China) earthquake: Constraints provided by InSAR and body wave seismology. *Journal of Geophysical Research: Solid Earth*, 116(B10).

Lindvall, S. C. and Rubin, C. M. (2008). Slip rate studies along the Sierra Madre-Cucamonga fault system using geomorphic and cosmogenic surface exposure age constraints: collaborative research with Central Washington University and William Lettis & Associates, Inc. *Final Technical Report, NEHRP External Grant Award Number 03HQGR0084*, page 13 p.

Liu, J., Hu, J., Li, Z., Ma, Z., Wu, L., Jiang, W., Feng, G., and Zhu, J. (2022a). Complete three-dimensional coseismic displacements due to the 2021 Maduo earthquake in Qinghai Province, China from Sentinel-1 and ALOS-2 SAR images. *Science China Earth Sciences*, 65(4):687–697.

Liu, J., Milne, R. I., Zhu, G.-F., Spicer, R. A., Wambulwa, M. C., Wu, Z.-Y., Boufford, D. E., Luo, Y.-H., Provan, J., Yi, T.-S., et al. (2022b). Name and scale matters: Clarifying the geography of Tibetan Plateau and adjacent mountain regions. *Global and Planetary Change*, page 103893.

Liu, Y., Shan, X., Qu, C., and Zhang, G. (2011). Earthquake deformation field characteristics associated with the 2010 Yushu M s 7.1 earthquake. *Science China Earth Sciences*, 54(4):571–580.

Liu, Y., Zhao, D., and Shan, X. (2022c). Asymmetric Interseismic Strain across the Western Altyn Tagh Fault from InSAR. *Remote Sensing*, 14(9):2112.

Lockner, D., Byerlee, J., Kuksenko, V., Ponomarev, A., and Sidorin, A. (1991). Quasi-static fault growth and shear fracture energy in granite. *Nature*, 350(6313):39–42.

Loveless, J. P. and Meade, B. J. (2011). Partitioning of localized and diffuse deformation in the Tibetan Plateau from joint inversions of geologic and geodetic observations. *Earth and Planetary Science Letters*, 303(1-2):11–24.

Lü, M., Chen, K., Chai, H., Geng, J., Zhang, S., and Fang, L. (2022). Joint inversion of InSAR and high-rate GNSS displacement waveforms for the rupture process of the 2022 Qinghai Menyuan M6.9 earthquake. *Chinese Journal of Geophysics*, 65(12):4725–4738.

Luo, H. and Wang, T. (2022). Strain partitioning on the western Haiyuan fault system revealed by the adjacent 2016 Mw5. 9 and 2022 Mw6.7 Menyuan earthquakes. *Geophysical Research Letters*, 49(16):e2022GL099348.

Lyakhovsky, V. and Ben-Zion, Y. (2009). Evolving geometrical and material properties of fault zones in a damage rheology model. *Geochemistry, Geophysics, Geosystems*, 10(11).

Lyakhovsky, V., Ben-Zion, Y., and Agnon, A. (1997). Distributed damage, faulting, and friction. *Journal of Geophysical Research: Solid Earth*, 102(B12):27635–27649.

Ma, S. (2008). A physical model for widespread near-surface and fault zone damage induced by earthquakes. *Geochemistry, Geophysics, Geosystems*, 9(11):Q11009.

Ma, S. and Andrews, D. (2010). Inelastic off-fault response and three-dimensional dynamics of earthquake rupture on a strike-slip fault. *Journal of Geophysical Research: Solid Earth*, 115(B4).

Maley, R. and Cloud, W. (1971). Preliminary strong-motion results from the San Fernando earthquake of February 9, 1971. In *The San Fernando, California Earthquake of February 9th, 1971*, pages 163 – 176. U.S. Geological Survey Professional Paper 733.

Manighetti, I., Campillo, M., Bouley, S., and Cotton, F. (2007). Earthquake scaling, fault segmentation, and structural maturity. *Earth and Planetary Science Letters*, 253(3-4):429–438.

Manighetti, I., Mercier, A., and De Barros, L. (2021). Fault trace corrugation and segmentation as a measure of fault structural maturity. *Geophysical Research Letters*, 48(20):e2021GL095372.

Marchandon, M., Hollingsworth, J., and Radiguet, M. (2021). Origin of the shallow slip deficit on a strike slip fault: Influence of elastic structure, topography, data coverage, and noise. *Earth and Planetary Science Letters*, 554:116696.

Marone, C. (1998). Laboratory-derived friction laws and their application to seismic faulting. *Annual Review of Earth and Planetary Sciences*, 26(1):643–696.

Marone, C., Scholtz, C., and Bilham, R. (1991). On the mechanics of earthquake afterslip. *Journal of Geophysical Research: Solid Earth*, 96(B5):8441–8452.

Martel, S. J., Pollard, D. D., and Segall, P. (1988). Development of simple strike-slip fault zones, Mount Abbot quadrangle, Sierra Nevada, California. *Geological Society of America Bulletin*, 100(9):1451–1465.

Massonnet, D., Rossi, M., Carmona, C., Adragna, F., Peltzer, G., Feigl, K., and Rabaute, T. (1993). The displacement field of the Landers earthquake mapped by radar interferometry. *Nature*, 364(6433):138–142.

Mazzotti, S. and Hyndman, R. D. (2002). Yakutat collision and strain transfer across the northern Canadian Cordillera. *Geology*, 30:495.

Mazzotti, S., Leonard, L. J., Hyndman, R. D., and Cassidy, J. F. (2008). Tectonics, dynamics, and seismic hazard in the Canada-Alaska Cordillera. *Washington DC American Geophysical Union Geophysical Monograph Series*, 179:297–319.

Meade, B. K. and Miller, R. W. (1973). Horizontal Crustal Movements Determined From Surveys After San Fernando Earthquake. In Murphy, L., editor, *San Fernando, California, Earthquake of February 9, 1971*, volume 3, pages 243 – 293. U.S. Department of Commerce, National Oceanic and Atmospheric Administration, Washington, D.C., USA.

Metzger, S., Schurr, B., Ratschbacher, L., Sudhaus, H., Kufner, S.-K., Schöne, T., Zhang, Y., Perry, M., and Bendick, R. (2017). The 2015 Mw7. 2 Sarez strike-slip earthquake in the Pamir interior: Response to the underthrusting of India's western promontory. *Tectonics*, 36(11):2407–2421.

Meyer, B., Tapponnier, P., Bourjot, L., Metivier, F., Gaudemer, Y., Peltzer, G., Shunmin, G., and Zhitai, C. (1998). Crustal thickening in Gansu-Qinghai, lithospheric mantle subduction, and oblique, strike-slip controlled growth of the Tibet plateau. *Geophysical Journal International*, 135(1):1–47.

Meyer, F. J., Webley, P. W., Dehn, J., Arko, S. A., McAlpin, D. B., and Gong, W. (2016). The SARVIEWS Project: Automated SAR Processing in Support of Operational Near Real-time Volcano Monitoring. *AGU Fall Meeting Abstracts*.

Miller, M. S., O'Driscoll, L. J., Porritt, R. W., and Roeske, S. M. (2018). Multiscale crustal architecture of Alaska inferred from P receiver functions. *Lithoshere*, 10(2):267–278.

Milliner, C., Donnellan, A., Aati, S., Avouac, J.-P., Zinke, R., Dolan, J. F., Wang, K., and Bürgmann, R. (2021). Bookshelf Kinematics and the Effect of Dilatation on Fault Zone Inelastic Deformation: Examples From Optical Image Correlation Measurements of the 2019 Ridgecrest Earthquake Sequence. *Journal of Geophysical Research: Solid Earth*, 126(3):e2020JB020551.

Milliner, C. W. D., Dolan, J. F., Hollingsworth, J., Leprince, S., Ayoub, F., and Sammis, C. G. (2015). Quantifying near-field and off-fault deformation patterns of the 1992 $M_W$ 7.3 Landers earthquake. *Geochemistry, Geophysics, Geosystems*, 16(5):1577–1598.

Mitchell, T. and Faulkner, D. (2009). The nature and origin of off-fault damage surrounding strike-slip fault zones with a wide range of displacements: A field study from the Atacama fault system, northern Chile. *Journal of Structural Geology*, 31(8):802–816.

Molenaar, C., Mull, C., and Swauger, D. (1987). *Geologic features of Ignek Valley and adjacent mountains, northeastern Alaska*, volume 1, pages 473–478. Cordilleran Section of the Geological Society of America.

Molnar, P. and Lyon-Caen, H. (1989). Fault plane solutions of earthquakes and active tectonics of the Tibetan Plateau and its margins. *Geophysical Journal International*, 99(1):123–153.

Molnar, P. and Stock, J. M. (2009). Slowing of India's convergence with Eurasia since 20 Ma and its implications for Tibetan mantle dynamics. *Tectonics*, 28(3).

Molnar, P. and Tapponnier, P. (1975). Cenozoic Tectonics of Asia: Effects of a Continental Collision: Features of recent continental tectonics in Asia can be interpreted as results of the India-Eurasia collision. *Science*, 189(4201):419–426.

Moore, T. (1992). The Arctic Alaska superterrane. In Bradley, D. and Dusel-Bacon, C., editors, *Geologic studies in Alaska by the U.S. Geological Survey, 1991: Geological Survey Bulletin*, volume 2041 of *Geological Survey Bulletin*, pages 238–244. U.S. Geological Survey, Washington, D.C.

Moore, T. E. and Box, S. E. (2016). Age, distribution and style of deformation in Alaska north of 60°N: Implications for assembly of Alaska. *Tectonophysics*, 691:133–170.

Moore, T. E., Wallace, W. K., Bird, K. J., Karl, S. M., Mull, C. G., and Dillon, J. T. (1994). Geology of northern Alaska. In Plafker, G. and Berg, H., editors, *The Geology of Alaska*, volume G-1 of *The Geology of North America*, pages 49–140. Geological Society of America, Boulder, CO.

Moore, T. E., Wallace, W. K., Mull, C. G., Adams, K. E., Plafker, G., and Nokleberg, W. J. (1997). Crustal implications of bedrock geology along the Trans-Alaska Crustal Transect (TACT) in the Brooks Range, northern Alaska. *Journal of Geophysical Research: Solid Earth*, 102(B9):20645–20684.

Mori, J., Wald, D. J., and Wesson, R. L. (1995). Overlapping fault planes of the 1971 San Fernando and 1994 Northridge, California earthquakes. *Geophysical Research Letters*, 22(9):1033–1036.

Morrison, N. L. (1973). Vertical Crustal Movements Determined From Surveys Before and After San Fernando Earthquake. In Murphy, L., editor, *San Fernando, California, Earthquake of February 9, 1971*, volume 3, pages 295 – 324. U.S. Department of Commerce, National Oceanic and Atmospheric Administration, Washington, D.C., USA.

Nason, R. D. (1973). Increased seismic shaking above a thrust fault. In Oakeshott, G., Benfer, N. A., Coffman, J. L., Bernick, J. R., and Dees, L. T., editors, *San Fernando, California, Earthquake of 9, February 1971*, volume 3, pages 123–126. U.S. Department of Commerce, Washington, DC.

Niu, P., Han, Z., Li, K., Lv, L., and Guo, P. (2023). The 2022 Mw 6.7 Menyuan Earthquake on the Northeastern Margin of the Tibetan Plateau, China: Complex Surface Ruptures and Large Slip. *Bulletin of the Seismological Society of America*.

O'Driscoll, L. J. and Miller, M. S. (2015). Lithospheric discontinuity structure in Alaska, thickness variations determined by Sp receiver functions. *Tectonics*, 34(4):694–714.

Oglesby, D. D. (2000). The Three-Dimensional Dynamics of Dipping Faults. *The Bulletin of the Seismological Society of America*, 90(3):616–628.

Oglesby, D. D. and Day, S. M. (2001a). Fault geometry and the dynamics of the 1999 Chi-Chi (Taiwan) earthquake. *Bulletin of the Seismological Society of America*, 91(5):1099–1111.

Oglesby, D. D. and Day, S. M. (2001b). The effect of fault geometry on the 1999 Chi-Chi (Taiwan) earthquake. *Geophysical Research Letters*, 28(9):1831–1834.

Okada, Y. (1985). Surface deformation due to shear and tensile faults in a half-space. *Bulletin of the Seismological Society of America*, 75(4):1135–1154.

Oskin, M. E., Arrowsmith, J. R., Corona, A. H., Elliott, A. J., Fletcher, J. M., Fielding, E. J., Gold, P. O., Garcia, J. J. G., Hudnut, K. W., Liu-Zeng, J., et al. (2012). Near-field deformation from the El Mayor–Cucapah earthquake revealed by differential LIDAR. *Science*, 335(6069):702–705.

O'Sullivan, P., Green, P., S.C., B., Decker, J., I.R., D., Gleadow, A., and D.L., T. (1993). Multiple phases of Tertiary uplift and erosion in the Arctic Wildlife Refuge, Alaska, revealed by apatite fission track analysis. *AAPG Bulletin*, 77(3):359–385.

O'Sullivan, P. B. and Wallace, W. K. (2002). Out-of-sequence, basement-involved structures in the Sadlerochit Mountains region of the Arctic National Wildlife Refuge, Alaska: Evidence and implications from fission-track thermochronology. *Geological Society of America Bulletin*, 114(11):1356–1378.

Ou, Q., Daout, S., Weiss, J., Shen, L., Lazeckỳ, M., Wright, T. J., and Parsons, B. E. (2022). Large-Scale Interseismic Strain Mapping of the NE Tibetan Plateau From Sentinel-1 Interferometry. *Journal of Geophysical Research: Solid Earth*, 127(6):e2022JB024176.

Pan, J., Li, H., Chevalier, M.-L., Tapponnier, P., Bai, M., Li, C., Liu, F., Liu, D., Wu, K., Wang, P., et al. (2022). Co-seismic rupture of the 2021, Mw7. 4 Maduo earthquake (northern Tibet): Short-cutting of the Kunlun fault big bend. *Earth and Planetary Science Letters*, 594:117703.

Perrin, C., Manighetti, I., Ampuero, J.-P., Cappa, F., and Gaudemer, Y. (2016). Location of largest earthquake slip and fast rupture controlled by along-strike change in fault structural maturity due to fault growth. *Journal of Geophysical Research: Solid Earth*, 121(5):3666–3685.

Poliakov, A. N., Dmowska, R., and Rice, J. R. (2002). Dynamic shear rupture interactions with fault bends and off-axis secondary faulting. *Journal of Geophysical Research: Solid Earth*, 107(B11):ESE–6.

Porter, C., Morin, P., Howat, I., Noh, M.-J., Bates, B., Peterman, K., Keesey, S., Schlenk, M., Gardiner, J., Tomko, K., Willis, M., Kelleher, C., Cloutier, M., Husby, E., Foga, S., Nakamura, H., Platson, M., Wethington, Michael, J., Williamson, C., Bauer, G., Enos, J., Arnold, G., Kramer, W., Becker, P., Doshi, A., D'Souza, C., Cummens, P., Laurier, F., and Bojesen, M. (2018). ArcticDEM. https://doi.org/10.7910/DVN/OHHUKH. Accessed: 12/05/2018.

Pousse-Beltran, L., Nissen, E., Bergman, E. A., Cambaz, M. D., Gaudreau, É., Karasözen, E., and Tan, F. (2020). The 2020 Mw 6.8 Elazığ (Turkey) earthquake reveals rupture behavior of the East Anatolian Fault. *Geophysical Research Letters*, 47(13):e2020GL088136.

Press, W. H., Teukolsky, S. A., Vetterling, W. T., and Flannery, B. P. (1992). *Numerical Recipes in C: The Art of Scientific Computing*. Cambridge University Press, Cambridge.

Priestley, K., Jackson, J., and McKenzie, D. (2008). Lithospheric structure and deep earthquakes beneath India, the Himalaya and southern Tibet. *Geophysical Journal International*, 172(1):345–362.

Proctor, R., Crook, R., J., McKeown, M., and Moresco, R. (1972). Relation of known faults to surface ruptures, 1971 San Fernando earthquake, southern California. *Geological Society of America Bulletin*, 83:1601–1618.

Qiao, X. and Zhou, Y. (2021). Geodetic imaging of shallow creep along the Xianshuihe fault and its frictional properties. *Earth and Planetary Science Letters*, 567:117001.

Quigley, M., Van Dissen, R., Litchfield, N., Villamor, P., Duffy, B., Barrell, D., Furlong, K., Stahl, T., Bilderback, E., and Noble, D. (2012). Surface rupture during the 2010 Mw 7.1 Darfield (Canterbury) earthquake: Implications for fault rupture dynamics and seismic-hazard analysis. *Geology*, 40(1):55–58.

Radiguet, M., Cotton, F., Manighetti, I., Campillo, M., and Douglas, J. (2009). Dependency of Near-Field Ground Motions on the Structural Maturity of the Ruptured Faults. *The Bulletin of the Seismological Society of America*, 99(4):2572–2581.

Reid, H. F. (1910). The mechanics of the earthquake. In *The California earthquake of April 18, 1906. Report of the State Earthquake Investigation Commission*, volume 2. Carnegie Institution, Washington, D.C.

Ren, J., Xu, X., Zhang, G., Wang, Q., Zhang, Z., Gai, H., and Kang, W. (2022). Coseismic surface ruptures, slip distribution, and 3D seismogenic fault for the 2021 Mw 7.3 Maduo earthquake, central Tibetan Plateau, and its tectonic implications. *Tectonophysics*, 827:229275.

Ren, Z. and Zhang, Z. (2019). Structural analysis of the 1997 Mw 7.5 Manyi earthquake and the kinematics of the Manyi fault, central Tibetan Plateau. *Journal of Asian Earth Sciences*, 179:149–164.

Rice, J. R., Sammis, C. G., and Parsons, R. (2005). Off-fault secondary failure induced by a dynamic slip pulse. *Bulletin of the Seismological Society of America*, 95(1):109–134.

Roger, F., Calassou, S., Lancelot, J., Malavieille, J., Mattauer, M., Zhiqin, X., Ziwen, H., and Liwei, H. (1995). Miocene emplacement and deformation of the Konga Shan granite (Xianshui He fault zone, west Sichuan, China): Geodynamic implications. *Earth and Planetary Science Letters*, 130(1-4):201–216.

Rosen, P. A., Hensley, S., Joughin, I. R., Li, F. K., Madsen, S. N., Rodriguez, E., and Goldstein, R. M. (2000). Synthetic aperture radar interferometry. *Proceedings of the IEEE*, 88(3):333–382.

Rosu, A.-M., Pierrot-Deseilligny, M., Delorme, A., Binet, R., and Klinger, Y. (2015). Measurement of ground displacement from optical satellite image correlation using the free open-source software MicMac. *ISPRS Journal of Photogrammetry and Remote Sensing*, 100:48–59.

Roten, D., Olsen, K., and Day, S. (2017). Off-fault deformations and shallow slip deficit from dynamic rupture simulations with fault zone plasticity. *Geophysical Research Letters*, 44(15):7733–7742.

Rowley, D. B. (1998). Minimum age of initiation of collision between India and Asia north of Everest based on the subsidence history of the Zhepure Mountain section. *The Journal of Geology*, 106(2):220–235.

Royden, L. H., Burchfiel, B. C., and van der Hilst, R. D. (2008). The geological evolution of the Tibetan Plateau. *Science*, 321(5892):1054–1058.

Ruppert, N. A. and West, M. E. (2020). The Impact of USArray on Earthquake Monitoring in Alaska. *Seismological Research Letters*.

Rutte, D., Ratschbacher, L., Khan, J., Stübner, K., Hacker, B. R., Stearns, M. A., Enkelmann, E., Jonckheere, R., Pfänder, J. A., Sperner, B., et al. (2017). Building the Pamir-Tibetan Plateau—Crustal stacking, extensional collapse, and lateral extrusion in the Central Pamir: 2. Timing and rates. *Tectonics*, 36(3):385–419.

Saltus, R. W., Hudson, T. L., and Connard, G. G. (1999). A new magnetic view of Alaska. *GSA Today*, 9(3):1–6.

Sangha, S., Peltzer, G., Zhang, A., Meng, L., Liang, C., Lundgren, P., and Fielding, E. (2017). Fault geometry of 2015, Mw7. 2 Murghab, Tajikistan earthquake controls rupture propagation: Insights from InSAR and seismological data. *Earth and Planetary Science Letters*, 462:132–141.

Savage, J., Burford, R., and Kinoshita, W. (1975). Earth movements from geodetic measurements. In Oakeshott, G., editor, *San Fernando Earthquake of 9 February 1971*, volume 196, pages 175 – 186. California Division of Mines and Geology, Sacramento, CA.

Savage, J. and Church, J. (1975). Evidence for afterslip on the San Fernando Fault. *Bulletin of the Seismological Society of America*, 65(4):829–834.

Scott, C. P., Arrowsmith, J. R., Nissen, E., Lajoie, L., Maruyama, T., and Chiba, T. (2018). The M7 2016 Kumamoto, Japan, earthquake: 3-D deformation along the fault and within the damage zone constrained from differential lidar topography. *Journal of Geophysical Research: Solid Earth*, 123(7):6138–6155.

Searle, M., Windley, B., Coward, M., Cooper, D., Rex, A., Rex, D., Tingdong, L., Xuchang, X., Jan, M., Thakur, V., et al. (1987). The closing of Tethys and the tectonics of the Himalaya. *Geological Society of America Bulletin*, 98(6):678–701.

Sethanant, I., Nissen, E., Pousse-Beltran, L., Bergman, E., and Pierce, I. (2023). The 2020 Mw 6.5 Monte Cristo Range, Nevada, Earthquake: Anatomy of a Crossing-Fault Rupture through a Region of Highly Distributed Deformation. *Bulletin of the Seismological Society of America*.

Sharp, R. V. (1975). Displacement on tectonic ruptures. In Oakeshott, G., editor, *San Fernando Earthquake of 9 February 1971*, volume 196, pages 187–194. California Division of Mines and Geology, Sacramento, CA.

Shi, F., Li, A., Yang, X.-P., Xu, X.-W., and He, H.-L. (2013). Research on late quaternary activity of the southeastern segment of Ganzi-Yushu fault zone. *Dizhen Dizhi(Seismology and Geology)*, 35(1):50–63.

Shipton, Z. K. and Cowie, P. A. (2003). A conceptual model for the origin of fault damage zone structures in high-porosity sandstone. *Journal of Structural Geology*, 25(3):333–344.

Snay, R. A., Freymueller, J. T., Craymer, M. R., Pearson, C. F., and Saleh, J. (2016). Modeling 3-D crustal velocities in the United States and Canada. *Journal of Geophysical Research: Solid Earth*, 121(7):5365–5388.

Soumaya, A., Ben Ayed, N., Rajabi, M., Meghraoui, M., Delvaux, D., Kadri, A., Ziegler, M., Maouche, S., and Braham, A. (2018). Active Faulting Geometry and Stress Pattern Near Complex Strike-Slip Systems Along the Maghreb Region: Constraints on Active Convergence in the Western Mediterranean. *Tectonics*, 37(9):3148–3173.

Stein, R. S., King, G. C., and Lin, J. (1994). Stress triggering of the 1994 M= 6.7 Northridge, California, earthquake by its predecessors. *Science*, 265(5177):1432–1435.

Sylvester, A. and Pollard, D. (1975). Afterslip on the Sylmar Fault Segment. In Oakeshott, G., editor, *San Fernando Earthquake of 9 February 1971*, volume 196, pages 227 – 233. California Division of Mines and Geology, Sacramento, CA.

Tan, F., Ge, Z., Kao, H., and Nissen, E. (2019). Validation of the 3-D phase-weighted relative back projection technique and its application to the 2016 $M_w$ 7.8 Kaikōura earthquake. *Geophysical Journal International*, 217(1):375–388.

Tang, X., Guo, R., Xu, J., Sun, H., Chen, X., and Zhou, J. (2021). Probing the fault complexity of the 2017 Ms 7.0 Jiuzhaigou earthquake based on the InSAR data. *Remote Sensing*, 13(8):1573.

Tapponnier, P., Meyer, B., Avouac, J. P., Peltzer, G., Gaudemer, Y., Shunmin, G., Hongfa, X., Kelun, Y., Zhitai, C., Shuahua, C., et al. (1990). Active thrusting and folding in the Qilian Shan, and decoupling between upper crust and mantle in northeastern Tibet. *Earth and Planetary Science Letters*, 97(3-4):382–403.

Tapponnier, P. and Molnar, P. (1977). Active faulting and tectonics in China. *Journal of Geophysical Research*, 82(20):2905–2930.

Tapponnier, P., Zhiqin, X., Roger, F., Meyer, B., Arnaud, N., Wittlinger, G., and Jingsui, Y. (2001). Oblique stepwise rise and growth of the Tibet Plateau. *Science*, 294(5547):1671–1677.

Taylor, M. and Yin, A. (2009). Active structures of the Himalayan-Tibetan orogen and their relationships to earthquake distribution, contemporary strain field, and Cenozoic volcanism. *Geosphere*, 5(3):199–214.

Templeton, E. L. and Rice, J. R. (2008). Off-fault plasticity and earthquake rupture dynamics: 1. Dry materials or neglect of fluid pressure changes. *Journal of Geophysical Research: Solid Earth*, 113(B9).

Thakur, P. and Huang, Y. (2021). Influence of fault zone maturity on fully dynamic earthquake cycles. *Geophysical Research Letters*, 48(17):e2021GL094679.

Thakur, P., Huang, Y., and Kaneko, Y. (2020). Effects of Low-Velocity Fault Damage Zones on Long-Term Earthquake Behaviors on Mature Strike-Slip Faults. *Journal of Geophysical Research: Solid Earth*, 125(8):e19587.

Thomas, M. Y. and Bhat, H. S. (2018). Dynamic evolution of off-fault medium during an earthquake: a micromechanics based model. *Geophysical Journal International*, 214(2):1267–1280.

Townley, S. D. and Allen, M. W. (1939). Descriptive catalog of earthquakes of the Pacific Coast of the United States 1769 to 1928. *Bulletin of the Seismological Society of America*, 29(1):1–297.

Tsutsumi, H. and Yeats, R. S. (1999). Tectonic setting of the 1971 Sylmar and 1994 Northridge earthquakes in the San Fernando Valley, California. *Bulletin of the Seismological Society of America*, 89(5):1232–1249.

Vallage, A., Klinger, Y., Grandin, R., Bhat, H., and Pierrot-Deseilligny, M. (2015). Inelastic surface deformation during the 2013 Mw 7.7 Balochistan, Pakistan, earthquake. *Geology*, 43(12):1079–1082.

Walker, R. T., Bergman, E. A., Szeliga, W., and Fielding, E. J. (2011). Insights into the 1968-1997 Dasht-e-Bayaz and Zirkuh earthquake sequences, eastern Iran, from calibrated relocations, InSAR and high-resolution satellite imagery. *Geophysical Journal International*, 187(3):1577–1603.

Wallace, W. (1992). Detachment folds above a passive-roof duplex: an example from the northeastern Brooks Range, Alaska. Alaska Division of Geological & Geophysical Surveys, U.S. Geological Survey - Public Data File 92-9.

Wallace, W. and Hanks, C. (1990). Structural Provinces of the Northeastern Brooks Range, Arctic National Wildlife Refuge, Alaska. *AAPG Bulletin*, 74(7):1100–1118.

Wan, Y.-G., Shen, Z.-K., Wang, M., Zhang, Z.-S., Gan, W.-J., Wang, Q.-L., and Sheng, S.-Z. (2008). Coseismic slip distribution of the 2001 Kunlun mountain pass west earthquake constrained by GPS and InSAR data. *Chinese Journal of Geophysics*, 51(4):753–764.

Wang, H., Wright, T., and Biggs, J. (2009a). Interseismic slip rate of the northwestern Xianshuihe fault from InSAR data. *Geophysical Research Letters*, 36(3).

Wang, H., Wright, T. J., Liu-Zeng, J., and Peng, L. (2019). Strain rate distribution in south-central Tibet from two decades of InSAR and GPS. *Geophysical Research Letters*, 46(10):5170–5179.

Wang, K., Dreger, D. S., Tinti, E., Bürgmann, R., and Taira, T. (2020). Rupture process of the 2019 Ridgecrest, California Mw 6.4 foreshock and Mw 7.1 earthquake constrained by seismic and geodetic data. *Bulletin of the Seismological Society of America*, 110(4):1603–1626.

Wang, K., Zhu, Y., Nissen, E., and Shen, Z.-K. (2021). On the relevance of geodetic deformation rates to earthquake potential. *Geophysical Research Letters*, 48(11):e2021GL093231.

Wang, M. and Shen, Z.-K. (2020). Present-day crustal deformation of continental China derived from GPS and its tectonic implications. *Journal of Geophysical Research: Solid Earth*, 125(2):e2019JB018774.

Wang, Q., Zhang, P.-Z., Freymueller, J. T., Bilham, R., Larson, K. M., Lai, X., You, X., Niu, Z., Wu, J., Li, Y., et al. (2001). Present-day crustal deformation in China constrained by global positioning system measurements. *Science*, 294(5542):574–577.

Wang, S., Fan, C., Wang, G., and Wang, E. (2008). Late Cenozoic deformation along the northwestern continuation of the Xianshuihe fault system, Eastern Tibetan Plateau. *Geological Society of America Bulletin*, 120(3-4):312–327.

Wang, S., Fang, X., Zheng, D., and Wang, E. (2009b). Initiation of slip along the Xianshuihe fault zone, eastern Tibet, constrained by K/Ar and fission-track ages. *International Geology Review*, 51(12):1121–1131.

Wang, S., Song, C., Li, S., and Li, X. (2022a). Resolving co-and early post-seismic slip variations of the 2021 Mw 7.4 Madoi earthquake in east Bayan Har block with a block-wide distributed deformation mode from satellite synthetic aperture radar data. *Earth Planet. Phys*, 6(1):108–122.

Wang, W., Zhang, P., Garzione, C. N., Liu, C., Zhang, Z., Pang, J., Wang, Y., Zheng, D., Zheng, W., and Zhang, H. (2022b). Pulsed rise and growth of the Tibetan Plateau to its northern margin since ca. 30 Ma. *Proceedings of the National Academy of Sciences*, 119(8):e2120364119.

Wang, W., Zheng, W., Zhang, P., Li, Q., Kirby, E., Yuan, D., Zheng, D., Liu, C., Wang, Z., Zhang, H., et al. (2017). Expansion of the Tibetan Plateau during the Neogene. *Nature communications*, 8(1):15887.

Ward, K. M. and Lin, F.-C. (2018). Lithospheric structure across the Alaskan cordillera from the joint inversion of surface waves and receiver functions. *Journal of Geophysical Research: Solid Earth*, 123(10):8780–8797.

Weber, F. H. (1975). Surface effects and related geology of the San Fernando earthquake in the Sylmar area. In Oakeshott, G., editor, *San Fernando Earthquake of 9 February 1971*, volume 196, pages 71–96. California Division of Mines and Geology, Sacramento, CA.

Wei, S., Zeng, H., Shi, Q., Liu, J., Luo, H., Hu, W., Li, Y., Wang, W., Ma, Z., Liu-Zeng, J., et al. (2022). Simultaneous rupture propagation through fault bifurcation of the 2021 Mw7.4 Maduo earthquake. *Geophysical Research Letters*, 49(21):e2022GL100283.

Weiss, J. R., Walters, R. J., Morishita, Y., Wright, T. J., Lazecky, M., Wang, H., Hussain, E., Hooper, A. J., Elliott, J. R., Rollins, C., et al. (2020). High-resolution surface velocities and strain for Anatolia from Sentinel-1 InSAR and GNSS data. *Geophysical Research Letters*, 47(17):e2020GL087376.

Wells, D. L. and Coppersmith, K. J. (1994). New empirical relationships among magnitude, rupture length, rupture width, rupture area, and surface displacement. *Bulletin of the Seismological Society of America*, 84(4):974–1002.

Wen, X.-Z., Ma, S.-L., Xu, X.-W., and He, Y.-N. (2008). Historical pattern and behavior of earthquake ruptures along the eastern boundary of the Sichuan-Yunnan faulted-block, southwestern China. *Physics of the Earth and Planetary Interiors*, 168(1-2):16–36.

Wentworth, C. M., Yerkes, R., and Allen, C. R. (1971). Geologic setting and activity of faults in the San Fernando area, California. In *The San Fernando, California Earthquake of February 9th, 1971*, pages 6 – 16. U.S. Geological Survey, Washington, D.C., USA.

Wesnousky, S. G. (1988). Seismological and structural evolution of strike-slip faults. *Nature*, 335(6188):340–343.

Wesnousky, S. G. (1990). Seismicity as a function of cumulative geologic offset: some observations from southern California. *Bulletin of the Seismological Society of America*, 80(5):1374–1381.

Wesnousky, S. G. (1994). The Gutenberg-Richter or characteristic earthquake distribution, which is it? *Bulletin of the Seismological Society of America*, 84(6):1940–1959.

Wessell, P., Smith, W., Scharroo, R., Luis, J., and Wobbe, F. (2013). Generic Mapping Tools: Improved Version Released. *Eos Transactions*, 94:409–410.

Whitcomb, J. H., Allen, C. R., Garmany, J. D., and Hileman, J. A. (1973). San Fernando earthquake series, 1971: focal mechanisms and tectonics. *Reviews of Geophysics*, 11(3):693–730.

Wolf, P. R. and Dewitt, B. A. (2000). *Elements of photogrammetry: with applications in GIS*, volume 3. McGraw-Hill New York.

Wollherr, S., Gabriel, A.-A., and Mai, P. M. (2019). Landers 1992 "reloaded": Integrative dynamic earthquake rupture modeling. *Journal of Geophysical Research: Solid Earth*, 124(7):6666–6702.

Wright, T. J., Elliott, J. R., Wang, H., and Ryder, I. (2013). Earthquake cycle deformation and the Moho: Implications for the rheology of continental lithosphere. *Tectonophysics*, 609:504–523.

Wright, T. J., Lu, Z., and Wicks, C. (2003). Source model for the Mw 6.7, 23 October 2002, Nenana mountain earthquake (Alaska) from InSAR. *Geophysical Research Letters*, 30(18).

Wright, T. J., Parsons, B. E., Jackson, J. A., Haynes, M., Fielding, E. J., England, P. C., and Clarke, P. J. (1999). Source parameters of the 1 October 1995 Dinar (Turkey) earthquake from SAR interferometry and seismic bodywave modelling. *Earth and Planetary Science Letters*, 172:23–37.

Wu, J.-W., Huang, X.-M., and Xie, F.-R. (2017). Late quaternary slip rate of the Garze-Yushu fault zone (Dangjiang Segment). *Chinese Journal of Geophysics*, 60(10):3872–3888.

Xu, L., Chen, Q., Zhao, J.-J., Liu, X.-W., Xu, Q., and Yang, Y.-H. (2021). An Integrated Approach for Mapping Three-Dimensional CoSeismic Displacement Fields from Sentinel-1 TOPS Data Based on DInSAR, POT, MAI and BOI Techniques: Application to the 2021 Mw 7.4 Maduo Earthquake. *Remote Sensing*, 13(23):4847.

Xu, L., Yunjun, Z., Ji, C., Meng, L., Fielding, E. J., Zinke, R., and Bao, H. (2023). Understanding the Rupture Kinematics and Slip Model of the 2021 Mw 7.4 Maduo Earthquake: A Bilateral Event on Bifurcating Faults. *Journal of Geophysical Research: Solid Earth*, page e2022JB025936.

Xu, X. (1999). Scientific investigation of the Manyi earthquake in North Tibet. In Liu, Y., editor, *Yearbook of China Earthquake Research*, pages 327 – 329. Seismological Press, Beijing, China.

Xu, X., Tong, X., Sandwell, D. T., Milliner, C. W., Dolan, J. F., Hollingsworth, J., Leprince, S., and Ayoub, F. (2016a). Refining the shallow slip deficit. *Geophysical Journal International*, 204(3):1867–1886.

Xu, X., Tong, X., Sandwell, D. T., Milliner, C. W., Dolan, J. F., Hollingsworth, J., Leprince, S., and Ayoub, F. (2016b). Refining the shallow slip deficit. *Geophysical Journal International*, 204(3):1867–1886.

Xu, X., Yeats, R. S., and Yu, G. (2010). Five Short Historical Earthquake Surface Ruptures near the Silk Road, Gansu Province, ChinaFive Short Historical Earthquake Surface Ruptures near the Silk Road, Gansu Province, China. *Bulletin of the Seismological Society of America*, 100(2):541–561.

Xu, X., Yu, G., Klinger, Y., Tapponnier, P., and Van Der Woerd, J. (2006). Reevaluation of surface rupture parameters and faulting segmentation of the 2001 Kunlunshan earthquake (Mw7.8), northern Tibetan Plateau, China. *Journal of Geophysical Research: Solid Earth*, 111(B5).

Yamashita, T. (2000). Generation of microcracks by dynamic shear rupture and its effects on rupture growth and elastic wave radiation. *Geophysical Journal International*, 143(2):395–406.

Yan, B. and Lin, A. (2015). Systematic deflection and offset of the Yangtze River drainage system along the strike-slip Ganzi-Yushu-Xianshuihe Fault Zone, Tibetan Plateau. *Journal of Geodynamics*, 87:13–25.

Yang, H., Wang, D., Guo, R., Xie, M., Zang, Y., Wang, Y., Yao, Q., Cheng, C., An, Y., and Zhang, Y. (2022). Rapid report of the 8 January 2022 Ms 6.9 Menyuan earthquake, Qinghai, China. *Earthquake Research Advances*, 2(1):100113.

Yao, S. and Yang, H. (2022). Hypocentral dependent shallow slip distribution and rupture extents along a strike-slip fault. *Earth and Planetary Science Letters*, 578:117296.

Yu, J., Zheng, D., Wang, W., Pang, J., Li, C., Wang, Y., Hao, Y., Zhang, H., and Zhang, P. (2023). Cenozoic tectonic development in the northeastern Tibetan Plateau: Evidence

from thermochronological and sedimentological records. *Global and Planetary Change*, 224:104098.

Yuan, D., Zhang, P., Ge, W., Liu, X., Zhang, H., and Liang, M. (2008). Late Quaternary strike-slip features along the western segment of Haiyuan-Qilianshan fault, NE Tibetan Plateau. In *AGU Fall Meeting Abstracts*, volume 2008, pages T33B–2057.

Yuan, Z., Li, T., Su, P., Sun, H., Ha, G., Guo, P., Chen, G., and Thompson Jobe, J. (2022). Large surface-rupture gaps and low surface fault slip of the 2021 Mw 7.4 Maduo earthquake along a low-activity strike-slip fault, Tibetan Plateau. *Geophysical Research Letters*, 49(6):e2021GL096874.

Yue, H., Shen, Z.-K., Zhao, Z., Wang, T., Cao, B., Li, Z., Bao, X., Zhao, L., Song, X., Ge, Z., et al. (2022). Rupture process of the 2021 M7.4 Maduo earthquake and implication for deformation mode of the Songpan-Ganzi terrane in Tibetan Plateau. *Proceedings of the National Academy of Sciences*, 119(23):e2116445119.

Zhang, P.-Z., Shen, Z., Wang, M., Gan, W., Burgmann, R., Molnar, P., Wang, Q., Niu, Z., Sun, J., Wu, J., et al. (2004a). Continuous deformation of the Tibetan Plateau from global positioning system data. *Geology*, 32(9):809–812.

Zhang, X., Feng, W., Du, H., Samsonov, S., and Yi, L. (2022). Supershear rupture during the 2021 MW 7.4 Maduo, China, earthquake. *Geophysical Research Letters*, 49(6):e2022GL097984.

Zhang, X., Xu, L.-S., Li, L., Yi, L., and Feng, W. (2019). Confirmation of the double-asperity model for the 2016 MW 6.6 Akto earthquake (NW China) by seismic and InSAR data. *Journal of Asian Earth Sciences*, 184:103998.

Zhang, Y., Chen, J., Gong, W., Han, N., Liu, Y., and Shan, X. (2023). Geodetic modeling of the 2022 Mw 6.6 Menyuan earthquake: Insight into the strain-partitioned northern Qilian Shan fault system and implications for regional tectonics and seismic hazards. *Geophysical Journal International*.

Zhang, Y., Chen, W., Yang, N., et al. (2004b). Ar-40/Ar-39 dating of shear deformation of the Xianshuihe fault zone in; west Sichuan and its tectonic significance. *Science in China*.

Zhao, D., Qu, C., Bürgmann, R., Gong, W., Shan, X., Qiao, X., Zhao, L., Chen, H., and Liu, L. (2022a). Large-Scale Crustal Deformation, Slip-Rate Variation, and Strain Distribution Along the Kunlun Fault (Tibet) From Sentinel-1 InSAR Observations (2015–2020). *Journal of Geophysical Research: Solid Earth*, 127(1):e2021JB022892.

Zhao, D., Qu, C., Burgmann, R., Shan, X., Li, T., Li, C., Chen, H., and Gong, W. (under revision, 2023). Deep, shallow and surface fault-zone deformation during and after the 2021 Mw7. 4 Maduo, Qinghai, earthquake illuminates fault structural immaturity. *Authorea Preprints*.

Zhao, D., Qu, C., Chen, H., Shan, X., Song, X., and Gong, W. (2022b). Tectonic and geometric control on fault kinematics of the 2021 Mw7.3 Maduo (China) earthquake inferred from interseismic, coseismic, and postseismic InSAR observations. *Geophysical Research Letters*, 48(18):e2021GL095417.

Zhao, D., Qu, C., Shan, X., Gong, W., Zhang, G., and Song, X. (2019). New insights into the 2010 Yushu Mw6.9 mainshock and Mw5.8 aftershock, China, from InSAR observations and inversion. *Journal of Geodynamics*, 125:22–31.

Zhao, D., Qu, C., Shan, X., Gong, W., Zhang, Y., and Zhang, G. (2018). InSAR and GPS derived coseismic deformation and fault model of the 2017 Ms7.0 Jiuzhaigou earthquake in the Northeast Bayanhar block. *Tectonophysics*, 726:86–99.

Zheng, A., Yu, X., Xu, W., Chen, X., and Zhang, W. (2020). A hybrid source mechanism of the 2017 Mw 6.5 Jiuzhaigou earthquake revealed by the joint inversion of strong-motion, teleseismic and InSAR data. *Tectonophysics*, 789:228538.

Zheng, G., Wang, H., Wright, T. J., Lou, Y., Zhang, R., Zhang, W., Shi, C., Huang, J., and Wei, N. (2017). Crustal deformation in the India-Eurasia collision zone from 25 years of GPS measurements. *Journal of Geophysical Research: Solid Earth*, 122(11):9290–9312.

Zheng, W.-J., Zhang, P.-Z., He, W.-G., Yuan, D.-Y., Shao, Y.-X., Zheng, D.-W., Ge, W.-P., and Min, W. (2013). Transformation of displacement between strike-slip and crustal shortening in the northern margin of the Tibetan Plateau: Evidence from decadal GPS measurements and late Quaternary slip rates on faults. *Tectonophysics*, 584:267–280. Active Tectonic Deformation of the Tibetan Plateau and Great Earthquakes.

Zhu, G., Liang, X., Tian, X., Yang, H., Wu, C., Duan, Y., Li, W., and Zhou, B. (2017). Analysis of the seismicity in central Tibet based on the SANDWICH network and its tectonic implications. *Tectonophysics*, 702:1–7.

Zhu, Y., Diao, F., Fu, Y., Liu, C., and Xiong, X. (2021). Slip rate of the seismogenic fault of the 2021 Maduo earthquake in western China inferred from GPS observations. *Science China Earth Sciences*, 64:1363–1370.

Zielke, O., Galis, M., and Mai, P. M. (2017). Fault roughness and strength heterogeneity control earthquake size and stress drop. *Geophysical Research Letters*, 44(2):777–783.

Zinke, R., Dolan, J. F., Van Dissen, R., Grenader, J. R., Rhodes, E. J., McGuire, C. P., Langridge, R. M., Nicol, A., and Hatem, A. E. (2015). Evolution and progressive geomorphic manifestation of surface faulting: A comparison of the Wairau and Awatere faults, South Island, New Zealand. *Geology*, 43(11):1019–1022.

Zinke, R., Hollingsworth, J., and Dolan, J. F. (2014). Surface slip and off-fault deformation patterns in the 2013 $M_w$ 7.7 Balochistan, Pakistan earthquake: Implications for controls on the distribution of near-surface coseismic slip. *Geochemistry, Geophysics, Geosystems*, 15(12):5034–5050.

Zinke, R., Hollingsworth, J., Dolan, J. F., and Van Dissen, R. (2019). Three-Dimensional Surface Deformation in the 2016 $M_W$ 7.8 Kaikōura, New Zealand, Earthquake From Optical Image Correlation: Implications for Strain Localization and Long-Term Evolution of the Pacific-Australian Plate Boundary. *Geochemistry, Geophysics, Geosystems*, 20(3):1609–1628.

Zubovich, A., Metzger, S., Schöne, T., Kley, J., Mosienko, O., Zech, C., Moldobekov, B., and Shsarshebaev, A. (2022). Cyclic Fault Slip Under the Magnifier: Co-and Postseismic Response of the Pamir Front to the 2015 Mw7. 2 Sarez, Central Pamir, Earthquake. *Tectonics*, 41(9):e2022TC007213.